- **TESI DOCTORAL UPF / 2012**

Brain activity during rest

A signature of the underlying network dynamics

Joana R. B. Cabral

Director de la tesi

Prof. Gustavo Deco

Department of Information and Communication Technologies

Universitat Pompeu Fabra

Barcelona, May 2012

In memory of the ones who dedicated
their life to neuroscience.

Acknowledgments

A fulfilled life is reached when you make an effort to follow your dreams.

During the spring of 2007, at the age of 23, driven by an insatiable eagerness for learning more about the fascinating field of neuroscience, I visited prof. Gustavo Deco in Barcelona with the possibility of pursuing my PhD studies in Theoretical and Computational Neuroscience. From that first day, Gustavo has given me unconditional support and motivation. Over the past five years, he has guided me through the paths of a research life always with a smile. Above all, he taught me how to *do* science, by listening to my ideas and telling me to explore them and prove them. For this and for all, I wish to thank him not only for supervising me, but also for inspiring me.

My aims to engage in a neuroscientist's career appeared while performing fieldwork for my Master's thesis at the Lisbon's Psychiatric Hospital with Prof. Mario Secca and Dr. Alberto Leal, with whom I got familiar with the unresolved mysteries of brain dynamics and particularly interested about the alterations observed in brain activity of subjects diagnosed with mental illnesses. I want to thank them for that and for supporting my PhD grant application.

This PhD would have hardly been possible without the wonderful sponsoring from the *Portuguese Foundation of Science and Technology* and the *European Social Fund,* to which I am grateful.

During my PhD research, I worked in close collaboration with several people to whom I am in debt. I would like to start with Etienne Hugues, to whom I want to express my gratitude for patiently guiding me through the complicated mathematical concepts of nonlinear dynamics, for carefully reviewing my simulation codes and for helping me understand the complex dynamics emerging from the simulations.

Outside academia, but not less important, I would like to start by acknowledging the ones who brought me to life, Carlos and Ni, who stimulated my brain since early ages by feeding me with puzzles and quizzes, who gave me unconditional love and support in every moment of my life, and provided me the tools and inspiration to become the person I am today. I also want to thank my lovely little (almost twin) sister Catarina, with whom I shared most of my life, and Tomás, who became my brother in law during this PhD. I want to thank all my large family, especially my grandmother, who I still tenderly call *Bábá*.

The most important source of support in my PhD came from a very special person: someone who listened carefully to incomprehensible theories, who gave me strength and motivation, who constantly lifted me up, and who makes me believe that, one day, I will uncover all the mysteries in the brain. *Merci* Duarte. It is by the side of someone like this that life should be lived. As I say in the beginning, '*A fulfilled life is reached when you make an effort to follow your dreams*', and if my previous dream was to become a neuroscientist, now that I am on track, I have a new one to follow.

I also want to thank my best friends, for always being there despite the distance, which I will cite in alphabetical order to avoid conflict: Babs, Beni, Joana, Juju, Maggie, Mariana AL, Mariana HV, Matilde, Sara, Sofia and Xica. You are all tremendously important in my life. Also, a special *thank you* to Francisca Figueiras, who came with me to Barcelona in May 2007 to visit research labs and who is depositing the PhD thesis on the exact same day as me, and Joana Mesquita.

Finally, I wish to acknowledge the Members of the Committee, for their time and interest, and all the future readers of this thesis.

I hope you enjoy reading it as much as I did writing it.

Abstract

Neural activity in the brain exhibits complex oscillatory phenomena that can be compared with the ones observed in artificial network models of coupled oscillators. In particular, neuroimaging studies of brain activity during rest have reported slow spatiotemporally organized fluctuations and correlated band-limited power modulations. Simultaneously, theoretical works on the area of physics have reported similar dynamic behaviours using simple models of coupled oscillators with intermittent modular synchronization.

In this work, for the first time, we use models of phase oscillators in networks inspired in the brain's wiring architecture. Results show the spontaneous emergence of a dynamics similar to the one observed experimentally. In addition, this correspondence is quantitatively comparable to neuroimaging data, which is suggestive of general integrative processes underlying cognition. Furthermore, we propose that altered brain activity observed in some psychiatric diseases might originate from structural disconnections, which affect the cooperative behaviour of coupled cortical regions.

Resumen

La actividad neuronal en el cerebro exhibe complejos fenómenos oscilatorios similares a los que se observan en modelos de redes artificiales con osciladores acoplados. Por un lado, estudios de neuroimagen sobre la actividad cerebral durante el reposo han demostrado la presencia de fluctuaciones lentas estructuradas y modulaciones de potencia a distintas frecuencias. Simultáneamente, se han publicado estudios teóricos en el ámbito de la física que muestran dinámicas similares usando osciladores acoplados con sincronización modular intermitente.

En este trabajo, por primera vez, se usan modelos de osciladores de fase en redes inspiradas en la arquitectura real del cerebro. Los resultados muestran la aparición espontánea de una dinámica similar a la observada experimentalmente. Además, esta correspondencia es comparable cuantitativamente con datos de neuroimagen, lo que sugiere procesos generales de integración subyacentes a la cognición. Por otra parte, se propone que la actividad cerebral alterada observada en algunas enfermedades psiquiátricas podría tener su origen en desconexiones estructurales que afectarían el comportamiento cooperativo de regiones corticales acopladas.

Preface

How cognition unfolds from the physical structure of the brain is still one of the leading unresolved mysteries of science. For its complexity, this investigation has been progressively extended from the medical field to theoretical sciences such as physics and mathematics. In particular, the approach of the brain as a complex dynamical system, where multiple units, be they neurons or cortical areas, interact with each other in a cooperative manner to integrate and process information, has only recently begun to be explored.

It is believed we are only now engaging in the era of Neuroscience. Constant innovation in neuroimaging techniques allows us to explore non-invasively brain structure and dynamics at increasingly higher spatial and temporal resolution. Every year, more than thirty thousand neuroscientists meet together to discuss and share the latest advances in Neuroscience at the *Society for Neuroscience* annual meeting. Furthermore, thanks to efficient publication mechanisms and to the immediate availability of literature in the internet, the cooperative work of neuroscientists from all over the world has increased exponentially. In the same way as neurons build cognition through cooperative processes, I expect the cumulative discoveries about the brain will lead, hopefully soon enough, to a complete understanding of the brain.

This thesis focuses on ongoing activity of the brain at rest, i.e., under no stimulation and in absence of any physical or mental task. At first sight, it may seem uninteresting to explore this particular mental state in which no cognitive process is engaged. Indeed, to do and think nothing is hard to accomplish for the normal human being. Like most animals, when we are awake, even at rest, we are naturally driven toward activity. It seems like there is an intrinsic instability that impels us to move, to think, to survive. Remarkably, this instability has been detected in neuroimaging studies revealing a rich dynamics with multiple coexisting spatiotemporal patterns.

In the Introduction of this thesis, we will start by reviewing the most important findings of resting-state activity, covering a range of neuroimaging modalities including fMRI, EEG and MEG (section I.I). These

functional studies are suggestive of an underlying network dynamics that is strongly shaped by white-matter connectivity. Therefore, in section I.II we focus on brain networks, both anatomical and functional. We explain how connections can be detected, how macroscopic networks can be built and which techniques are available to analyze them. In section I.III we review existing modelling studies, which, by means of reduced neural-mass models, simulate the dynamics of coupled cortical regions with brain-inspired connectivity and reproduce important features resting-state dynamics. Finally, in section I.V, we introduce the motivation for the work presented in this thesis.

In chapter II, we introduce the Kuramoto model of coupled oscillators. We explain how cortical regions can be represented in an abstract way as phase oscillators and study the influence of parameters such as delays, coupling strength and frequency dispersion in the dynamics of coupled phase-oscillators, when these are connected according to the macroscopic wiring architecture of the brain.

To test if our theoretical predictions can explain resting state dynamics, we compare our modelling results with data obtained in neuroimaging studies from healthy subjects during rest. In chapter III, we match our results with BOLD fMRI functional connectivity, showing that slow hemodynamic fluctuations can originate from slow fluctuations in the synchrony degree of subsets of nodes. In order to explore the relationship with ongoing activity occurring at faster time scales revealed by electrophysiological studies, in chapter IV we compare our results with data recorded with MEG. We find that slow band-limited power fluctuations can be explained as well by fluctuations in the synchrony degree, making the link between fast and slow spontaneous dynamics. Finally, in chapter V we study the impact of a structural disconnection in the topological properties of resting-state functional networks. These results are suggestive of the mechanisms leading to functional alterations occurring in psychiatric diseases such as schizophrenia.

Contents

I - Introduction

I.I - Brain activity during rest

Someone who is awake but not performing any task, physical or mental, is said to be resting. In this state, unlike sleeping, the person is conscious and ready to respond promptly to any sort of external stimulation or cognitive requirement. One could say that the person is somehow in *stand-by*: although still and quiet, she is awake, ready to suddenly chase a fly that lightly lands on her arm, or to immediately turn her head towards the least disturbing sound. Notably, while the person is resting and the body is static, the brain instead seems to be actively engaged, exhibiting spatiotemporally organized fluctuations of neuronal activation. These resting-state fluctuations emerge spontaneously during quiet wakeful rest and vanish either when triggered by a task or when attention to the external environment fades and the person falls asleep (Larson-Prior et al., 2011).

Several studies have speculated on the link between this resting brain activity and underlying high-order cognitive processes such as moral reasoning, self-consciousness, remembering past experiences or planning for the future (Saxe and Kanwisher, 2003, Wagner et al., 2005, Morcom and Fletcher, 2007, Buckner et al., 2008). However, findings of resting brain patterns in anesthetized monkeys (Vincent et al., 2007) and, more recently, in rats (Lu et al., 2012), make proof of a more primitive origin of resting brain activations (Figure 1). Evidence of coordinated brain activity during rest has been detected with a wide range of functional imaging modalities, including functional magnetic resonance imaging (fMRI) (Biswal et al., 1995), optical imaging (Arieli et al., 1996), positron-emission tomography (PET) (Raichle et al., 2001), electrophysiology (Laufs et al., 2003, Leopold et al.,

2003) and, more recently, magnetoencephalography (de Pasquale et al., 2010, Brookes et al., 2011b). This consistency across imaging techniques, which provide more or less direct measures of neuronal activation, makes proof of a robust intrinsic brain dynamics happening at multiple time-scales.
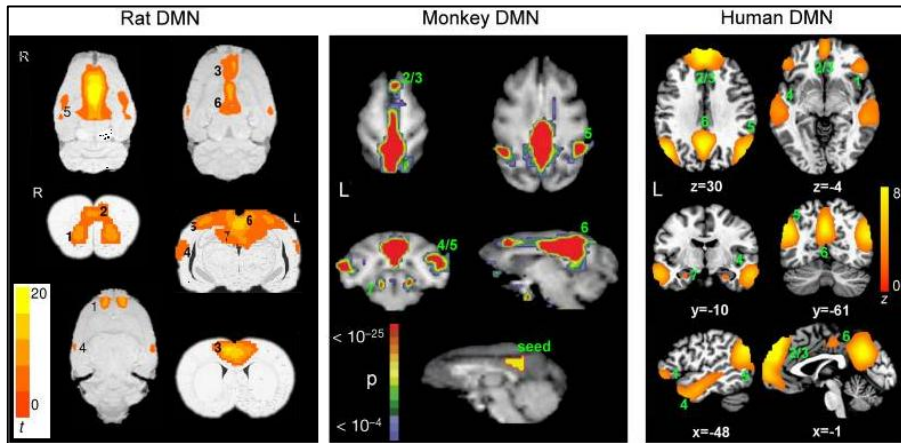
Figure 1 - Comparison of the Default Mode Network (DMN) in rats, monkeys and humans.
The regions composing the DMN exhibit correlated neuronal activations during rest. Adapted from Lu et al. (2012).

Furthermore, explorations into the organization of resting-state activations across the brain have revealed the existence of temporally correlated activity across subsets of spatially segregated brain structures, defining the so-called Resting State Networks (RSNs). Most of these RSNs have been shown to greatly overlap with functional architectures present during goal-directed activity, such as vision, language, executive processing, and other sensory and cognitive processes. On the other hand, one particular set of regions spatially distributed over the medial prefrontal, parietal, and posterior cingulate cortices has been found to exhibit correlated activations especially during rest, and therefore this specific RSN has been labelled as 'default-mode network' (DMN).

To investigate the origin of the co-activation patterns defining RSNs, several studies have inspected their relationship with the underlying map of long-range axonal connections using imaging techniques that allow the detection of white matter pathways in the living brain (Sporns et al., 2000, 2002). Although a remarkable match has been found between the neuro-anatomical network and resting-state functional connectivity patterns,

anatomical information alone does not uncover the dynamical mechanisms governing resting state activity in the temporal and frequency domains. Actually, since cortical regions are dynamical units (built of millions of highly interconnected excitatory and inhibitory neurons), we need to take into account the way these regions interact in the network to understand the origin of correlated fluctuations. At the regional level, in vivo electrophysiological recordings have shown that neural activity of large ensembles of neurons usually exhibits oscillations with a moderate level of synchrony. Following different reduction lines, a number of theoretical studies have attempted to describe most part of the population dynamics using only a few differential equations (Fitzhugh, 1961, Nagumo et al., 1962, Wilson and Cowan, 1972, Breakspear et al., 2003). These equations represent neural-mass models and are particularly useful for computational neuroscience, because they allow simulating the temporal dynamics of a large neuronal ensemble at low computational costs. When these dynamical units are embedded in the neuronatomic network, they interact with each other through excitatory-to-excitatory connections. Furthermore, if we consider axonal conduction speed to be finite, these long-range interactions are time-delayed, which, together with noise naturally present in the brain, introduce additional degrees of complexity to the system. To explore this complex network dynamics, computational models are valuable tools since they allow exploring the relationship between structural and functional connectivity not by simply comparing the corresponding spatial maps, but by considering the dynamics of interacting cortical regions.

To understand the natural mechanisms permitting the exploratory dynamics observed in the wakeful resting state, one can look at the brain as a dynamical system. Indeed, the complex space-time structure of the brain's wiring diagram, together with a myriad of biochemical processes, form a dynamical framework capable of holding an infinite number of mental states over which cognition unfolds (Tononi et al., 1994, Kelso, 2012). The existence of different input-dependent stable states in the brain has been evident since the first human electrophysiological recordings, which revealed that strong Alpha rhythms (8–13 Hz) were substituted by Beta rhythms (13-30Hz) when subjects opened their eyes (Berger, 1929). From the perspective of complex systems science, this phenomenon can be seen as a transition between two stable states, triggered by an external input. In

other words, while the eyes are closed we can imagine the brain finds a stable equilibrium in a regime in which Alpha oscillations emerge. Once the eyes are open, the incoming stimuli provoke a dynamical transition in phase space and another equilibrium point is found, in which Beta oscillations appear. Even before, in 1875, Richard Caton had already noticed that different brain states could be characterized by a particular electrical signature as noticed by Berger (1929):

"Caton has already published experiments on the brains of dogs and apes in which bare unipolar electrodes were placed either on the cerebral cortex and the other on the surface of the skull. The currents were measured by a sensitive galvanometer. There were found distinct variations in current, which increased during sleep and with the onset of death strengthened, and after death became weaker and then completely disappeared. (Berger, 1929)[1].

Despite referring to non-human species, Caton's findings seem to be the first to describe different brain states (i.e. wakefulness and sleepiness) according to their electrophysiological signature. However, the genesis of these frequencies, as well as the transition between brain states, remains until today incompletely understood.

Over the years, electrophysiological studies have identified characteristic brain rhythms ranging from 0.5 to 100Hz that appear and disappear according to the mental state in which the brain in engaged. Moreover, with the improvement of neuroimaging techniques, it became possible to map the sources of such rhythms across the brain, resulting in a temporal and a spatial pattern for each brain regime. Notably, consistency was found in the spatio-temporal signature of brain states across healthy humans. Although many brain states are only activated by means of stimulation, such as a sensory perception or a mental operation, other brain states, like resting and sleeping, occur spontaneously from intrinsic brain processes. Still, little is known about the physical mechanisms underlying the spatio-temporal patterns of different brain states and the dynamical transitions between them.

---

[1] *Translated from German to English by Cohen, 1959.*

Among all brain regimes, the resting state is particularly interesting from the perspective of dynamical systems because it exhibits not one, but several coexisting spatio-temporal patterns. These findings suggest that, during rest, the brain is routinely exploring different brain states, resulting in a multistable stationary regime. Deco et al. (2009) proposed that this spontaneous switching between brain states could be due to noisy transitions from one equilibrium point to another in the state space of the brain. Furthermore, they made a nice analogy to explain this behaviour: '*the resting state is like a tennis player waiting for the service of his opponent. The player is not statically at rest, but rather actively moving making small jumps to the left and to the right, because in this way, when the fast ball is coming, he can rapidly react'.* On receiving an external stimulus, the stability of the state involved in processing that input increases with respect to the others, allowing a rapid switch between brain states at the onset of a task.
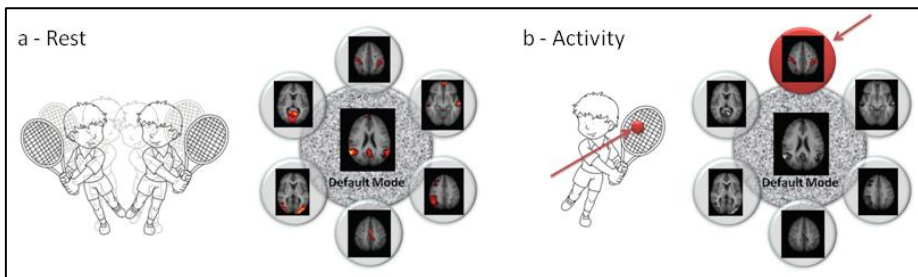
Figure 2 - Allegorical illustration of resting-state versus active-state. (a) During rest, the brain is in a multistable regime exploring different available mental states, like a tennis player who jumps from left to right while waiting for the service of his opponent. (b) In this way, upon receiving a stimulus, the brain can rapidly react and engage the regions in charge of processing the stimulus.

While the real mechanisms underlying resting-state activity remain unclear, the better way to explore this intriguing dynamics is to combine existing concepts of theoretical physics and experimental electrophysiology with brain-inspired network structures and, by means of computational models, investigate the natural conditions under which such type of nonlinear complex dynamics could emerge.

In this chapter, we will start by introducing the state of the art in resting-state neuroimaging studies, including hemodynamic and electro-physiological results, followed by the recent advances in brain connectivity

focusing on anatomical and functional brain networks, and a detailed description of existing models of resting-state activity. Finally, we explain the motivation and goals of the research undergone during my PhD studies.

I.I.1– Resting-state hemodynamic fluctuations

When unexpected results emerge from a scientific experimentation, history tells us that they should not be left unexamined. In the same way as Penzias and Wilson (1965) accidentally discovered cosmic background radiation while trying to eliminate all recognizable interference from their radio receiver (and later won the Nobel prize for it), Biswal and colleagues (1995) also found resting-state activity quite by accident. Actually, while they were trying to identify the brain regions that co-activated during bilateral finger tapping, they found that the areas involved in hand movement exhibited correlated activations not only during finger movement, but also during rest. Even after removing heart and respiratory frequencies and ensuring that the hands were immobilized, Biswal and colleagues found slow (<0.1Hz) fluctuations in the activation levels of the sensorimotor cortex that were strongly correlated even across hemispheres. This observation was particularly disturbing for current neuroimaging studies, which aimed to detect task-related (evoked) neuronal activations using the blood-oxygen-level dependent (BOLD) contrast (Ogawa et al., 1990) with functional Magnetic Resonance Imaging (fMRI)[1], since these studies rely on the comparison with a baseline activity. Studies using optical imaging in cat visual cortex verified that the variability of evoked responses resulted from the dynamics of ongoing activity (Arieli et al., 1996). Further complicating the story, a number of neuroimaging studies reported that some regions recurrently exhibited deactivations in task-related studies (Shulman et al., 1997, Mazoyer et al., 2001).

In order to take into account these unexplained task-independent functional activations that vanished during a task, it became necessary to define a baseline of brain activity (Gusnard et al., 2001). The implications of such a baseline for the understanding of brain function quickly became a new topic in neuroscience research. Raichle and colleagues (2001) measured the

---

[1] More details about functional neuroimaging techniques, including fMRI, EEG and MEG and, are provided in section *I.II.2.a – Measuring brain function.*

oxygen extraction fraction in the resting brain using PET and verified the physiological basis of resting-state BOLD fluctuations. Furthermore, they proposed that this baseline activity should be considered as a *default mode* of brain activity. Later, Greicius and colleagues (2003) performed the first resting-state connectivity analysis of the default mode and provided evidence for the existence of a cohesive default mode network (DMN). Regions within the DMN were found to exhibit correlated activation - or functional connectivity - during passive resting-state, and decrease activity during a task. For this reason, the DMN is called a task-negative RSN. Deeper explorations into resting-state dynamics revealed that other brain regions, independent from the DMN, exhibited correlated activations as well, with BOLD signal changes comparable with the signal changes found in task-related experiments (Beckmann et al., 2005, Damoiseaux et al., 2006).
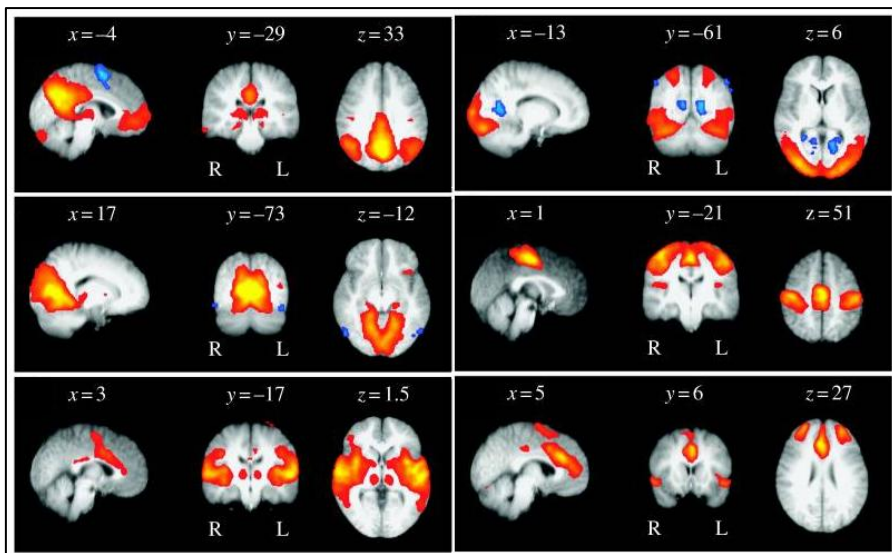
Figure 3 - Consistent resting-state networks across healthy subjects detected with fMRI.
Different resting patterns estimated from a group of 10 subjects corresponding to different spatial maps associated with low-frequency resting patterns using probabilistic independent component analysis. All functional images have been co-registered into a standard structural MRI template (MNI). Adapted from Beckmann et al. (2005).

The mapping of such functional networks[1] uncovered cortical systems that are usually involved in active cognitive processes, such as vision, language,

---

[1] In section *I.II.b – Resting-state Functional Networks* we describe in more detail how these networks can be defined.

movement, executive processing and other sensory and cognitive processes (Fox et al., 2005, Damoiseaux et al., 2006, De Luca et al., 2006). Unlike the DMN, these functional networks exhibit stronger functional connectivity when engaged in a task. The spontaneous and recurrent activation of such task-positive RSNs during rest appears to result from an intrinsic instability of the DMN.

Over the last decade, the robustness of resting-state dynamics has been validated by consistency across healthy subjects and high-reproducibility across research groups. Recently, Biswal et al. (2010) assembled over 1400 healthy resting-state fMRI data collected independently at 35 international centres and performed the biggest fMRI study of the healthy brain to date[1]. By analyzing these data with various different metrics, the authors demonstrated high reproducibility across datasets and individuals revealing a universal architecture of positive and negative functional connections, as well as consistent regions of inter-individual variability. This variability was essentially determined by the individual's sex and age. Regarding age, previous studies had reported affected RSN integrity in advanced aging. In particular, Andrews-Hanna et al. (2007) compared long-range connectivity among 93 adults aged 18 to 93 years old and demonstrated that aging is characterized by significant reductions in the co-activation between two regions composing the DMN during rest (i.e. the posterior cingulate and the medial prefrontal cortex). Furthermore, this functional disconnection in advanced aging was associated with lower white matter integrity and poorer cognitive performance. These results indicate that cognitive decline in normal aging (free from Alzheimer's disease) arises from functional disruption in the coordination of large-scale brain systems that support cognition. Regarding the differences between males and females, Liu et al. (2009) had reported significant sex-related differences in the functional lateralization of resting brains in a study with 300 subjects (43% men). However, the study from Biswal et al. (2010) was more complete and reported sex-related differences in specific locations in the brain, supposedly related to phenotypic variations due to the sexual dimorphism in

---

[1] To encourage neuroscientists to explore brain functional networks, the dataset from the 1000 Functional Connectomes Project is freely available at: www.nitrc.org/projects/fcon_1000/.

genomic expression. Based on their findings, the authors suggest that an individual's functional connectome could serve as a phenotype for genetic studies.

I.I.2 - Electrophysiological signatures of resting-state activity

Due to the very slow time-scale of resting-state fluctuations, functional MRI has been the most successful technique in detecting the spatial patterns of RSNs, in spite of its temporal resolution being in the order of a couple of seconds. However, the neurophysiological basis of resting-state dynamics occurring at faster time-scales and the nature of the coupling that binds cortical regions together cannot be accurately assessed using this technique. On the other hand, electrophysiology is at least three orders of magnitude better at tracking dynamic aspects of neural activity relevant for cognition and behaviour. If the spontaneous BOLD fluctuations are indeed a reflection of underlying neural activity, we may expect some components of electrophysiological signals to exhibit low-frequency spontaneous fluctuations with large-scale correlation patterns similar to those observed with resting-state fMRI. In this section, we report in chronological order some of the major experimental investigations of the electrophysiological counterpart of resting-state BOLD activity.

To explore the relationship between BOLD signal and the underlying neural activity, Logothetis et al. (2001) performed simultaneous fMRI and intra-cortical electrical recordings in anesthetized monkeys, showing that spontaneous fluctuations in local-field potentials (LFP) correlated positively with the local fMRI signal around the electrode. Although these results show unequivocally that a spatially localized increase in the BOLD contrast directly and monotonically reflects an increase in neural activity, the extension of these measurements to the whole brain or even to humans is highly restricted due to the invasiveness of intra-cortical recordings. The solution (in healthy humans) lies in placing electrodes at the scalp level and measuring the electroencephalographic (EEG) signals at the expense of spatial accuracy.

To investigate the relation between BOLD signal fluctuations and electrical signals over the whole brain in resting humans, Laufs et al. (2003) recorded simultaneous fMRI and EEG in awake healthy subjects at rest with eyes

closed. After filtering EEG signals into distinct frequency bands, they compared the power fluctuations of each frequency band (or band-limited power (BLP), see Figure 4) with the BOLD time courses in each voxel in the brain.
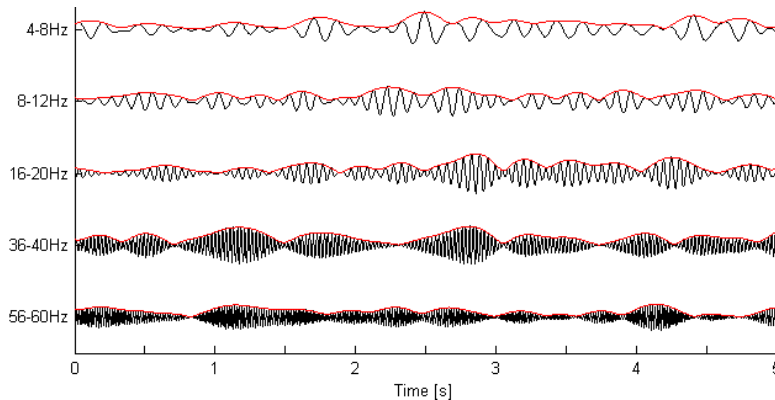
Figure 4 - Band-limited power fluctuations (BLP) at different frequency bands. BLPs (red) correspond to the envelope (or amplitude modulations) of oscillations filtered in a restricted frequency range (black). However, the frequency range (or carrier frequency) that best captures BOLD fluctuations remains under debate.

They found that the power of 17-23Hz oscillations (in the Beta-band) was positively correlated with the hemodynamic fluctuations found in the posterior cingulate, the precuneus and the left and right temporo-parietal and dorsomedial prefrontal areas. As commented by the authors, these regions are similar to the ones identified by Greicius et al. (2003) as the DMN. In addition, other band-limited power fluctuations were found to be correlated with fMRI activations. For example, there was strong and widespread negative correlation of BOLD activity with alpha power (8–12 Hz) in lateral frontal and parietal cortices that are known to support attentional processes. These findings suggest that fluctuations in BOLD signal at rest may at least in part reflect band-limited power fluctuations of neuronal activity happening at faster frequencies.

For a deeper exploration of power fluctuations during rest, Leopold et al. (2003) used multiple electrodes to record neural activity at different locations of the visual cortex of awake monkeys. They observed that the power of the local field displayed fluctuations at many time-scales, with particularly large amplitudes at very low frequencies (<0.1 Hz). Furthermore,

they found that these fluctuations exhibited high coherence between distant electrode pairs (but still in the visual cortex), particularly for power fluctuations in the gamma-frequency range. They proposed that such power fluctuations might make a significant contribution to the high amplitude fluctuations observed in the time course of resting state signals obtained with fMRI.

Further developments in resting-state fMRI studies revealed the existence of robust RSNs characterized by particular temporal signals using independent component analysis (ICA) (Beckmann et al., 2005). To investigate if the temporal signals of each RSN could be related to EEG power fluctuations in a particular frequency band, Mantini and colleagues (2007) recorded simultaneous fMRI and EEG and, applying ICA to the BOLD signals identified six robust RSNs over a group of 15 healthy subjects. The temporal signal associated with each RSN (i.e. the corresponding temporal ICs) were then correlated with the EEG power variations of delta (δ), theta (θ), alpha (α), beta (β), and gamma (γ) rhythms. They found that each RSN was characterized by a specific electrophysiological signature that involved the combination of different brain rhythms. For example, in agreement with the results from Laufs et al. (2003) their findings indicate that the functional activation of the DMN correlates better with Beta-frequency EEG power (13-30Hz). However, due to the low spatial resolution of EEG, investigations were limited to temporal signals and did not explore the correspondence between the cortical maps of EEG rhythms and the spatial maps of the RSNs detected with fMRI.

Later, in a similar experimental set as the one from Logothetis et al. (2001), Shmuel and Leopold (2008) simultaneously recorded fMRI time-series and intra-cortical electrophysiological signals from 1 single recording site in the visual cortex of anesthetized monkeys. They demonstrated correlations between slow fluctuations in BOLD signals and concurrent neuronal activity, when the neural signal consisted of either the spiking rate of a small group of neurons or band-limited power fluctuations (especially in the gamma band potential). BOLD fluctuations in widespread areas in visual cortex of both hemispheres were significantly correlated with neuronal activity from the single recording site in the primary visual cortex. To the extent that their findings can be generalized to other cortical areas, these findings reinforce

the idea that fMRI-based functional connectivity between remote regions during rest can be linked to slow synchronized increases in neuronal activation levels happening at faster time-scales.

The first resting-state study using intracranial electrophysiological recordings in humans was performed in 2008 by Nir and colleagues. They found slow (<0.1 Hz, following 1/f-like profiles) spontaneous fluctuations of neuronal activity with significant inter-hemispheric correlations as expected from fMRI results. These fluctuations were evident mainly in neuronal firing rates and in gamma (40–100 Hz) LFP power modulations. Furthermore, multiple intracranial recordings revealed clear selectivity for RSNs in the spontaneous gamma LFP power modulations (He et al., 2008, Miller et al., 2009). These results point to slow spontaneous modulations in firing rate and gamma LFP as the likely correlates of spontaneous fMRI fluctuations in the human sensory cortex, in agreement with the results from Shmuel and Leopold (2008).

Finally, a recent study by Scheeringa and colleagues (2011) investigated how the BOLD signal in humans performing a cognitive task is related to neuronal synchronization across different frequency bands. They simultaneously recorded EEG and BOLD while subjects engaged in a visual attention task known to induce sustained changes in neuronal synchronization across a wide range of frequencies. Trial-by-trial BOLD fluctuations correlated positively with trial-by-trial fluctuations in high-EEG gamma power (60–80 Hz) and negatively with alpha and beta power. Gamma power on the one hand, and alpha and beta power on the other hand, independently contributed (in an anti-correlated manner) to explaining BOLD variance. These results indicate that the BOLD-gamma coupling observed in animals can be extrapolated to humans performing a task and that neuronal dynamics underlying high- and low-frequency synchronization contribute independently to the BOLD signal.

I.I.3 - Detection of resting-state patterns using MEG

Since the electrical currents occurring in the brain produce perpendicular magnetic fields, it is also possible to capture measures of neuronal activation during rest using magnetoencephalography (MEG). With a spatial resolution comparable to fMRI (i.e. a few mm) and a temporal resolution

equivalent to electrophysiological recordings (i.e. better than 1ms), MEG offers the best of both worlds in imaging brain function.

It seems that the first study dedicated to investigate the neuronal correlates of resting BOLD signal using MEG was performed by Nikouline et al. (2001). The authors investigated inter-hemispheric phase synchrony and amplitude correlation of beta oscillations in a resting condition, revealing that beta oscillations in the left and right hemisphere exhibited transient synchronized activity and the index of synchronization was strongest when these oscillations had large amplitude. Importantly, they reported that the amplitude of spontaneous beta oscillations (which is equivalent to the band-limited power in the β frequency) was also found to be correlated across hemispheres over long time intervals (>1s). The authors suggested that the low-frequency amplitude modulation of spontaneous rhythmic activity may be the source of correlations of low-frequency hemodynamic responses, generally interpreted as functional connectivity. This work appears to be the first demonstration of band-limited power correlations between the two hemispheres during rest.

Almost a decade later, and following the electrophysiological studies suggesting that spontaneous BOLD fluctuations could be driven by slow amplitude modulations of neural oscillations, Liu et al. (2010) characterized the power modulations of spontaneous MEG rhythms recorded from human subjects during wakeful rest (with eyes open and eyes closed) and light sleep. Through spectral, correlation and coherence analyses, they found that resting-state MEG rhythms demonstrated ultraslow (< 0.1 Hz) spontaneous power modulations that synchronized over a large spatial distance, especially between bilaterally homologous regions in opposite hemispheres. Their observations suggest that coherent power modulations of spontaneous rhythmic activity (especially in the β-band) reflect the electrophysiological signature of the large-scale functional networks, in agreement with the results from Nikouline et al. (2001). A couple of months later, de Pasquale and colleagues (2010) used a seed-based method to characterize the MEG signatures of two well-characterized RSNs: the dorsal attention and the default mode networks. Taking into account the non-stationarity of MEG activity, they found that the band-limited power of the RSN seeds were only synchronized for restricted periods in time, resulting in

a transient formation of RSNs. Their results indicate that RSNs manifest in MEG as synchronous modulations of band-limited power primarily within the theta, alpha, and beta bands, which correspond to rhythms slower than the γ-frequency oscillations generally associated with the electro-physiological correlates of event-related BOLD responses.

The first work to show that MEG can independently measure the spatial pattern of RSNs, in the same manner that has been demonstrated in fMRI, was recently performed by Brookes and colleagues (2011b).
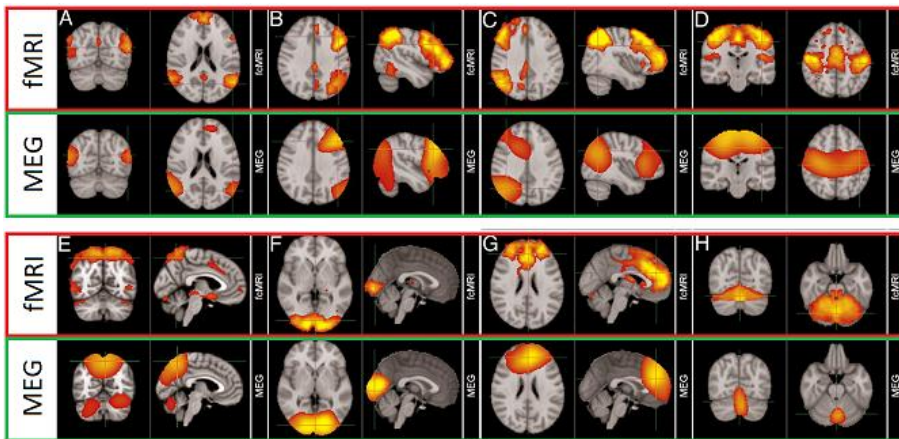
Figure 5 - Comparison of brain networks obtained using ICA independently on MEG and fMRI data. (A) DMN; (B) left lateral frontoparietal network; (C) right lateral frontoparietal network; (D) sensorimotor network; (E) medial parietal regions; (F) visual network; (G) frontal lobes including anterior cingulate cortex; (H) cerebellum. All networks were identified using β-band power fluctuations, except the DMN, which was detected using α-band power fluctuations. Adapted from Brookes et al. (2011b).

As a first step, the MEG data was frequency filtered into bands of interest (δ, θ, α, β, and γ) and projected into source space using a beamformer spatial filter. Then, ICA was applied to the band-limited power fluctuations, resulting in RSNs with significant similarity to the RSNs derived independently using fMRI. Importantly, most resting-state networks were linked to β-band power fluctuations. This outcome confirms the neural basis of hemodynamic networks and demonstrates the potential of MEG as a tool for understanding the mechanisms that underlie RSNs.

Furthermore, in a recent MEG study, Hipp et al. (2012) found that spontaneous oscillatory neuronal activity exhibited frequency-specific

spatial correlation structure in the human brain. Overall, they found that correlation of power across cortical regions was strongest in the alpha to beta frequency range (8–32 Hz) and correlation patterns depended on the underlying oscillation frequency. Global hubs resided in the medial temporal lobe in the theta frequency range (4–6 Hz), in lateral parietal areas in the alpha to beta frequency range (8–23 Hz) and in sensorimotor areas for higher frequencies (32–45 Hz). These data suggest that interactions in various large-scale cortical networks may be reflected in frequency-specific power envelope correlations (or BLP correlations).
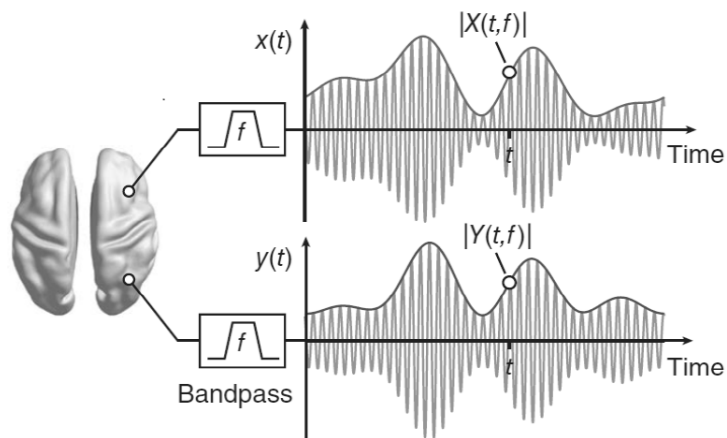
Figure 6 - Power envelope correlation. Illustration of spectrally resolved power envelopes for one exemplary carrier frequency f (that is, center frequency of the bandpass filter). The gray sinusoidal lines represent bandpass-filtered neuronal signals estimated at two source locations. The corresponding blue and red lines, the amplitude envelopes, quantify the evolution of the signal amplitude at a slower timescale. Adapted from Hipp et al. (2012).

In summary, all electrophysiological and MEG works presented in the previous sections have aimed to investigate the neurophysiological counterpart of resting-state BOLD fluctuations with some similar conclusions. Overall, results show that resting-state fluctuations are driven by slow modulations of neural activity, which are manifested by transient increases in the amplitude (or power) of fast oscillations in a certain frequency range. The slow band-limited power (BLP) fluctuations can be captured by filtering the signal into frequency bands and subsequently computing the Hilbert transform to obtain the envelope of the oscillations in each frequency range.

Interestingly, BLP rhythms from different frequency bands lead to different spatial patterns of pairwise correlations, suggesting a complex interplay between multiple frequency bands (Mantini et al., 2007, de Pasquale et al., 2010) which in turn may reflect different aspects of neuronal processing (Womelsdorf et al., 2007, Palva and Palva, 2012). Regarding the question whether there is a specific carrier frequency whose power modulations serve as the best candidate for the neuronal correlates of spontaneous fMRI fluctuations, there seem to be two potential frequency ranges in debate. On one side, the intra-cortical recordings performed by Leopold et al. (2003), Nir et al. (2008) and Shmuel and Leopold (2008) propose a direct relationship with gamma-frequency BLP, whereas the MEG studies from Nikouline et al. (2001), Liu et al. (2010) and Brookes et al. (2011) suggest the beta (and sometimes alpha) band BLP as the electro-physiological counterpart of spontaneous BOLD-fMRI fluctuations. Since each technique has intrinsic limitations, both scenarios from previous studies could coexist. Indeed, according to the results from Scheeringa et al. (2011), a negative correlation exists between the BLPs at high and low frequencies, indicating that the BOLD signal might be associated to interactions between these high (gamma) and low (alpha and beta) frequency bands. However, an accurate answer requires simultaneous recordings of both fMRI and electro-physiological signals across the whole brain, which is unavailable in the present days. Alternatively, we can explore the mechanism at the genesis of these electrophysiological power fluctuations (or amplitude modulations) by means of computational models. In chapter *IV – Predicting resting-state MEG band-limited power correlations with the Kuramoto model* we provide a possible scenario for such findings.

I.I.4 – Altered resting-state activity in disease

Over the last decade, a large number of studies have reported altered resting brain activity in a wide range of mental illnesses. These results not only illustrate the importance of resting-state dynamics for an optimal cognitive function, but also provide insights to understand the intrinsic mechanisms leading to these diseases.

Resting-state functional connectivity has been shown to decrease in patients with Alzheimer's disease (AD). It has been noted that the default mode

network is not as homogenous as in healthy brains and several fractionations of the DMN have been proposed. In early stages of the disease, results have shown decreased connectivity in patients versus controls in the posterior DMN, and increased connectivity in the anterior and ventral DMNs. However, as the AD disease progresses, connectivity within all systems eventually deteriorates (Greicius et al., 2004, Zhou et al., 2010, Damoiseaux et al., 2012). Furthermore, Supekar et al. (2008a) characterized resting-state functional networks using graph theory and found that functional brain networks in AD showed loss of small-world properties, characterized by a significantly lower clustering coefficient, indicative of disrupted local connectivity.

Regarding schizophrenia, Liang et al. (2006) reported widespread functional disconnectivity in schizophrenia with resting-state fMRI supporting the hypothesis that schizophrenia may arise from the disrupted functional integration of widespread brain areas. Further analysis of resting-state activity in schizophrenia using graph theory indicate a subtle randomization of functional networks, with decreased small-world properties, lower clustering coefficients and less high-degree hubs (Liu et al., 2008, Lynall et al., 2010, Bassett et al., 2012).

Resting-state alterations have been found in many other mental illnesses including dementia (Buckner et al., 2000, Rombouts et al., 2009), autism (Cherkassky et al., 2006, Kennedy et al., 2006, Lai et al., 2010, Weng et al., 2010, Cornew et al., 2011), mild cognitive impairment (Rombouts et al., 2005), multiple sclerosis (Bonavita et al., 2011, Schoonheim et al., 2011, Faivre et al., 2012) and major depression (Greicius et al., 2007, Sheline et al., 2009, Veer et al., 2010). However, the clinical use of resting-state connectivity requires consistency across studies before it can be used in a meaningful way at the single-patient level (Greicius, 2008, Fox and Greicius, 2010)

In some cases, resting-state connectivity was found to correlate with cognitive performance (i.e. in Lynall et al, 2010), which suggests that resting-state correlations are closely related to the binding mechanisms that support the integration of segregated information in the brain.

*'The brain is a world consisting of a number of unexplored continents
and great stretches of unknown territory.'*
Santiago Ramón y Cajal

I.II - Networks of the brain

Our brain has a complex network organization allowing the functional integration of spatially segregated information in the nervous system (Tononi et al., 1992, 1994, Jirsa and Kelso, 2000, Sporns et al., 2000). Spatially distributed and functionally specialized brain areas are continuously communicating and co-operating to respond to cognitive demands, perceive sensory stimuli and generate coordinated movement. The communication between brain areas is made through axonal fibres that project from one area to the other, serving as the means of transport for the action potentials travelling in the brain. Since regions are spatially segregated, signals take a significant time to travel from one region to the other, resulting in time-delayed interactions. Although the neuronal mechanisms under which cortical regions communicate remains unclear, the space-time structure of the neuro-anatomical network is believed to serve as the structural substrate upon which coordinated functional integration occurs (Bressler and Tognoli, 2006, Jirsa and McIntosh, 2007, Ghosh et al., 2008, Knock et al., 2009).

Combining functional and structural imaging modalities has revealed that resting-state functional connectivity reflects, to some extent, the underlying structural connectivity (Damoiseaux and Greicius, 2009, Greicius et al., 2009, van den Heuvel et al., 2009, van den Heuvel and Hulshoff Pol, 2010). However, the bond between structural and functional connectivity is not straightforward: although structural connectivity is a good predictor of functional connectivity – i.e. if there is a direct anatomical connection, there is likely a functional connection – the opposite is not necessarily true. Robust functional connectivity has been observed in the absence of a direct anatomical link (Koch et al., 2002) and, as will be shown in section *I.III - Large-scale models of resting-state dynamics*, computational models of neural network dynamics are valuable tools to investigate this relationship.
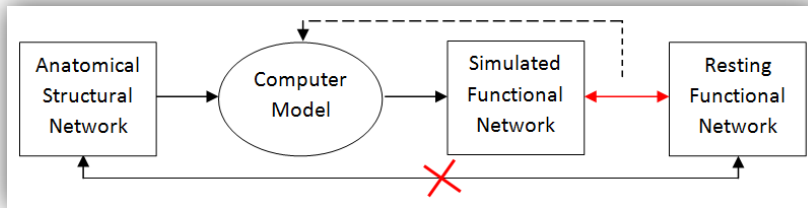
Figure 7 - Exploring the structure-function relationship using computational models. Diagram illustrating how computational models can serve to explore the relationship between anatomical structural networks and resting functional networks. The dashed line (--) indicates the feedback of the model's performance, that is necessary to tune the parameters of the model.

In the next sections of this chapter, we describe in detail how these structural and functional brain networks are constructed and evaluated. In particular, we will explain how white matter tracts are detected, which criteria define a brain region, how statistical dependencies in hemodynamic signals can imply a functional connection and, finally, how these networks can be evaluated using graph theory.

I.II.1 – Anatomical structural networks

The brain's anatomical connectivity, or connectome (Hagmann, 2005, Sporns et al., 2005), is defined as the map of neural connections in the brain. The human cerebral cortex alone is thought to contain at least 10^{10} neurons linked by 10^{14} synapses, defining a highly complex, multi-scale and hardly tractable network (Sporns, 2009). The only organism from which the full connectome is known in its entirety is the one millimeter-long worm *C.elegans*, but it took British researchers over a decade to complete the identification of its 300 neurons and 7,000 connections during the 1970s and 1980s. Since we are essentially interested in large-scale human brain patterns, we go beyond the cellular scale and focus essentially on the long-range white matter pathways upon which large populations of neurons interact. These phylogenetically and ontogenetically determined large-scale connections are particularly important because they strongly constrain how brain regions communicate, defining the wiring diagram over which distributed cognitive processes unfold.

Historically, the mapping of white matter connections was performed post-mortem by histological dissection and staining, by degeneration methods or by axonal tracing. These classical techniques, however, were time-consuming and generally applied to restricted areas in the brain. In an attempt to assemble data from different white matter tracing studies of the macaque brain, Rolf Kötter (Kötter, 2004) created the online database for the "Collation of Connectivity on the Macaque brain" (CoCoMac www.cocomac.org), allowing for continuous updating and refinement of such anatomical connection maps. From this database, Kötter and Wanke (2005) derived a realistic connectivity map of one hemisphere of the primate brain, proposing a coarse parcellation of the primate cerebral cortex into 38 regions, which reflected broad and rather uncontroversial divisions. This connectivity map has been used in models of large-scale brain activity (Honey et al., 2007, Deco et al., 2009) revealing that the large-scale connectivity topology of cerebral cortex, together with time delays and in the presence of noise, defines a dynamic framework from which the resting patterns emerge.
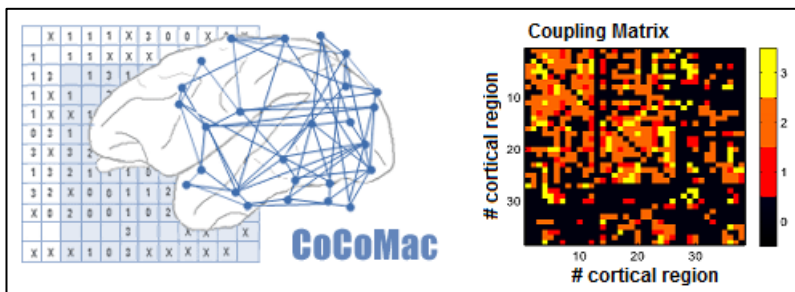
Figure 8 - The Macaque connectivity. The coupling weights C_{np} indicate the strength of connections (classified as weak (1), medium (2) or strong (3)) from region p to n (directed). The CoCoMac database, created by Rolf Kötter, represents the first attempt to obtain the anatomical connectivity map of the whole brain.

Since the manual tracing of white matter pathways has not been performed from human brains, some works have tried to infer human anatomical networks from cortical thickness and gray matter volume measurements obtained with structural MRI. This approach relies on the fact that cortical thickness is strongly correlated between regions that are axonally connected (Lerch et al., 2006). Thus, a whole-brain anatomical network can be abstracted from human MRI data by compiling a matrix of correlations in

cortical thickness (or volume) between all pairs of brain regions across subjects and then applying a threshold to create a graph representing strong correlations as connections between regions (He et al., 2007, Bassett et al., 2008, Chen et al., 2008). However, a direct proof that correlations of gray matter volume over the whole brain across subjects are indicative of axonal connectivity via white matter tracts has not been provided.

In recent years, a revolution in *connectomics* (i.e. the science concerned with assembling and analyzing connectome data sets (Hagmann, 2005)) appeared hand-in-hand with the technological advancements in Diffusion MRI. This method allows for a non-invasive *in vivo* detection of white matter fibre pathways. Together with efficient computational tractography algorithms, this technique permits the rapid and almost automatic construction of comprehensive maps of brain connectivity. In the same line of the CoCoMac project but in a much larger scale, the Human Connectome Project (www.humanconnectomeproject.org) aims to provide an unparalleled compilation of neural connectivity data based on Diffusion MRI studies. Collectively, advances in human connectomics open up the possibility of studying how brain connections mediate brain function and hence behaviour.
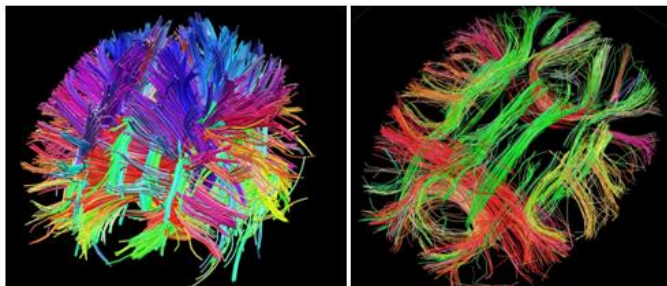
Figure 9 - White matter fibres detected in vivo using Diffusion MRI. Images from the gallery of the Connectome Project (by Randy Buckner).

The first mappings of human whole-brain anatomical connectivity using Diffusion MRI tractography were performed almost simultaneously by Hagmann and colleagues (2007) and Iturria-Medina and colleagues (2007). Initially, in Hagmann et al. (2007), anatomical networks were composed by 500 to 4000 nodes and were derived from the brains of 2 healthy subjects. At the same time, Iturria-Medina et al. (2007) analyzed anatomical connectivity at lower resolution, focusing on the connectivity between 71

gray matter structures, across 5 healthy subjects. A few months later, Iturria-Medina et al. (2008) extended the study to 20 healthy participants and divided gray matter into 90 cortical and subcortical regions according to a widely used neuroimaging parcellation template (the AAL template, see *I.II.1.b - Brain parcellation*). Briefly after, Hagmann et al. (2008) proposed a low-resolution parcellation as well, this time dividing the cortex into 66 regions. This anatomical network was used in the first large-scale model of human resting-state functional connectivity (Honey et al., 2009) (see section *I.III - Large-scale models of resting-state dynamics*).

In the following sub-sections, we describe the physical and technical concepts behind Diffusion MRI and present different parcellation schemes used to label brain regions according to their function or anatomic properties.

I.II.1.a - Diffusion tractography

Diffusion MRI uses a specific MRI sequence that is sensitive to the direction of water diffusion in the body. If the water diffuses equally in all directions, it is termed *isotropic* diffusion. Conversely, if the water molecules diffuse in a medium with barriers, such as cell membranes, the diffusion is uneven and is termed *anisotropic*. Detecting white matter fibres using Diffusion MRI relies on the simple fact that water propagates along the orientation of the fibres because the myelin sheath provides a barrier perpendicular to the fibres.

Diffusion Tensor Imaging (DTI) (Wedeen et al., 1995) is a diffusion MRI method that estimates the direction and strength of anisotropic diffusion in each voxel. In more detail, if most water molecules in one voxel move in the same direction, then the fractional anisotropy is ≈1, and it is considered that a fibre might be crossing that voxel in that direction. On the other hand, if the water molecules in a voxel move in all directions, then the fractional anisotropy is ≈0. Diffusion maps can be constructed by estimating the main direction and strength of anisotropic diffusion for each voxel.

The detection of fibre tracts, or tractography, is a post-processing method estimates fibre trajectories by constructing three-dimensional curves of maximal diffusion coherence using computational algorithms. The main

limitation of DTI is that it assumes only one direction per voxel and is incapable of resolving fibre crossings (see Figure 10). Overcoming that limitation, Diffusion Spectrum imaging (DSI) explores the strength of anisotropy in all directions, allowing the crossing of multiple fibres in a single voxel (Wedeen et al., 2005).
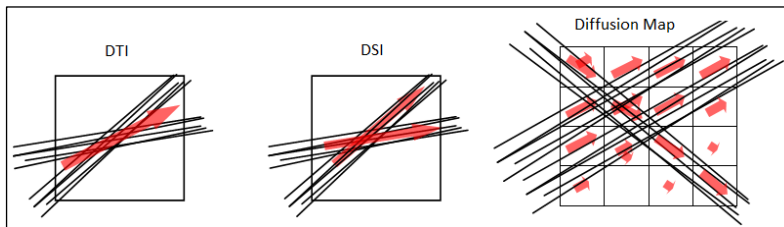
Figure 10 – Detection of fibre directions using DTI and DSI. DSI is able to detect crossing fibres in one voxel.

I.II.1.b - Brain parcellation

Prior to defining the connectome, it is necessary to divide gray matter at the desired scale according to specific strategies for anatomical or functional partitioning. Several brain parcellation templates are available in the literature, ranging from the canonical classification into lobes (i.e. frontal, parietal, temporal and occipital lobes) to as much as several thousand regions of interest. Once the parcellation scheme is defined, computational algorithms are used to count the number of fibre tracts detected between a pair of regions (See Figure 11).
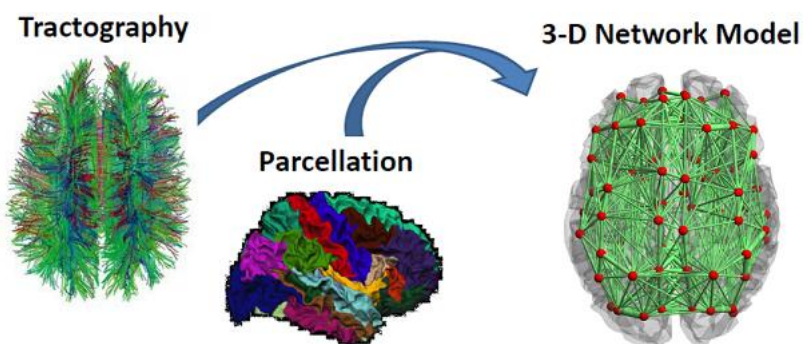
Figure 11 - Building a 3-D network model of the brain's anatomical coupling architecture. The weight of each connection is derived from the number of fibre tracts detected between a pair of regions defined in a parcellation template. The spatial distance between regions adds an additional complexity level to the space-time structure of the neuro-anatomical network.

One of the first and most widely known parcellation schemes of the human cortex was performed by the German anatomist K. Brodmann (1909) using staining methods. Although the division was based solely on the cytoarchitectural organization of neurons, some of the 52 Brodmann areas have been later closely correlated to diverse cortical functions. However, parcellation methods defined based on the function rather than on the anatomy provide a better understanding of the distributed functional organization of the brain. If a population of neurons share certain distinguishing functional properties, such as being activated by the same category of stimuli or seem to be involved in similar cognitive tasks, different from the stimuli or tasks that activate neurons in the neighbouring areas, then these neurons are grouped in the same functional region.

Previous to the work presented in this thesis, existing models of human resting-state functional connectivity (Alstott et al., 2009, Honey et al., 2009) have used a human connectome derived by Hagmann and colleagues using DSI (Hagmann et al., 2008). To obtain the connectome, first they segmented an average brain into white matter, cortex and deep cerebral nuclei using Freesurfer (surfer.nmr.mgh.harvard.edu). Secondly, gray matter was divided into 66 cortical regions (Figure 12) and then individually subdivided into small regions of interest (ROIs) resulting in 998 ROIs, each covering 1.5 cm^2 of the cortical surface. Two labelled meshes (one mesh with the 66 regions and another with the 998 ROIs) were created on the average brain and were registered onto the brain of individual participants using Freesurfer. A recent paper from the same group (Cammoun et al., 2012) propose a robust method for constructing normalized whole-brain structural connection matrices derived at different scales. In that work, the 998 cortical ROIs are regrouped iteratively into bigger ROIs, resulting in 5 scales of cortex parcellation into 66, 133, 241, 483 and 998 regions. This hierarchical parcellation can be used to explore network dynamics at different levels.
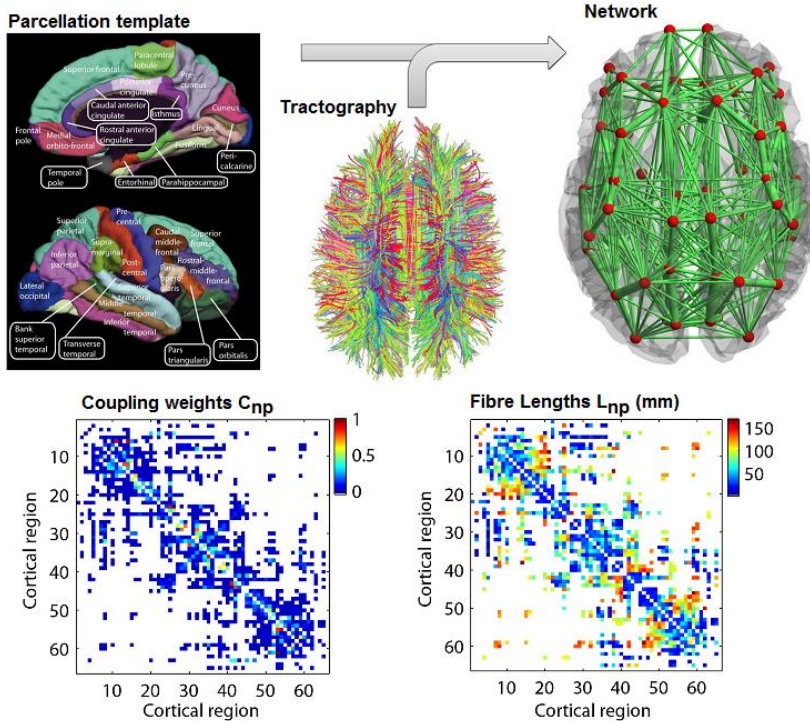
Figure 12 - Anatomical network with 66 cortical regions. Anatomical connectome derived by Hagmann et al. (2007) using DSI averaged over 5 healthy subjects. (Top-Left) Parcellation scheme dividing the cortex into 33 anatomically segregated regions in each hemisphere (adapted from Honey et al. (2008)). (Top-Middle) White matter tracts detected using DSI and tractography (adapted from Honey et al. (2007)). (Top-Right) Schematic representation of the anatomical network, where regions are represented by red spheres placed at their centre of gravity and the link's thickness is proportional to the number of fibre tracts detected in each connection. (Bottom-Left) The coupling weights are proportional to the number of tracts detected. White colour means that no fibre connecting the two corresponding regions was detected. Weights were normalized so that $0 \leq C_{np} \leq 1$. (Bottom-Left) Distance between regions given as the average length of the fibres connecting a pair of regions. The list of brain regions and corresponding indexes is reported in Appendix A.I Table 4.

Another well-known parcellation scheme was proposed by Tzourio-Mazoyer et al. (2002) with the intention of standardizing the anatomical labelling of brain regions in neuroimaging studies. This so-called Automated Anatomical Labelling (AAL) was performed on a brain template consisting on a high-resolution structural MRI scan from a healthy male supplied by the Montreal Neurological Institute (MNI) (Collins et al., 1998). First, the brain was segmented in eight classes including gray matter, white matter, cerebrospinal fluid, fat, muscle/skin, skin, skull, and glial matter. Subsequently, gray matter was carefully divided into 90 cortical regions

delimited by sulci and arbitrary boundaries when necessary (45 in each hemisphere). In this template, several subcortical regions are included, such as the thalamus, basal ganglia and hippocampus. The AAL parcellation template is included in the Statistical Parametric Mapping (SPM) package (Friston et al., 1994) and is freely available to the neuroimaging community. To date, more than 2,000 research articles have used the AAL parcellation template (based on citation index), including studies of resting-state functional connectivity (Salvador et al., 2005, Achard et al., 2006, Achard and Bullmore, 2007, Liu et al., 2008, Supekar et al., 2008a, Lynall et al., 2010, Sanz-Arigita et al., 2010, Bassett et al., 2012, Braun et al., 2012). Moreover, the largest sample to date of healthy structural brain networks was derived by Gong et al. (2009a) from 80 young adults using DTI and the AAL parcellation.

Formally, brain connectivity data can be represented in matrix format (Figure 13). A network with N cortical regions results in a matrix with N columns and N rows, where each entry in the matrix $C(n,p)$ or C_{np}, corresponds to the weight of connectivity between region n and region p. This weight can represent any measure used to estimate the connectivity between two regions.
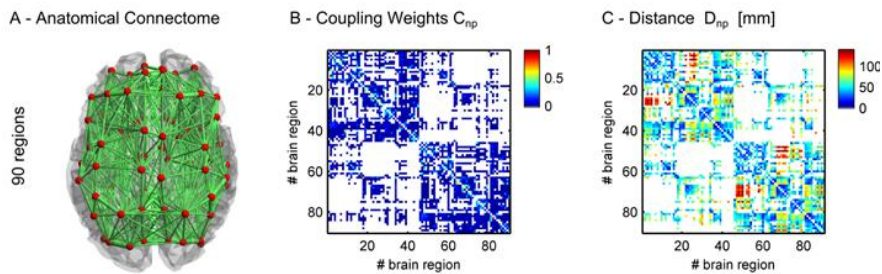
Figure 13 - Anatomical network in the AAL parcellation scheme (90 regions). Connectome derived from DTI using the AAL template. **(A)** Schematic representation of the anatomical network. **(B)** The coupling weights are proportional to the number of tracts detected. $0 \leq C_{np} \leq 1$, white = no connection. **(C)** Distance between regions, given as the Euclidean distance between centres of gravity. The list of brain regions and corresponding indexes is reported in Appendix A.I Table 5.

In the particular case of anatomical brain networks derived from Diffusion MRI, the connection strength C_{np} is scaled by the number of white matter tracts detected between two anatomically defined regions, which can range from 0 to as much as several thousand tracts per connection. This procedure

relies on the assumption that the number of tracts is an indicator of structural connectivity strength.

I.II.2 – Dynamic Functional Networks

The simultaneous activation of selected functionally specialized brain regions provides a framework for cooperative processing and integration in the brain. The spatio-temporal properties of such functional networks (e.g. the evolving patterns of interacting brain areas) are an expression of cognitive function in real time. Unlike structural networks, functional networks are only active for a period in time, representing a transient brain state where different brain areas activate simultaneously, supposedly integrating segregated information (Tononi et al., 1994, Tononi et al., 1998, Bressler and Tognoli, 2006).
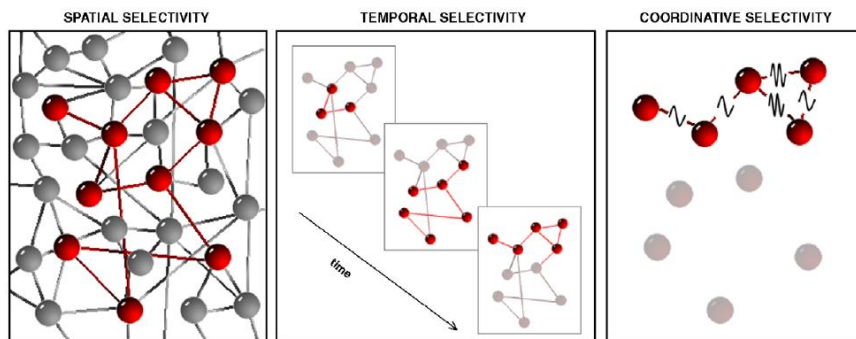
Figure 14 - Properties of functional networks. A functional network is configured by the joint activation of a set of regions –or nodes- (spatial selectivity). The configuration changes at successive instants of time (temporal selectivity). Specific patterns of coordination occur between co-active brain areas (coordinate selectivity). Adapted from Bressler and Tognoli (2006).

Evoked neuronal activations can be easily captured by comparing the data obtained while the task was being performed with baseline data sets. During rest, however, the definition of an activation paradigm becomes unfeasible. Still, even if no task-related process is triggering the co-activation of regions belonging to a certain functional network, it is possible to extract patterns of co-activation from the low-frequency fluctuations of neuronal activation appearing during rest. In this section, we start by providing a chronological overview over the existing methods to measure brain functional activation,

and then describe different approaches used to estimate neuronal interactions, or functional connectivity, during rest.

I.II.2.a – Measuring functional activations

While exploring the electric activity in the brains of rabbits and monkeys, Caton (1875) discovered that different motor and sensory tasks induced electrophysiological responses in distinct cortical regions. Although segregated functional specialization had already been suggested by neuro-anatomical studies, his measurements were probably the first to localize functional responses in the brain.

The identification and characterization of functional activation sites requires techniques that are sensitive to neural activity levels in the brain. For almost a century, brain activity was mainly detected using electrophysiological measurements, which consist in registering voltage fluctuations resulting from ionic current flows that occur when a large number of neighbouring neurons discharge simultaneously (Niedermeyer and Lopes da Silva, 1982). Electrophysiological recordings can be performed directly from the cortex of exposed brains either by placing electrodes over the cortical surface – a technique called Electrocorticography (ECoG) –, or to explore deeper brain structures, by introducing intra-cortical electrodes. Although these direct recordings permit the measurement of functional activation with high spatial and temporal precision, they are extremely invasive and can only be performed in humans under specific clinical conditions (i.e. for epileptic foci detection). Alternatively, electrophysiological measurements can be obtained by placing electrodes at the scalp level, using EEG. Apart from being non-invasive, EEG is easy to implement, can be carried around and is relatively cheap when compared to other functional imaging methods such as MEG and MRI scanners. However, it encounters other limitations on the measurement of localized functional activations. First, the detection of electric activity from deep sources using EEG scalp electrodes is difficult because voltage fields decrease with the square of distance and, in addition, are distorted by the skull and the scalp. Furthermore, the source-reconstruction of electric sources detected by EEG poses an ill-solved problem with infinite solutions, and the activation sites can only be estimated with low spatial precision (in the order of a couple of

centimetres). Even so, the remarkable temporal resolution of EEG (around 1 KHz, in the same way as all other electrophysiological techniques) makes it valuable tool to perform temporal and spectral analysis of brain activity under all types of mental conditions, including rest[1].

Based on Maxwell's equations, which stipulate that any electrical current produces an orthogonally oriented magnetic field, Cohen (1968) designed the magnetoencephalogram (MEG), a neuroimaging device capable of recording the magnetic fields produced by the cortical electrical currents. Since magnetic fields are less distorted by the skull and scalp than electric fields, MEG functional images have a better spatial resolution than EEG (in the order of a couple of millimetres). However, MEG detects only the tangential components of cortical activity (from the sulci), whereas scalp EEG measures the tangential and radial components capturing electric currents emerging from both sulci and gyri. Since the brain's magnetic field is considerably smaller than the ambient magnetic noise, the data acquisition must be performed in a magnetically shielded room and with highly sensitive magnetic sensors. Current MEG scanners use arrays of hundreds of superconducting quantum interference devices (SQUIDs), requiring cryogenic refrigeration, which are capable to detect neuro-magnetic fields with high precision. In addition, MEG, like EEG, is capable of detecting electric variations as short as 1 millisecond, allowing the exploration of high-frequency oscillations which are unattainable using other functional imaging methods such as fMRI and PET[2].

Despite its low temporal resolution –around a couple of seconds-, functional MRI is probably the most widely used imaging technique to study brain function since the mid-90's (Biswal et al., 1995, Friston et al., 1995, Buckner et al., 1996, Bullmore et al., 1996). fMRI is an indirect measure of neuronal activation because it measures the income of oxygenated haemoglobin (Hb) to a brain region (Logothetis et al., 2001). This oxygen is needed to build energy for ionic pumps responsible of resetting the (negative) resting

---

[1] Information regarding the characterization of resting-state activity using electrophysiology is provided in section *I.I.2 - Electrophysiological signatures of resting-state activity*.
[2] Evidence of resting-state patterns detected with MEG is reported in section *I.I.3 - Detection of resting-state patterns using MEG.*

membrane potential of neurons after a discharge. With the increase of Hb, the fraction of deoxygenated haemoglobin (dHb) decreases. This difference leads to an improved MR signal (due to less distortion from paramagnetic dHB) that can be captured at the voxel level using the blood-oxygen-level-dependent (BOLD) contrast (Ogawa et al., 1990). Unlike other functional contrast methods, the BOLD contrast consists in a specific MRI acquisitin paradigm and does not require the injection of substances or radiation exposure. Furthermore, it allows the spatial mapping of event-related neural responses with high spatial resolution. During rest, the BOLD signal exhibits low-frequency fluctuations (<0.1Hz) that are independent from heartbeat and respiratory frequencies, suggesting the transient activation of neuronal ensembles[1].

Changes in neural activity (based on local changes in blood flow) can also be mapped using Positron Emission Tomography (PET) (Phelps et al., 1975, Ter-Pogossian et al., 1975, Raichle, 1985). PET is a functional imaging technique that detects pairs of gamma rays emitted indirectly by a positron-emitting radionuclide, which is injected into the body on a biologically active molecule. Raichle et al. (2001) used PET images to measure the oxygen extraction fraction during rest and found the existence of an organized, baseline default mode of brain function that is suspended during specific goal-directed behaviours. However, since PET involves exposure to significant ionizing radiation, and due to the short half-lives of most positron-emitting radioisotopes, resting-state studies involving healthy volunteers are generally performed using fMRI.

I.II.2.b – Functional Connectivity during rest

To estimate functional interactions from resting-state fluctuations, several approaches can be undertaken, including correlation measures, ICA, PCA, mutual information, covariance and coherence analysis.

The classic and most widely used method to infer the strength of interactions (or functional connectivity – FC) consists in estimating the linear (Pearson) correlation coefficient between temporal BOLD signals (Bandettini

---

[1] In section *I.I.1– Resting-state hemodynamic fluctuations* we describe how the BOLD signal is organized during rest.

et al., 1993, Biswal et al., 1995). If two regions activate (BOLD increase) and deactivate (BOLD decrease) at the same time, the correlation is high (≈1) meaning that there is a functional connection. The Pearson correlation coefficient between two series X and Y of size N is given by the following equation:

$$\rho_{X,Y} = \frac{\sum_{n=1}^{N}(X_n - \bar{X})(Y_n - \bar{Y})}{\sqrt{\sum_{n=1}^{N}(X_n - \bar{X})^2}\sqrt{\sum_{n=1}^{N}(Y_n - \bar{Y})^2}}$$

Using correlation measures to investigate resting-state patterns, two levels of analysis are possible: 1) looking at the correlation between one specific region and the rest of the brain, i.e. seed-based correlation, or 2) exploring all possible functional connections by studying the correlation matrix. To perform an analysis at the seed level, prior information regarding the coordinates of the main activation sites of a certain RSN must be provided. After identifying the seeds belonging to an RSN, then maps of seed co-activations can be built by overlapping the correlation maps of each seed (Fox et al., 2005). The brain regions that correlate with all the seeds from an RSN are identified as part of that RSN.

Performing the correlation matrix between BOLD signals provides information regarding all pair correlations in the brain. Actually, each line in the matrix corresponds to a seed, and the entries in that line correspond to the correlation coefficient between the BOLD activation in that seed and all the remaining regions (columns). One advantage of computing correlation matrices is that they can be studied using graph theory, not only to evaluate the topological properties of functional networks, but also for the detection of functional modules and hubs. Investigating correlation matrices at the voxel level can be computationally costly so it is common to average the BOLD signals from voxels falling in the same cortical region (defined according to a certain parcellation scheme), and then analyse the correlation matrix at a much lower resolution (Honey et al., 2009). Moreover, wavelet analysis can be applied to the fMRI data to compute frequency-dependent correlation matrices. For example, this approach allows searching for the frequency range over which maximal differences are observed between healthy controls and subjects (Supekar et al., 2008a, Lynall et al., 2010, Bassett et al., 2012). Despite its usefulness for detecting

linear statistical dependencies, the correlation analysis has certain limitations. The most important relies on the fact that RSNs are not spatially independent and can overlap. In other words, the same cortical region can belong to more than one RSN at a time and therefore activates whenever one or another RSN is engaged. In this way, the activation pattern of that region turns out to be a sum of the activation patterns of each RSN it belongs, which cannot be captured using correlation measures.

Recent studies propose the use of ICA to extract RSN spatial maps from coordinated BOLD fluctuations (Beckmann et al., 2005, Damoiseaux et al., 2006, De Luca et al., 2006, Mantini et al., 2007, Beckmann, 2012). This method relies on the assumption that resting state activity is a mixed signal resulting from the additive combination of independent temporal signals, in the same way as a symphony is composed by different musical instruments in an orchestra. ICA is a particular case of blind source separation and the BOLD signal in each voxel $x_n(t), n = 1, \dots, N$ can be written as a composition of the different independent components $IC_k(t), k = 1, \dots, K$ with coefficients $a_{n,k}$ in the following way:

$$x_n(t) = a_{n,1}IC(t)_1 + a_{n,2}IC_2(t) + \dots + a_{n,K}IC(t)_K$$

An important note to consider in ICA is that the number of independent components K is, in theory, equal to the number of sources N (i.e. number of voxels or number of cortical regions), since ICA cannot sort (nor scale) the source signals in correct order. However, reducing the number of sources (or dimensions) is possible by previously performing principal component analysis (PCA). PCA performs a linear mapping of the data to a lower dimensional space in such a way that the variance of the data in the low-dimensional representation is maximized. In practice, it is obtained by computing the eigenvalue decomposition of the covariance matrix of the temporal signals. Then, the eigenvalues are sorted according to the proportion of variance they account for. Dimension reduction is possible by selecting the eigenvalues (i.e. principal components) that represent most of the variance.

ICA is particularly rich because it allows mapping the areas in the brain that are contributing to each independent temporal signal, resulting in a characteristic spatial map for each IC corresponding to a functional network.

Beckmann et al. (2005) found that these networks exhibit high spatial consistency across subjects and closely resemble discrete cortical functional networks such as visual cortical areas or sensory-motor cortex, suggesting that each RSN can be linked to a particular low-frequency temporal signature (or IC). In 2006, De Luca and colleagues found 5 RSN patterns that were reproducible across different subjects, closely matching the functional networks recruited by specific types of cognitive processes. A few months later, Damoiseaux et al. (2006) identified 10 robust RSNs across healthy subjects with potential functional relevance, consisting of regions known to be involved in motor function, visual processing, executive functioning, auditory processing, memory, and the so-called default-mode network, each with BOLD signal changes up to 3%. Moreover, they report that each of these networks exhibits significant baseline dynamics, with percentage BOLD signal change comparable with the signal changes found in task-related experiments. The extraction of RSNs from whole-brain resting-state BOLD signals using ICA is particularly important because it does not require any prior information regarding the expected location of RSNs.
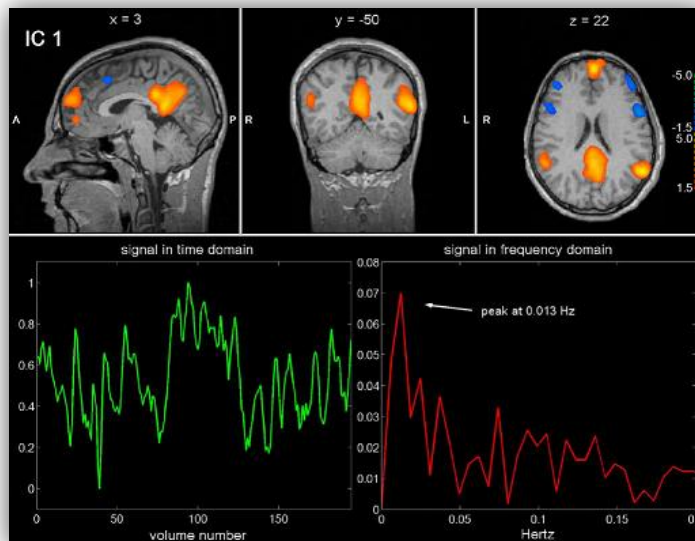
Figure 15 - Identification of an RSN using ICA. An independent temporal component $IC_k(t)$ is extracted from the BOLD signals using ICA (green), and then mapped over the brain (top) by selecting the set of voxels n whose BOLD signals, $x_n(t)$, have stronger contributions from $IC_k(t)$ as indicated by the coefficients $a_{n,k}$. The spectral properties of the IC waveform reveal a peak <0.1Hz. Adapted from Mantini et al. (2007).

Both correlation and IC analysis rely on the linear relationship between regions. Other nonlinear FC measures from information theory, such as mutual information, have been applied to resting-state data (Hartman et al., 2011). Hlinka et al. (2011) defined FC matrices using both linear (Pearson correlation) and non-linear FC measures and evaluated the resulting networks using graph theory. Their results show that, at least from a graph-theoretical perspective, the nonlinearity effects in resting-state activity are practically negligible when compared to the inter-subject variability of the graph measures and, on the group-average graph level, the nonlinearity effect is unnoticeable. In addition, Lynall et al. (2010) analyzed resting-state data using both mutual information and correlation measures at different wavelet scales, and found that correlation measures allowed a better distinction between healthy controls and schizophrenia patients. The linear dependency of resting-state BOLD time-series is probably linked to the slow time-scale inherent to fMRI (i.e. in the order of a couple of seconds), which does not allow the detection of fast time-delayed (or causal) interactions. Also for this fact, coherence analysis is not commonly applied in resting-state fMRI data, since phase-lagged interactions between oscillatory signals, like those occurring at faster frequencies, are only detected at higher temporal resolution.

I.II.3 – Characterizing complex networks using graph theory

Brain networks, in the same way as biological, social, chemical, and Internet networks, are systems composed by a large number of complexly interconnected dynamical units. The first approach to capture the organizational properties of such systems is to model them as graphs whose nodes represent the dynamical units, and whose links stand for the interactions between them. A large number of measures have been defined in the field of graph theory to characterize the topology of such complex wiring architectures (Sporns et al., 2002, Boccaletti et al., 2006, Rubinov and Sporns, 2010). Moreover, with the availability of free Matlab libraries for graph analysis such as the Brain Connectivity Toolbox (www.brain-connectivity-toolbox.net Rubinov and Sporns (2010)) and the MatlabBGL Toolbox (www.cs.purdue.edu/homes/dgleich Gleich (2007)) have allowed neuroscientists to efficiently implement the graph algorithms to explore and compare brain networks.

Here, we introduce some important graph theoretical measures that were used for the work presented in chapter *V – Effect of structural disconnections on resting-state functional networks.* Please note that we restrained ourselves to the properties of undirected binary graphs. An extension of the equations to weighted graphs is provided by Rubinov and Sporns (2010). Furthermore, we review a number of studies involving the characterization of both anatomical and functional brain networks, which provide fundamental insights into integrative aspects of brain function.

Brain connectivity measures, both anatomical and functional, can be represented in the form of a matrix C, with each of the elements C_{np} encoding the connection strength between two system elements n and p, $\forall n, p \in N$. Since the connection strength may vary depending on the pair of regions considered, this matrix is generally weighted. However, to be studied using graph theory, the connectivity matrix C may be binarized into an adjacency matrix A, where $A_{np} = 1$ if a connection exists between regions n and p, or $A_{np} = 0$ otherwise. To binarize this matrix, one needs to define the minimum weight necessary to consider it as an actual link. The definition of this threshold has direct impacts on the density of connections (or sparsity) of the network, which may have non-negligible effects on the graph properties of the network (van Wijk et al., 2010, Bassett et al., 2012).
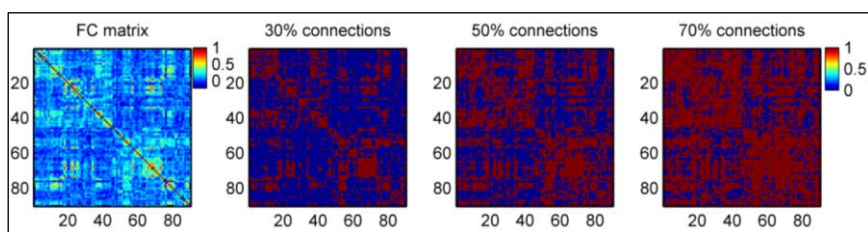
Figure 16 - Thresholding weighted matrices into binary graphs. Thresholding functional connectivity (FC) matrices into graphs with distinct connection densities can result in graphs with different properties.

Another crucial step on the definition of brain graphs is the size of the network, which is taken as the number of nodes. Since the brain can be parcellated at different scales (such as neurons, voxels or cortical regions) different graph properties may arise, and therefore the properties of brain networks must be taken in the light of the parcellation and the thresholding

technique employed. Still, two review studies on human brain graphs (Bassett and Bullmore, 2009, He and Evans, 2010) reported that some complex network properties are consistent over a range of spatial and time scales, and across modalities of neuroimaging data. Conserved principles include small worldness, high efficiency/low wiring cost, modularity and hubs, consistently found in brain networks obtained with structural MRI (He et al., 2007, Bassett et al., 2008, Chen et al., 2008), diffusion MRI (Hagmann et al., 2007, Iturria-Medina et al., 2008), fMRI (van den Heuvel et al., 2008, Ferrarini et al., 2009, Wang et al., 2009a), EEG (Micheloyannis et al., 2009, Rubinov et al., 2009), and MEG (Valencia et al., 2008, Stam et al., 2009). In addition, both structural and functional network metrics have been found to be heritable and to change with normal aging (Meunier et al., 2009, Micheloyannis et al., 2009). Furthermore, clinical studies principally in Alzheimer's disease and schizophrenia have identified abnormalities in the topological organization of resting-state functional networks in patients (Liu et al., 2008, Supekar et al., 2008a, Lynall et al., 2010).

At the regional level, nodal characteristics can be measured by several metrics such as degree, path length, efficiency, and clustering coefficient, which can be used to sort nodes according to their role in the network. The node degree is defined as:

$$d_n = \sum_{p=1}^{N} A_{np}.$$

The degree distribution is given as the probability distribution of node degrees over the whole network (Boccaletti et al., 2006) which provides information on the global organization of links over the network. Considering $p(k)$ as the probability of a node having a degree $d_n = k$, the cumulative degree distribution of the network (Barabasi and Albert, 1999) is given by:

$$P(k) = \sum_{k' \geq k} p(k').$$

Sorting nodes in descending order of degree allows identifying the hubs of the network (i.e. nodes that have more connections). Hubs are generally

crucial elements for the integrity of the network. For example, if high-degree hubs are removed from the network (also called a targeted attack), then the network may fractionate into two or more independent sub-networks. Robustness measures have been defined to characterize the resilience of the network to attacks, both targeted and random. To estimate the robustness of a network, each time a node was removed from the network, the size of the largest connected component, s, is recalculated (using for example the corresponding function in the MatlabBGL Toolbox (Gleich, 2007)). Plotting the size s versus the number of nodes removed, $s(n)$, the robustness parameter is defined as the area under this curve (Achard et al., 2006), normalized by $N(N-1)/2$, so that the maximum robustness is 1. Networks that are more robust retain connectedness even when a large proportion of nodes have been eliminated.

It seems that the most striking and widely studied property of brain networks is their small-world organization (Watts and Strogatz, 1998, Sporns and Zwi, 2004, Bassett and Bullmore, 2006, Sporns and Honey, 2006). To understand how the small-world index is calculated, we need previously to introduce the concepts of path length and clustering.
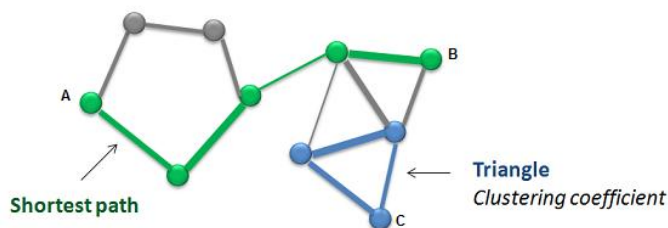
Figure 17 – Illustration of the shortest path from node A to node B (green), and of a triangle (blue), where the neighbours of node C are also connected with each other.

The path length consists on the average number of links (or paths) connecting every pair of nodes in the network. It can be calculated as: $l_{np} = \sum_{A_{uv} \in g_{n \leftrightarrow p}} A_{uv}$ (Rubinov and Sporns, 2010), where $g_{n \leftrightarrow p}$ is the shortest path (geodesic) between n and p. Note that $l_{np} = \infty$ for all disconnected pairs n, p. The average shortest path length between all pairs of nodes in the network, is known as the characteristic path length of the network (Watts and Strogatz, 1998), and provides a measure of functional integration:

$$L = \frac{1}{N} \sum_{n=1}^{N} L_n = \frac{1}{N} \sum_{n=1}^{N} \frac{\sum_{p=1, p \neq n}^{N} l_{np}}{N-1},$$

where L_{ni} is the average distance between node n an all other nodes, representing the nodal path length. Considering that a network with a short characteristic path length will be more efficient in integrating information, Latora and Marchiori (2001) defined a measure of global efficiency E, as

$$E = \frac{1}{N} \sum_{n=1}^{N} \frac{1}{L_1}.$$

The efficiency E may be meaningfully computed on disconnected networks, because disconnected nodes are defined to have zero efficiency, while the path length L is infinite in such cases (Achard and Bullmore, 2007).

The clustering coefficient provides information on how densely neighbouring nodes are connected. At the nodal level, if two neighbours of n are also connected between themselves, they form a triangle. C_n indicates the proportion between the number of triangles with a vertex in n and the total number of possible triangles if all neighbours of n would be directly connected with each other too. Computing the number of triangles of a node i as:

$$t_n = \frac{1}{2} \sum_{p=1, q=1}^{N} A_{np} A_{nq} A_{pq},$$

the clustering coefficient of a graph C is defined in the following way:

$$C = \frac{1}{N} \sum_{n=1}^{N} C_n = \frac{1}{N} \sum_{n=1}^{N} \frac{2 t_n}{k_n (k_n - 1)}.$$

A graph is considered small-world if its average clustering coefficient C is significantly higher than for a comparable random graph R (See Figure 18 for an illustration) but the mean shortest path length L is approximately the

same as in a comparable random graph (Watts and Strogatz, 1998, Humphries et al., 2006).
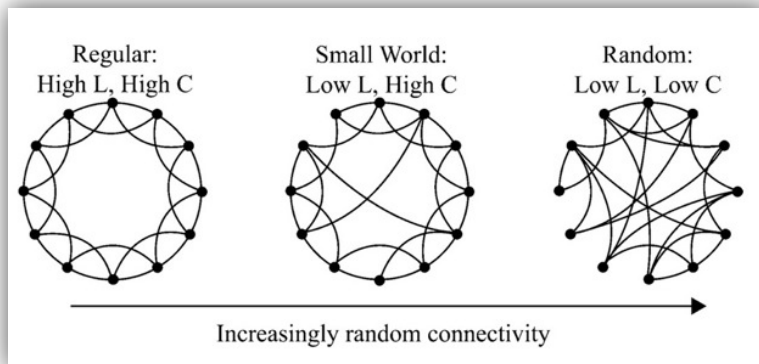
Figure 18 - Small-world networks. Random rewiring procedure for interpolating between a regular ring lattice (left) and a random network (right), without altering the number of vertices or edges in the graph. Adapted from Watts and Strogatz (1998).

Since the mean shortest path length can be estimated as the inverse of global efficiency, small-worldness SW can be formulated in the two following ways (Achard and Bullmore, 2007, Humphries and Gurney, 2008):

$$SW = \frac{C/C_{rand}}{L/L_{rand}} = \frac{C\,E}{C_{rand}E_{rand}}.$$

The more SW is above 1, the more the graph is considered to be small-world. The small-world architecture is particularly rich in complex brain networks because it supports both segregated modular specialization and distributed functional integration. In addition, it maximizes the efficiency of information transfer at a relatively low wiring cost. Notably, it seems to be a common self-organizing principle of complex natural systems, such as biological, chemical and even social networks (i.e. the famous "six degrees of separation" between living people). The importance of a small-world topology for an optimal cognitive performance is corroborated by reports of disrupted small-world properties in diseases such as schizophrenia (Liu et al., 2008, Lynall et al., 2010, Bassett et al., 2012), Alzheimer's disease (Supekar et al., 2008a) and attention-deficit/hyperactivity disorder (ADHD) (Wang et al., 2009b).

A hierarchical network is defined so, if the nodes with larger degree (or hubs) are also poorly clustered, meaning that they are serving as a bridge between nodes poorly connected to each other. The hierarchy coefficient, β, is the (positive) exponent of the power-law relationship between the clustering C and the degree d of the nodes in the network such that $C \sim d^{-\beta}$ (Ravasz and Barabasi, 2003, Bassett et al., 2008).

Another important network metric is the modularity, which identifies modules of linked nodes that work together to achieve distinctive functions (Newman, 2006, Leicht and Newman, 2008). Connections are usually denser within modules than between them. Detecting and characterizing modules of the brain can allow us to identify groups of anatomically and/or functionally associated components that may subserve specific behavioural functions. For example in a model of resting-state dynamics, Deco et al. (2009) used a modularity algorithm to divide one hemisphere of the macaque anatomical network into 2 communities. Exploring the dynamics of the two modules independently, they found that each module exhibited a specific temporal pattern of synchronization, and notably, the synchronization level between the two modules was anti-correlated, which could be explained by stochastic resonance in a dynamical system with multistability. These results reinforce the idea that the topological organization of structural brain networks constrain and mould brain dynamics at multiple levels.

'Occurrences in this domain are beyond the reach of exact prediction
because of the variety of factors in operation,
not because of any lack of order in nature.'
Albert Einstein, 1941

I.III - Large-scale models of resting-state dynamics

The dynamics unfolding from the interplay between brain areas, when these
are embedded in the neuroanatomical network, has been attracting a
growing body of research in computational neuroscience (Jirsa et al., 2010,
Deco et al., 2011). Combining generative models of neuronal activity with
realistic structural connectivity patterns has allowed exploring, through
simulations, how large-scale interactions between neural systems can give
rise to the spontaneous emergence of spatiotemporally organized
fluctuations similar to the ones reported in resting-state neuroimaging
studies.

To investigate this dynamics at the whole-brain scale, it is useful to go
beyond the microscopic activity of individual neurons and consider instead
the mesoscopic behaviour of large ensembles of neurons, or neuronal
populations (for a review see Deco et al. (2008)). Although simulations of
detailed models at the cellular (and even sub-cellular) level are becoming
computationally feasible (Markram, 2006, Izhikevich and Edelman, 2008),
reduced neural-mass models, despite their low spatial resolution, allow a
comprehensive study of the large-scale interactive dynamics with relatively
low parametric complexity. This approach is motivated by neuroimaging
observations that neurons within a densely connected neural ensemble tend
to share the same physiological properties, exhibit dense reciprocal
interconnectivity and show strong dynamical correlations. Neural-mass
models can be extended to neural-field models, where the expected state of
a neuronal population becomes a function of both time and position on the
brain's spatially continuous cortical sheet. However, for simplification, all
the models described herein refer to isolated points in space (or point-
masses).

Following different reduction lines, a number of studies have contributed for
the understanding of resting-state dynamics using neural-mass models

coupled according to the brain's anatomical architecture (Ghosh et al., 2008, Deco et al., 2009, Honey et al., 2009, Deco and Jirsa, 2012)(Hugues et al., in preparation). In the following, we describe the neural-mass models used in these works and describe how the simulated neural activity was transformed in a hemodynamic signal. Finally, we comment on the conclusions of the existing models, including the role of the main factors influencing functional connectivity during rest: couplings, delays and noise. Finally, we report the results of modelling studies that examined the dynamical consequences of structural lesions on resting-state activity.

I.III.1– Modelling the dynamics of a cortical region

I.III.1.a - Conductance-based biophysical model

The first work to investigate the cooperative behaviour of neural systems coupled through a realistic anatomical wiring scheme was achieved by Honey and colleagues (2007). They used a biophysical neural-mass model introduced by Breakspear and colleagues (2003) together with the interregional anatomical connectivity of the macaque cortex (Kötter, 2004). Later, the same model was extended to incorporate human neuro-anatomical connectivity and results were compared with resting-state fMRI functional connectivity from healthy humans (Honey et al., 2009). Finally, the same group used this model to study the dynamical impact of lesions in the brain (Honey and Sporns, 2008, Alstott et al., 2009), which we will describe in section *I.III.4*.

The neural-mass dynamics in these works was derived from a conductance-based model of neuronal dynamics (Morris and Lecar, 1981) extended for neural population activity (Larter et al., 1999). The coupling between neural masses (or cortical regions) was introduced via weak long-range excitatory-to-excitatory connections, mimicking glutamate-induced synaptic currents (Breakspear et al., 2003, Breakspear et al., 2004).

The main dynamical variable in that model is the mean membrane potential of pyramidal cells V, which is governed by the conductance of sodium (g_{Na}), potassium (g_K) and calcium (g_{Ca}) ions through voltage-gated channels, plus the passive conductance of 'leaky' ions (g_L). The total current flow across pyramidal cell membranes is given by:

$$C\frac{dV}{dt} = -g_{Ca}m_{Ca}(V - V_{Ca}) - g_{Na}m_{Na}(V - V_{CNa}) - g_K W(V - V_K)$$
$$- g_L(V - V_L)$$

where g_{ion} is the maximum conductance of each population of ions, m_{ion} is the fraction of open ion channels (W for potassium ion channels), and V_{ion} is the Nernst potential for that ion species. All equations and parameters are non-dimensional and normalized to neural capacitance $C = 1$. Each voltage-gated channel opens when the membrane potential overcomes a given threshold, T_{ion}. For a large population of ion channels, T_{ion} assumes a Gaussian distribution (with variance δ_{ion}) and hence, the fraction of open ion channels is given by the following (sigmoid-shaped) function:

$$m_{ion} = 0.5 \left(1 + \tanh\left(\frac{V - T_{ion}}{\delta_{ion}}\right)\right).$$

The fraction of open potassium channels W is defined differently because these channels 'relax' from one state to another at an exponential rate. Therefore, W is governed by

$$\frac{dW}{dt} = \frac{\phi(m_K - W)}{\tau}$$

where ϕ is a temperature scaling factor and is τ the 'relaxation' time constant.

To introduce synaptic interactions between neurons within the same neural ensemble, the average firing-rates of excitatory (Q_V) and inhibitory neurons (Q_Z) is calculated and introduced as a feedback term subsequent to cell firing to represent neurotransmitter release. At the cell soma, the membrane potential triggers an action potential if it exceeds a threshold. Averaging this over the ensemble of neurons and assuming once again a Gaussian distribution, the cell firing rates can be obtained by the following equations:

$$Q_V = 0.5 \times Q_{Vmax}\left(1 + \tanh\left(\frac{V - V_T}{\delta_V}\right)\right),$$

$$Q_Z = 0.5 \times Q_{Zmax}\left(1 + \tanh\left(\frac{Z - Z_T}{\delta_Z}\right)\right),$$

where Q_{max} are the maximum rates of firing of the excitatory and inhibitory neurons respectively. The firing of each population feeds back onto the ensemble and raises or lowers the membrane potential accordingly.

Excitatory-to-inhibitory and inhibitory-to-excitatory connections are modelled as additional inputs to the flow of ions across the membrane channel, weighted by functional synaptic factors, a_{ei} and a_{ei} respectively. In addition, excitatory-to-excitatory connections are modelled with greater physiological detail: the mean firing rate Q_V is assumed to lead to a proportional release of glutamate neurotransmitter across the synapse, which diffuses onto two classes of ligand-gated ion channels. On one side, AMPA receptors open additional sodium channels, increasing the net conductance of sodium flow. On the other, NMDA receptors open an additional population of voltage-gated calcium channels, increasing the maximum conductance of voltage-gated calcium channels. Incorporating these specifications, the membrane potential of excitatory (V) and inhibitory (I) is given by:

$$
\begin{aligned}
\frac{dV}{dt} = &-(g_{Ca} + r_{NMDA} a_{ee} Q_V) m_{Ca}(V - V_{Ca}) \\
&- (g_{Na} m_{Na} + a_{ee} Q_V)(V - V_{Na}) - g_K W(V - V_K) \\
&- g_L(V - V_L) + a_{ie} Z Q_Z + a_{ne} I_\delta,
\end{aligned}
$$

$$
\frac{dZ}{dt} = b(a_{ii} I_\delta + a_{ni} V Q_V),
$$

Where I_δ corresponds to 'nonspecific' subcortical excitation with amplitude I modulated by a random noise component of amplitude δ added to both populations with weights a_{ne} and a_{ni}. a_{ee} scales the local excitatory-to-excitatory synaptic strength and r_{NMDA} denotes the number of NMDA receptors relative to that of AMPA receptors.

These equations depict the behaviour of one population of densely interconnected excitatory and inhibitory neurons. To model the cooperative behaviour of N coupled neural-masses it is necessary to introduce long-range excitatory projections between pyramidal cells. These long-range projections are modelled to target the same populations of NMDA and AMPA receptors targeted by the short-range excitatory projections.

Representing each node with an index $n = 1, \ldots N$, the following equation describes the mean membrane potential of pyramidal cells at position x_n:

$$\begin{aligned}
\frac{dV(x_n)}{dt} = -(g_{Ca} &+ (1-c)r_{NMDA}a_{ee}Q_V(x_n) \\
&+ c\, r_{NMDA}a_{ee}\langle Q_V(x)\rangle)m_{Ca}(V(x_n) - V_{Ca}) \\
&- (g_{Na}m_{Na} + (1-c)a_{ee}Q_V(x_n) + c\, a_{ee}\langle Q_V(x)\rangle)(V(x_n) \\
&- V_{Na}) - g_K W(V(x_n) - V_K) - g_L(V(x_n) - V_L) \\
&+ a_{ie}ZQ_Z(x_n) + a_{ne}I_\delta,
\end{aligned}$$

where $\langle\ \rangle$ represents spatial averaging over neural-masses. Parameters were set to values that replicate realistic conductances. Using a regular connectivity these values had previously been reported to show complex, spontaneous activity, including intermittency, phase synchrony, and marginal stability (Breakspear et al., 2003, Breakspear et al., 2004).

When computing the network dynamics using realistic anatomical connectivity from the macaque (Honey et al., 2007) or the human (Honey et al., 2009) brains, the inter-node coupling was set to a value at which synchronous dynamics is weakly stable, allowing spontaneous switching between synchronous epochs and desynchronous bursts. Since neither noise nor delays are introduced in the model, activity in the system arises purely from nonlinear instabilities due to the complex structural connectivity and the chaotic dynamics at the neural-mass level. Under this parameterization the neural interactions in the model occur at multiple time-scales and reflect spontaneously arising 'self-organizing' patterns. In this configuration, the authors identify BOLD network activations, which favourably compare to resting-state functional connectivity.

I.III.1.b - The FitzHugh-Nagumo model

The neuro-anatomical architecture of the brain shapes not only the connectivity between regions, but also the distance over which these connections occur, defining in this way a space-time structure of couplings and delays, which is essentially constant over relatively short time scales. In order to explore the behaviour of neural-masses in this dynamic framework, Ghosh et al. (2008) studied the ongoing dynamics of FitzHugh-Nagumo units

(Fitzhugh, 1961, Nagumo et al., 1962) coupled according to anatomical connectivity of one hemisphere of the macaque brain (Kötter, 2004). Importantly, the interaction between regions was time-delayed, with delays proportional to the distance between regions[1].

The node model was implemented by defining two state variables, u_n and v_n, representing the membrane potential and the recovery potential correspondingly, for each node n. A parameter c scales all connection strengths without altering the connection matrix C_{np} nor affecting the associated time delays Δt_{np}. The following differential equations describe the dynamics of the state variables, with corresponding additive noise n_u and n_v:

$$\dot{u}_n(t) = g(u_n, v_n) - c \sum_{n=1}^{N} C_{np} \, u_p\big(t - \Delta t_{np}\big) + n_u(t)$$

$$\dot{v}_n(t) = h\big(u_p, v_n\big) - n_v(t)$$

The functions g and h are based on FitzHugh-Nagumo systems (Fitzhugh, 1961, Nagumo et al., 1962) and are defined as follows:

$$g(u_n, v_n) = \tau \left[v_n + \gamma u_n - \frac{u_n^3}{3} \right],$$

$$h(u_n, v_n) = -(1/\tau)[u_n - \alpha + \beta v_n]$$

In absence of connectivity, the network nodes display damped oscillatory dynamics. Nodes were then coupled with brain-inspired connectivity and delays and the stability of the resulting dynamics was investigated as a function of finite signal transmission speeds and increasing coupling strengths[2]. For a restricted interval of velocities (5-20m/s) and for a sufficiently strong coupling, the system exhibits increased instability. At the

---

[1] Note that the space-time structure is only approximately estimated, since the locations of the regions were based on a standard human atlas (AAL), whilst the connections were derived from macaque brains.

[2] For details on the parameter set, see Ghosh A, Rho Y, McIntosh AR, Kötter R, Jirsa VK (2008) Noise during rest enables the exploration of the brain's dynamic repertoire. PLoS computational biology 4:e1000196..

border of instability, and in the presence of noise, neural-masses display the emergence of oscillatory dynamics (at 10Hz) with fluctuating amplitude (see Figure 19).
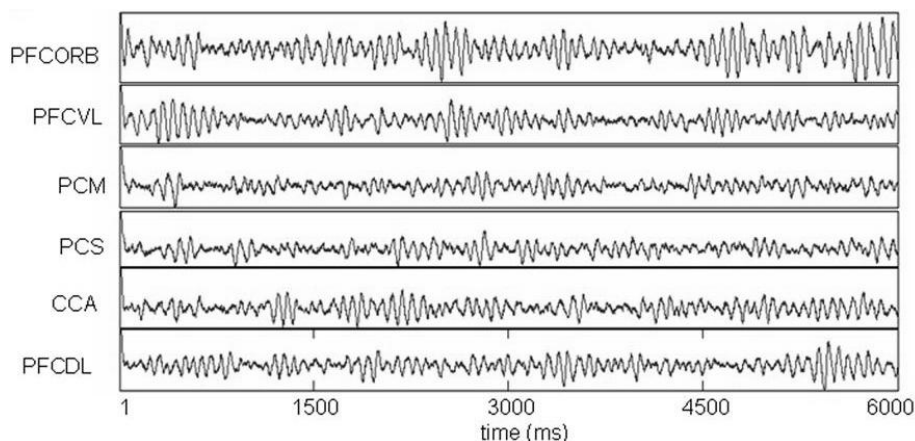
Figure 19 - Time series of coupled FitzHugh-Nagumo units at the border of instability with noise. Adapted from Ghosh et al., (2008).

The network connectivity is found to shape the dynamic repertoire of the entire network, giving rise to slow fluctuations in the power of the 10Hz oscillations (i.e. fluctuations in band-limited power). To test for the emergence of ultra-slow oscillations, the BOLD signal was computed[1], giving rise to rest-like fluctuations that were correlated across distant areas. Furthermore, simulated BOLD signals were found to exhibit correlations within the DMN as transmission velocities ranged between 5 and 10m/s, which falls in the interval of expected realistic speeds in myelinated axons.

In addition to the results presented in their study, the authors have tested multiple oscillator types which are commonly used in neural-mass modelling including Hopf oscillators, Wilson-Cowan systems, FitzHugh-Nagumo systems, and finally mixed populations of coupled FitzHugh-Nagumo neurons (Assisi et al., 2005), all of which provided similar results.

I.III.1.c - The Wilson-Cowan model

Another important modelling study of large-scale resting-state dynamics was developed by Deco and colleagues (2009) using the same space-time

---

[1] See section *I.III.2 - Transforming neuronal activity into BOLD signal.*

structure as Ghosh et al. (2008), i.e. the macaque's anatomical connectivity (CoCoMac; Kötter (2004)) and time delays derived from a human template. At the node level, the dynamics of a neural population was modelled using Wilson–Cowan units (Wilson and Cowan, 1972, 1973). Wilson and Cowan analyzed the collective properties of large ensembles of excitatory and inhibitory neurons using methods from statistical mechanics, based on the *mean-field* approach. They proposed that typical dynamics in a cortical region could be obtained by considering a population of excitatory neurons coupled with a population of inhibitory neurons.

It consists on a set of differential equations that describe the time evolution of the mean level of activity of a neural population, using a nonlinear sigmoid function to represent the interactions between the populations. The activity of a pool of excitatory (pyramidal) neurons without external input, $E(t)$, is given by the following equation:

$$\tau \frac{\partial E(t)}{\partial t} = -E(t) + \phi\big(E(t)\big),$$

where τ is the membrane time constant, $-E(t)$ means that the activity decays in time if no stimulation is received, and the last term takes into account the recurrent excitatory stimulation from all the neurons in the same pool. The response function transforming the current into discharge rates is given by:

$$\phi(x) = \frac{c}{1 - exp^{-a(x-b)}}.$$

Considering now the two populations of the Wilson-Cowan module are coupled together, one with only excitatory neurons, $E(t)$, and another with only inhibitory neurons, $I(t)$, the dynamics of such module is given by the following 2 differential equations:

$$\tau \frac{\partial E(t)}{\partial t} = -E(t) + \phi\big(I_b + w_+ x(t) - I(t)\big) + \delta(t),$$

$$\tau' \frac{\partial I(t)}{\partial t} = -I(t) + \phi\big(w_I E(t)\big) + \delta(t),$$

where I_b is a diffuse spontaneous background input, and δ is additive independent Gaussian noise with mean value zero. The noise level is given by the variance $\langle\delta\rangle^2$.
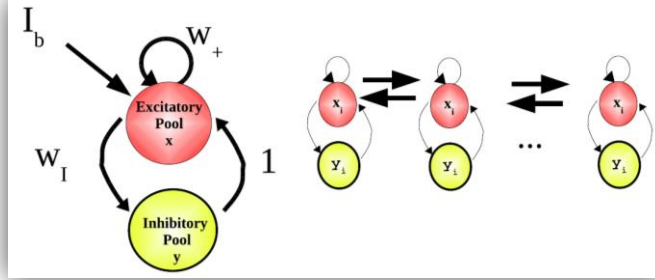
Figure 20 – Schematic illustration of a Wilson-Cowan unit. The model consists in two pools, one representing a population of excitatory neurons and the other a population of inhibitory neurons that are coupled to each other. Adapted from Deco et al. (2012).

To model the network dynamics at the macroscopic level, $N = 38$ Wilson-Cowan modules, each representing a cortical region, were coupled according to the macaque's neuro-anatomic connectivity, using the connectivity matrix C_{np} and the assumed delays D_{np}. The global dynamics is given by

$$\tau\frac{\partial E_n(t)}{\partial t} = -E_n(t) + \phi\left(I_b + \sum_{p=1}^{N} \alpha C_{pn} E_p(t - D_{pn}) - I_n(t)\right) + \delta_n(t),$$

and

$$\tau\frac{\partial I_n(t)}{\partial t} = -I_n(t) + \phi(w_I E_n(t)) + \delta_n(t).$$

α regulates the global coupling strength and recurrent couplings wre set to $C_{nn} = w_+/\alpha$. In all simulations Deco et al. (2009) used $\tau = 1$, $\tau' = 0.2$, $w_I = 1.5$, $a = 0.1$, $b = 40$ and $c = 100$.

Taking into account the bifurcation diagram of a single Wilson-Cowan module as a function of the parameters I_b and w_+, these 2 parameters were selected such that the node dynamics is at the border of a Hopf bifurcation, but still in a non-oscillatory low-activity state. The idea is that,

when modules are coupled ($\alpha > 0$), they go spontaneously to an oscillatory state in the gamma-frequency band (40Hz). Notably, for the range of couplings, time delays, and noise parameters used in Deco et al. (2009), the coupled modules behave similarly to single isolated and noise-free Wilson-Cowan oscillators.

In a regime where neural-masses exhibit self-sustained oscillations in the gamma-frequency range, it was found that the system was organized into 2 functional networks who competed to synchronize. For a certain level of noise, the synchronization level of the two networks was found to fluctuate slowly (0.1Hz) and in an anti-correlated way, in agreement with previous reports of anti-correlated functional networks during rest (Fox et al., 2005).

I.III.1.d - Node model in asynchronous state

The model of resting-state activity presented in this section was derived by Etienne Hugues, extending work done in (Mattia and Del Giudice, 2002). It has been used in the work presented in *Chapter V*. This model builds on the assumption that local neural networks are in a stable asynchronous state where no oscillations develop, and where small perturbations of the neural activity around this state are induced by internal and external fluctuations of the otherwise constant external stimulation.

The evolution of the activity of a large population of spiking neurons can be described by the probability distribution of their internal variables (the membrane potential in the simplest case), which obeys the Fokker-Planck equation (Risken, 1989). An associated equation gives the neural population firing-rate. Under the hypothesis that the network has a stable asynchronous state, the steady solution of the Fokker-Planck equation is stable and therefore these equations can be linearized around this solution. In this case, the node dynamical model describes only the firing rate deviations of the neural mass around its asynchronous state. Decomposing the probability distribution using the infinite series of eigenmodes of the Fokker-Planck equation, we arrive to a linear dynamical equation for each of the coefficients of the series' expansion plus an equation for the rate fluctuations. The solution of this infinite set of linear equations is controlled by the infinite set of eigenvalues $\lambda_k = -1/\tau_k + i\omega_k$ where $\omega_k/2\pi$ is an oscillation frequency and τ_k is a damping timescale. Among these modes,

very few have a sufficiently large damping timescale so that they effectively contribute to the dynamics. Usually, one mode has a real eigenvalue which describes perturbations that simply decay exponentially in time, with a timescale τ_0. As the model is intended to simulate the BOLD signal, the dynamics produced by the (fast) oscillatory perturbations will be filtered out. Therefore, the dynamics we are interested herein can be approximately described by the exponentially decaying perturbations responsible for the low-frequency part of the neuronal activity. Finally, for the local network n, the firing rate deviations $r_n(t)$ obey the following first order stochastic differential equation:

$$\tau_0 \frac{dr_n}{dt} = -r_n(t) + \frac{k}{c_1} \sum_{p=1}^{N} C_{np} r_p(t - \tau_{np}) + \sigma \eta_n(t), n = 1, \dots, N.$$

k is the global excitatory coupling level between nodes ($k > 0$). C_{np} and τ_{np} are the structural coupling strength and the conduction delay from region p to region n, specified by the structural connectivity (SC). As C has positive coefficients, the Perron-Frobenius theorem shows that this matrix has a real eigenvalue c_1 such that all other eigenvalues are lower in modulus, and therefore have a lower real part. σ is the noise level and the terms $\eta_n(t)$ are uncorrelated white Gaussian noises with zero mean and unit variance ($\langle \eta_n(t) \rangle = 0$ and $\langle \eta_n(t)\eta_p(t') \rangle = \delta_{np}\delta(t - t')$, where δ_{np} is the Kronecker symbol and $\delta(t)$ denotes the Dirac delta function). This noise is not necessarily of external origin (i.e. stimulation noise) and can be generated internally: finite size networks have been shown to intrinsically induce noise in the dynamics (Mattia and Del Giudice, 2002). As equations are linear, σ only scales the level of the rate deviations. Given τ_0, which is given by the internal state of local networks ($\tau_0 = 20$ ms here), the dynamics depends only on one parameter: k. As long-distance connections are excitatory, the reverberated activity over the network can destabilize the damped local dynamics, and therefore the asynchronous states. For this reason, k must be bounded from above. For null delays, a classical stability analysis gives the stability condition: $k < 1$ (explaining why we have scaled down the coupling by c_1 in the previous equation). When delays are finite, this remains a very good approximation.

Without noise, the dynamics of the firing rate deviations around an otherwise constant state would always tend to zero after some time, as long as the stability condition is verified. In the presence of noise, the model permanently produces ongoing fluctuations across the large-scale network by the excitatory reverberation of local activity on this recurrent network. Consequently, even if individual noises are independent, the SC makes the rate fluctuations not independent, explaining in principle the finding of large-scale structure in the brain fluctuations.

To gain theoretical insight into the large-scale network dynamics, it is useful to consider the case of null delays. This case corresponds to the Ornstein-Uhlenbeck process in N dimensions (Gardiner, 2004) but, what makes the dynamics interesting here is the complicated –or disordered- connectivity matrix C, which is the main ingredient in explaining the emergence of functional networks as will be shown below. In this case, and using the eigenvectors frame of C, the firing rate deviations can be written as $r(t) = \sum_{p=1}^{N} R_p(t) V_p$, where $r(t)$ and $R(t)$ are the column vectors of the original and transformed rate perturbations, respectively. V_p is the p–th unit right eigenvector of the matrix C, associated with the eigenvalue c_p. As the network has a three-dimensional representation, V_p represents a spatial map (Note that, when considering the case of non-symmetric connectivity matrices, pairs of complex conjugate eigenvalues appear and therefore both conjugate eigenvectors need to be used to define physically meaningful spatial maps). We sorted these eigenvalues in descending order of the real parts: $c_1 > \mathrm{Re}[c_2] > \ldots > \mathrm{Re}[c_N]$ ($\mathrm{Re}[x]$ denoting the real part of x). Each transformed rate perturbation, or mode, $R_p(t)$ has temporal fluctuations described by the timescale $\tau_p = \tau_0 / (1 - \frac{k \mathrm{Re}[c_p]}{c_1}) > 0$. From the ordering of the eigenvalues of C, we have $\tau_1 > \tau_2 > \ldots > \tau_N$. Therefore, the global dynamics of the large-scale network is a superposition of these temporal modes, but with distinct spatial maps for each mode. In particular, the modes associated to the eigenvalues with the largest real parts have the largest timescales, and therefore are the slowest ones. Moreover, when the coupling k increases, all modes up to mode p (for which $\mathrm{Re}[c_p] > 0 > \mathrm{Re}[c_{p+1}]$), get slower and the others get faster. The timescale of the first mode $\tau_1 = \tau_0 / (1 - k)$ increases faster than all the other timescales τ_p,

with $p \geq 2$, and even diverges as $k \rightarrow 1$. If we add the fact that the variance of mode $R_p(t)$ is proportional to τ_p, the fluctuations in the network dynamics will be dominated (in variance) by the slowest modes, and dominantly by $R_1(t)$, leading to correlations in the low-frequency part of the neural activity. In particular, the BOLD signal, which can be seen in a first approximation as a low-pass filtering of the neural activity (Cabral et al., 2011), will present spatial correlations. As a result, the mean of the correlation distribution of the BOLD correlation or FC matrix will shift towards positive values.

Because of the finite axonal conduction velocity -in the range $5 - 10$ m/s-, delays are in fact finite but shorter than 50 ms in humans. Delays theoretically introduce an infinite number of degrees of freedom but their practical effect on the dynamics depends on their magnitude. When the linear dynamical equations are written in the frequency domain, for a given frequency f, delays enter in terms $\exp(i2\pi f \tau_{np})$. Here, we are only interested in the BOLD signal generated by the neural activity. Because the model used to calculate the BOLD signal (see section *I.III.2- Transforming neuronal activity into BOLD signal*) first filters the neural activity with a low-pass filter with approximate cut-off at $f_c = 0.4$ Hz (Cabral et al., 2011), and since $f_c \tau_{np} < 0.02$, the delays have a very small effect on the slow part of the neural activity which is responsible for the BOLD signal. Simulations with and without delays confirm, in the particular case of this model, the negligible effect of the delays.

Simulations with the model generated slow BOLD signal fluctuations that revealed the underlying anatomical connectivity, correlating significantly with empirical functional connectivity.

I.III.1.e – Attractor network of spiking neurons

In a recent work, Deco and Jirsa (2012) propose a resting-state model with an increased degree of realism at the node level. Each node in the network was modelled as a biophysically realistic attractor network consisting of mutually interconnected populations of excitatory pyramidal neurons and inhibitory neurons. This type of attractor network of spiking neurons is a dynamical system with an intrinsic tendency to settle in stationary states – also called "attractors"- typically characterized by a stable pattern of firing

activity. Small perturbations due to external (or even internal) noise may provoke the destabilization of an attractor, inducing transitions between different stable attractors.

Individual neurons were modelled as integrate-and-fire (IF) spiking neurons with excitatory (AMPA and NMDA) and inhibitory (GABA-A) synaptic receptor types. The dynamics of an IF neuron is described by its membrane potential $V(t)$, defined as:

$$C_m \frac{\partial V(t)}{\partial t} = -g_m(V(t) - V_L) - I_{syn}(t),$$

where $g_m = 1/R_m$ is the membrane leak conductance, V_L is the resting potential, and $I_{syn}(t)$ is the incoming synaptic current. The membrane time constant is defined by $\tau_m = C_m/g_m$. When the voltage across the membrane reaches the threshold V_{thr}, the neuron generates a spike, which is then transmitted to other neurons, and then the membrane potential is instantaneously reset to V_{reset} and maintained there for a refractory time τ_{ref}. The synaptic input $I_{syn}(t)$ depends nonlinearly on 1) the excitatory currents received from other neurons, 2) the excitatory and inhibitory currents received through recurrent connectivity and 3) an external background input from 800 external neurons emitting uncorrelated Poisson spike trains (see Deco and Jirsa (2012) for details).

Each of the 66 nodes in the macroscopic network of the brain contains 100 excitatory pyramidal neurons and 100 inhibitory neurons, resulting in a total of 13200 neurons with nonlinear interactions. Integrating the full spiking model is too computationally expensive to allow the exploration of the parameter space to find the parametric conditions matching the experimental findings. Alternatively, performing a mean-field approximation reduces the number of integration variables for each neural population (Brunel and Wang, 2001) and allows determining the number of fixed points –or attractors- of the population firing rates in the parameter space (the so-called "attractor landscape" Figure 21 Left). By manipulating the global coupling weight, it is found that the model optimally predicts empirical data (Figure 21 Right) when the brain network operates at the brink of a bifurcation that separates the stable equilibrium low activity state from the

multistable state region where many attractors corresponding to high activity in different brain areas coexist.
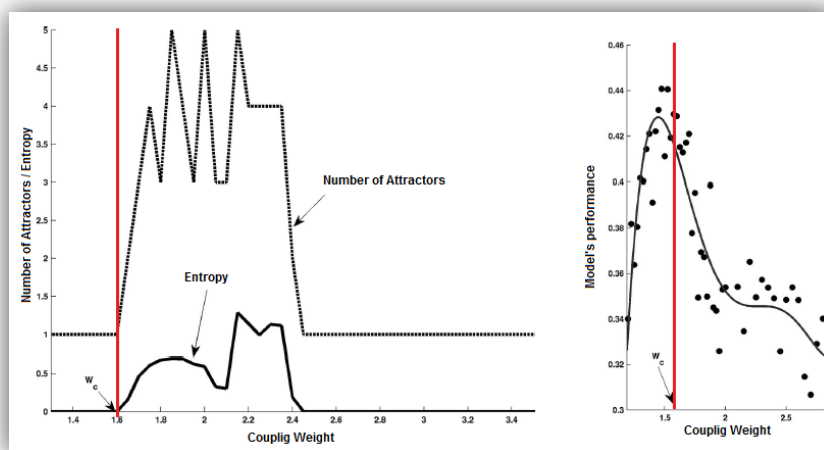
Figure 21 – Comparing the model's performance with the attractor landscape. (Left) Mean-field analyses of the attractor landscape of the cortical spiking network as a function of the global inter-areal coupling weight. The dashed line plots the number of stable attractors, whereas the continued line shows the entropy of the attractors. **(Right)** Fit of simulated data with empirical functional connectivity, as a function of the global coupling weight. The best fit is achieved at the edge of the bifurcation (vertical line). Adapted from Deco and Jirsa (2012).

The results from this work demonstrate that resting state networks in fMRI can result from structured noise fluctuations around the trivial low firing equilibrium state induced at the edge of a bifurcation by the presence of latent "ghost" multistable attractors corresponding to distinct foci of high firing activity in particular brain areas.

I.III.2 - Transforming neuronal activity into BOLD signal

To estimate BOLD signal changes associated with the simulated neural activity, all the previous models have used the Balloon-Windkessel hemodynamic model (Friston et al., 2003)[1]. This model specifies the neurovascular coupling of neural activity into blood perfusion changes. The BOLD signal is taken to be a static nonlinear function taking into account the normalized voxel content of deoxyhemoglobin, the normalized venous volume, the net oxygen extraction fraction by the capillary bed during

---

[1] In our works presented in chapters II, III and IV, the same model was implemented.

resting and the resting blood volume fraction. To estimate the BOLD-signal estimation we built on the assumption that the physical quantity whose variations underlie BOLD signal is the firing rate of the neuronal population $r_n(t)$. In the model, the firing rate fluctuates around a fixed value and these fluctuations are given by a periodic function of the local node phase. We have made the simple choice of the sine function, that is $r_n(t) = r_0 \sin(\theta_n(t))$, with a fixed amplitude $r_0 = 1$.

The neural activity at node n, $r_n(t)$, causes an increase in a vaso-dilatory signal s_n that is subject to auto-regulatory feedback. Inflow f_n responds in proportion to this signal with concomitant changes in blood volume v_n and deoxyhemoglobin content g_n. The equations relating these biophysical variables with the BOLD signal γ_n are:

$$\frac{\partial s_n(t)}{\partial t} = r_n - k_n s_n - \gamma_n(f_n - 1)$$

$$\frac{\partial f_n(t)}{\partial t} = s_n$$

$$\frac{\tau_n \partial v_n(t)}{\partial t} = f_n - v_n^{\frac{1}{\alpha}}$$

$$\frac{\tau_n \partial q_n(t)}{\partial t} = \frac{f_n\left(1 - (1 - \rho_n)^{\frac{1}{f_n}}\right)}{\rho_n} - \frac{v_n^{\frac{1}{\alpha}} q_n}{v_n}$$

where ρ_n is the resting oxygen extraction fraction. The BOLD signal is taken as a static nonlinear function of volume and deoxyhemoglobin that comprises a volume-weighted sum of extra- and intravascular signals:

$$y_n = V_0\left(7\rho_n(1 - q_n) + 2\left(1 - \frac{q_n}{v_n}\right) + (2\rho_n - 0.2)(1 - v_n)\right)$$

where $V_0 = 0.02$ is the resting blood volume fraction. The biophysical parameters were taken as in Friston et al. (2003).

I.III.3 - Conclusions from previous resting-state models

At the macroscopic level, all models presented in this section have used a brain-inspired connectome and have found the emergence of slow BOLD fluctuations that correlate across spatially segregated brain areas. Moreover, all studies agree on the key role of the coupling matrix in shaping the spatial patterns of BOLD correlations. However, at the mesoscopic level, different reduction lines were followed to characterize the spontaneous dynamics of neural masses and their cooperative behaviour (See Table 1 for a comparison between models).

Concerning the dynamical regime of neural populations, different assumptions were made regarding their intrinsic spontaneous behaviour. According to the literature in resting-state models, three major stationary regimes are possible for an isolated ensemble of neurons: a fixed-point attractor, a limit-cycle attractor or a chaotic attractor (see Figure 22). On the case the neural ensemble is in a stable asynchronous state, i.e. all neurons in the network fire irregularly, the dynamics can be described by a fixed-point attractor. In this case oscillations –if they exist- manifest only transiently as resonances in the network response (Mattia and Del Giudice, 2002). This type of dynamics was considered in the resting-state models of Ghosh et al. (2008), Deco and Jirsa (2012) and Hugues et al., (in preparation). On the other hand, if the neuronal populations in the network fire synchronously with rhythmic periodicity due to recurrent excitation and inhibition, then population exhibits self-sustained oscillations (Brunel, 2000, Borgers and Kopell, 2003, Brunel and Wang, 2003, Bartos et al., 2007) and the dynamics is described by a limit-cycle attractor. In the resting-state model of Deco et al. (2009), the Wilson-Cowan units were under this regime. Finally, if we consider that, due to nonlinear interactions between neurons, the local network exhibits intrinsic instabilities where nonperiodic intermittent oscillations occur (as in Honey et al. (2007, 2009)), then they instantiate a chaotic dynamics (Aihara et al., 1990). Although there is a qualitative difference between these three dynamical regimes, assuming different reduction lines permit to consider the neural-mass in any of these dynamical states during rest.
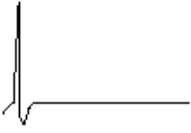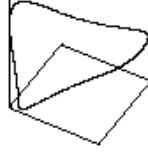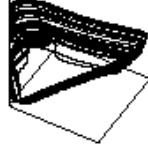
Attractors	Dynamics	Trajectories in State Space	Time Series
Equilibrium Point	Static		
Limit Cycle	Periodic		
Strange Attractor	Chaotic		

Figure 22 - Three possible dynamical regimes of a neural-mass. Adapted from Aihara (2008).

Due to fundamental differences in the models, noise and/or delays may -or not- play a fundamental role in resting-state dynamics. Indeed, as can be seen in Table 1:

- In Honey et al. (2007, 2009) neither noise nor delays were considered.

- In Ghosh et al. (2008) and Deco et el. (2009) both noise and delays play a fundamental role.

- In Deco and Jirsa (2012) and in Hugues et al. (unpublished) only noise plays a fundamental role in the slow BOLD dynamics and delays can be neglected.

Both delays and noise are naturally present in the brain. Time delays arise principally from finite axonal transmission speed and from synaptic and dendritic processes and are usually on the order of 10–100 ms. Neglecting time delays reduces significantly the cost of numerical computations. However, the question whether time delays need or not to be considered when studying BOLD signal fluctuations depends on the assumptions regarding the intrinsic neurophysiology of the mechanism that binds cortical regions together. If we consider that the neural populations have an oscillatory local dynamics with non-negligible delays compared to the oscillation period, and that the BOLD signal is generated by interactions between these fast oscillatory rhythms, neglecting the time delays does not

seem permissible (Ghosh et al., 2008). On the other hand, if we consider that neurons in a population fire asynchronously and neglect the oscillatory physiological signals, then time delays do not alter the slow dynamics of neural activity and may be neglected (Deco and Jirsa, 2012). However, it is important to note that delays may reduce the stability of the oscillatory network states (Jirsa and Ding, 2004, Jirsa, 2009).

Regarding the role of noise, the question of whether or not it plays an essential role in resting-state dynamics depends again on the dynamics at the node level. From the experimental literature, it seems that the brain during rest wandering between different states, where different subsets of brain regions (RSNs) form temporary coalitions, which alternate in time. When the dynamics at the node level is non-chaotic (Ghosh et al., 2008, Deco et al., 2009, Deco and Jirsa, 2012) the dynamical transitions between stable states occur due to the presence of noise fluctuations. However, if there are intrinsic instabilities in the system, either due to nonlinear interactions in the local network (Honey et al. 2007, 2009) or generated by the complex spatial structure of the brain[1], transitions between different stable states can occur in the absence of noise. In conclusion, we believe it is essentially a question whether there is an external source of noise or if the model by itself is capable of generating internal instability.

---

[1] In chapters II, III and IV we will show results where multistability occurs in a network of limit-cycle oscillators in the absence of external noise.

Table 1 – Comparison between previous models of resting-state activity[1].

	Node Model	Neural-mass in the network	Network Dynamics	Origin of BOLD fluctuations	BOLD correlations	Role of Delays	Role of Noise	Connectome
Honey et al. (2007,2009)	Conductance-based biophysical model	Chaotic activity	Chaotic activity with sporadic synchrony	Intermittent self-organizing patterns	Self-organizing patterns	No	No	Macaque 1 hemisphere
Ghosh et al. (2008)	FitzHugh-Nagumo Unit + noise	Stable asynchronous state with 10Hz oscillations	Network reverberation of oscillatory damped fluctuations	Slow modes for sufficient coupling	Slow modes dominate in variance	Yes	Yes	Macaque N=38
Deco et al. (2009)	Wilson-Cowan Unit + noise	Limit-cycle Oscillations (40Hz)	Slow fluctuations in synchrony degree	Slow fluctuations in the synchrony degree	Synchronization of structural modules	Yes	Yes	Macaque N=38
Deco and Jirsa (2012)	Network of spiking neurons + noise	Stable asynchronous state (no oscillations)	Noise induced wandering in the presence of ghost attractors	Noise excursions at the border of multistability	Ghost attractors	No	Yes	Human N=66
Hugues et al. (unpublished)	Rate fluctuations + noise	Stable asynchronous state	Network reverberation of damped fluctuations	Slow modes for sufficient coupling	Slow modes dominate in variance	No	Yes	Human N=66

[1] In Table 3 (p.160) we complete this table with the results presented in this thesis.

I.III.4 – Modelling the impact of lesions

The complex connectivity of the neuroanatomical connectome has been shown to play a fundamental role in the global integrative aspects of brain function. As a consequence, structural damage at the local level, as a result of stroke, traumatic brain injury, cancer or degenerative brain disease, can produce behavioural deficits not only through the disruption of neural circuits local to the lesion site, but also by disrupting information flow along larger-scale pathways or by unbalancing competitive inter-regional interactions. Therefore, to understand (or even predict) the effects of a cortical lesion, it is necessary to consider the lesion-induced changes in the dynamics at the macroscopic scale. Some modelling studies have studied the impact of lesions in functional connectivity during rest (Honey and Sporns, 2008, Alstott et al., 2009). In these works, lesions were simulated by removing nodes -or cortical areas- in the brain using the macaque (Honey and Sporns, 2008) or the human (Alstott et al., 2009) connectomes. Findings indicate that lesions produce specific patterns of altered functional connectivity among distant regions of cortex, often affecting both cortical hemispheres. These patterns are highly dependent on the location of the lesion in the network and its impact depends on the properties of the node (for example, its clustering coefficient).

I.IV – Motivation

Over the years, neuroscience research has been centred on the systematic gathering of experimental data and tentative induction of the universal laws governing brain dynamics from empirical observations. This classical inductivist form of scientific method was first introduced by Sir Francis Bacon in 1620 (Bacon, 2010). However, the application of this so-called *Baconian method* to large complex systems, like the brain or the universe, has proven to be largely unfruitful due to contributions from countless unpredicted undergoing physical and chemical processes.

Considering that scientific theories are abstract in nature and can only be tested rather than induced, Sir Karl Popper supported a form of scientific method based on making *falsifiable predictions* (Popper, 1934). For example, Newton anticipated the motion of planets in a concise set of mathematical equations that made precise predictions. Although Newton's laws had major flaws and his equations failed to be the final answer, they are a beautiful example of a theory that makes strong falsifiable predictions, which can be further experimentally tested (Gamez, 2012).

In the same way as Newton did not have access to the state of every molecule in every planet to predict their behaviour, it is probable that a high level of abstraction - beyond the behaviour of single neurons or realistic neural-mass models - is needed to understand the universal laws governing brain dynamics. Indeed, although the existing resting-state models largely reproduce features of macroscopic resting-state dynamics, they still generate complex and hardly interpretable simulated data, making it difficult to extract the pure mechanisms at the genesis of BOLD signal fluctuations.

In this work, our main motivation was to go beyond existing resting-state models and explore an even higher level of abstraction. We tested if the interaction of cortical regions could be modelled as coupled oscillators,

using a mathematical equation derived by Kuramoto (1984) that applies to a wide range of coupled oscillatory systems in nature. Adopting a *Popperian* method, we expect our approach to lead to strong –though falsifiable- predictions that could guide future theoretical and experimental neuroscience research.

In the following chapter, we explain in detail the Kuramoto model, its synchronization behaviour and its extension to time-delayed interactions. In chapters III and IV, we report our results when introducing neuroanatomical connectivity with realistic delays and compare with experimental resting-state data (BOLD and MEG). Finally, in chapter V we study the outcome of disconnection effects in resting-state dynamics and compare with results from schizophrenia patients. In addition, in chapter V, we performed additional simulations with a more realistic neural-mass model and compare the results with the Kuramoto model.

'Fools ignore complexity.
Pragmatists suffer it.
Some can avoid it.
Geniuses remove it.'
Alan Perlis

One of the most captivating cooperative phenomena occurring in nature is the spontaneous emergence of order from chaos through synchronization. The synchronous flashing of fireflies is a good illustration, but examples range from cardiac pacemaker cells to orbiting planets, from sleep cycles to coupled pendulums, and many other biological, chemical, physical or social systems in the universe (Pikovski et al., 2001, Strogatz, 2003). Spontaneous order is observed in galaxies, cells, ecosystems and human beings, who are capable of assembling themselves against the laws of thermodynamics dictating exactly the opposite: that nature should inevitably degenerate toward a state of disorder and greater entropy. Although the origin of this unifying force remains a mystery, the dynamics of oscillator systems is mathematically tractable in a simple, yet very insightful manner, using a differential equation derived by Yoshiki Kuramoto (1984). Importantly, the Kuramoto equation can be used in computer models to predict the collective behaviour of coupled oscillators. In this section, we describe the Kuramoto model in detail and depict the most important synchronization phenomena occurring from it.

II.I – The concept of a phase oscillator

An autonomous dynamical unit whose parameters evolve periodically in time, describing a stable periodic orbit, even after small perturbations occur, is called a limit-cycle oscillator. A periodic self-sustained oscillator can be described as a mathematical object by means of a single variable, the phase. This phase, θ, parameterizes the motion along the cycle, and its evolution in time is given by:

$$\frac{\partial \theta}{\partial t} = \omega_0,$$

where ω_0 is the natural (or intrinsic) frequency of the oscillator.

Self-sustained rhythmic activity occurs frequently in nature, one the most striking examples of it happening in the brain. Indeed, as revealed by most electrophysiological experiments a myriad of coherent brain rhythms emerge naturally in the brain, closely linked to specific mental states. Furthermore, some self-sustained oscillations in the cortex are known to emerge from the interaction of large numbers of excitatory and inhibitory neurons (Brunel and Wang, 2003, Bartos et al., 2007). Interestingly, regular periodic firing has been observed even in cortical slices *in vitro*. Sanchez-Vives and McCormick (2000) demonstrated that slices of ferret neocortex maintained in vitro generate a slow (< 1 Hz) rhythm when placed in a bathing medium that mimics the extracellular ionic composition in situ (see Figure 23). This slow oscillation results from a recurrent excitatory interaction between pyramidal neurons that is regulated by inhibitory networks.
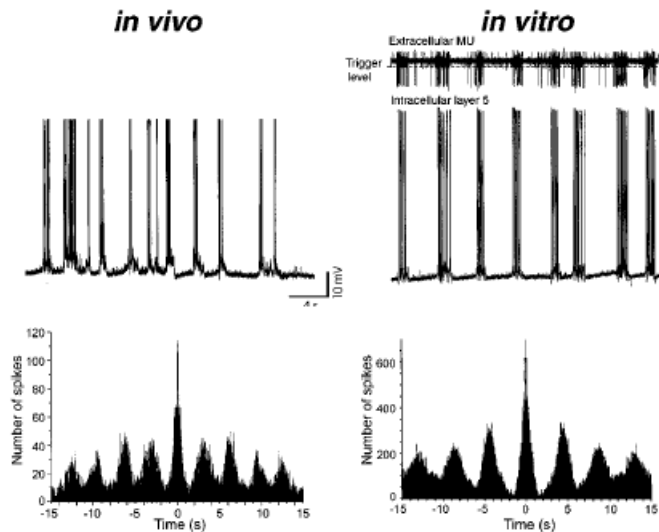
Figure 23 - Generation of a slow self-sustained oscillations in vivo and in vitro. (Left) Intracellular recording in the primary visual cortex of an anesthetized cat reveals a rhythmic sequence of depolarized and hyperpolarized membrane potentials. **(Right)** Simultaneous intracellular and extracellular recordings in ferret visual cortical slices maintained *in vitro*. The intracellular recording is from a layer 5 intrinsically bursting neuron. **(Bottom)** Autocorrelograms of the intracellular recordings show a marked periodicity of a few seconds. Adapted from Sanchez-Vives and McCormick (2000).

When engaged in rhythmic firing, the neural ensemble follows a closed periodic trajectory in phase space and therefore it can be considered as limit-cycle oscillator. This phase reduction approach provides a direct link between neural-mass models exhibiting self-sustained oscillations (as observed for example in Deco et al. (2009)) and a phase oscillator. Furthermore, Hoppensteadt and Izhikevich (1997) showed that weakly-coupled Kuramoto oscillators and weakly-coupled Wilson–Cowan oscillators have similar interaction dynamics. However, the formal reduction from a Wilson–Cowan model to a phase oscillator implies disregarding the amplitudes of the oscillators and working only with their phases. Schuster and Wagner (1990) formally applied this reduction and reproduced observations of synchronization between cortical columns in the visual system, suggesting that cortical columns interact through phase modulations.

II.II - The Kuramoto model of coupled oscillators

The reduction of neural-mass models to phase-oscillators restricts the neural ensemble dynamics to a single scalar measure, i.e. its phase. Although this may seem highly restrictive, Kuramoto (1984) showed that an ensemble of phase oscillators interacting through an appropriate functional form approximates the long-term behaviour of any ensemble of interacting oscillatory systems as long as the coupling is weak and the subsystems are nearly identical. In a network with N coupled oscillators (or nodes) and denoting by θ_n the phase of node n, Kuramoto derived the following dynamical equation to predict the behaviour of node n taking into account the phase of all nodes in the network:

$$\frac{\partial \theta_n}{\partial t} = \omega_n + k \sum_{p=1}^{N} C_{np} \sin\left(\theta_p(t) - \theta_n(t)\right) \tag{1}$$

ω_n is the natural frequency of node n on its limit cycle when uncoupled. Natural frequencies are, in the original formulation of the model, distributed with a given probability density $g(\omega)$. k scales the global coupling weight and C_{np} is the coupling strength from node p to node n. If we consider that each node in the network represents a cortical region and that this connection is mediated by neuroanatomical pathways, the coupling C_{np} can

be approximately obtained from the number white matter tracts detected with tractography connecting regions n and p. However, please note that some parcellation schemes[1] divide the brain in regions with different size, assigning a different number of neurons to each node. Since the activity in the target region is sensitive to the number of incoming axons per neuron, it is important to consider this factor in the coupling weight C_{np}. This is achieved by dividing the total number of incoming white matter tracts by the relative size of the target region n, resulting in a non-symmetric connectivity matrix whenever the size of regions in the network is heterogeneous.

Scaling the coupling strength by the number of white matter tracts relies on the assumption that there is a linear relationship between the latter and the efficiency of synaptic transmission. However, some diseases may provoke a disruption at the synaptic level and even if white matter tracts remain intact, the coupling strength is reduced. Furthermore, this reduction can occur either in a specific connection or at the global level, and for this reason, the coupling variables k and C_{np} are considered to encompass both axonal and synaptic mechanisms.

Frequency dispersion and noise are both naturally present in the brain. To study the effects of stochasticity in the dynamics, it is possible to extend the Kuramoto model by adding a noise term $\eta_n(t)$ in equation (1). η_n represents external noise received by the oscillators and expresses itself in terms of phase fluctuations. It is usually taken as uncorrelated Gaussian white noise with mean value zero ($\langle \eta_n(t) \rangle = 0$) and variance σ_n^2 in radians.

II.II – Synchronization and the Kuramoto Order Parameter

According to the Kuramoto model, a system of N identical oscillators (i.e. $\omega_n = \omega_0, \forall n \in N$) initialized with random phases, $\theta_n \in [-\pi\ \pi]$, will tend in time to a fully synchronized state if the coupling is sufficiently strong (i.e. above a critical coupling k_c). In order to characterize the collective dynamics of the whole population, Kuramoto (1984) derived an *order*

---

[1] See section *I.II.1.b - Brain parcellation*

parameter, which measures the phase of the oscillatory ensemble over time, ϕ(t), as well as the phase uniformity among nodes, given by $R(t)$:

$$R(t)e^{i\phi(t)} = \frac{1}{N}\sum_{n=1}^{N} e^{i\theta_n(t)}$$

The degree of synchrony is given by modulus of the order parameter, $R(t)$. If the whole system is too weakly coupled (i.e. below the critical coupling k_c), then all nodes in the network (initialized randomly) continue firing independently at their intrinsic frequency ω_0, and $\lim_{t\to\infty} R(t) = 0$. In this case, the system is in a stable asynchronous (or incoherent) state. When the coupling is higher than k_c, $\lim_{t\to\infty} R(t) = 1$, and the oscillators become phase-locked. In this case, the phases of all nodes are coherent over time with $\langle\theta_n(t)\rangle = \phi(t), \forall\, n \in N$. For sufficient synchrony, $\phi(t)$ describes the movement of the oscillator ensemble around the unit circle, and $\frac{\partial\phi}{\partial t}$ is the collective frequency of the system.
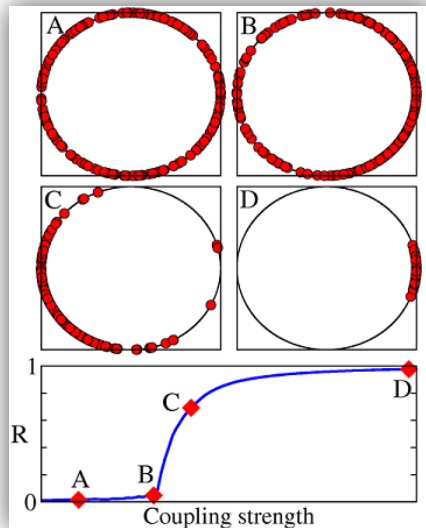
Figure 24 - Synchronization in the Kuramoto model. (Bottom plot) Order parameter *R* versus the coupling strength. (Top) Snapshots for couplings A,B,C and D of the phases of all nodes in the phase plane. Adapted from (Popovych et al., 2011)

In the case of a fully connected network (all-to-all connectivity), this synchronization occurs almost simultaneously for all network nodes. However, if the network has a non-homogeneous connectivity structure,

meaning that some nodes are more coupled than others forming clusters of highly connected nodes (or modules), then, in the transient to synchronization, modular structures of synchronized nodes emerge in different time scales (see Figure 25), ordered in a hierarchical way (Arenas et al., 2006).
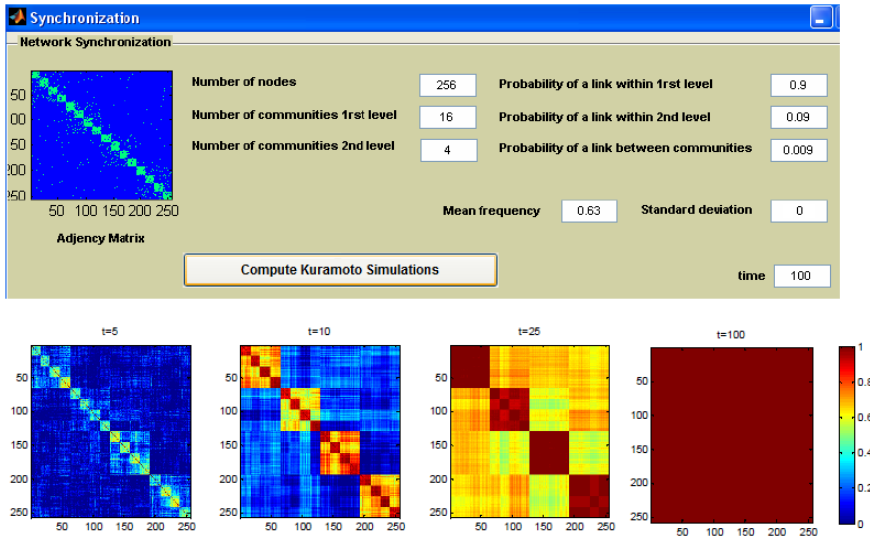
Figure 25 - Synchronization reveals topological scales. (Top) Matlab interface programmed to perform simulations using the Kuramoto model. In a first step, an artificial binary network is constructed by defining an adjacency matrix A_{np}, where the user inserts the total number of nodes and the number of communities in each of the two topological levels. After setting the probability of connections in each level (light green pixels=connection; blue=no connection), the mean and standard deviation of natural frequencies (in proportion to the time step), and the simulation time (number of time steps), the user clicks the button "Compute Kuramoto Simulations" and the programs runs the Kuramoto model with the given parameters. **(Bottom)** Matrices indicating the instantaneous phase coherence, computed as $\rho_{np}(t) = \langle \cos (\theta_n(t) - \theta_p(t)) \rangle$, at different times (t=5;10;25;100) revealing the emergence of modular structures in hierarchical order over time. At t=100, the system reaches full synchrony as indicated by $\langle \rho(t = 100) \rangle \cong 1$.

These results show that the network's map of connections (Figure 25 - Top) expresses itself in the dynamical behaviour of the system (Figure 25 - Bottom). Groups of densely inter-connected regions, have a stronger tendency to be synchronized together, and, at an intermediate stage between incoherence and full synchrony (for example at t=10 in Figure 25), they form synchronized modules that oscillate coherently at a different phase of other modules. However, after a transient period, all oscillators inevitably synchronize.

Many networks in nature, like the brain, have a complex wiring architecture[1], and their synchronization patterns have been closely linked to the underlying structure (Strogatz, 2001). In Honey and Sporns (2008), cortical interactions were modelled with the Kuramoto model. However, as no frustration was added to the system, after a transient period, all nodes synchronized together and therefore their study was restrained to the transient period towards full synchrony (as in Arenas et al., 2006).

In the brain, stable large-scale synchronized states can occur for a period in time, such as during sleep or under anaesthesia. However, the wakeful state (and especially during rest) is characterized by a multiplicity of coexisting and more ephemeral rhythms. To obtain such a dynamical framework, heterogeneity and/or frustration parameters naturally present in the brain need to be considered in the coupling term. Several studies have shown that the introduction of frequency dispersion (Kuramoto, 1984, Acebron et al., 2005, Popovych et al., 2005), phase shifts (Breakspear et al., 2010, Shanahan, 2010) and time-delays (Yeung and Strogatz, 1999, Earl and Strogatz, 2003, Montbrio et al., 2006), introduce intrinsic instabilities to the system. These instabilities occur because nodes are involved in competing interactions. In those cases, and under specific parametric conditions, the network may display multiple meta-stable equilibria (Strogatz, 2001).

If the system is in a regime with more and less synchronized stable states, the order parameter $R(t)$ fluctuates in time. These fluctuations can be captured by the standard deviation of R(t), σ_R, which indicates the level of metastability of the network (Shanahan, 2010). On the other hand, the mean, $\bar{R}$, is an index of the global synchronization level over time.

II.III – Time delays in the Kuramoto model

A crucial step toward neurobiological plausibility of coupled oscillators systems as models of macroscopic brain activity is the incorporation of time delay effects. Time delays between coupled cortical regions arise principally from finite axonal transmission speed and dependent on inter-areal distance and myelination level, as well as on synaptic and dendritic processes. The

---

[1] See section *I.II.3 – Characterizing complex networks using graph theory.*

original Kuramoto model can be extended in the following way to include time-delayed interactions:

$$\frac{\partial \theta_n}{\partial t} = \omega_n + k \sum_{p=1}^{N} C_{np} \sin \left(\theta_p (t - \tau_{np}) - \theta_n(t) \right).$$

The delay τ_{np} between regions n and p can be estimated from the distance between nodes D_{np} by assuming a conduction velocity v such that:

$$\tau_{np} = \frac{D_{np}}{v}.$$

Under this condition, each oscillator interacts with the others in terms of the phase that they had at the time they sent a synchronizing signal. Whenever two oscillators n and p are in phase, i.e. $\theta_n(t) = \theta_p(t)$, if $\tau_{np} > 0$ and τ_{np} is different from the oscillation period, the phase coherence is disrupted since $\sin \left(\theta_p (t - \tau_{np}) - \theta_n(t) \right) \neq 0$.
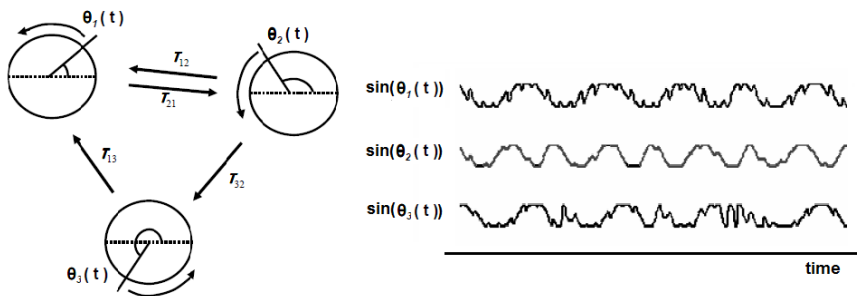
Figure 26 - Graphical representation of three interacting oscillators with delayed coupling. (Left) Set of 3 coupled phase oscillators, with delayed interactions T_{np}, where the angle on the circle represents the phase on the limit cycle of self-sustained neuronal oscillations. (Bottom) Example of 3 time series obtained from $\sin(\theta_n(t))$.

Time delays can substantially change the dynamical properties of coupled systems. In general, the dynamic behaviour becomes much richer and still surprising in the current knowledge. One might think that time delays tend to break coherence -or to make it difficult- in populations of interacting units, but this is not always the case (Pikovski et al., 2001). In the presence of delays, and under certain parametric conditions, stable synchronized states are still possible, but occur at reduced collective frequencies (Niebur

et al., 1991). Furthermore, as observed by Niebur et al. (1991), the systems decays to a state with the lowest possible common frequency, Ω, which obeys to the following equation:

$$\Omega_{min} \approx \omega_0/(1 + kN\tau) \quad (1)$$

Therefore, the frequency at which a system of N globally coupled oscillators is decreases as the coupling k and delays τ increase, as shown in Figure 27 (as a function of τ).
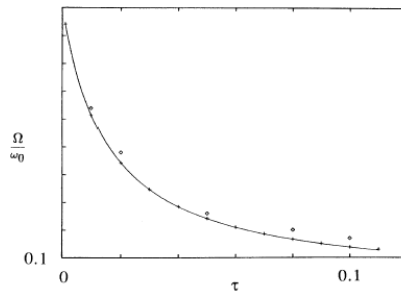
Figure 27 - Frequency suppression as a function of time delay τ for two coupled oscillators (diamonds), for a two-dimensional array of 16384 oscillators (crosses), and the prediction from Eq. (1) (line). The average frequency Ω is plotted as a fraction of the intrinsic frequency ω_0.

In addition, Kim et al. (1997) found that for a range of delays (uniform delays in their treatment), the system shows multistability between synchronized and desynchronized states. In the synchronized states, they found multiple states with different collective frequencies. The authors propose that this multistability presents a possible mechanism for information storage in the nervous system. Furthermore, Zanette (2000) found that, at a state of frequency synchronization (where all the oscillators have the same collective frequency), the distribution of phases over space is nontrivial but constant over time. These results indicate that a fully synchronized state in a system with time delays can have a Kuramoto order parameter $R < 1$ because oscillators can be phase shifted from the others, but phase-locked at a collective frequency. In another study, Yeung and Strogatz (1999) found that, depending on τ and k, bistability between synchronized and incoherent states can happen, as well as unsteady solutions with time-dependent order parameters indicating non-Gaussian fluctuations in the synchrony degree.

All above-mentioned theoretical studies of coupled oscillators with time delays have focused in cases where the delay τ is identical between all entities, with $\tau_{np} = \tau, \forall n, p \in N$. Since the complex 3-dimensional configuration of the neuroanatomical network contains connections of different lengths (see Figure 28), it is important to consider the case of heterogeneous delays. Although the lengths of the fibre tracts can be estimated with a millimetric accuracy (as in the connectome used in our work (Cabral et al., 2011)), the exact speed of transmission is unknown, and therefore the structure of delays cannot be inferred with precision. To consider the role of the conduction velocity in the dynamics, it is taken as a variable parameter in our simulations.
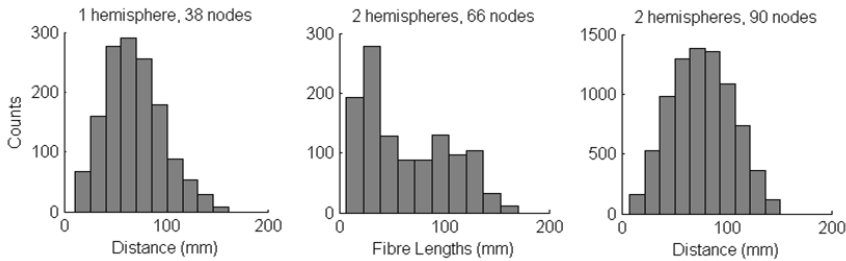
Figure 28 - Histograms of the connection lengths from 3 distinct connectomes used in this work. (Left) In the connectome from the CoCoMac database, the lengths correspond to the 3D Euclidean distances between the equivalent regions in the AAL human template. (Middle) In the connectome derived by Hagmann and colleagues, the length of the fibre tracts detected was computed. (Right) In the AAL connectome (provided by Prof. Kringelbach) the distances refer to the 3D Euclidean distances between the central coordinates of each region.

The case of a distribution of delays has been recently addressed theoretically by Lee et al. (2009) on the dynamics of globally coupled phase oscillators, finding that delay heterogeneity induces increased complexity in the dynamics. According to their results, the critical coupling k_c (above which the system synchronizes) is a function of both the mean delay (T) and the distribution of delays (in particular a gamma distribution of delays with exponent n) (see Figure 29). When the delay distribution is sufficiently large compared to its mean (that is for small n), the critical coupling $k_c(T)$ is found to be an increasing function (see Figure 29B with n=10). Even so, they considered all-to-all connectivity, whereas in the brain, the connectivity is sparse, with modular structures and highly heterogeneous, introducing an even higher degree of complexity to the system that remains unexplored (Jirsa, 2004).
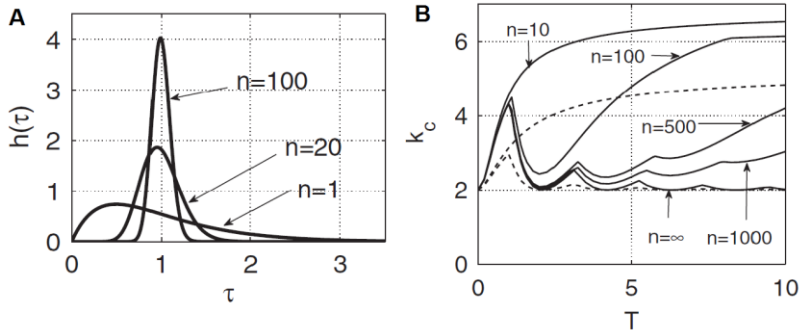
Figure 29 – Effects of the delay distribution on the critical coupling. (A) Different shapes of delay distributions (gamma functions controlled by the parameter *n*). **(B)** Solid curves are plots of the critical value of k_c versus the mean delay T for different delay distributions. Adapted from Lee et al. (2009).

Similar dynamical phenomena, including multistability, have been obtained in networks with constant phase-shifts between entities (Breakspear et al., 2010, Shanahan, 2010). However, it is important to stress the difference between fixed phase shifts α_{np} and fixed time delays τ_{np}. If we consider a constant delay τ_{np} between two nodes, and the nodes are not fully synchronized, than the phase difference between the two nodes is variable over time. Therefore, the phase-shift provoked by time-delayed interactions is a function of $\theta_n(t)$, $\theta_p(t)$ and τ_{np} and the approximation to a fixed term α_{np} is a highly abstract case, only comparable to time delays when the oscillators are phase-locked.

II.IV – Kuramoto dynamics with brain-inspired connectivity

The wiring diagram defined by the white matter pathways connecting brain areas is complex and the corresponding delays are highly heterogeneous. Consequently, theoretical predictions of the dynamics emerging from the Kuramoto model with brain-inspired connectivity can only be approximately guessed. In this and subsequent chapters, conclusions were essentially drawn from simulations and compared with existing theoretical literature where similar dynamic behaviours were observed with simplified connectivity structures.

In Figure 30, we show two connectomes derived from (left) one hemisphere of the macaque brain (CoCoMac database (Kötter and Wanke, 2005)) and (right) the human brain (Hagmann et al., 2007, 2008).
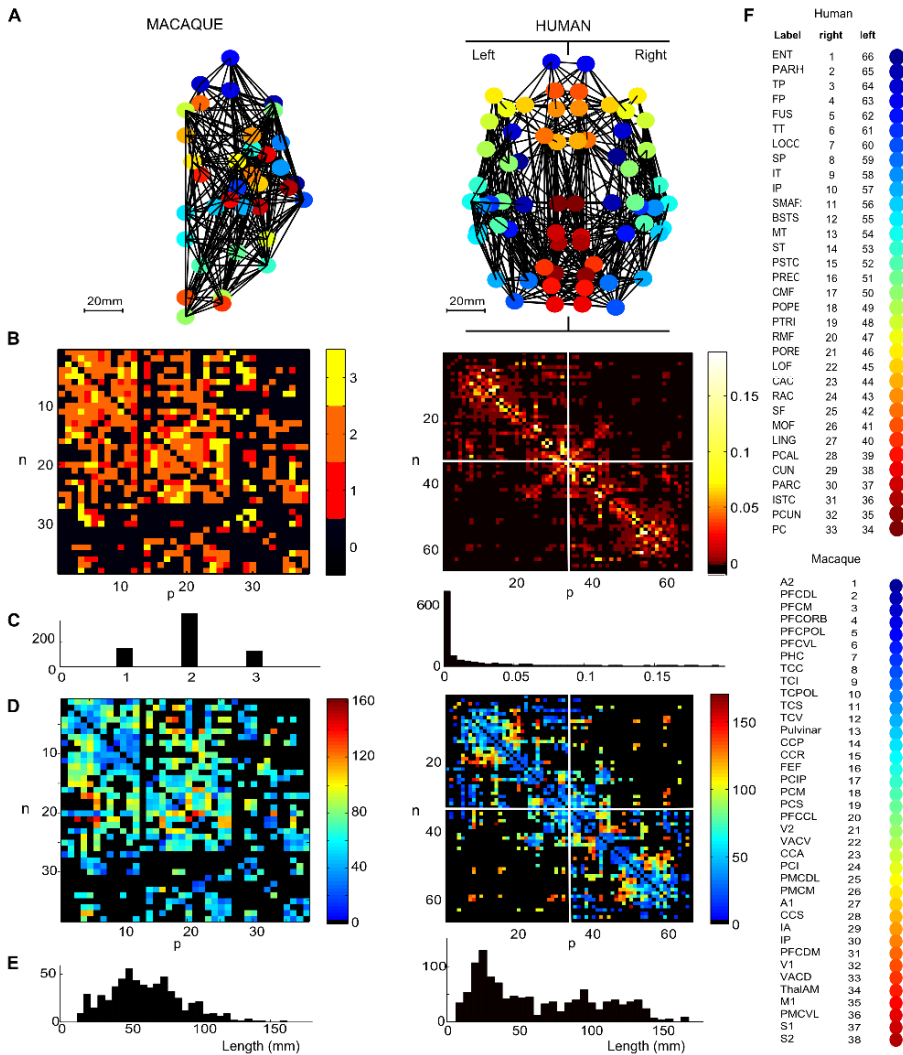
Figure 30 - Structural connectivity of the macaque and the human cortex. **(A)** Graphical representation of the macaque (left) and the human (right) networks. **(B)** Coupling matrices, and **(C)** corresponding histograms. **(D)** Distance of existing connections, and **(E)** corresponding histograms. The human matrices are ordered in such a way that corresponding contra-lateral regions are symmetrically arranged with respect to the matrix centre. The white lines separate the two hemispheres. **(F)** Indexing of cortical regions: In (A) the regions are color-coded whereas in *C* and *D* the matrix entries n and p indicate the source or target region, correspondingly.

In both cases, we have tried to rearrange the matrices according to modules with substantially denser connectivity inside specific node ensembles than with the complementary part of the network. However, even if some degree

of modularity can be found, modules can overlap, and multiple arrangements are possible. Furthermore, the distributions of couplings and distances shown in Figure 30B-C exhibit a large range of values (except for the coupling strengths of the macaque where they were only classified in 3 levels). Importantly, this non-randomness of the connectivity matrices, together with the heterogeneity of couplings and delays, has consequences on the dynamics as we will demonstrate below.

Unlike theoretical studies, here the couplings C_{np} and the distances D_{np} are given. Therefore, the model dynamics depends on the following parameters: the global coupling k, the conduction velocity V - or the mean delay τ_m-, the individual frequencies ω_n drawn from the frequency distribution $g(\omega)$ and the noise level σ_{noise}. Since exploring the whole parameter space takes a long time, we started by restraining to the (τ_m, k) plane (as in Lee et al., 2009), and considered homogeneous frequencies (in the gamma-band range) and no noise. The system of N Kuramoto equations with time delays was numerically integrated (Euler scheme, time-step $\Delta t = 0.1$ ms). Due to delays, we had to start the simulations by specifying the phases for a sufficiently long interval, choosing to evaluate the phases as in a non-interacting network. We always discard the first 20 s of simulations (=200000 time steps) to avoid dependence of the results on the initial conditions (in the following, always refer to the remaining simulated time). When exploring the (τ_m, k) parameter space, we simulate the previous system for 300 s.

As illustrated in Figure 31A (left), for the macaque network, the critical coupling above which the system synchronizes exhibits a very similar behavior to the one found theoretically by Lee et al. (2009). However, in the human case (Figure 31A (right)) the transition to synchrony is smoother. In the intermediate regime between incoherence and global synchrony (the area coloured in light blue in Figure 31A (right)) subsets of nodes -or clusters- particularly more coupled within the cluster than with the remaining network, tend to synchronize below the global critical coupling. However, due to competitive network interactions these partially synchronized states are unstable (or metastable). Consequently, in this region the metastability index is increased (Figure 31B).
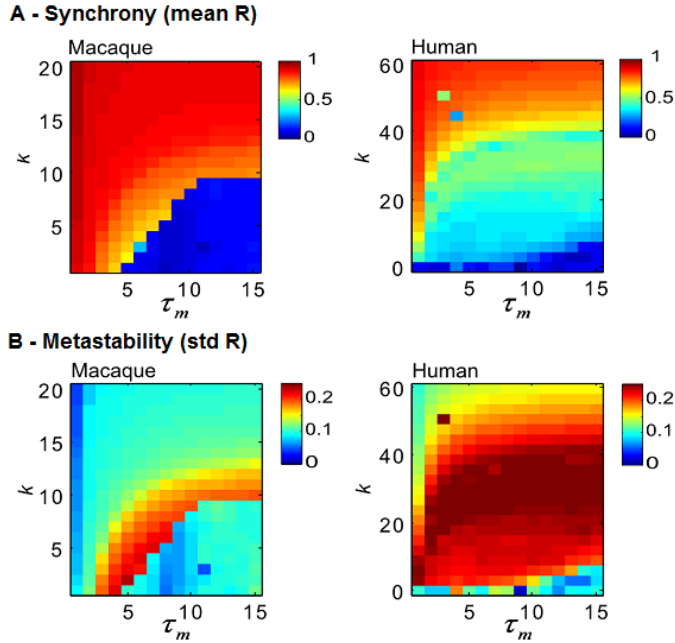
Figure 31 - Global dynamics as a function of the mean delay and the global coupling for the macaque (left) and for the human networks (right). (A) Global level of synchrony measured as the mean of the order parameter, $\bar{R}$. **(B)** Degree of metastability, as indicated by the standard deviation of R, σ_R. Here we used a homogeneous frequency $\omega_n = 60Hz, \forall n$ and no noise.

To understand better the network behaviour in the metastability region, we explore the dynamics in the frequency domain. In addition, we compare with a fully connected artificial network corresponding to the case studied by (Lee et al., 2009) with a delay distribution fitting the real one (gamma distribution with $n = 4$). In Figure 32B we plot the power spectrum (averaged across all oscillators) as a function of k for a fixed mean delay ($\tau_m = 15$ ms).

Starting from the macaque case (cocomac), we observe that, for low k, all nodes are oscillating at 40Hz (their natural frequency here). As the coupling increases until k_c we observe a frequency dispersion around 40Hz. At the border of synchrony, we observe the emergence of different frequency peaks, until, in the region of high synchrony a strong peak at a reduced collective frequency <10Hz emerges.
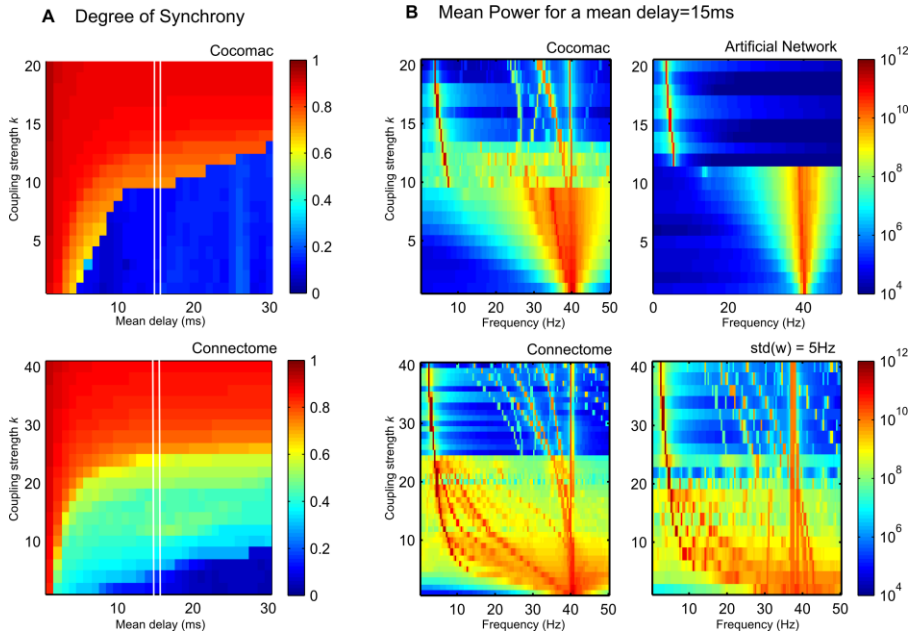
Figure 32. Dynamics in the frequency domain. (A) Mean Order Parameter in the parameter space for the macaque (top) and human network (bottom). **(B)** Power spectrum as a function of k for $\langle\tau\rangle$=15 ms ($v\sim4$ m/s) and $\omega_0 = 40Hz$ for: **(top left)** the macaque network; **(top right)** a fully connected network and with a distribution of delays fitted to a gamma function (with n=4); **(bottom left)** the human connectome; **(bottom right)** the human connectome with a Gaussian distribution of frequencies with mean=40Hz and std=5Hz.

In the case of the artificial network with global connectivity, the transition between the incoherent regime (peak at 40Hz) and full synchrony (peak at a reduced collective frequency) is sharp ($11 < k < 12$). In the case of the human matrix (bottom), the dynamics is more complex and clusters start to synchronize at very low levels of coupling. As the coupling increases, clusters progressively merge to form bigger clusters (with lower collective frequencies), finally merging into a single one. This may be due to the higher complexity of the SC and to the distribution of the coupling strengths, which is exponential-like. To study the effect of frequency heterogeneity among the nodes, we repeated the simulations choosing this time the node frequencies according to a Gaussian distribution $g(\omega)$ with mean 40Hz and standard deviation 5Hz. The same qualitative behaviour is observed, although the frequency peaks slightly change. This suggests that SC has a stronger impact on the observed dynamics than the frequency dispersion.

The fact that the collective frequency is suppressed as the coupling increases had already been observed by Niebur et al. (1991). Furthermore, the coexistence of multiple frequencies had been observed by Kim et al. (1997). Therefore, we believe the dynamics emerging from the brain connectome, despite its complexity, can be compared with previous theoretical studies from the Kuramoto literature.

For a deeper exploration of the dynamics emerging with the human connectome in the frequency and temporal domains, we chose a working point in the region of high metastability (i.e. $\tau_m = 15$ ms and $k = 11$). In Figure 33 we show the activity at the node level (i.e. right hemisphere N=33). Furthermore, from the simulated neural activity, we have estimated the BOLD signal using the Balloon-Windkessel hemodynamic model (Friston et al., 2003)[1].
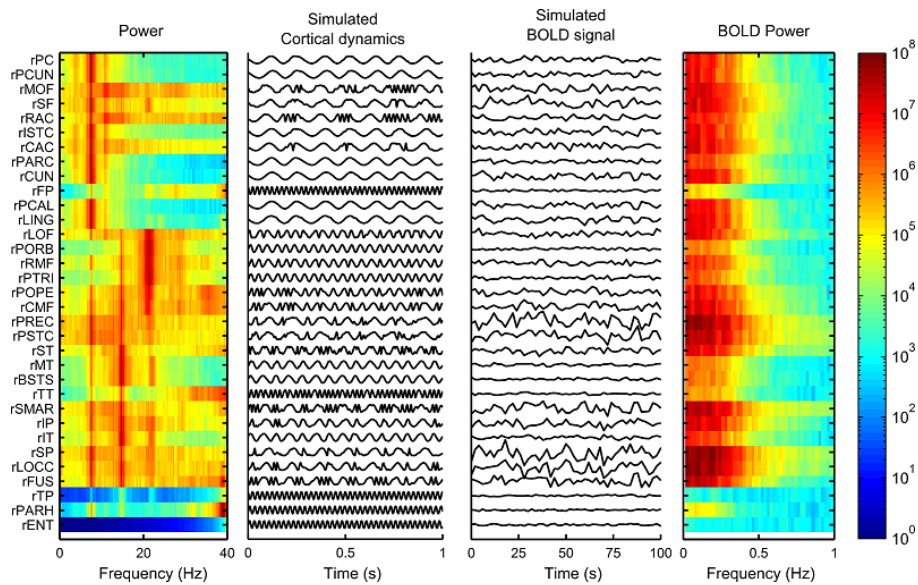
Figure 33 – Fast and slow dynamics at the node level (right hemisphere) in a regime with increased metastability. (Left) Power spectra of each node computed for the whole simulated time (i.e. 280 s). We observe that different frequencies engage different groups of nodes. Furthermore, the same node can be engaged in more than one frequency. **(Middle-Left)** Plot of the simulated "neural activity" over 1 second. We observe that some regions switch intermittently between different frequencies, while others remain synchronized or desynchronized for longer periods. **(Middle-Right)** Simulated BOLD signal for a 100 s interval. We observe that some regions have stronger fluctuations than others, which reflects in the power of the BOLD signal **(Right)**. $\tau_m = 15$ ms, $k = 11$, $\omega_0 = 40$Hz, $\sigma_{noise} = 0$rad.

---

[1] See section *I.III.2 - Transforming neuronal activity into BOLD signal* for details.

As can be observed in Figure 33, the dynamics of identical gamma-band (40Hz here) oscillators coupled with brain-inspired connectivity and delays leads to the spontaneous emergence of a rich dynamics with multistability, cross-frequency interactions and slow BOLD signal fluctuations even in the absence of noise and frequency dispersion. Furthermore, it can be seen that some nodes exhibit more than one frequency peaks with equivalent strength (for example the superior parietal (rSP)). This means that the oscillators are intermittently engaged by two different clusters (which have different collective frequencies) who compete to synchronize. Notably, nodes involved in such competitive interactions are the ones with stronger fluctuations in the BOLD signal.

The activity of two nodes that are entrained by the same cluster, will exhibit some degree of correlated activity. Therefore, we computed the covariance matrix of the activity at the 66 nodes and calculated the number of principal components necessary to explain 95% of the variance. These principal components indicate the number of modes in the network. As can be seen in Figure 34A, in the region of metastability, the activity is characterized by several (>5) modes. Furthermore, we plot the mean BOLD power (which indicates the degree of slow (<0.2Hz) fluctuations) in the (τ_m, k) parameter space (Figure 34A), and observe that strong slow fluctuations occur mainly in the region of metastability.
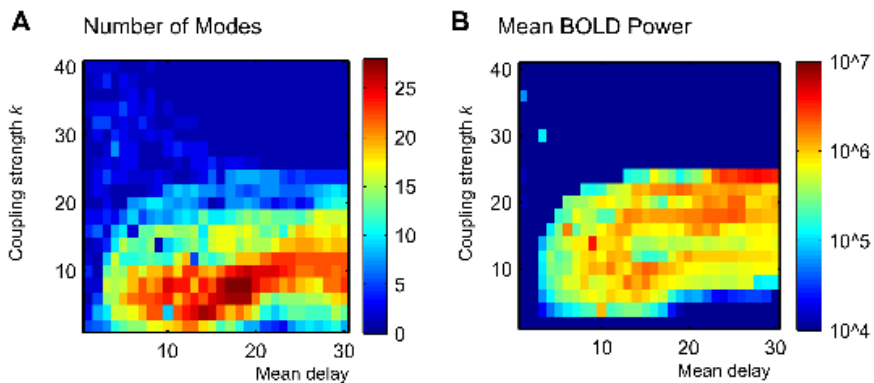
Figure 34 – Number of principal components (A) and BOLD power (B) of the simulated neural activity.

Finally, we have investigated if the slow frequencies observed in the alpha and beta ranges could be explained by collective frequencies due to delayed

interactions, as predicted by Niebur et al. (1991). In this case, we used another connectome network (which we use again in chapters IV and V)[1]. As shown in Figure 35AB, we performed a synchrony analysis in the parameter space, and found a metastability region. Furthermore, to test the predictions of Niebur et al. (1991), at each point we calculated the frequency with the most power, by detecting the peak in the mean power spectrum averaged across all regions (Figure 35C). In Figure 35D, we plot the theoretical prediction from Niebur et al. (1991). We observe that, for every simulation where the mean degree of synchrony (Figure 35A) is above a threshold (here around 0.2), the peak frequency corresponds closely to the one predicted in the literature.
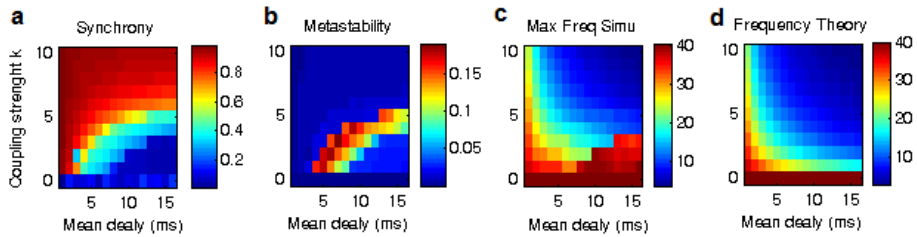
Figure 35 – Prediction of collective frequency. Study of the mean synchrony (A) and the metastability (B) in the parameter space of couplings and delays. (C) Peak frequency of the mean power spectrum and (D) collective frequency predicted by Niebur et al. (1991). $\omega_0 = 40$Hz.

Based on a number of experimental studies that reveal the existence of gamma-band oscillations across the brain, Basar-Eroglu et al. (1996) suggest, in a review study, the existence of a distributed system of gamma (40Hz) generators in the brain. Importantly, they suggest an interpretation on gamma rhythms as universal functional building blocks. In agreement with these predictions, our results show that gamma-band oscillators can serve as fundamental units to build a complex multi-frequency dynamics even in the absence of external stimulation or background noise. However, to validate these predictions, the model needs to be compared with experimental data from the brains of healthy subjects at rest, which we will do in the following chapters.

---

[1] See *A.III – DTI data collection and building of anatomical connectomes.*

III – Predicting BOLD resting-state functional connectivity with coupled gamma-band oscillators.

'Pure mathematics is, in its way, the poetry of logical ideas.'
Albert Einstein

III.I – Introduction

During rest, the mammalian brain exhibits robust low-frequency fluctuations (<0.1 Hz) that are revealed using the fMRI BOLD contrast. The spatial patterns of such fluctuations suggest the existence of an organized dynamics emerging spontaneously from intrinsic brain processes[1]. This slow dynamics seems to be highly structured by anatomical connectivity but the mechanisms behind it and its relationship with neural activity, particularly in the gamma frequency range, remains largely unknown.

To address these questions, we investigated if locally generated gamma-band oscillations can induce correlations at the BOLD level using a large-scale model of weakly coupled gamma-band oscillators linked together according to realistic brain connectivity[2]. A key ingredient of the model was a structural brain network derived empirically from white-matter tracing studies[3]. Each network node represents a neural population, assumed to oscillate spontaneously in the gamma frequency range. When these oscillatory units are integrated in the network, they are assumed to behave as weakly coupled oscillators. The time-delayed interaction between nodes

---

[1] See *I.I - Brain activity during rest.*
[2] Most of the results presented in this chapter are published in:
Cabral J, Hugues E, Sporns O, Deco G (2011) Role of local network oscillations in resting-state functional connectivity. Neuroimage 57:130-139.
[3] See *I.II.1 – Anatomical structural networks.*

is simulated using the Kuramoto model of phase oscillators, a biologically based model of coupled cyclic systems. For a realistic setting of axonal conduction speed, we show that time-delayed network interactions lead to the emergence of slow neural activity fluctuations, whose patterns correlate significantly with the empirically measured functional connectivity. The best agreement of the simulated FC with the empirically measured FC is found for a set of parameters where subsets of nodes (or clusters) tend to synchronize although the network is not globally synchronized. The simulated BOLD signal between nodes within the same cluster is found to be correlated, instantiating the empirically observed RSNs. Between clusters, patterns of positive and negative correlations are observed, as described in experimental studies. These results are robust with respect to a biologically plausible range of model parameters. The present model demonstrates how resting-state neural activity can originate from the interplay between the local neural dynamics and the large-scale anatomical network.

III.II – Methods

III.II.1 - Anatomical connectivity

We used an anatomical connectome (AC) with 66 regions of the human brain (see Figure 36) obtained and described in Hagmann et al. (2008) and in Honey et al. (2009). Five high-resolution connectomes from healthy subjects were provided, with 998 regions of interest (ROIs) of same size covering the whole cortical surface. Since tractography does not give fibre directionality, the connectivity matrix is symmetric at the ROI level. The AC was then averaged across subjects. To down-sample the AC to 66 regions of different size, the connection strength between two regions was calculated by summing all fibre tracts incoming to the target region, and dividing by its region-dependent number of ROIs, resulting in a non-symmetric down-sampled connectivity matrix. This normalization by the number of ROIs — that have approximately the same surface on the cortex and subsequently the same number of neurons— is required because neuronal activity is sensitive to the number of incoming fibres per neuron in the target region. As the dynamical model of one region already takes into account the effect of its internal connectivity, the connection of a region to itself was set to 0 in the connectivity matrix for the simulations (see Fig. 1B). The length L_{np} of

the fibres connecting the region p to the region n was calculated as the average length across all the fibres connecting them.
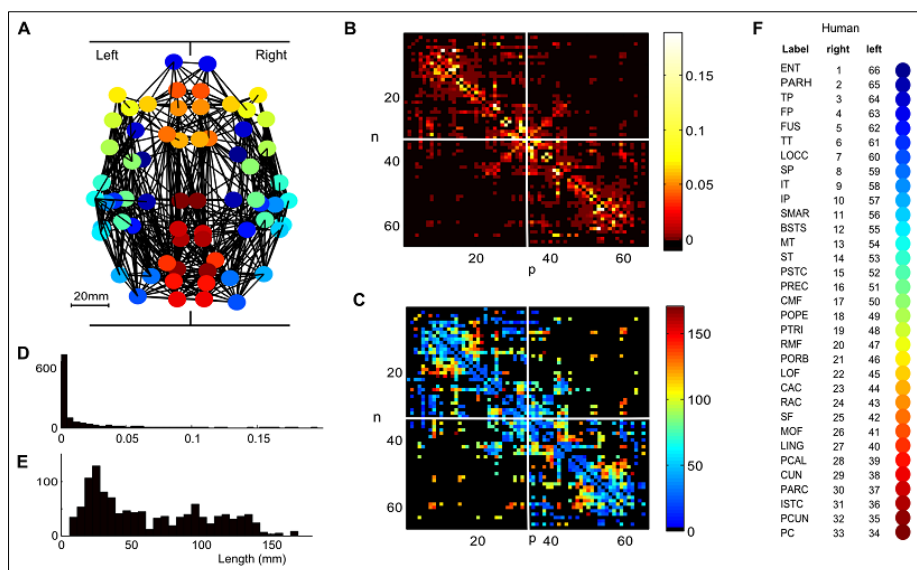
Figure 36 - Structural connectivity of the Human Connectome. (*A*) 2-dimensional representation of the network structure (view from above), the nodes representing anatomical regions placed at their central coordinates. (*B)* Connection strength matrix where *n* is the source region and *p* is the target, ordered in a way such that corresponding contra-lateral regions are symmetrically arranged with respect to the matrix centre, the anti-diagonal revealing the existing connections between these contra-lateral regions. The white lines separate the two hemispheres. (*C*) Histogram of the strength of existing couplings. (*D*) Fiber length matrix of existing connections between nodes *n* and *p*. The lengths correspond to the average length of all the fibers connecting nodes *n* and *p*. (*E*) Histogram of the fiber lengths of existing couplings. (*F*) Color-code and indices of cortical regions used in *A, B & C*.

III.II.2 - Resting-state functional connectivity

For the same five subjects, the correlation matrix of BOLD signals was provided at the ROI level. In more detail, the BOLD signal was acquired for a total of 20 min (TR=2 s), while the subjects were resting with eyes closed. A number of pre-processing steps were applied to the BOLD time series (see Honey et al. (2009) for details) including the regression of the global signal (Fox et al., 2005). Then, the correlation matrix was calculated to obtain the functional connectivity matrix (FC). The down-sampled FC between a pair of regions was obtained as the average of all interregional FC correlations at the ROI level.

III.II.3 - Network model of coupled oscillators

In the model of resting-state activity from Deco et al. (2009), neural masses were modelled as Wilson–Cowan units that exhibited self-sustained oscillations[1] in the gamma-frequency band. In this work, we achieve a higher level of abstraction by modelling cortical regions as simple phase oscillators with a natural frequency in the gamma-band. To model their cooperative behaviour in the network, we used the Kuramoto model with time delays[2] and noise, according the following expression:

$$\frac{\partial \theta_n}{\partial t} = \omega_n + k \sum_{p=1}^{N} C_{np}\sin\left(\theta_p\left(t - \tau_{np}\right) - \theta_n(t)\right) + \eta_n(t), n = 1, \dots, N.$$

The delay τ_{np} between node p and node n is calculated using $\tau_{np} = \frac{L_{np}}{V} = L_{np}\frac{\langle\tau\rangle}{\langle L\rangle}$. The connectivity matrix C and the delay matrix τ are fixed in their structures: only their scaling can be varied with k and $\langle\tau\rangle$, respectively. $f_n = \omega_n/2\pi$ is the intrinsic frequency of node n on its limit cycle, and is drawn from a fixed Gaussian distribution $g(f)$ with mean f_0 ($f_0 = 60Hz$ here) and standard deviation σ_f. The terms $\eta_n(t)$, represent the noise received by the local networks and correspond to uncorrelated Gaussian white noise with zero mean ($\langle\eta_n(t)\rangle = 0$) and variance σ_n^2/T ($\langle\eta_n(t)\eta_p(s)\rangle = \delta_{np}\delta(t - s)\sigma_n^2/T$), where δ_{np} is the Kronecker delta, $\delta(.)$ is the Dirac delta function, σ_n is in radians and T is a given timescale ($T = 1$ s here).

The present model depends on for main free parameters: $\langle\tau\rangle$, k, σ_f and σ_n. After an extensive numerical exploration of this parameter space, we have found the main free parameters to be the mean delay $\langle\tau\rangle$ and the global coupling strength k, for which we have performed an exhaustive parametric study. For biological realism, we also considered the effect of σ_f and σ_n. However, due to their relatively small influence on the behaviour of the

---

[1] See *I.III - Large-scale models of resting-state dynamics,* subsection *I.III.1.c - The Wilson-Cowan model.*

[2] For a full description of the model see section *II.III – Time delays in the Kuramoto model*

network (in their respective plausible range) and due to the high cost of simulating the complete four-dimensional parameter space, we conducted only a partial parametric study. We investigated the influence of large values of σ_f and σ_n in the results across the $(\langle\tau\rangle, k)$ plane. In addition, we explored how these parameters influence the results for the chosen working point $(\langle\tau\rangle, k) = (11, 18)$.

Phases θ_n were initialized randomly, as if cortical regions are completely desynchronized from each other. Due to delays, we had to specify the phases for a sufficiently long interval as in a non-interacting (and non-noisy) network. We always discarded the first 20 s of simulations to avoid the dependence of our results on initial conditions. In the following, we always refer to the remaining simulated time. When exploring the parameter space $(\langle\tau\rangle, k)$, we simulated the system's dynamics for 300 s. For the chosen $(\langle\tau\rangle, k)$ pair we extended the simulation time to 1200 s (20 min) to compare with experimental FC. The system of N dynamical equations was numerically integrated with a time-step $\Delta t = 0.1$ ms using an Euler scheme adapted to noise (Platen, 1999). All calculations were performed using MATLAB (www.mathworks.com).

III.II.4 - Characterizing the behaviour of the network

At the global level, the synchronization behaviour of the network was evaluated by the order parameter $R(t)$, which varies between 0 for a fully desynchronized - or incoherent - state to 1 for a fully synchronized state[1]. To evaluate the synchrony level within particular sets of nodes, or clusters, we calculated the order parameters $R_c(t)$ and $\Phi_c(t)$, where the sum is performed over nodes belonging to a cluster c.

To understand why the BOLD signal is generally correlated for nodes inside the same cluster, we need to decompose the neural activity using the following identity:

$$e^{i\theta_n(t)} = R_c e^{i\Phi_c(t)} + e^{i\Phi_c(t)}\left(e^{i\Delta\theta_n(t)} - R_c(t)\right)$$

---

[1] See section *II.III – Synchronization and the Kuramoto Order Parameter* for more details.

where $\Delta\theta_n(t) = \theta_n(t) - \Phi_c(t)$ is the relative angle of the node inside its cluster, and we then took the imaginary part to recover $r_n(t)$. When the cluster is synchronized, the more the absolute value of the first term tends towards 1, and the more the absolute value of the second tends towards 0. Therefore, when the cluster synchrony is sufficiently stable, the first term in the equation, which is common for all nodes inside the cluster as an intrinsic characteristic of the cluster, increases its value relatively to the second one, and the dynamics of different nodes inside the same cluster becomes correlated.

III.II.5 - Simulated BOLD and functional connectivity

To transform the simulated local neural activity to a hemodynamic signal like the BOLD, we used the Balloon-Windkessel hemodynamic model (Friston et al., 2003)[1]. For the neurovascular coupling we built on the assumption that the physical quantity whose variations underlie BOLD signal is the firing rate of the local neuronal population, which is the basic quantity associated to the phase model. In the model, the firing rate $r_n(t)$ of node n fluctuates around a fixed value and these fluctuations are given by a periodic function (here the sine) of the local node phase, that is $r_n(t) = r_0 \sin(\theta_n(t))$. By definition of the phase oscillator model, these fluctuations have a fixed amplitude r_0. In the simulations, we have considered relatively small amplitude ($r_0 = 1$), such that the Balloon-Windkessel model is linear and analogue to a linear filter (see Figure 37).

As shown in Figure 37, the low-pass filtered (<0.35 Hz) dynamics is strongly correlated to the BOLD signal. Using a small amplitude r_0, we guarantee that our results depend only on the fluctuations generated by network interactions, and not on intrinsic non-linearities of the BOLD model. Note that, using more biophysical and/or neural mass models, a number of additional neurovascular couplings have been considered in the literature (Kilner et al., 2005; Rosa et al., 2010; Friston et al., 2010). However, in our model, local dynamics is described by a single variable (the firing rate) and therefore we have to rely on this variable.

---

[1] A detailed description of the model is provided in section *I.III.2 - Transforming neuronal activity into BOLD signal.*
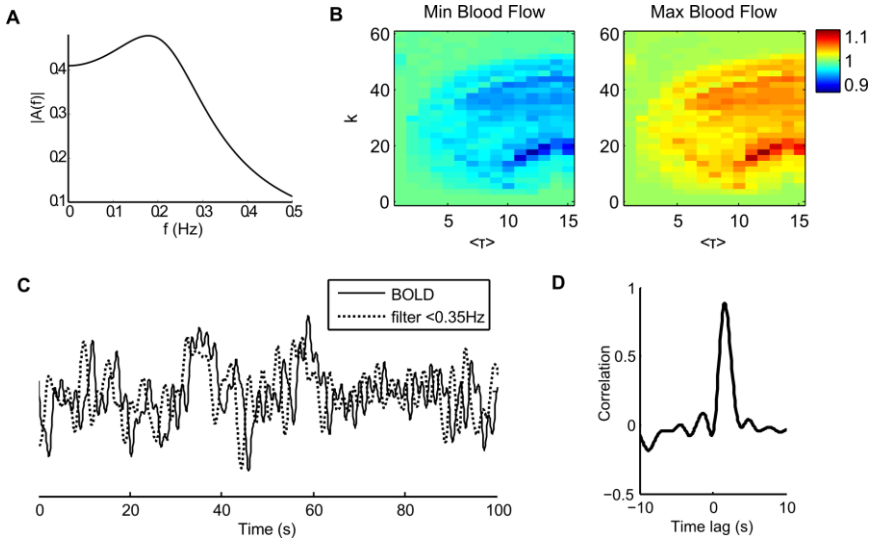
Figure 37 - Characteristics of the BOLD signal from the Balloon-Windkessel model. (A) Amplitude of the linear filter in the Balloon-Windkessel model as a function of frequency. (B) Diagrams representing the minimum value (left) and the maximum value (right) of the blood flow as a function of the mean delay, $< \tau >$, and the coupling strength, $\boldsymbol{k}$. This was obtained considering $\boldsymbol{r_0} = \boldsymbol{1}$, i.e., simulated rates fluctuate between -1 and 1. The blood flow fluctuates 15% at most. This means that for the value of $\boldsymbol{r_0}$ we have chosen, the Balloon model is behaving essentially linearly, proving that the patterns we observe at the BOLD level come essentially from the network dynamics. (C) Comparison between the BOLD signal (solid line) and the corresponding low-pass filtered neural activity with a cut-off frequency of 0.35Hz (dotted line). (D) Cross-correlation between the two signals; the peak around 1.6 s (correlation coefficient = 0.88) corresponds to the lag of the hemodynamic response.

III.II.6 – Comparison with empirical results

To compare the model results with the empirical FC, we low-pass filtered (<0.25 Hz) and down-sampled the simulated BOLD time series at 2 s to achieve the same resolution as in Honey et al. (2009). The low-pass filtering eliminates small and non-physiological high frequency components in the BOLD signal that can induce spurious correlations. Finally, the simulated FC was obtained after regressing the global signal (average over all regions) out of the regional BOLD time series (Fox et al., 2005, 2009), and by computing the correlation matrix. To compare the simulated and the empirical FCs, we calculated the Pearson correlation and the distance between the two matrices only for the structurally connected pairs (to increase the effectiveness of these measures). Later, for the chosen working point, we

used a seed approach and compared the two matrices row by row, calculating the Pearson correlation coefficient between rows, and the corresponding *p*-value. This gives the probability of getting a correlation as large as the observed one when the true correlation is zero. The correlation is significant when p<0.05. For clarity, all the methods used in this chapter are summarized in Figure 38.
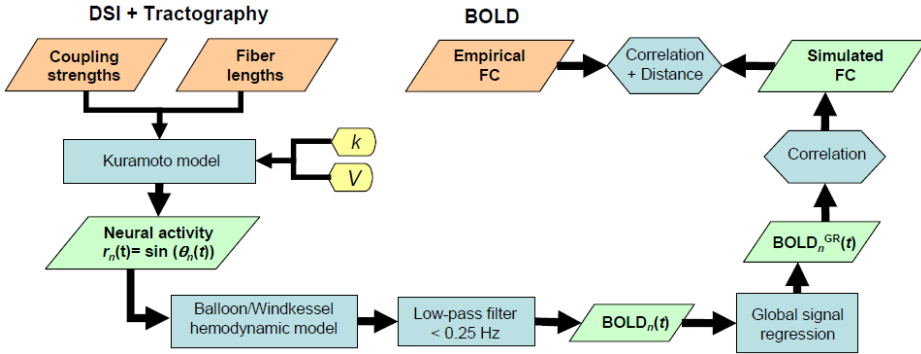
Figure 38 - Flowchart illustrating all the methods employed here to go from the empirical SC to the simulated FC. (Orange: experimental inputs, Green: simulated data, Blue: processes, Yellow: free parameters).

III.III - Results

III.III.1 - Structural connectivity

We consider the network dynamics supported by the AC of the human brain (Hagmann et al., 2007, 2008). A geometrical view from above of the considered network is represented in Figure 36A. The connectivity strength matrix together with the fibre length matrix is shown in Figure 36B and C, respectively. For each region, the abbreviations corresponding to the indices are indicated in Figure 36F (see *Appendix A.I* Table 4 for the complete names of brain regions). The distribution of strength values decreases sharply (Figure 36F) and the fibre length distribution exhibits a bimodal shape (Figure 36E). Confirming previous observations about the small-world structure of brain networks (Bullmore and Sporns, 2009), the region reordering (done by hand) revealed a complex modular structure in the anatomical network. It specifically unveiled the presence of node clusters, which are much more connected inside than outside the cluster to which they belong. As we will demonstrate below, this non-randomness of

adjacency matrices together with fibre strength and length, have consequences on the dynamics.

III.III.2 - Network dynamics

The behaviour of the Kuramoto model has been described theoretically essentially as a function of the global coupling strength k (Acebrón et al., 2005). For a large network ($N \rightarrow \infty$), there is a critical value of coupling, k_c, above which the network exhibits a synchronization transition between an incoherent motion of the oscillators (if $k < k_c$, $R = 0$) and synchrony (if $k > k_c$, $R = 0$). In the following, the region below the critical coupling will be called the incoherent region. After a thorough numerical exploration of the 4-dimensional parameter space for the biologically plausible range of values for σ_n and σ_f, and taking into account the theoretical results about the behaviour of the Kuramoto model, we have found that the synchrony transition exhibits the highest sensitivity to the $(\langle \tau \rangle, k)$ plane. To understand the role of each parameter, we report here the exploration of this plane using $(\sigma_{n,} \sigma_f) = (0,0); (0,3); (2,0); (2,3)$.
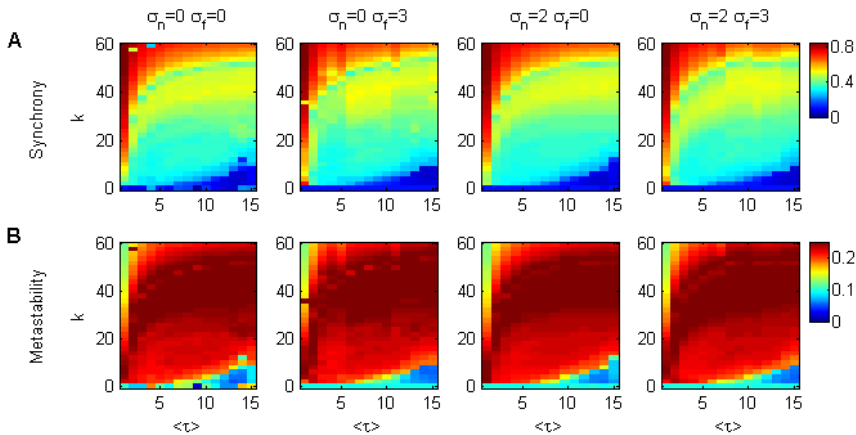
Figure 39 – Effects of noise σ_n and frequency dispersion σ_f on the global synchronization dynamics explored in the parameter space of delays coupling. $(\sigma_{n,} \sigma_f) = (0,0); (0,3); (2,0); (2,3)$. (*A*) Global level of synchrony measured as the mean of the order parameter $R(t)$. (*B*) Global level of metastability, given by the standard deviation σ_R of $R(t)$. We observe that the dynamics at the global level is only slightly affected by the dispersion of intrinsic frequencies and noise.

In Lee et al. (2009), the case of delay heterogeneity was addressed theoretically for an infinite network with homogeneous coupling. In that

case, delays are distributed according to a gamma probability function, and the critical coupling $k_c(\langle\tau\rangle)$ was found to be an increasing function when the delay distribution was sufficiently large compared to its mean, meaning that synchrony requires higher coupling as the mean delay increases.

Despite the high heterogeneity of the finite-size human SC when compared to the theoretical case studied in Lee et al. (2009), the transition towards synchrony draws a line of similar shape, but is smoother (see Figure 39 top). In more detail, for sufficiently small delays, the network synchronizes even for a very weak coupling. In the same way as in theoretical case, as the mean delay increases, synchrony fades away, and the network needs increasingly higher coupling to synchronize. As the heterogeneity of couplings and delays frustrate the stability of the system, we observe higher indexes of metastability in the system, which manifests itself in the standard deviation σ_R of the order parameter $R(t)$, as shown in Figure 39B. For sufficiently large coupling but below full synchronization, $R(t)$ exhibits large fluctuations and the standard deviation σ_R is the highest (as illustrated in Figure 40A middle collumn by the black line).
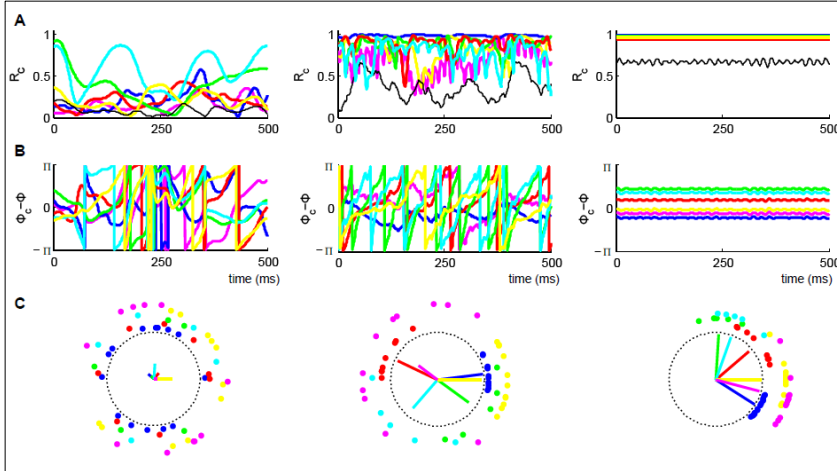
Figure 40 – Network dynamics with increasing coupling (k = 2 (left), 18 (middle) and 60 (right), with $\langle\tau\rangle = 11$ ms. (*A*) Order parameter, $R(t)$ as a function of time for the whole network (black) and individual clusters, $R_c(t)$ (each color represents a subset of nodes). (*B*) Cluster phase $\Phi_c(t)$ relative to the global network phase $\Phi(t)$ as a function of time. (*C*) Snapshot of the phases at $t = 250$ ms (nodes have the color of the cluster to which they belong). Inside the circle and for each cluster, we represent the corresponding order parameter using a vector whose length is $R_c(t)$ and phase is $\Phi_c(t)$. As k increases, clusters go progressively from incoherence (left) to cluster synchrony (middle) until reaching global synchrony (right).

The most irregular dynamics is found in this intermediate regime, similarly to what has been found for a finite-size Kuramoto network with full connectivity and no delays (Popovych et al., 2005). Due to the heterogeneous connectivity of the SC, in this intermediate parametric region, subsets of nodes (or clusters) can exhibit a high level of synchrony while the global synchrony value is still low (see Figure 40 middle column). This represents an intermediate regime between incoherence and global synchronization. For this reason, the transition to synchrony was found to be less abrupt than for homogeneously or randomly coupled networks as predicted by theory. In this region, the nodes of a cluster are entrained by the global cluster ensemble but, due competitive interactions with other nodes and with their natural frequency, they still move independently in relation to the cluster phase, Φ_c. This affects the stability of partially synchronized states, explaining the temporal fluctuations of the cluster synchrony levels (see Figure 40 middle column). As the coupling increases, clusters progressively merge to form bigger clusters, finally merging into a single one (see Figure 40 right column).

Even if cortical oscillations in the gamma-frequency band are observed across brain areas, usually there is some discrepancy in their peak frequency. For the gamma band considered here, we modelled the dispersion of frequencies around 60 Hz as a Gaussian distribution, such that $0\text{Hz} \leq \sigma_f \leq 5\text{Hz}$. Considering noise, we limited ourselves to the interval $0\,\text{rad} \leq \sigma_f \leq 3\,\text{rad}$ so that noise-induced fluctuations are sufficiently weak not to perturb too strongly the dynamics. In their plausible range, both frequency dispersion and noise, considered either separately or simultaneously, were found to have a small effect on the dynamics. Indeed, the qualitative features of the stationary dynamics are preserved, such as the formation of clusters for sufficient mean delay and intermediate coupling. Moreover, the mean and the variarance of the order parameter behave very similarly to the case where $(\sigma_n, \sigma_f) = (0,0)$ in the whole $(\langle \tau \rangle, k)$ plane (see Figure 39). Particularly, a region of high metastability with transient partially synchronized states is still present. The robustness of the dynamics to frequency dispersion or noise perturbations is due to the fact that nodes are still mainly attracted towards cluster ensembles or their natural individual attractor. Overall, these results show that the spatiotemporal organization of the network dynamics is quite robust, and

reinforce the importance of SC in the dynamical organization of the network.

III.III.3 - Resting-state functional connectivity

The fMRI BOLD signal is intrinsically a low-frequency signal due to the temporal scale of the hemodynamic response function. Similarly, the Balloon-Windkessel model of Friston et al. (2003), which estimates the BOLD signal from a given neural activity, gives a low-frequency BOLD signal. The model first calculates the blood flow using a low-pass filter up to approximately 0.5 Hz (see Figure 37A) before calculating the BOLD signal using a nonlinear model. The blood flow fluctuations are therefore proportional to the neural activity amplitude r_0. For the amplitude we have used in the simulations ($r_0 = 1$), we have verified that the blood flow fluctuations remain relatively small (see Figure 37B), in such a way that the Balloon/Windkessel model behaves as a linear filter. Consequently, our results at the BOLD level are not linked to non-linearities of the BOLD model but emerge directly from neural activity. The low-pass filtered (<0.35Hz) simulated neural activity correlates strongly (cc=0.88) with the corresponding simulated BOLD signal, with a lag corresponding to the time-to-peak of the correlation function (see Figure 37C–D). Therefore, finding correlations in the BOLD signal is similar to finding these correlations in the slow fluctuations of the neural activity. In the regions of the $(\langle \tau \rangle, k)$ plane where the network synchronizes or is fully incoherent, the dynamics is too regular and fast, and therefore the BOLD signal has a small amplitude and power. On the other hand, in the intermediate region, the irregularity of neural activity creates significant power at low frequency and consequently in the BOLD signal.

To identify the region of the parameter space where the model best reproduces the empirical FC, we computed the Pearson correlation and the distance between the empirical and the simulated FC matrices (see Figure 41A). Both indicators are complementary as each has its own limitations. In doing so, we only took into account the FC for directly connected pairs of regions since these were essentially the ones that varied substantially across the parameter space. The region of simultaneous large correlation and small distance corresponds to a sub-region of the incoherent region where

dynamical clusters of nodes appear. It coincides with a mean delay between 9 and 14 milliseconds. For a given point in this region, the correlation matrix of neural activity clearly exhibits blocks of large positive correlation (see Figure 41 B left, where $(\langle \tau \rangle, k) = (11, 18)$), revealing the existence of synchronized clusters. When comparing with the BOLD correlation matrix (see Figure 41 B right) we see that the simulated BOLD signals are correlated within nodes in the same cluster.
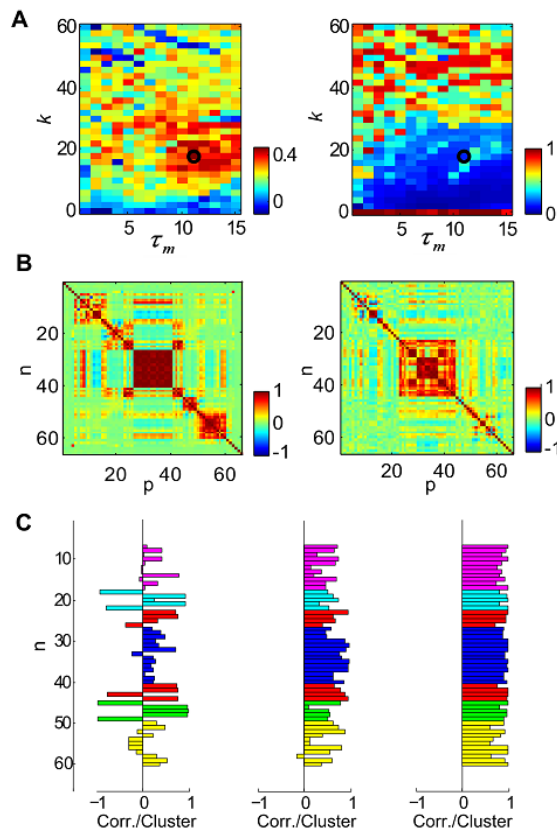
Figure 41 - Behavior of the simulated FC in the parameter space. (A) Pearson correlation (left) and mean squared error (right) between the empirical and the simulated FC in the whole parameter space considering only the connected pairs of regions. These results reveal an extended region (in red in the left plot) of large delay and intermediate coupling where the agreement is the best. (B) (left) Correlation matrix of the simulated neural activity and (right) correlation matrix of the corresponding BOLD signal for the selected working point $(\langle \tau \rangle, k) = (11, 18)$ (black circle in A). (C) Correlation of the low-pass filtered signal (<0.35Hz) between a node and the cluster to which it belongs, for k=2 (left), 18 (middle) and 60 (right). As the cluster synchrony level increases, the slow dynamics of its nodes becomes correlated.

Why is the agreement between simulated and empirical FC best in the region where metastable synchronized clusters form? The highest empirical

FC_{np} corresponds mainly to pairs directly linked by SC_{np} (Honey et al., 2009). Therefore, we find the best agreement when the simulated FC reveals the SC. In Figure 41C, we have plotted the correlation of the low-pass filtered signal (<0.35Hz) of a node and the cluster to which it belongs. As k increases (from left to right), partially synchronized clusters form and the slow temporal components —and therefore the BOLD signals— of the nodes within a cluster become correlated.

For the chosen working point, the FC obtained with small frequency dispersion and noise remains very stable to perturbations. To examine the influence of these parameters, we have looked at their separate effects by varying them continuously for the chosen working point (see Figure 42). In their respective biologically plausible range (σf<5 Hz and σ_n < 3 rad), the high correlation and low distance with the empirical FC is essentially maintained.
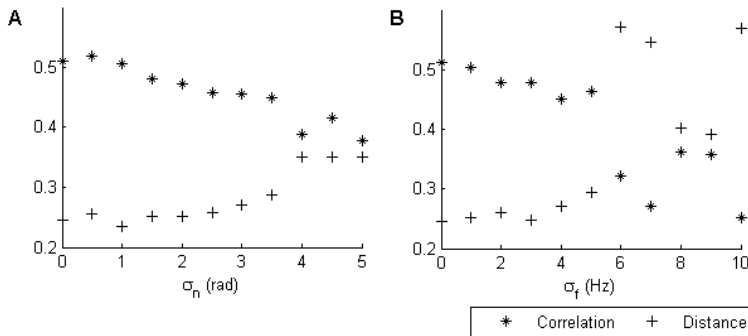
Figure 42 - Robustness of model results with respect to (A) noise standard deviation σ_n and (B) frequency distribution σ_f. $(\langle \tau \rangle, k) = (11, 18)$. (*) Pearson correlation and (+) distance between the simulated and the empirical FC, for anatomically connected pairs of regions. In the biologically realistic range of frequency dispersion ($\sigma_f \leq 5$ Hz), and noise ($\sigma_n \leq 3$ rad), the performance of the model is only slightly changed.

In the parametric region of best agreement with empirical FC, i.e. a sub-region where synchronized clusters appear, we have selected the working point $\langle \tau \rangle = 11$ ms and $k = 18$. This corresponds to a transmission speed of 6 m/s, which is in the physiologically realistic range of propagation velocities (around 5–20 m/s) for the adult primate brain according to Ghosh et al. (2008a). For increased biological realism, we added noise with $\sigma_n = 1.25$ rad. For this working point, a detailed comparison between the simulated and the empirical data is presented below. We present the SC, the empirical

FC and the simulated FC for three seeds in relation to all other nodes. Two of these seeds are known to be part of the Default-Mode Network (DMN), namely the right precuneus (Figure 43left) and the left posterior cingulate cortex (Figure 44A). In addition, we choose a seed from a distinct network, the left Cuneus (Figure 43right). We observe that the model predictions go beyond the SC and predict negative correlations as well. In Figure 44C, we can see that the correspondence between simulated and empirical seed correlation maps is significantly high for all seeds. Furthermore, as previously reported in Honey et al. (2009), FC is positively correlated with SC for directly connected node pairs.
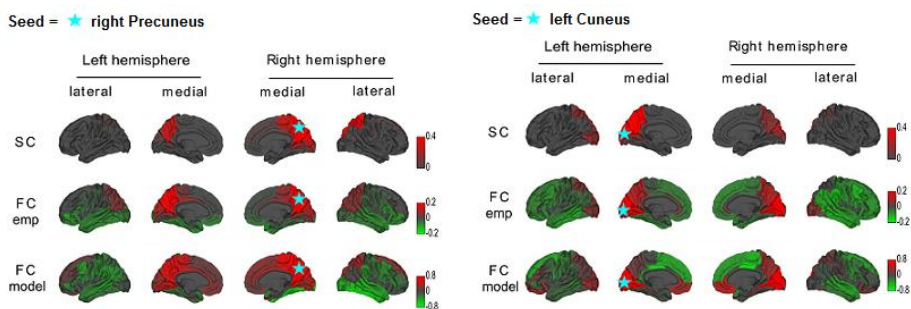
Figure 43 – Seed connectivity. Structural connectivity (top - SC) and comparison between the empirical functional connectivity (middle – FC emp) and the one predicted by the model (bottom – FC model), for two different seeds. Seed location indicated by a light blue star. $(\langle\tau\rangle, k) = (11, 18)$.

Furthermore, the simulations predict many details of the empirical FC between DMN regions along the medial axis (Figure 44B middle horizontal bars). On the other hand, correlation maps of more distant seeds are less well-predicted (Figure 44B top and bottom horizontal bars). It is important to mention that, beyond the model quality —i.e. the way the dynamics at the local node level is modelled— results also depend crucially on the quality of the SC matrix. Some fibre tracts, for example long inter-hemispheric connections between lateral cortices (see Figure 45), are likely missing due to the limited resolution of current imaging techniques (Hagmann et al., 2008). These missed pathways have direct repercussions on the model results. Also, the fact that empirical FC has smaller values than the simulated one is due in part to the effect of averaging while down-sampling the high-resolution empirical FC.
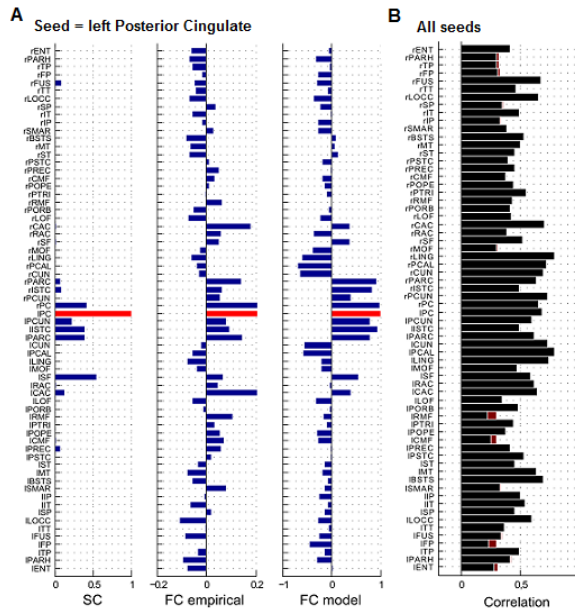
Figure 44 - Comparison between SC, empirical and simulated FC at the seed level. (*A*) SC, empirical and simulated FC for the left Posterior Cingulate (red). (*B*) Pearson correlation between empirical and simulated FCs for each individual seed. This demonstrates that the model reproduces many details of the empirical FC. $(\langle\tau\rangle, k) = (\mathbf{11}, \mathbf{18})$.
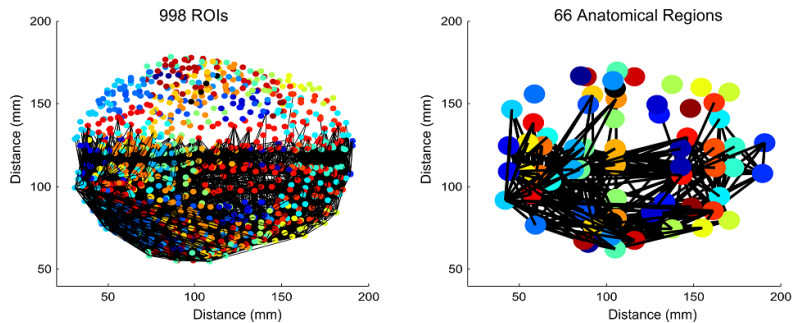
Figure 45 – Connectivity to the right hemisphere. Graphical representation (view from above) of the 998 ROIs (left) and the 66 anatomical regions (right), with all the connections with targets in the right hemisphere. It can be seen by visual inspection that very few inter-hemispherical connections were detected, even in the high resolution connectome.

Regarding the patterns of correlations between nodes belonging to different clusters, it is difficult to infer analytically if two different clusters will lead to correlated or anti-correlated BOLD signals, since clusters seem to interact in

a non-trivial way (s previously shown in Figure 40 middle). However, a comparison between empirical and simulated correlations patterns can be done. In Figure 46, we checked if the model could reproduce anti-correlated networks as observed in Fox et al. (2005). Indeed, the posterior cingulate (PC) exhibits positive correlation (cc=0.5) with the superior frontal (SF), and negative correlation (cc=−0.3) with the lateral occipital cortex (LOCC) in the model. This result agrees with the empirical measures. In particular, these correlations can be seen directly in the simulated BOLD signal time series of the 3 seeds (Figure 46 bottom).
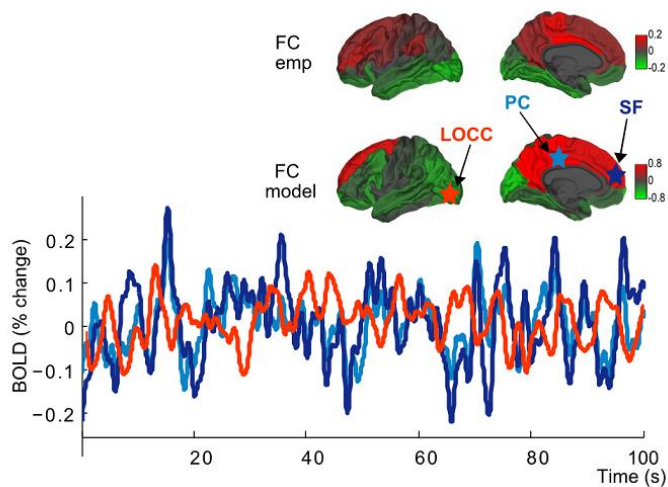
Figure 46 - Correlation between different regions $(<\tau>,k) = (11,18)$**.** (Top) Representation on the cortical surface of the empirical and the simulated FC map of the left posterior cingulate (PC). (Bottom) Simulated BOLD signal for 3 seeds (PC, light blue; SF, dark blue; and LOCC, orange). Both in the empirical and in the simulated data, the FC between PC and SF is positive, while their FC with LOCC is negative (results shown are from the left hemisphere).

III.IV - Discussion

In this chapter, we propose a large-scale neural network model to explain the origin of spatio-temporal patterns of slow fluctuations observed in the BOLD signal during rest. Several studies have found a counterpart for BOLD signals in the neural activity, in particular in the slow power fluctuations of the LFP in the gamma frequency range (Leopold et al., 2003; Shmuel and Leopold, 2008; Nir et al., 2008; Miller et al., 2009). Here, we investigate if local gamma activity alone can induce correlations at the BOLD level. In vivo electrophysiological studies have reported the existence of oscillations in

this frequency band and much experimental and theoretical evidence supports that gamma oscillations are generated at the level of local neuronal populations (Brunel and Wang, 2003; Bartos et al., 2007). In our model, we assume that each node spontaneously exhibits sustained gamma oscillatory activity. We have used here a simple model —the Kuramoto model with time delays— whose behaviour has been studied theoretically in simpler parameter settings (Kuramoto, 1984; Yeung and Strogatz, 1999; Acebrón et al., 2005). In the present study, BOLD fluctuations are found to correspond to a slow component of neural activity mainly related to the metastable synchronization of subsets of nodes.

To constrain the model, we calculated the simulated FC for a range of parameters and compared it to the empirical one. After numerically exploring the parameter space, we have identified a range of parameters where the simulated FC best matches the empirical one. In a range delimited by an interval of coupling and realistic transmission delays, subsets of well-connected nodes exhibit fluctuations in their level of synchrony, while the global network is still in a globally incoherent regime. Across nodes within a cluster, the BOLD signal is correlated because the ensemble is driven in and out of synchrony simultaneously. This leads to a shared part of the dynamics between the nodes even if the cluster itself, as characterized by the behaviour of its order parameters, has non-stationary dynamics. We propose that these fluctuations are at the origin of the power found at very low frequencies, in particular in the frequency range characteristic of the BOLD signal. Therefore, in the model, the RSNs are instantiated in the metastability region by partially synchronized clusters. Between clusters, we also found patterns of positive and negative correlations that reproduced observed empirical patterns. Although the patterns of FC are largely dependent on the SC, as noticed in the empirical data (Honey et al., 2009; Bullmore and Sporns, 2009), they also emerge from the interplay of SC and local oscillatory dynamics. Beyond the role of the connectivity matrix, the delay matrix was also found to play a major role in preventing the full synchronization of the network. Actually, the network globally synchronizes when the mean delay is too small, even when biologically plausible dispersion of intrinsic frequencies and noise level are considered. Moreover, the region of best agreement with empirical FC was obtained when the mean delay was above a certain bound (about 9 ms

here). All these results were found to be robust to the dispersion of intrinsic frequencies and to noise, both important sources of variability. The agreement of the model results with the empirical data depends not only on the type of dynamics and on the precise mathematical model that we have considered at the local level, but also on the quality of the SC. Although the empirical FC is related to the actual brain dynamics, errors in the measurement of SC can obscure actual contributions of SC to FC. For example, very few inter-hemispherical connections were detected between regions outside the cortical midline. Actually, the detection of structural connections when tracking small fibres perpendicular to major fascicles and across the corpus callosum is still difficult with diffusion MRI and tractography. These missing connections may be responsible for the lower agreement between empirical and simulated FC when the seed is not placed in or near to medial cortical regions. Other brain regions not captured in the structural scans (e.g. the thalamus) might also have an important role in shaping FC. Still, despite methodological limitations and using only cortical SC, we have been able to identify a number of important features of the empirical FC. Previous modelling studies have investigated the brain's neural dynamics during rest and the relationship between SC and FC in this behavioural state, using similar large-scale networks but with more biologically detailed models for the node dynamics. In these cases, all conclusions were based on numerical simulations, and no analytic link to a theoretical understanding of the network dynamics in simple parameter settings (as shown here) was possible. In Ghosh et al. (2008a, 2008b) and Knock et al. (2009), using the CoCoMac database of the macaque's anatomical brain connectivity (Kötter and Wanke, 2005), a down-sampled human SC and a two-dimensional reduced model for the node dynamics including damped alpha oscillations at the local level, slow fluctuations were believed to be induced by noise. This noise led to excursions of neural activity in the vicinity of the stable equilibrium state of the brain network, inducing patterns of alpha waves across the brain network. In Honey et al. (2009), using the high-resolution human SC and a neural mass model at the local level, a similar performance in the comparison with empirical FC as with our model was obtained, but no theoretical explanation for the nature of slow fluctuations was presented. In Deco et al. (2009), Wilson–Cowan units were used at the local level with the CoCoMac connectivity, and the

model exhibited similar self-sustained oscillatory behaviour as described here. The network was divided a priori into two node communities using a modularity algorithm. What was found was that the synchrony levels of these communities fluctuated in an anti-correlated way under the influence of noise, reproducing experimental observations (Fox et al., 2005). Without the availability of empirical FC for the macaque, the results from the latter model could not be directly compared with experimental data. Therefore, the goal of the present study was to address all these questions in more detail, using the same dynamical scenario. In the model of Honey et al. (2009), the chaotic node model did not allow for a good understanding of the origin of the global dynamics. In the other models, either damped oscillations (Ghosh et al., 2008a, 2008b; Knock et al., 2009) or sustained oscillations like here (Deco et al., 2009) were hypothesized at the local level and, even if the dynamics might be mainly linear in the first case, the dynamics was intrinsically nonlinear in the latter. However, in all cases, connectivity, delays and noise were found to be important to reproduce features of the empirical FC, and among them RSNs. For the present model, we find that noise is not necessary to create slow resting-state fluctuations. However, this result does not contradict the results in Deco et al. (2009) as noise was found to play a role in the interaction between clusters, a question that does not overlap with our study.

This study suggests several lines of future research. Although the situation considered here remains too complicated for an analytical treatment, our results predict that the network dynamical behaviour we have described could be the origin of fluctuation patterns observed in the BOLD signal during rest. These results emphasize the need for a deeper understanding of the dynamics of phase oscillator networks for complex networks, such as those encountered in the brain. Beyond understanding cluster formation and the emergence of correlations in the slow node dynamics inside clusters, the way these clusters interact and how correlations or anti-correlations emerge between clusters remain unknown. Addressing these questions in future research may help comprehend the organization of neural dynamics at the macroscopic level.

Previous models of resting-state activity have considered quite different models of neural masses at the node level. Despite their differences, all

have shown a degree of agreement with experimental data. This suggests an important role of SC in the generation of FC. As an example, the DMN is known to represent a densely connected sub-network within the cortex (Hagmann et al., 2008; Honey et al., 2009). However, as we show here, the simulated FC is a priori the product of the interplay between SC and the local dynamics. Therefore, improving human connectome data will definitely bring progress to this research field.

In this chapter, we have mainly focused on correlations of slow BOLD signal fluctuations. However, recent electrophysiological findings have found that RSNs could be independently revealed by MEG band-limited power fluctuations (Brookes et al., 2011). In the next chapter, we explore if our model is able to explain this behaviour, in order to obtain a better understanding of the relationship between spontaneous activity observed in slow and fast neural activity and the mechanism that binds cortical regions together during rest.

IV – Predicting resting-state MEG band-limited power correlations with the Kuramoto model

"The scientist is not a person who gives the right answers;
He is the one who asks the right questions."
Claude Lévi-Strauss

IV.I – Introduction

The majority of studies of resting brain activity have used fMRI to measure temporal correlations between BOLD signals from different brain areas. Although there is a global consensus that BOLD temporal correlations imply that brain areas are functionally connected, the BOLD contrast is a measure related to blood flow and is limited by poor temporal resolution due to the protracted hemodynamic response[1]. For this reason, the electrodynamic mechanisms that mediate resting-state correlations cannot be accurately elucidated using this technique. Magnetoencephalographic experiments have detected functional connectivity between segregated cortical regions during rest, when considering the slow band-limited power (BLP) fluctuations (or envelopes) of neural oscillations (Nikouline et al., 2001, Liu et al., 2010, Brookes et al., 2011, Hipp et al., 2012)[2]. In general, these results indicate that functional connectivity in BOLD responses is intimately related to neural oscillations, and exclude the hypothesis where it would be the BOLD signals, on their slow time scale, that interact with each other across areas leading to resting-state fluctuations. However, the mechanism at the genesis of these electrophysiological amplitude modulations, or BLPs, and the link to the hemodynamic fluctuations detected in fMRI remains unknown.

In particular, the study from Brookes et al. (2011) using MEG has found that segregated cortical areas exhibit correlated BLP only in a specific range of

---

[1] See section *I.I.1– Resting-state hemodynamic fluctuations* for more details.
[2] See section *I.I.3 - Detection of resting-state patterns using MEG* for a comprehensive compilation of experimental studies.

carrier frequencies. As seen in Figure 47, they found that significant correlations within seeds of the DMN only appear when considering the BLP of frequencies between 10 and 30 Hz, with a peak around 18Hz (in the low-beta frequency band). These results suggest an underlying binding mechanism that modulates the power of 10-30Hz oscillations in a correlated way across regions from the same RSN. Furthermore, applying ICA to the BLP fluctuations, revealed sub-networks that closely matched the RSNs identified in BOLD studies, in a consistent way across subjects (see Figure 5 in section *I.I.2 - Electrophysiological signatures of resting-state activity*). According to their results, the temporal signature of the DMN was most prominent in alpha-band power fluctuations, and the remaining RSNs were found with beta-band carrier frequencies.
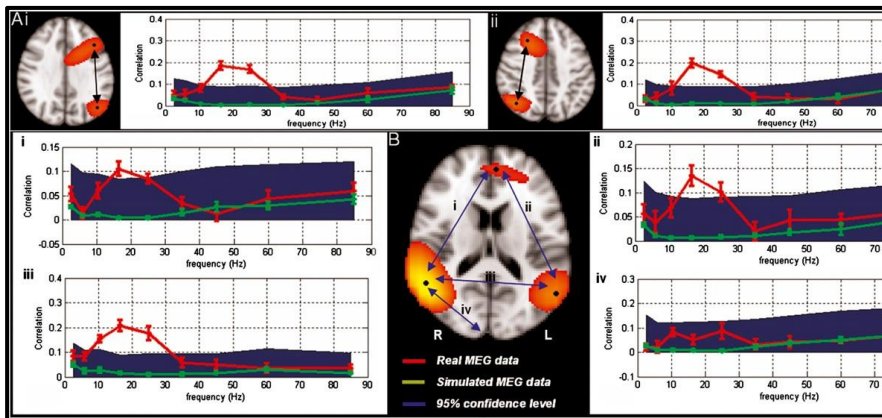
Figure 47 – Frequency specificity of long-range correlations using MEG band-limited power fluctuations. (A) The parietal and prefrontal cortices exhibit significant correlations in the BLP from 10 to 30Hz, while the BLP at other frequencies is not correlated. (B) DMN. (B, i) Anterior cingulate, inferior parietal lobules (B, iv) Connectivity between right inferior parietal lobule and the right primary visual cortex. Adapted from Brookes et al. (2011).

In the previous chapter, BOLD signal fluctuations were generated by fluctuations in the synchrony degree, where partially synchronized states emerged periodically, and were naturally disrupted due to competitive mechanisms between multiple stable states (Cabral et al., 2011). In the present chapter, we use the same Kuramoto model of weakly coupled oscillators with brain-inspired couplings and delays, to show that instability in the degree of synchrony not only explains BOLD signal fluctuations, but also induces band-limited power fluctuations. In particular, when a cluster of regions becomes temporarily synchronized, this occurs at a reduced

collective frequency, and therefore the power at this frequency increases simultaneously for all nodes belonging to the cluster. Under realistic parametric conditions, these cluster frequencies fall in the alpha- and beta-bands. Moreover, the BLP fluctuations are found to define functional networks that are similar to the ones extracted from real resting-state MEG recordings.

The work presented in this chapter is the first to propose a unified theory encompassing both BOLD fluctuations and BLP modulations of electrophysiological signals to explain the physiology of resting-state spatiotemporal patterns at the macroscopic level.

IV.II Methods

IV.II.1 – MEG data collection and analysis

Ten normal healthy participants underwent an eyes-closed resting state MEG scan lasting five minutes[1]. The MEG signal was frequency filtered into 15 bands of interest (each 4Hz wide, between 0 and 60Hz) and subsequently projected into 90 intracranial sources, each one placed at the centre of gravity of the brain areas from the AAL parcellation scheme (Tzourio-Mazoyer et al., 2002) (see Figure 48 A). According to previous experimental (Liu et al., 2010, Brookes et al., 2011a, Brookes et al., 2011b) resting-state functional connectivity in MEG data was found to be best captured by considering the *slow* amplitude fluctuations of the time series at each location. This is found by estimating the absolute value of the oscillatory signal, computed via the Hilbert transform, which captures the instantaneous power of the signal (see Figure 48 B for an illustration. Furthermore, the oscillatory amplitude envelope was temporally down-sampled by dividing the envelope into equal windows of length 1 s and calculating the mean envelope value for each window (which effectively low-pass filters the envelope signal). For each frequency, the pair-wise 90x90 correlation matrix was estimated, giving a total of 15 correlation matrices for each subject. The correlation matrices were averaged across the 10 subjects to give a single set of 15 correlation matrices.

---

[1] A full description of these methods is provided in the Appendix section *A.2 - MEG Data Collection and Analysis.*
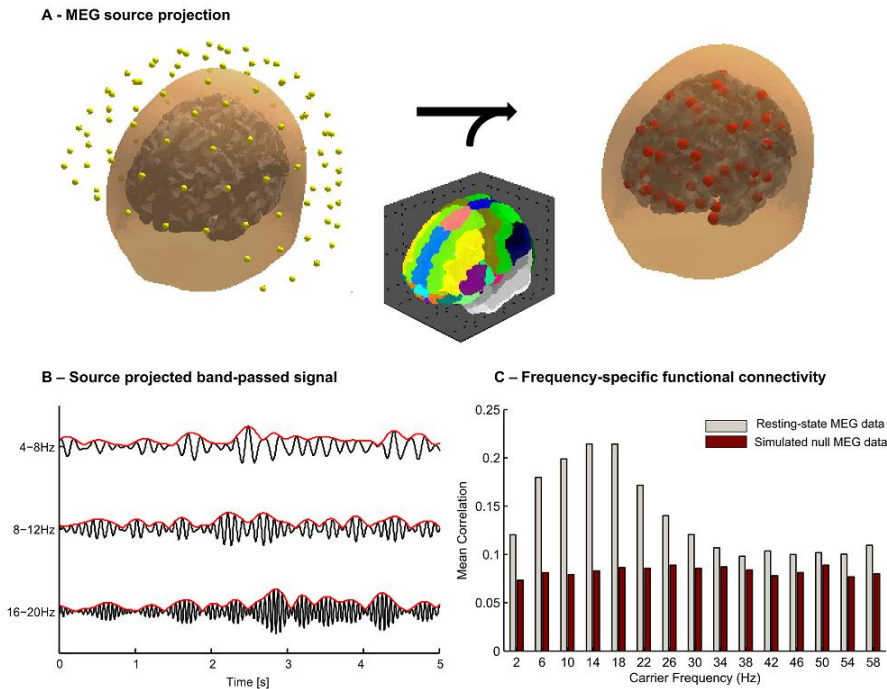
Figure 48 - MEG data collection and analysis. (*A*) The signals detected by the MEG sensors (yellow) were beamformed into 90 sources (red) representing functionally distinct cortical and subcortical regions defined according to the AAL parcellation template. (*B*) Resting-state MEG signal from one cortical region in 3 frequency bands (black) and the corresponding amplitude (or power) envelopes (red). (*C*) Functional connectivity strength – taken as the mean of all pairwise envelope correlations - as a function of the carrier frequency (centre frequency ±2Hz) from which the envelopes are extracted. The functional connectivity attains a maximum when the power of 16 to 20 Hz oscillations is considered.

To take into account artefact correlations generated by intrinsic properties of either the MEG scanner or the source-projection algorithm, the same correlation matrices were computed, but this time with an empty-scanner dataset with additive subject-matched uncorrelated coloured noise.

IV.II.2 – Anatomical connectome

For our simulations, we used a brain-inspired coupling architecture, in the same way as in previous chapters. In this case, the DTIs of the brains of 21 healthy subjects were acquired and the corresponding connectomes at the voxel level were built using a tractography algorithm[1]. Subsequently, brain

---

[1] See the *Appendix* section *A.3 – DTI data collection and building of anatomical connectomes* for details.

areas were defined using the AAL parcellation template, and the number of fibre tracts detected connecting each pair of regions was taken as an index of the coupling strength, resulting in a coupling matrix C for each subject. Matrices were averaged across subjects, resulting in a single group-representative coupling matrix. The distances between the 90 AAL regions were taken as the Euclidean distance between the corresponding centres of gravity.
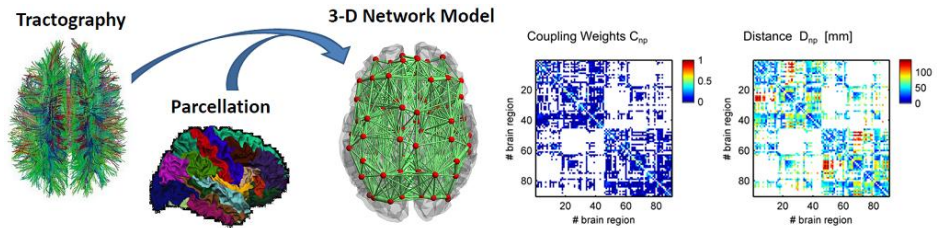
Figure 49 - Building the model's coupling architecture. The coupling strength between regions was derived from the average number of fibers detected with tractography connecting any pair of regions defined in the AAL template. The distance was computed as the 3-D Euclidean distance between centers of gravity.

IV.II.3 - Model of weakly coupled oscillators

To simulate the dynamical interaction of cortical regions in the brain's large-scale anatomical network, we have used the previously described Kuramoto model (Kuramoto, 1984, Acebron et al., 2005) taking into account the interaction delays[1] (Yeung and Strogatz, 1999). The Kuramoto model has been used to simulate synchronization phenomena in a wide variety of fields including biological systems (Pikovsky et al., 2001, Strogatz, 2003) and has only recently been applied to macroscopic brain dynamics (Cabral et al., 2011). The dynamics emerging from weakly coupled gamma-band oscillators when coupled with complex topology, like the brain, has revealed complex synchronization behavior such as multistability and metastable cluster synchrony (Cabral et al, 2011).

In order to find the parametric conditions under which multistability in this new connectome occurs, we performed simulations for 300 s for a range of global coupling strengths k and mean delays $\langle \tau \rangle$. In the previous chapter, the synchronization dynamics was found to show the highest sensitivity to

---

[1] See section *II.III – Time delays in the Kuramoto model.*

these two parameters. Phases were initialized randomly, and simulations were run in a non-interacting way for a sufficiently long interval (due to delays). The first 20 s of simulations were discarded to avoid any dependency on initial conditions and we always refer to the remaining simulated time in the following. Once the optimal set of parameters was chosen, we simulated the model for 1200 s (20 minutes) to compare with experimental data. The system of N dynamical equations was numerically integrated with a time-step $\Delta t = 0.1$ms using an Euler scheme. All calculations were performed using MATLAB (www.mathworks.com).

At the global level, the network synchrony was evaluated by the Kuramoto order parameter $R(t)$ (see section *II.II – Synchronization and the Kuramoto Order Parameter*).

IV.II. 4 - Comparing simulations with experimental results

The simulated neural activity at each region, taken as $r_n = sin(\theta_n)$. To compare with the experimental MEG data, r_n was band-pass filtered into 15 frequency bands (between 0 and 60Hz, each 4Hz wide). Furthermore, in the same way as we did in the experimental MEG data, the Hilbert envelope was computed and was temporally down-sampled using a 1 s sliding window. For each frequency, the pair-wise correlation matrix was estimated, giving a total of 15 frequency-specific correlation matrices.

IV.III – Results

IV.III.1 - MEG Functional Connectivity

The set correlation matrices computed from the envelope fluctuations at each of the 15 frequency bands is plotted in Figure 50. Notably, as observed in Figure 48C, the overall functional connectivity (i.e. the mean of all pair correlations) is stronger when 8-20Hz carrier frequencies are considered, with a peak around 14-18Hz. These BLP correlations are significant and are independent of artifact correlations (Figure 48C red). Performing a visual inspection to the correlation matrices in Figure 50, we can see that the functional connectivity between some node pairs varies as a function of the carrier frequency, where $FC_{np}(f_C)$ exhibits a peak for 10Hz $< f_C < 20$Hz.
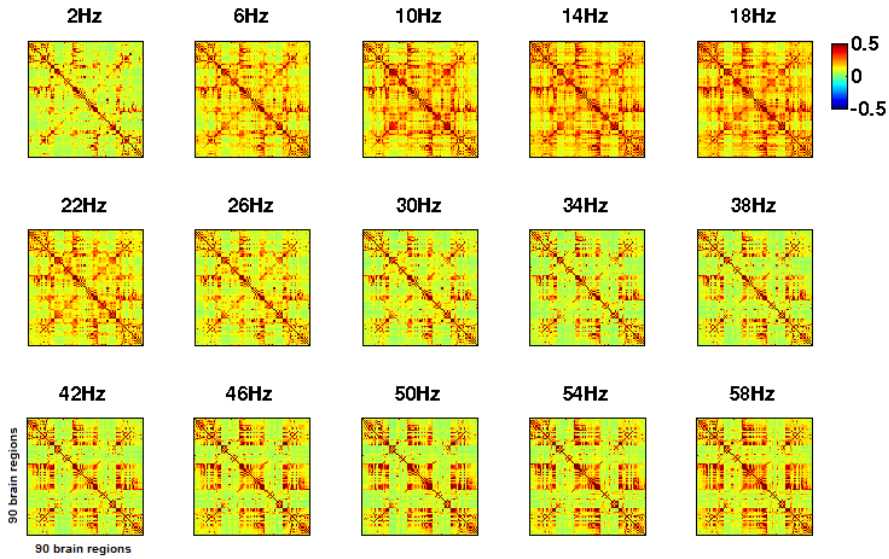
Figure 50 – Band-specific functional connectivity. Correlation matrices of band-limited power fluctuations obtained at 15 non-overlapping frequency bands (between 0 and 60Hz, each 4Hz wide).

In order to explore the behavior of power fluctuations over time, we plot in Figure 51 the average of all 90 envelopes in three distinct frequency bands. By computing the average over all nodes we are able to explore the dynamics at the global level, but further explorations should be performed at the level of individual RSNs. We observe that the power of 16-20Hz oscillations fluctuates strongly in time, and in a non-Gaussian manner, suggesting multistability. Although the likelihood plot indicates more stability at low power (indicating that the brain spends more time with low power in this frequency band), high-power states occur with significant likelihood. Moreover, the power fluctuates slowly, in a time-scale comparable to the BOLD fluctuations (i.e <0.1Hz). So far, the origin of these band-limited power fluctuations remains unclear. In the gamma-band (Figure 51 bottom) however, the average power fluctuates around its mean, indicating a stable regime in this frequency band.
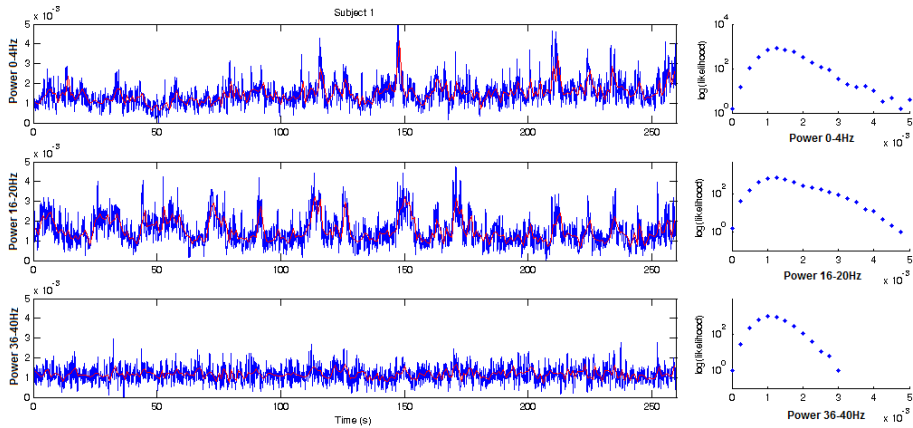
Figure 51 – Power fluctuations in 3 frequency bands from one subject with eyes closed during rest. (Left) Mean of all 90 envelopes obtained from the MEG signals from subject 1 of the 0-4Hz, 16-20Hz and 36-40Hz oscillations. Increases in the power indicate that the amplitude of the corresponding oscillations is increased in the brain. (Right) Plots of the likelihood of the power at each of the frequency bands shown in the left. A single stable state with only noisy fluctuations around its mean generally exhibit a bell-shaped distribution, whereas multistable regimes exhibit more complex or multimodal distributions.

IV.III.2 - Simulated network dynamics

To explore the mechanisms underlying the complex dynamics observed in MEG data, we built a model of large-scale brain dynamics considering the coupling architecture of the neuroanatomical network. At the individual level, brain regions were assumed to maintain self-sustained oscillations in the gamma frequency band. To minimize the number of parameters we assumed pure 40Hz oscillations. The interacting behavior of oscillatory brain regions was simulated by the Kuramoto model of weakly coupled oscillators with time delays for sufficient time to be in a stationary regime. As shown in Figure 52, the model optimally predicts MEG functional connectivity for a range of parameters where the oscillators exhibit relatively low levels of synchrony but the degree of metastability is high. This is found for average delays between 10 to 20ms (corresponding to transmission speeds between 3 to 6 m/s) and for coupling strengths sufficiently weak to avoid full synchrony but strong enough to engage metastable partially synchronized states. Notably, this corresponds to the same dynamical regime where the best agreement with BOLD functionally connectivity was found in our previous work (Breakspear et al., 2010, Cabral et al., 2011).
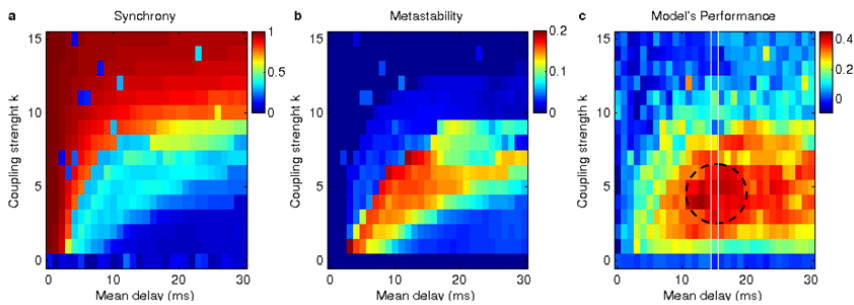
Figure 52 - Synchronization dynamics and model's performance in the $(\langle\tau\rangle, k)$ parameter space. (a) Mean synchrony degree (1=full synchrony; 0=incoherence) as a function of the coupling strength and the mean delay (after a transient period of 100s with a time step of 0.1ms). The system exhibits a high degree of synchrony when the delays are small (tau<4ms). For larger delays, synchrony is possible with an increased coupling strength. (b) The metastability index indicates how the synchrony degree fluctuates in time. These fluctuations are stronger in the region between incoherence and full synchrony, indicating a multistable regime. (c) For each set of parameters, the 15 simulated correlation matrices were concatenated, and the values reported correspond to the Pearson's correlation between the real and simulated correlation matrices. The black dashed circle indicates a broad region of parameters where the model optimally predicts real MEG functional connectivity. The white vertical lines highlight the set of parameters considered in Figure 53, corresponding to a mean delay of 15 ms (i.e. a speed of 3.7 m/s).

IV.III.3 - Frequency specificity and power modulations

In the intermediate regime between incoherence and full synchrony, the synchrony degree fluctuates in time, these fluctuations being captured by the metastability index (Shanahan, 2010). For high metastability, multiple partially synchronized states alternate in time with periods of incoherence. Remarkably, during periods of increased cluster synchrony, the nodes involved start oscillating at a reduced collective frequency, as has been described for systems of coupled oscillators with time delays (Niebur et al., 1991). This reduced collective frequency depends parametrically on the natural frequency of the oscillators, on the mean coupling strength, on the mean delay and on the number of nodes involved. Therefore, due to the heterogeneity of the anatomical connectome, when different subsets of nodes synchronize, they will have different collective frequencies, resulting in a rich power spectrum with multiple peaks. In Figure 53 we show the average power spectrum of the system (in each line), for increasing coupling strengths using a fixed mean delay of 15ms. For null coupling, $k = 0$, all nodes behave independently and oscillate at their own intrinsic frequency,

i.e. 40Hz. Conversely, for $k = 15$, all oscillators are synchronized at a global reduced frequency (here, around 4Hz). Using 40Hz oscillators and biologically plausible delays (i.e. 15ms here), strong peaks between 10 to 20Hz emerge in the metastability region ($2 < k < 7$).
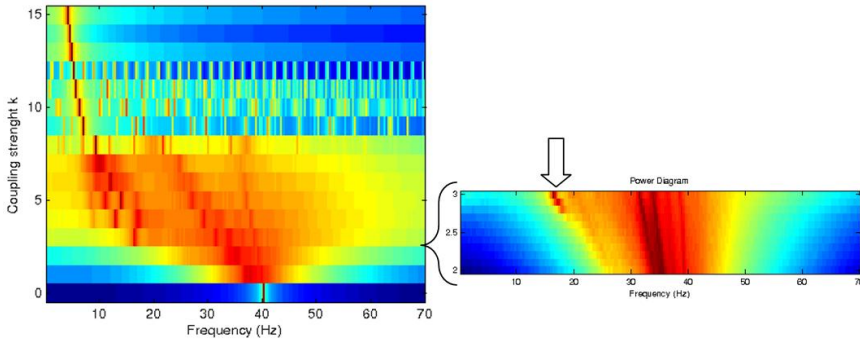
Figure 53 - Power spectrum as a function of the coupling strength. Left – Each line corresponds to the average power spectrum of all the nodes in the network. Starting from the bottom, at k=0, all the nodes oscillate at their natural frequency 40Hz, and therefore, the mean power spectrum reveals a single peak at 40Hz. When k>0, the oscillators interact with each other, distorting the pure 40Hz oscillations and broadening the spectrum of frequencies of the system. Due to the heterogeneity of the connectome, some groups of nodes (sub-networks, or clusters) are more strongly coupled than others. Therefore some clusters are able to synchronize at weaker global coupling. Since the delays force the synchrony to occur at a reduced collective frequency, when a sub-network starts synchronizing, a new frequency peak appears.

While synchrony among a group of nodes is maintained, the power of the corresponding collective frequency is kept high. However, if the synchronized state is only stable for some periods in time and is naturally disrupted by competitive states, then the power of the reduced frequency fluctuates accordingly. In this way, the degree of synchrony of the cluster $R_C(t)$ modulates the power of its reduced collective frequency $\frac{\partial \varphi_C}{\partial t}$.

To get a better picture of the dynamics occurring in the network, we plot in Figure 54 the synchrony degree of the whole network over time (top) and the corresponding power between 10 to 20Hz (middle), for different levels of coupling k. As expected, for weak couplings (A), the system is in an incoherent state, with low synchrony degree. As all oscillators are essentially driven by their own intrinsic frequency (i.e. 40Hz), the power between 10-20Hz is low. As the coupling increases, we observe the sporadic emergence of metastable synchronized states that emerge spontaneously from

incoherence, last for some seconds, and then disappear again (B). While synchronized, and due to delays, the nodes in the cluster are phase-locked at a reduced collective frequency (here between 10-20Hz). When the synchrony fades away, the power in this frequency vanishes, and oscillators are driven again by their intrinsic frequency at 40Hz. Furthermore, under fine-tuned parametric conditions, the 10-20Hz power fluctuates slowly, with a time scale similar to the one detected by the BOLD signal (i.e. around 0.1Hz).
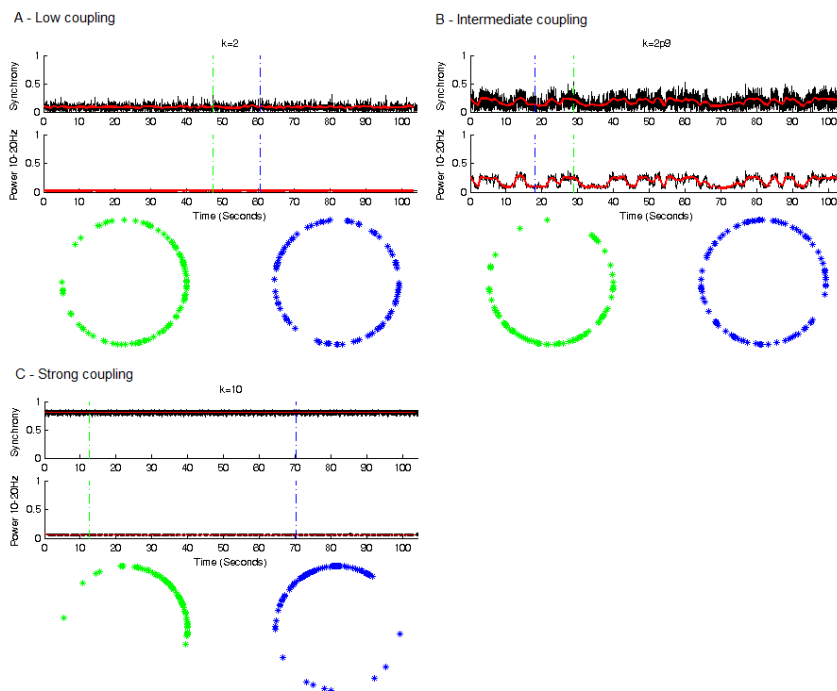
Figure 54 - Meta-stable synchronized states induce slow fluctuations in the power between 10 to 20Hz. (A-C) **Top** – Plots of the synchrony degree measured at each instant of time (black) and smoothed with a 1s sliding window (red). Increasing the coupling strength (from A to C), the synchrony degree rises from nearly 0 (total incoherence) towards 1 (full synchrony). The dash-dotted lines indicate the instants of time where higher (green) and lower (blue) synchrony degree was detected. **Middle** – Average power between 10-20Hz at each instant of time (black) and smoothed with a 1s-sliding window (red). In the region of higher metastability (B) the smoothed degree of synchrony correlates more than 90% with the smoothed power fluctuations showing that the fluctuations in the power are originated by slow fluctuations in the synchrony degree. **Bottom** – Phase-plots illustrating the phases of all nodes (*) at a given instant of time. Green phase plots were captured at an instant of higher synchrony (corresponding to the green dashed lines), and blue phase-plots correspond to the most desynchronized state. In (B), synchronized and desynchronized states alternate in time.

To further explore the origin of these band-limited power (BLP) fluctuations, we have computed the correlation between the order parameter and the BLP in two frequency ranges. As can be seen in the plots in Figure 55 ADH, the order parameter $R(t)$ correlates strongly with the amplitude modulations of 10-20Hz oscillations (cc=0.55). Furthermore, this correlation increases significantly if $R(t)$ is low-pass filtered <1Hz (cc=0.86).
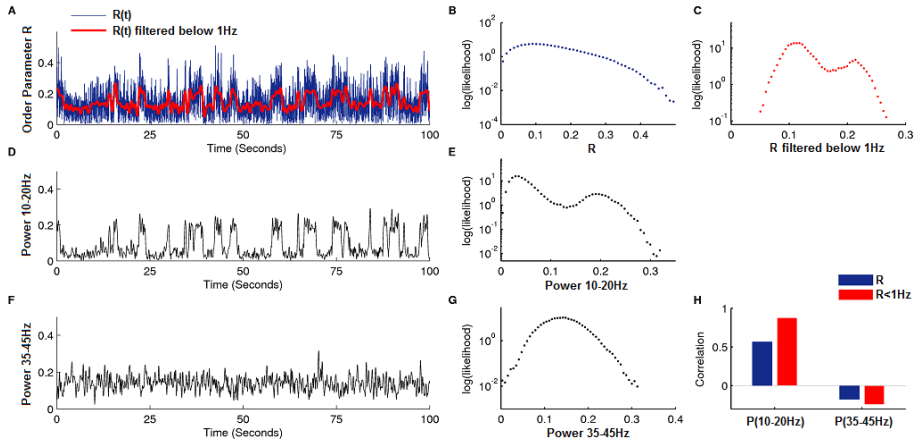
Figure 55 – Relationship between the order parameter and band-limited power fluctuations (for $\langle \tau \rangle$= 15ms; k=2.8). **(A)** The synchrony degree of the system of 90 coupled oscillators (blue) and low-pass filtered at cut-off frequency of 1Hz (red). **(B-C)** Probability distribution of the synchrony degree at 2 different time scales: fast (B) and low-pass filtered below 1Hz (C). The bi-stability of the synchrony degree is most clearly detected in the slow component of the signal. **(D-F)** Instantaneous power of the system in the 10-20Hz (D) and 35-45Hz (F) frequency ranges over time. **(E-G)** Probability distribution of the power in the 10-20Hz (H) and 35-45Hz (I) frequency ranges. While the power at lower frequencies is characterized by a bimodal distribution -which is indicative of a bi-stable regime-, the power at higher frequencies is mainly Gaussian. **(H)** Correlation between the synchrony degree and the 10-20Hz (left) and 35-45Hz (right) power fluctuations. The 10-20Hz power fluctuations are highly correlated with the synchrony degree, particularly when this one is filtered below 1Hz. A-H correspond to a simulation time of 1200 s, where the fist 100s were discarded.

It seems that only long enough periods of synchrony result in collective frequency decays, which subsequently induce metastability. Consequently, the non-Gaussian regime of the order parameter is much more clearly seen when fast fluctuations are filtered out (see the histograms in Figure 55B and C). On the other hand, as can be observed in Figure 55F-G, the power around the oscillators' natural frequency (40Hz ±5Hz to allow for small perturbations in the limit cycle) remains high, with only relatively small amplitude perturbations. One explanation for this fact is that, even when

the oscillators are entrained by the collective behavior of the cluster, they still oscillate in relation to it, being constantly driven by their own limit-cycle dynamics[1]. Even so, these 35-45Hz amplitude fluctuations exhibit small negative correlation with the order parameter (Figure 55H). In other words, in periods of high synchrony, the amplitude of 40Hz oscillations is slightly decreased.

The stability of synchronized states is highly sensitive to the coupling strength. Increasing only slightly the coupling (from to $k = 2.8$ to $k = 2.9$ in our case) increases the stability of synchronized states, and these can last for long periods of more than ten seconds (See Figure 56).
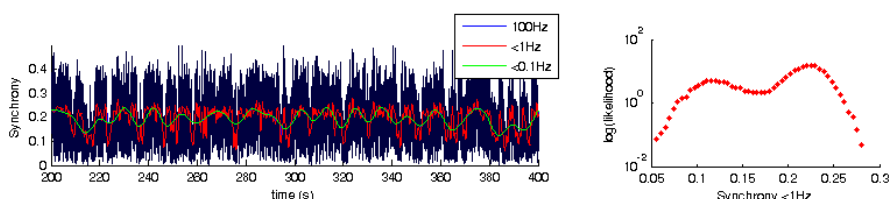
Figure 56 – The stability of synchronized states (right peak in the likelihood plot) increases with the coupling k (here for $\langle \tau \rangle$= 15ms; k=2.9).

From experimental studies, we know that the envelopes of alpha- and beta-band oscillations can be correlated across regions belonging to the same RSNs (Brookes et al., 2011). However, the phase relationship of these oscillations remains unclear. In order to reproduce a regime in which the envelopes are correlated in phase only in a certain frequency band, but where the underlying oscillations are uncorrelated, the coupling needs to be sufficiently weak so that the incoherent state is more stable than the synchronized one (as in Figure 55C, where the likelihood of the more synchronized state (right) is lower than the likelihood of the incoherent state (left)). In this case, oscillations are only periodically in phase, but envelopes are correlated over the whole time.

---

[1] An analogy for this type of stable dynamical state where one oscillator is simultaneously entrained by its individual frequency and the system's frequency is the earth in the solar system. We can imagine the earth as an oscillatory entity, which rotates about its axis at approximately one cycle per day, and additionally, performs a yearlong revolution around the sun.

As can be seen in Figure 57A, the 16-20Hz envelopes of the left and right superior parietal are highly correlated. However, for other frequency bands, this correlation decreases significantly, showing that the connectivity is frequency specific (see Figure 57B black). In fact, since the optimal frequency depends on parameters of the model, it can be tuned in order to match the frequency at which the MEG signals of these two cortical regions are optimally correlated (Figure 57B gray). As can be observed in Figure 57C, the 16-20Hz oscillations of the two regions are only phase-locked for some periods in time, during which the amplitude increases, resulting in correlated envelopes.
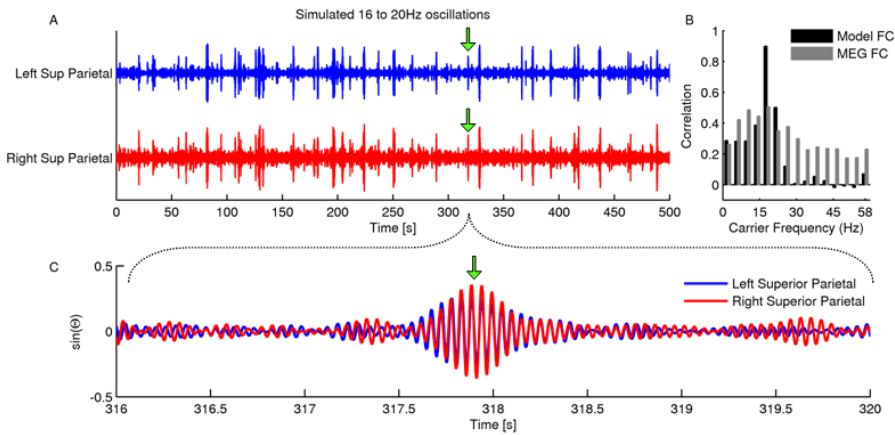
Figure 57 - Power fluctuations and phase synchronization between the left and right Parietal cortices. (A) Simulated $sin(\theta_n)$ band-pass filtered between 16 to 20Hz. **(B)** Functional connectivity of the two seeds as a function of the carrier frequency $FC_{np}(f_C)$ obtained from simulations (black) and from real MEG data (grey). The correlation peaks for a carrier frequency between 16 to 20Hz. Gamma-band oscillations (>30Hz) of these 2 seeds do not exhibit correlated power fluctuations. **(C)** Zoom into a 4 seconds period of the band-pass filtered oscillations (16-20Hz) shown in (A), at the time where a high amplitude peak occurs. When the two signals are in phase, their amplitudes increase simultaneously. Conversely, low-amplitude oscillations are not synchronized. The simulations shown here correspond the working point <τ> = 15ms and k=2.7.

IV.III.4 - Comparison with MEG functional Connectivity

The parameter choice was constricted by 3 factors: good agreement with the 15 MEG functional connectivity matrices (overall correlation >0.35), stronger functional connectivity in the power of 16-20Hz oscillations and overall low degree of synchrony (R<0.3) to avoid correlated oscillations. For the set of parameters where these constraints were satisfied, we chose

arbitrarily a mean delay of 15 ms and tuned the coupling to be sufficiently strong to engage only sporadic synchronized states, as shown in Figure 55 ($k = 2.8$). For this working point simulations were reran for 1200s.

The correlation between real and simulated functional connectivity for all possible FC pairs in the 15 frequency bands -corresponding to 60,075 pairs- was at cc=0.39 (p-value<10[-20]) (see Figure 58A). Note that this is a low-resolution (90 regions only) and simplified model (i.e. equal oscillators, no noise) for which quite low correlation values are expected, as long as they are significant. Figure 58B shows the correlation between real and predicted values for each of the 15 frequency bands (4,005 FC pairs each). The model's prediction is significant for all frequency bands (p-value < 10^{-20}). In addition, stronger functional connectivity was found in power modulations around 16-20Hz (Figure 58B), showing a similar frequency specificity as the real MEG signals shown in Figure 48C.
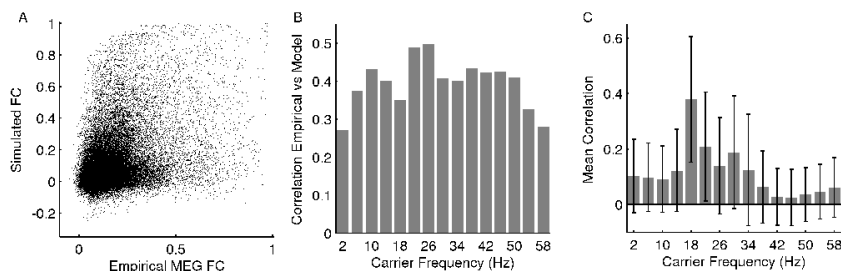
Figure 58 - Simulated functional connectivity and comparison with empirical MEG data. (A) Plot showing the empirical and simulated functional connectivity values for all possible $FC_{np}(f_C)$ values. (B) Correlation between real and predicted FC matrices obtained at each of the 15 frequency bands. (C) Functional connectivity strength – taken as the mean of all pairwise envelope correlations - as a function of the carrier frequency (centre frequency ±2Hz) from which the envelopes are extracted. The functional connectivity attains a maximum when the power of 16 to 20 Hz oscillations is considered.

On a seed by seed basis, the model was able to predict seed functional maps with correlations up to 0.9. In Figure 59 we report the connectivity (anatomical and functional, empirical and simulated) for 2 representative seeds, at 3 frequency bands: 4 to 8Hz, 16 to 20Hz and 40 to 44Hz. It can easily be observed by visual inspection, that the correlations emerging in the 16-20Hz FC (blue) can be quite surprisingly predicted by the model. Moreover, the connectivity map of the left Frontal Superior Medial area (Figure 59A) shows a different pattern of connectivity from the left Cuneus (Figure 59B). Indeed, the correlation between these 2 seeds is quite low,

which reveals that they belong to different sub-networks, each with a particular synchronization pattern.
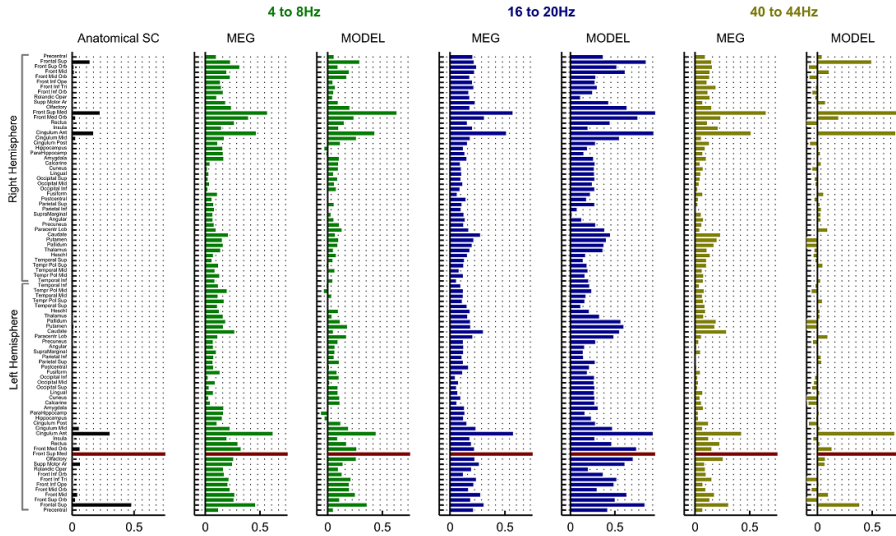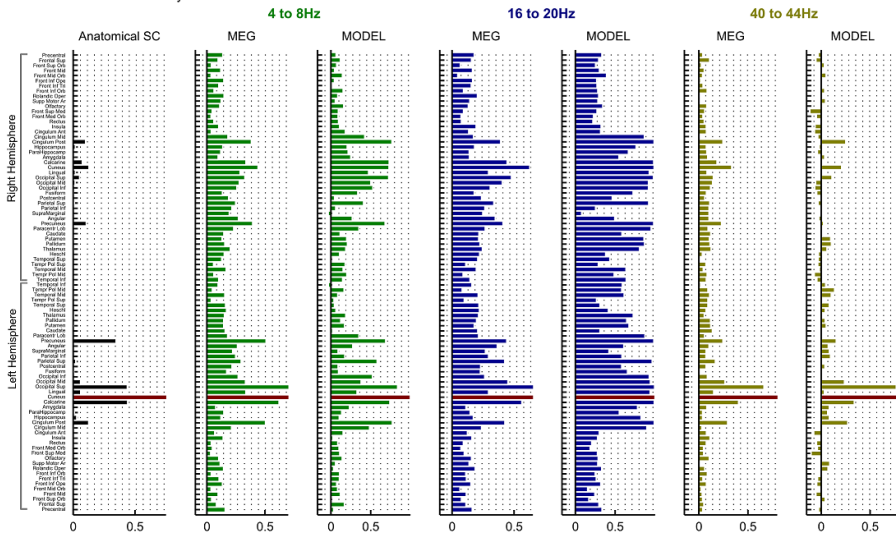
Figure 59 – Seed-based connectivity maps at multiple levels. The connectivity of the Frontal Superior Medial area (A) and the left Cuneus (B) with all other regions in the brain (rows). (Left) The black horizontal bars in the first column indicate the structural connectivity (proportional to the number of white matter tracts detected) between the seed and all other regions in the brain. All subsequent columns correspond to functional connectivity, measured as the correlation between 4-8Hz (green), 16-20Hz (blue) and 40-44Hz (brown) fluctuations. At high frequencies, the FC in the model derives mainly from directly connected pairs SC. However, especially in the 16-20Hz band, the FC increases almost globally, and nodes that are not directly connected exhibit strong correlated amplitude modulations.

120

For each seed, we observe that the FC with disconnected regions is notably increased when 16-20Hz fluctuations are considered, which shows that this reduced frequency allows for long-range functional connectivity in the brain.

To plot the envelopes at the node level, we chose 2 pairs of contra-lateral seeds: the left and right superior motor area and the left and right anterior cingulate. We filtered the simulated time-series in the 12-16Hz frequency band and observe that the power fluctuates in a correlated way across contra-lateral regions (Figure 60). Furthermore, as observed in the previous figure, w can see that there are different modes of amplitude fluctuations in the network, as indicated by the different amplitude modulations of the superior motor areas and the anterior cingulate areas.
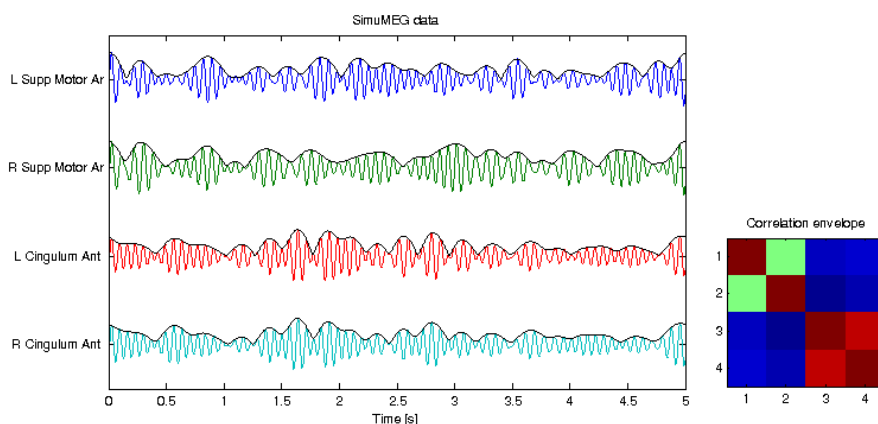
Figure 60 - BLP correlations across pairs of contra-lateral regions. (Left) Simulated time-series filtered in the 12-16Hz frequency band and corresponding power envelopes (in black). **(Right)** Correlation between envelopes showing that pairs of contra-lateral regions are correlated (i.e. left and right superior motor area and the left and right anterior cingulate), but the BLP of the superior motor areas is not correlated with the BLP at the anterior cingulate. Scale of the correlation matrix: [0 1].

In order to take into account the artifact correlations generated by the source-projection algorithm, we have compared our results with real and null MEG data. The high correlations appearing in the null MEG data (Figure 61A) were found to be independent of the carrier frequency (as shown previously in Figure 48C, red) and occurred essentially between spatially neighbour regions. In general, these neighbour regions, for being also structurally connected, exhibit some degree of *real* functional connectivity, and therefore artefact correlations cannot be simply subtracted from the real MEG signal from resting subjects. Alternatively, we evaluated the

121

performance of the model in reproducing long-range correlations appearing in real MEG data, by comparing our results with both real and null MEG data, considering only the connections between distant pairs, for which the artefact correlations were small ($FC_{nullMEG}(n, p) < 0.2$). As seen in Figure 61B and C, the model predicts real long-range functional connections that are inexistent in the null MEG data.
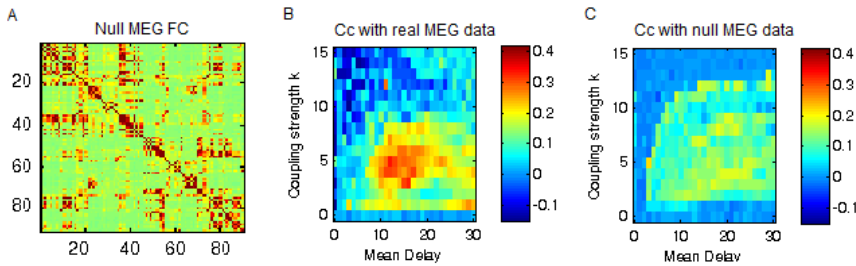
Figure 61 – Comparison with null MEG data obtained with an empty scanner. (A) FC matrix of simulated null MEG data. Due to intrinsic limitations of the source-projection algorithm, neighbour regions exhibit strong correlated activity. Due to the strong local connectivity of the brain connectome, most of these short-range correlations are also present in real and simulated MEG data. However, to test if the model predicts the long-range correlations existing in real MEG signals (independent from artefacts), we compare our model results with real (B) and null (C) MEG data by considering only the connections between distant pairs, for which the artefact correlations were smaller than cc=0.2.

IV.IV – Discussion

In this chapter, we explored if our simple model of weakly coupled oscillators could predict the spatiotemporal patterns of band-limited power fluctuations observed resting-state MEG. In general, our results reproduce important features of resting-state MEG activity, both in the temporal and spatial domains. On one side, the simulated neural activity exhibits multistability and band-limited power fluctuations emerge, in the same way as observed experimentally. In particular, using identical 40Hz oscillators, we observe strong fluctuations in the power in the 10-20Hz frequency range. Furthermore, the spatial patterns drawn by correlations between BLP fluctuations are significantly similar to the ones found in resting-state MEG data across subjects.

These results go in agreement with previous MEG studies that found resting-state functional connectivity, similar to BOLD signal correlations, using the band-limited power fluctuations of fast oscillations (de Pasquale et al., 2010;

Brookes et al., 2011). In particular, long-range FC was found to be related to simultaneous increases in the power of alpha- and beta-band oscillations between distant areas in the brain. However, by the simple empirical analysis of electrophysiological data it has been difficult to uncover the physiological mechanisms leading to this temporary frequency synchronization (or coherence) between brain areas. Therefore, the employment of brain-inspired computational models, like the one proposed here, can help to explore origin of these periodic coherent states.

Our simulation results suggest that the binding between cortical areas, expressed through temporary coherence, emerges due to metastable synchronized states. In other words, when the coupling is only sufficiently strong, some groups of regions (or clusters) tend to synchronize together. When this happens, all nodes involved are engaged at a reduced collective frequency and their power in the corresponding band increases simultaneously. However, due to competitive interactions with the rest of the network, this coherent state is unstable, leading to the spontaneous disruption of synchrony after some time. When synchronization fades away, all nodes in the cluster disengage from the collective frequency, and therefore the BLP around this frequency decreases simultaneously for all nodes in the cluster. Since the engagement and disengagement of cluster synchronization occurs periodically, this leads to correlated fluctuations in the BLP around the cluster frequency for all nodes in belonging to the same cluster. Furthermore, due to the complex connectivity structure of the brain, the same node may be engaged in an alternated way in different clusters. Due to the heterogeneity of couplings and delays, the collective frequency of each cluster is different, since it depends directly on the number of nodes and the mean delay of the cluster, as predicted by Niebur et al. (1991)[1]. Although a similar behavior had been observed in a theoretical study of weakly coupled oscillators with uniform time delays (Kim et al., 1997), this is the first time this type of dynamics is reported with brain-inspired connectivity and realistic delays.

Despite its simplicity, the Kuramoto model has proven to be a helpful tool to study synchronization phenomena in neural systems (Breakspear et al.,

---

[1] See section *II.III – Time delays in the Kuramoto model.*

2010). One of the main assumptions made when applying the Kuramoto model to large-scale brain dynamics is that individual cortical regions exhibit self-sustained oscillations in the gamma-frequency band. This assumption is supported by theoretical and experimental studies, who found that ensembles of densely connected excitatory and inhibitory neurons are capable of engaging in a limit-cycle with a natural frequency in the gamma-range (Brunel and Wang, 2003; Bartos et al., 2007). Furthermore, electrophysiological recordings suggest the existence of a distributed system of gamma-band generators in the brain (Basar-Eroglu et al., 1996), and they have been suggested as universal functional building blocks in the brain. According to our model, when gamma-band oscillators are coupled in the macroscopic space-time structure of the brain connectome and there is no external (or even internal/mental) stimulation, strong frequency peaks appear at lower frequencies. These results suggest that the strong rhythms appearing in the brain below the gamma-frequency range originate from distributed network interactions in contrast with theories that suggest the existence of local alpha- or beta-band generators at the neuronal level. In addition, these results do not contradict the role of the cortico-thalamic loop in generating alpha rhythms (which is actually included in the AAL connectome). Instead, we suggest that several loops (or sub-networks) coexist in the brain, and their frequency is tuned by their length (or mean delay*number of nodes).

According to our model results, during rest, different sub-networks compete to synchronize at reduced collective frequencies. Interpreting the results from the perspective of information processing in the brain, we can imagine that under stimulation, the synchronization of one sub-network is enhanced, and the corresponding sub-units become phase locked (coherent). This goes in agreement with current theories of long-range communication through coherence in the brain (Fries, 2005).

Our results can be related to a recent modelling study by Freyer et al. (2011), who proposed a mechanism for alpha-power modulations during rest using a biophysical model with simpler cortico-thalamic connectivity and time-delayed interactions. Although our model is more abstract at the node level, we believe some similarities can be detected, since there was a significant delay between the cortex and the thalamus, and intermittent

increases in alpha power (10Hz) could be related to sporadic synchrony between the thalamus and the cortical layer.

We would like to note the fact that, in the current implementation of the model, all cortical regions have identical natural frequencies at 40Hz. However, gamma band activity in the brain has a broader spectrum (35-100Hz). Based on theoretical studies with frequency dispersion (but in simpler networks though) and in our results presented in section *II.IV – Kuramoto dynamics with brain-inspired connectivity* (Figure 32), we believe that the same dynamical behavior would emerge, but with different (and possibly more) collective frequencies emerging. Furthermore, due to the model's sensitivity to delays, using fiber lengths instead of the Euclidean distances between centers of gravity could improve the model's prediction of real data in the frequency and temporal domains.

Finally, we provide testable predictions for future experimental studies. Based on our results, we expect that two regions exhibiting correlated BLPs in resting-state MEG data should be phase-locked during periods of increased power in the alpha- and/or beta- bands. These predictions suggest new analytical approaches for resting-state MEG studies. This theoretical scenario brings a new light into the mechanisms leading to functional connectivity between distant regions.

'Men ought to know that from the brain and from the brain only,
arise our pleasures, joy, laughter and jests,
as well as our sorrows, pains, grieves, and tears.'
Hippocrates

V.I – Introduction

Growing evidence from experimental and theoretical studies indicates that the spatial patterns observed in brain activity during rest are shaped by the underlying anatomical structure (Skudlarski et al., 2008, Bullmore and Sporns, 2009, Jirsa et al., 2010). The availability of whole-brain maps of anatomical connections (Kötter, 2004, Sporns et al., 2005, Hagmann et al., 2008) together with computational models of the brain's large-scale neural dynamics have shed light on the relationship between anatomical and functional connectivity (Honey et al., 2007, Ghosh et al., 2008, Deco et al., 2009, Honey et al., 2009, Cabral et al., 2011). Importantly, they can be used to predict the effects of structural lesions on brain dynamics (Honey and Sporns, 2008, Alstott et al., 2009), which is beyond reach on the experimental side, making models a unique tool for the comprehension of brain diseases resulting from structural alterations.

In this chapter, we focus on the effects of brain-wide structural disconnections on the topological properties of resting-state functional networks. Both anatomical and functional networks have been widely studied by means of graph theory (Bullmore and Sporns, 2009, Rubinov and Sporns, 2010). The application of graph theoretical measures to functional networks derived from BOLD fMRI signals registered during rest has shown clinical relevance. Indeed, this procedure has revealed significant alterations

in the resting-state patterns of patients with neuropathologies such as schizophrenia (Liu et al., 2008, Lynall et al., 2010, Bassett et al., 2012) and Alzheimer's coupling strength disease (Supekar et al., 2008b), among others.

To simulate disconnection effects, we model the ongoing brain activity and manipulate the coupling weights between cortical regions. Brain activity was simulated using two different models at the local level: the Kuramoto model with time delays, where nodes exhibit intrinsic oscillatory behaviour in the gamma-band[1], and a simplified model of neural dynamics where nodes are in a stable asynchronous state derived by Hugues et al. (in preparation)[2]. In both models, the coupling weights scale the long-distance excitatory strength between brain areas encompassing simultaneously the number of white matter fibre tracts detected using DTI/DSI tractography and the excitatory synaptic weights. On a first stage, we simulate a widespread disconnection by decreasing the coupling at a global level. Then, we explore the effects of local disconnections by removing links in a random fashion. From the simulated ongoing brain activity, we estimated the hemodynamic response and inferred functional connectivity by computing the Pearson correlation between BOLD signals. Subsequently, simulated functional networks were characterized using graph theory (for a reliable comparison with an experimental work we followed the methodology from Lynall et al. (2010)). We started by studying how the topological organization of simulated functional networks depends on the global coupling strength. We found that, for a range of global coupling levels, the simulated functional networks have graph properties that correspond to the ones reported in healthy people (Lynall et al., 2010). By decreasing the coupling strength, the resulting functional networks display significant topological alterations and, at an extreme degree of disconnection, exhibit random network properties.

---

[1] The results presented in this chapter using the Kuramoto model are published in: Cabral J, Kringelbach ML, Deco G (2012b) *Functional graph alterations in schizophrenia: a result from a global anatomical decoupling?* Pharmacopsychiatry *In press.*

[2] The results using the model from Hugues et al. (in prep.) are published in: Cabral J, Hugues E, Kringelbach ML, Deco G (2012a) Modeling disconnection effects on resting-state functional connectivity. NeuroImage (In press).

As a disease long-time hypothesized to be related with disconnection effects, we have compared our results with experimental measures from schizophrenia patients (Lynall et al., 2010, Bassett et al., 2012). We found that the reorganization of resting-state functional networks observed between healthy volunteers and people with schizophrenia could be explained by a weak (~5%) structural disconnection. Overall, these results support the hypothesis that the functional network alterations underlying schizophrenia are caused by a disconnection (encompassing putative local/global axonal/synaptic mechanisms), in agreement with current theories of schizophrenia (Wernicke, 1906, Friston and Frith, 1995, Bullmore et al., 1997, Winterer and Weinberger, 2004, Stephan et al., 2006, Skudlarski et al., 2010, Zalesky et al., 2011). Taken beyond the schizophrenia disorder, our results could provide a new light towards the understanding of altered resting-state functional connectivity occurring in other mental illnesses characterized by disconnection.

V.II – Methods

V.II.1 - Anatomical networks

In order to be general and since the results can be influenced by the parcellation scheme (Zalesky et al., 2010, Bassett et al., 2011), in this work we used two distinct structural networks (see Figure 62), one with *N=90* brain regions defined using the AAL template (Tzourio-Mazoyer et al. (Tzourio-Mazoyer et al., 2002), and another with *N=66* brain regions derived by Hagmann and colleagues (2007). In both networks, the connectivity strength C_{np} between regions *n* and *p* was assumed to be proportional to the number of fibres incoming to region n and the size of that region (as in Cabral et al. (2011)).

The anatomical brain network with 90 regions was constructed using diffusion tensor imaging (DTI) from the brains of 21 healthy participants (see *A.3 – DTI data collection and building of anatomical connectomes* and Cabral et al. (2012b) for details). Following the methodology from Gong et al. (2009b), for each subject a 90x90 weighted network was constructed. Networks were then averaged across subjects resulting in a reliable representation of the anatomical organization of cerebral cortex. For this network, the distance D_{np} between a pair of regions was taken as the

Euclidean distance between the corresponding centres of gravity in the AAL template.

The network with 66 regions - previously used in resting-state computational models in Honey et al. (2009) and Cabral et al. (2011) - was derived from diffusion spectrum imaging (DSI) by Hagmann and colleagues (2007) according to the Freesurfer parcellation scheme (surfer.nmr.mgh.harvard.edu (Desikan et al., 2006)) and averaged over 5 healthy subjects. In this case, the distance D_{np} between two regions was given as the average length of the fibres detected connecting these two regions.

The anatomical connectivity (AC) in both parcellation schemes, AC_{90} and AC_{66}, is given by the matrices C and D (see Figure 62 B-C).
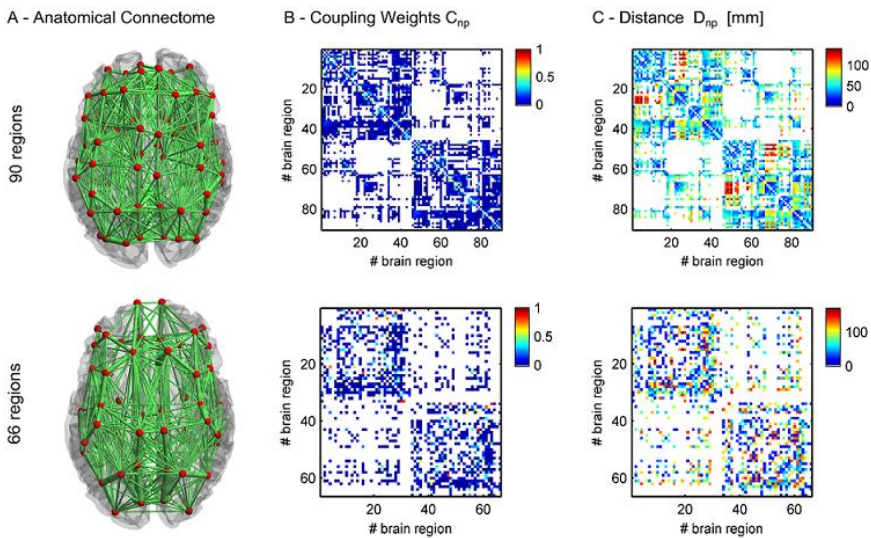
Figure 62 - Large-scale healthy anatomical connectomes used in the model. Top: 90 brain areas (including subcortical regions). Bottom: 66 cortical regions (Hagmann et al. (2007)). (**A**) Spatial representation of the anatomical connectome. Red spheres represent individual regions (or nodes in the network) and links are proportional to the coupling strength given in (B). (**B**) Connections weights are proportional to the number of fibres detected. (**C**) Distance between regions (in mm), given as (top) the Euclidean distance between centres of gravity and (bottom) the average length of the fibres connecting a pair of regions. The list of brain regions and corresponding indexes is reported in A.1 Table 4 and Table 5.

V.II.2 - Neural Dynamics Model

Spontaneous brain activity was simulated using two different neural-mass models. On a first approach, the dynamics of each node, representing a brain region, was modelled in a reduced way as a phase oscillator θ_n with homogeneous intrinsic frequency $\omega_n = \omega_0, \forall n \in N$ in the gamma range (here $\omega_0 = 40Hz$). We used the Kuramoto model with time delays (here $\langle \tau \rangle = 20$ms) to simulate network interactions (previously described and used in chapters II to IV), with the AC_{90} and studied the effects of a widespread disconnection by manipulating the parameter k in the following equation:

Oscillatory model:

$$\frac{\partial \theta_n}{\partial t} = \omega_n + k \sum_{p=1}^{N} C_{np} \sin\left(\theta_p\left(t - \tau_{np}\right) - \theta_n(t)\right)$$

In order to allow for an analytical prediction of the effects of a structural disconnection, we used as well a simplified model of neural dynamics where the neural-mass is assumed to be in a stable asynchronous state. In this case, fluctuations occur due to correlated noise perturbations (see *I.III.1.d - A simplified model of neural dynamics* for details and Hugues et al. (in preparation)). The firing rate of each region obeys to the following equation:

Non-oscillatory model:

$$\tau_0 \frac{dr_n}{dt} = -r_n(t) + \frac{k}{c_1} \sum_{p=1}^{N} C_{np} r_p\left(t - \tau_{np}\right) + \sigma \eta_n(t).$$

The coupling k is normalized by the first eigenvalue c_1 of the coupling matrix C, such that the dynamics for $k/c_1 < 1$ is in a stable asynchronous state (at least for the case of null delays). With this model, we used both the AC_{90} and the AC_{66} and studied the effects of both global and local disconnections on the macroscopic properties of functional networks, by manipulating either the global coupling k or the coupling matrix C_{np}.

Equations were numerically integrated using the Euler method with a time-step of 0.1 ms. For every set of parameters considered, we simulated the system for 1200 s (20 min). All calculations were performed using Matlab®.

V.II.3 - Simulating Disconnection

In the model, local neural networks are connected with each other according to the weight matrix K, with $K_{np} = kC_{np}$. In general, disconnection implies that some or all of these weights decrease in comparison to the healthy case where $k = k^h$, meaning that the disconnected weight matrix K^d has coefficients $K_{np}^d \leq K_{np}^h$.

As a first implementation of disconnection, all weights decrease in equal proportion, which is done by decreasing the global coupling strength k, and $K^d = k^d C$, where $k^d < k^h$).

In a second implementation (and only with the non-oscillatory model), we have chosen to remove links randomly from the original structural matrix AC_{90}, a method called random pruning. To simulate the progression of a disconnection disease, we generated a sequence of pruned matrices $C_1^p, \ldots, C_m^p, \ldots, C_M^p$ from the original one, where at each step a fixed number of links was removed randomly. The corresponding weight matrix writes $K_m^p = kC_m^p$, where the original prefactor k is kept unchanged. Choosing to remove 1% of the total possible links of the AAL matrix (that is $0.01(90)^2 = 81$ links), which has about 39% of the possible links, a sequence of M=39 pruned matrices was generated.

V.II.4 - Simulated BOLD signal and Functional Connectivity

The BOLD signal for each region was estimated from the neural population activity using the Balloon-Windkessel hemodynamic model proposed by Friston and colleagues (Friston et al., 2000, 2003)[1]. We focused our investigation on low frequency (0.06–0.125Hz) fluctuations of the BOLD signal, which have previously been shown to be particularly sensitive to disease-related alterations in schizophrenia (Lynall et al., 2010, Bassett et al., 2012). Simulated BOLD signals were band-pass filtered in that frequency

---

[1] See section *I.III.2 - Transforming neuronal activity into BOLD signal* for details.

window (0.06Hz-0.125Hz) and finally down-sampled at 2 s to have the same temporal resolution as the MR scanner.

To evaluate functional connectivity (FC) we computed the Pearson correlation of band-passed simulated BOLD signals in different brain areas. This measure is widely employed to derive resting-state functional networks from fMRI signals (Biswal et al., 1995, Fox and Raichle, 2007) and provides a simple characterization of temporal interactions between brain regions. Moreover, comparing with measures from information theory (more precisely the mutual information) which unravels all types of nonlinear interactions, it has recently been shown that correlation captures most of the interaction, and is a very good tool to study the functional connectivity graphs (Hartman et al., 2011, Hlinka et al., 2011). The resulting correlation matrix -or FC matrix- can be then studied using graph theory (Achard et al., 2006, Lynall et al., 2010, Rubinov and Sporns, 2010, Bassett et al., 2012). Note that, only to compare the simulated FC_{66} matrix with the empirical one, the global signal was regressed out (see section *V.II.5 - Empirical Functional Connectivity).*

To obtain a measure of global integration (*GI*), we applied principal component (PC) analysis to the simulated BOLD covariance matrix and calculated the ratio of the first eigenvalue λ_1 to the sum of all the others (Tononi et al., 1994, Friston, 1996):

$$GI = \lambda_1 \Big/ \sum_{j=2}^{N} \lambda_j \,.$$

V.II.5 - Empirical Functional Connectivity

The model of weakly coupled oscillators has already been shown in previous chapters to reproduce with good agreement healthy resting-state functional connectivity. However, the non-oscillatory model needs to be validated. To do so, we evaluated the model's performance in reproducing healthy resting-state functional connectivity by comparing the simulated functional networks with an empirically derived FC matrix previously used to validate the models from Honey et al. (2009) and Cabral et al. (2011). This empirical FC matrix was constructed in the parcellation scheme from Hagmann et al.

(2007) (66 regions) from the resting brain activity of 5 healthy subjects with eyes closed -the same subjects from which the corresponding AC_{66} was obtained. It consists on the correlation matrix of the mean BOLD signal in each of the 66 regions. Before computing the correlation, the BOLD signal was pre-processed for artefact removal including global signal regression (see Honey et al. (2009) for details). Simulated and empirical FC_{66} matrices were compared using Pearson correlation.

V.II.6 - Building graphs from functional networks

The set of synthetic functional networks generated with the use of the computational model was characterized using graph theory. To evaluate functional networks by means of graph theory, the FC matrix needs be binarized into an adjacency matrix (A_{ij}) where correlations above a certain threshold are set to 1 and 0 otherwise. The definition of thresholds depends on either one wishes to create equi-sparse graphs (ensuring a fixed percentage of edges) or equi-threshold graphs (ensuring a minimum correlation value to define an edge, resulting in a variable number of edges) (Bassett et al., 2012). Since the employed graph-theoretical measures are known to depend on the graph's connection density (Bassett et al., 2008, van Wijk et al., 2010, Bassett et al., 2012) all our measures refer to equi-sparse graphs defined over a fixed range of connection densities to overcome this dependency. In more detail, from each FC matrix, 14 graphs were constructed with connection densities ranging from 37 to 50% (1% increment) in the same way as in Lynall and colleagues (2010). Moreover, our networks have 90 and 66 nodes, whereas the experimental results refer to only 72 nodes -a subgroup of the 90 regions defined in the AAL scheme-. To overcome the complex dependency of the measures on the number of nodes (Fornito et al., 2010, van Wijk et al., 2010) and on the parcellation scheme (Wang et al. 2009a), we have selected the exact same 72 nodes from the AAL template when analysing the 90x90 functional networks obtained from simulations and discarded the remaining 18 nodes (see *Appendix A.1 Table 5* for the list of regions discarded). We also report the results using the AC_{66} to investigate the impact of a different number of nodes in the results.

The various graph measures were estimated for graphs obtained at densities in the range 37-50%, with the exception only for degree distribution parameters, which were only estimated for graphs with 37% density. Measures were averaged across the cost range, providing global measures of the topology of each FC matrix. In addition, the same thresholding technique was applied to 100 random graphs with the same range of connection costs to compare with the simulation results.

Finally, the coupling matrices C_{90} of the 21 healthy subjects were characterized using graph theory, and binary graphs were obtained by thresholding the coupling matrix as $G_{90} = C_{90} > 0$.

V.II.7 - Graph theoretical measures

The graph theoretical measures employed were evaluated using the Brain Connectivity Toolbox (Rubinov and Sporns, 2010) and the MatlabBGL Toolbox (Gleich, 2006).

For all simulated FC matrices, we first estimated well-known graph measures such as efficiency, clustering and small-worldness. The efficiency is the inverse of the mean shortest path length, i.e. the average number of links (paths) necessary to connect any pair of regions (Latora and Marchiori, 2001). The average clustering indicates the probability of two regions connected to a third one being also connected to each other, forming triangles. Small-worldness depends directly on the two previous measures and evaluates if high efficiency coexists with high clustering, when compared to an equivalent random graph (Watts and Strogatz, 1998, Humphries et al., 2006)[1].

We also estimated the hierarchy coefficient β, which is taken as the (positive) exponent of the power-law relationship between the clustering C_i and the degree d_i of the nodes in the network such that $C \sim d^{-\beta}$ (Ravasz and Barabasi, 2003, Bassett et al., 2008). β was estimated using the least-squares nonlinear fitting function from Matlab®. The higher the hierarchy coefficient, the more network hubs -defined so for having a large number of

---

[1] See section *I.II.3 – Characterizing complex networks using graph theory* for more details.

connections- have low clustering, meaning that they are more connected to nodes poorly connected to each other.

In addition, we calculated robustness measures, which indicate the graph's resilience to the removal of nodes. When a node is removed either randomly (random attack) or in descending degree (targeted attack), the graph can fragment into independent sub-graphs. To estimate the robustness of a graph, each time a node was removed, we recalculated the size of the largest connected component, s. Plotting the size s versus the number of nodes removed, $s(n)$, the robustness parameter is defined as the area under this curve (Achard et al., 2006). Networks that are more robust retain a larger connected component even when a large proportion of nodes have been eliminated. To take into account the size of the network, we normalized this value by $N(N-1)/2$, so that the maximum robustness is 1.

Finally, we evaluated the degree distribution of graphs obtained at 37% connection density. This distribution gives the probability of node degrees (Boccaletti et al., 2006), where the node degree is simply defined as the number of edges connecting a node. For each simulation, we determined the variance of the degree distribution and, in addition, the degree distribution was fitted to a gamma distribution $P(d) \propto d^{\alpha-1} e^{(-d/d_c)}$, which was found to be the best fit for experimental results (Bassett et al., 2008, Lynall et al., 2010). The power exponent, α, and the lower exponential degree cut-off, d_c, were estimated using the least-squares nonlinear fitting function from Matlab®.

V.III - Results

V.III.1 – Topological properties of the anatomical network

In this subsection, we analyzed the topological properties of the anatomical connectome AC_{90} (as in Cabral et al. (2012b)). The 21 anatomical networks obtained from healthy participants 21 healthy (11 males and 10 females, age: 22–45 years) have an average connection density of 32%. Each connection (link) is composed by around 208 fibres. However, between some pairs of brain regions, up to 3000 fibres have been detected (see the histogram in Figure 63C). From the degree distribution shown in Figure 63D,

we can see that each region is connected to an average of 25 other regions and this distribution is quite homogeneous (bell-shaped).
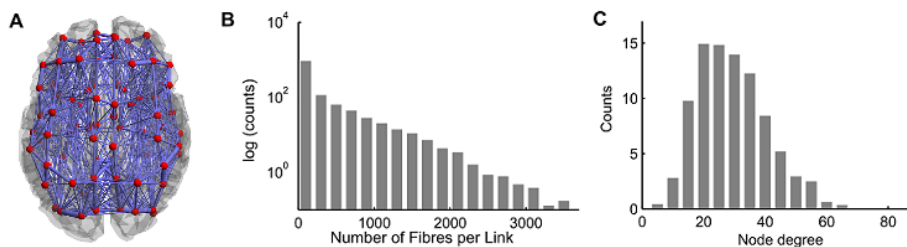
Figure 63 – Properties of the anatomical brain network (90 regions). (**A**) Representation of the network in the AAL parcellation (**B**) Histogram of the number of fibres per pairwise connection and (**C**) node degree histogram both averaged across participants.

In addition, the anatomic networks were characterized by means of graph theory (See Table 2). Anatomic networks were found to be "small-world" (small-worldness> 1), which means that networks are not only efficient (short average path length) but also highly clustered when compared with an equivalent random graph. In addition, the networks have a positive hierarchy, meaning that high degree nodes –or hubs- are the less clustered and vice versa. Furthermore, networks were found to be robust to either random or targeted attack ($r \approx 1$), maintaining strong connectedness as nodes are removed either randomly or by descending node degree.

Table 2 – Properties of the anatomical network (mean±1 standard deviation across 21 subjects).

Connection density (%)	: 32.7 ± 4.6	**Small-worldness**	: 1.96 ± 0.20
# Fibres/connection	: 208 ± 17	**Hierarchy**	: 0.139 ± 0.016
Global efficiency	: 0.65± 0.03	**Robustness (random)**	: 0.993 ± 0.008
Average clustering	: 0.64 ± 0.02	**Robustness (targeted)**	: 0.9244 ± 0.02

V.III.2 - Simulated functional connectivity

In general, we have found that the properties of functional networks generated with both oscillatory and non-oscillatory models depend largely on the underlying structural coupling. First, using intact healthy ACs we studied how parameters such as correlation strength, global integration and similarity with the underlying AC vary as a function of the global coupling

strength k for both models. We remind that k uniformly scales all the connection weights C_{np} between brain regions defined by the neuro-anatomical network.

As we have seen in previous chapters, the dynamics of Kuramoto oscillators varies as a function of the coupling strength. As observed in Figure 64A, for weak couplings, the phases are almost completely desynchronized, and the order parameter is close to zero. As the coupling increases, regions become more and more synchronized with each other. In the region between incoherence and synchrony $(2 < k < 10)$, the metastability index is increased (Figure 64B), indicating that the network is in a non-stationary regime, where the order parameter fluctuates in time due to meta-stable synchronized clusters.
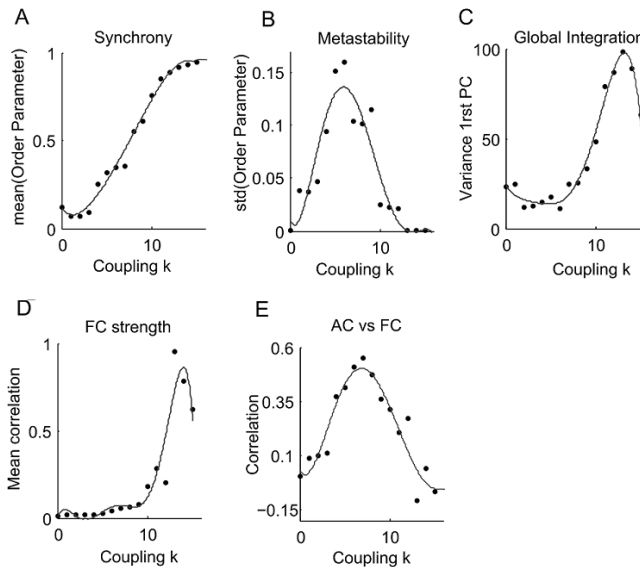
Figure 64 - Dynamics of coupled oscillators as a function of the coupling strength k. (A) The mean synchrony degree varies from desynchrony (<R>≈0) to full synchrony (<R>≈1). In (B) the standard deviation of the order parameter indicates the metastability of the system is higher in the intermediate region between desynchrony and synchrony. (C) The variance of the first PC also increases with the coupling strength, meaning that the BOLD signals become more globally integrated. (D) The functional connectivity strength, measured as the average correlation between simulated BOLD signals, increases together with the global integration. (E) The correlation between the anatomical and the functional connectivity is increased in the metastability region.

As described in Cabral et al. (2011) and in the previous chapters II-IV, the metastability is important in oscillators' models to generate low frequency

fluctuations in brain activity. However, above a certain coupling value (i.e. $k > 13$) the neuronal oscillations become too synchronized and the metastability index is brought down to zero. In that case, slow fluctuations disappear. This explains why, above this critical coupling value, equi-sparse functional networks become less globally integrated and less globally correlated (Figure 64C-D). Furthermore, we report the correlation between anatomical connectivity (AC) and simulated BOLD functional connectivity (FC). As expected, it is in the region of metastability that the functional networks are shaped by the underlying anatomical structure (Figure 64E).

Regarding the non-oscillatory model (Figure 65), we report the properties of functional networks obtained with the AC_{66} and the AC_{90}, i.e. FC_{66} and FC_{90}. Furthermore, we have removed from the FC_{90} the 18 regions discarded in Lynall et al. (2011)[1] resulting in a functional network with 72 regions, FC_{72}. For low couplings ($k < 0.5$) we found that the simulated BOLD signals are weakly correlated (Figure 65A) because there is no dominant mode in the neural activity, as seen by the global integration measure (Figure 65B).
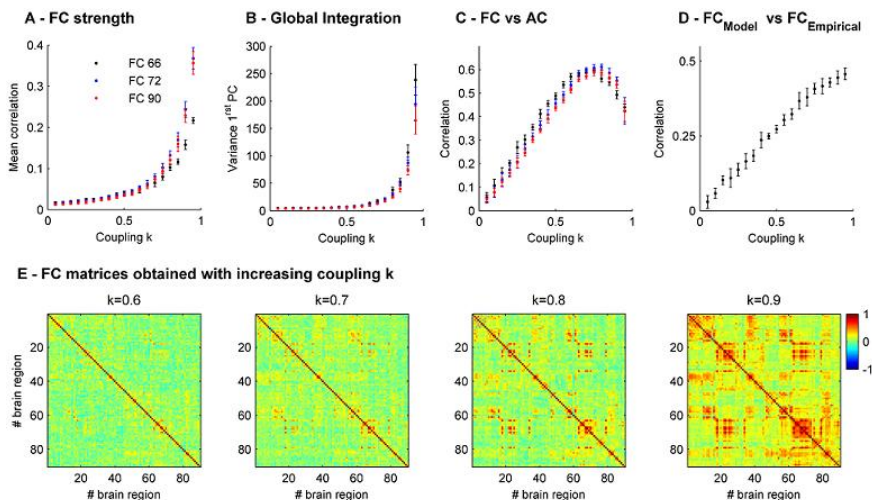
Figure 65 - Dependency of functional connectivity (FC) on k simulated with the non-oscillatory model. (**A**) Mean correlation of simulated BOLD signals. (**B**) Global integration of the BOLD covariance matrix. (**C**) Correlation between the FC and the underlying AC. In plots A-C we report the values for FC_{66}, FC_{72} and FC_{90}. (**D**) Correlation between empirical and simulated FC_{66}. The values reported are averaged over 10 runs of 1200s (error bars = ±1 standard deviation). (**E**) Example of simulated FC matrices, obtained with increasing coupling strengths k.

---

[1] see *Appendix A.1 Table 5* for the list of regions discarded.

As the coupling strength increases, and due to the progressive emergence of a dominant mode, positive correlations build up and the FC matrix becomes increasingly shaped by the underlying SC (Figure 65C). Above a sufficient coupling, more and more regions that are not structurally connected become also correlated: the correlation with the empirical FC keeps increasing (Figure 65D), while the correlation between SC and FC decreases (Figure 65C). However, in the proximity of the critical coupling the dynamics becomes too globally integrated ($\lim_{k_c \to 1}(GI) = \infty$)(see Figure 65B). Note that the properties of simulated FC obtained with both ACs are found to depend similarly on the coupling strength parameter. The variance in the results (error bars) is due to the additive noise in the non-oscillatory model and due to the finite duration of the simulated time series (1200 s here).

V.III.3 - Graph properties of simulated functional connectivity

In this section, we analyze the simulated functional networks using a number of measures from graph theory. As we will show in the following, the topological organization of synthetic functional networks appears to vary with the coupling strength in a continuous fashion, independently of the model or the AC considered.

In Figure 66, we report the results obtained with the oscillatory model. We observe that some measures from graph theory, namely the average clustering, the small-worldness and the variance of the degree distribution were found to decrease as the coupling weights became weaker, while others such as the hierarchy, the global efficiency and the robustness increased as the regions became more disconnected. These alterations mean that, when the connectivity between brain regions is deficient, the emergent patterns of functional connectivity tend to be slightly randomized, with less clustered structure and fewer low- and high-degree nodes. This happens because, when the coupling is weak, the spontaneous dynamics tends towards an incoherent regime where the phases of all oscillators are out of synchrony. Consequently, the BOLD fluctuations are uncorrelated and the resulting functional networks share properties of random networks.
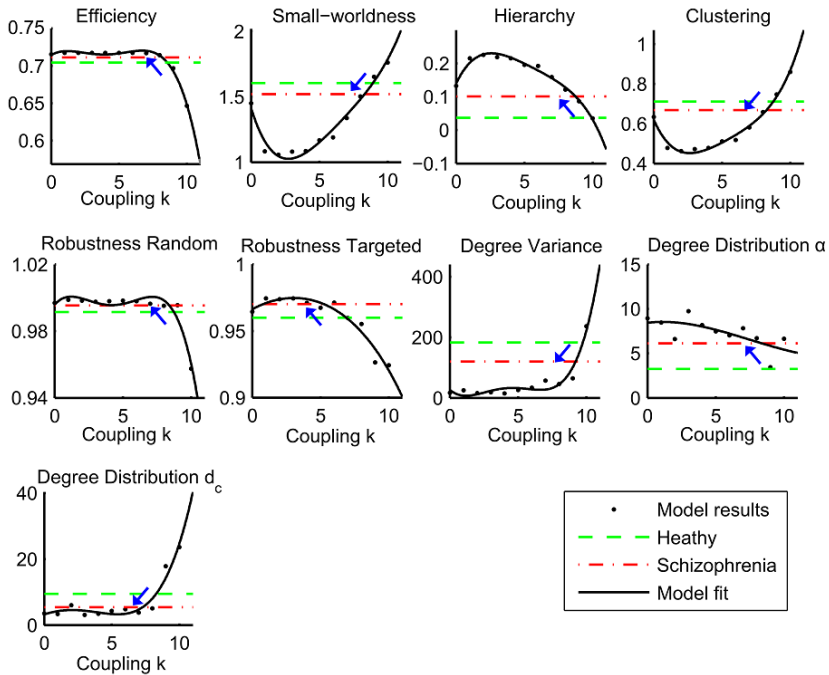
Figure 66 – Graph properties of functional networks obtained with the Kuramoto model. Graph-theoretical measures for $0 < k < 10$ (above that value networks become too correlated, with consequent loss of realism). The measures vary as a function of k: solid lines show the fit to fourth order polynomial functions. For reference, the measures reported experimentally for resting-state functional graphs from healthy controls and schizophrenia patients (Lynall et al., 2011) are indicated as green dashed lines and red dot-dashed lines, correspondingly. The blue arrows indicate the decrease or increase of the respective graph-theoretical measurements as the coupling is decreased, emulating the passage from health to schizophrenia.

As the coupling weights are increased in the model, the organizational properties of the resulting synthetic networks evolve towards values characteristic of functional networks from healthy brains (reported as green dashed horizontal lines). The simulated graphs exhibit higher small-worldness, the clustering coefficient increases and the degree distribution is wider with higher probability of high degree hubs. Interestingly, the organizational properties of functional graphs from people with schizophrenia (red dashed horizontal lines) are generally found in-between graphs from healthy people and random graphs, suggesting a subtle randomization of functional networks in schizophrenia.

Regarding the non-oscillatory model, similar qualitative results were obtained. As can be observed in Figure 67, when the coupling value is too small ($k \leq 0.5$), the small-world index is close to 1 (Figure 67B), the average clustering coefficient is low (Figure 67D) and the degree distribution is narrow (Figure 67I) and bell-shaped (Figure 67G-H and J (left)), typical of a random graph. Because of having less high-degree hubs, random graphs are more robust to attacks, because these can maintain connectedness even after the removal of a large number of nodes (Figure 67E-F). On the other hand, a higher hierarchy in random graphs indicates that nodes with higher clustering are the ones with lesser degree (Figure 67C). As the coupling increases from 0.5 to 0.95 the functional networks reorganize and most of the metrics evolve towards values characteristic of healthy human FC (reported in blue) (Lynall et al., 2010). Namely the clustering coefficient and the small-world index increase, the hierarchy decreases and the degree distribution becomes wider (Figure 67I and J(right)).
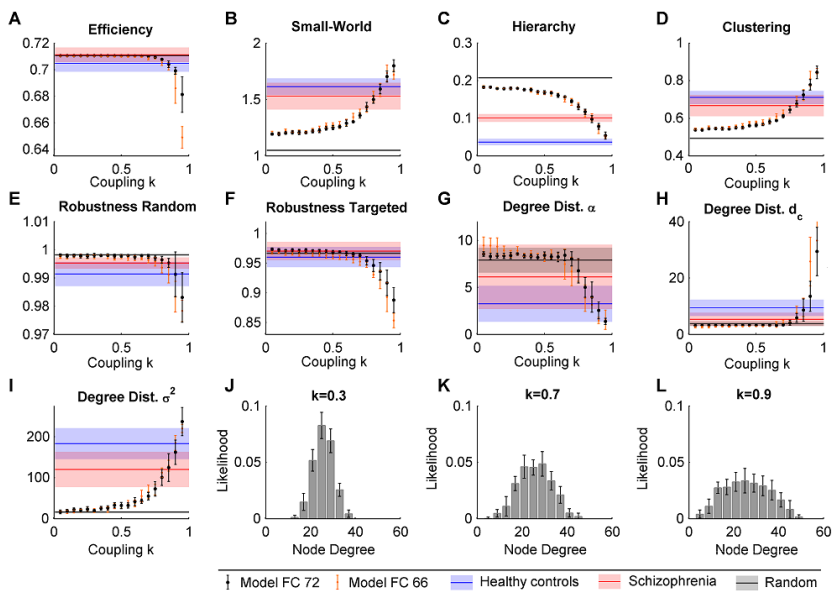
Figure 67 – Graph properties of functional networks obtained with the non-oscillatory model. (**A-I**) Topological properties of functional networks obtained with increasing k. For comparison we indicate the values reported for healthy controls (blue) and schizophrenia patients (red) in the work from Lynall et al. (2010). Shaded bands indicate the confidence interval of 1 STD. In addition, measures of equivalent random networks are reported (grey). As the coupling is decreased (from right to left), simulated functional networks become randomized. (**J**) Example of degree distributions obtained with increasing coupling k. Error bars indicate the confidence interval of 1STD across 10 simulation runs.

In addition, functional networks become less robust to the removal of nodes, especially high-degree ones (Figure 67E-F). Remarkably, we find that healthy human FC graph properties can be approximately obtained when the coupling is in the range $0.85 < k < 0.9$.

V.III.4 - Effects of localized disconnections

Using only the non-oscillatory model, we considered an additional disconnection scheme where links were randomly removed from the anatomical network while the absolute coupling strength k remained fixed (see *Methods V.II.3 - Simulating Disconnection*). We started using a fixed coupling value of $k^h/c_1 = 0.87$, with which we obtained approximate healthy human FC graph properties.
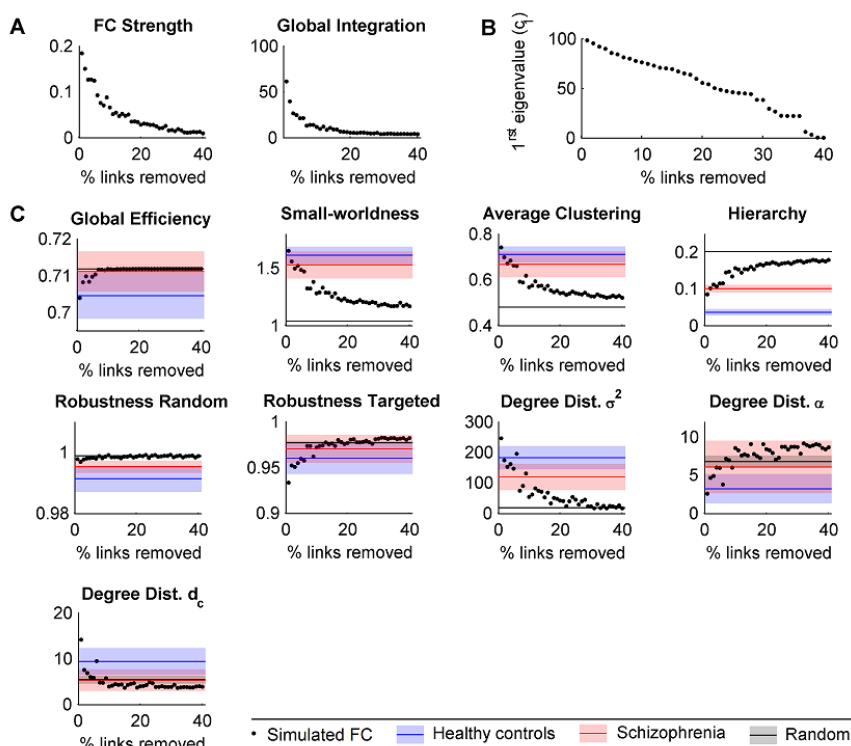
Figure 68 - Effects of pruning links in the anatomical connectivity (AC) on the properties of emergent FC obtained with fixed coupling (k=0.87). (A) The mean correlation and the global integration of BOLD signals decrease as links are removed from the anatomical connectivity. **(B)** First eigenvalue of the pruned matrices as links are removed from the AC matrix. **(C)** Graph theoretical properties of simulated FC_{90} obtained with increasingly pruned AC matrices. Pruning consisted on successively removing 1% of the possible links in a random fashion.

As illustrated in Figure 68AC, we found that successive pruning induces monotonic changes in the properties of emergent FCs, in the same way as decreasing the global coupling. Furthermore, calculating the leading eigenvalue $c_{m,1}^p$ of the pruned matrices C_m^p we found that it decreases as pruning progresses (see Figure 68B). Therefore, keeping the absolute global coupling level k^h constant is equivalent to have decrease the global coupling since $k_m^p = k^h(c_{m,1}^p/c_1)$ (see Figure 69 and *Appendix A.IV* for a theoretical demonstration). In conclusion, pruning the matrix is equivalent to decrease the global coupling, and graph properties change then in the same direction as for the previous disconnection scheme.
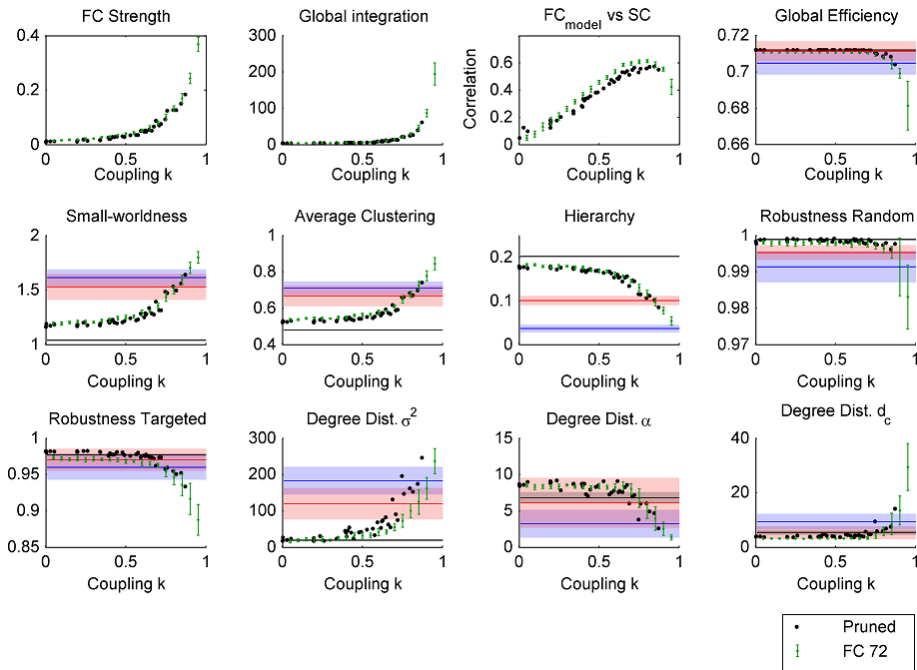
Figure 69 - Graph theoretical results of FCs obtained from the sequence of pruned anatomical matrices as a function of k and comparison with the results obtained with the intact matrix (FC$_{72}$). In contrast with Figure 68, where we plot the properties as a function of the percentage of removed links, here we plot as a function of the equivalent coupling $\textbf{\textit{k}}$, which, for a fixed absolute coupling, decreases with the pruning sequence, in the same way as the first eigenvalue of the pruned matrices. In this case, the pruning increases from right to left, so that the black dot at k=0.87 corresponds to the intact matrix. This figure shows that the properties of FCs obtained with increasingly pruned anatomical matrices are very similar to those obtained when the global coupling is decreased.

More generally, as theoretically demonstrated in *Appendix A.IV*, for any conceivable disconnection, the leading (positive) eigenvalue of a connectivity matrix decreases, at least when this matrix is symmetric. This generalization includes even the case of removed nodes (as done by Alstott et al. (2009) to simulate lesions), where removing a node is equivalent in the model to remove all connections to that node. Here, we found numerically the same behaviour for non-symmetric connectivity matrices. In conclusion, with the present model, any disconnection leads to the same resting-state functional graph alterations reported here for a decrease of the global coupling.

Importantly, we found that when the AC is only partially pruned (up to 15% of removed links), it is possible to recover the graph properties of healthy functional networks by increasing the global coupling strength such that $k_m^p/c_{m,1}^p = k^h/c_1$ (See Figure 70). Only when the underlying AC is further disconnected (>15% of removed links), then the few remaining links are not sufficient to shape the resulting FC with graph properties characteristic of humans, and remain random even at high global coupling (Figure 70 red).
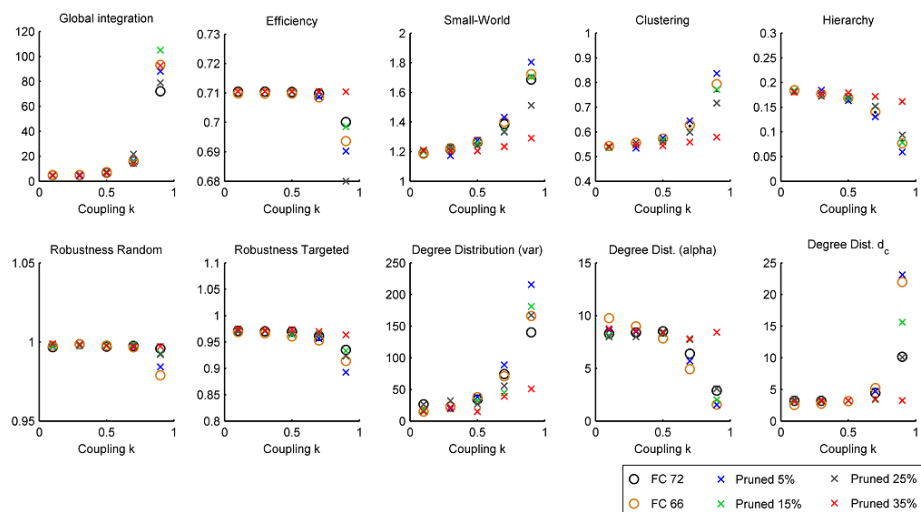
Figure 70 - Comparison between the FCs simulated for a range of coupling values with different pruned matrices (5%, 15%, 25%, 35%) and the intact ones. This figure shows that the static topology of the anatomical matrix is quite robust to pruning (up to 15 % at least - where 39% is the maximum), since the graph properties of simulated FCs vary with the coupling in a similar way to the intact matrices. Note that the coupling *k* here is the relative one defined in the text (divided in the equations by the first eigenvalue of each anatomical matrix).

V.III.5 - Simulated functional networks in schizophrenia

In this section, we analyze our results in light of the schizophrenia literature, mainly focusing on a recent study from Lynall and colleagues (2010) who reported altered resting-state functional networks in people with schizophrenia in terms of graph theory. In the work from Lynall and colleagues (2010) the graph measures explored herein were found to expose significant differences between functional networks from healthy controls and patients with schizophrenia. Notably, they found that functional networks from people with schizophrenia were more efficient, less small-world, more hierarchical, less clustered, more robust, and with more homogeneous regional degrees (i.e narrower degree distribution) than healthy functional networks.

In the present work, we hypothesize that disrupted functional networks in schizophrenia are related to a widespread decrease in the long-range excitatory strength between brain regions, i.e the coupling parameter k in the model. This decreased coupling could be caused by a pathological disconnection, in agreement with current pathophysiological theories of schizophrenia (Stephan et al., 2006). On one side, the disconnection could be due to a decrease in white matter connectivity (Wernicke, 1906), supported by a number of studies reporting lower fractional anisotropy (Lim et al., 1999, Mitelman et al., 2006, Skudlarski et al., 2010), less axonal fibres interconnecting gray-matter regions (Zalesky et al., 2011) and myelin-related dysfunction (Davis et al., 2003) in patients with schizophrenia. Even so, the hypothesis of anatomical disconnection in schizophrenia still needs further validation (see for example van den Heuvel et al. (2010)). Alternatively, the decoupling in the model could still be interpreted as related to a damage occurring at the synaptic level, associated to a deficient modulation of synaptic plasticity (Friston, 1998, Stephan et al., 2006) and/or possibly related to reports of dopaminergic (Winterer and Weinberger, 2004, Winterer, 2006), cholinergic (Winterer, 2010, Mobascher et al., 2011), or glutamatergic (Coyle et al., 2003) malfunction in schizophrenia. Importantly, the mechanisms leading to a decreased coupling strength are not necessarily exclusive and could coexist (Stephan et al., 2006).

In order to compare our graph theoretical results in a statistical way with the ones from Lynall et al. (2010), we started by defining two groups of coupling strengths (with 30 values each), one representative of healthy controls, K_H, and another of patients with schizophrenia, K_S. We have chosen to define these values based on the global integration of BOLD signals[1], which was found in Lynall et al. (2010) to be significantly reduced in people with schizophrenia (GI_S=32.6±11%) compared to healthy volunteers (GI_H=43.1±8.4%). Based on these measures, we defined a set of 30 values taken from a Gaussian distribution $g(GI_H)$ with mean= 43.1 and 8.4% standard deviation and 30 values taken from another distribution $g(GI_S)$ with mean= 32.6 and 11% standard deviation (see Figure 71*A* for an illustration). Then, we extrapolated the coupling strengths necessary in the model (here, the non-oscillatory model) to match each of the expected *GI* values. We obtain in this way two groups of coupling strengths with 30 values each (K_H=0.85±0.01STD and K_S=0.81±0.02STD), statistically representative of the healthy controls and the patients with schizophrenia in terms of global integration of BOLD signals. Subsequently we ran simulations using these coupling values and analyzed the resulting functional networks using graph theory.

In a first step, we analyzed the sensitivity to fragmentation of functional graphs obtained at K_H and K_S. Basset and colleagues (2012) found that equi-threshold graphs built from resting-state functional networks from healthy controls lose connectedness at lower costs than the ones from schizophrenia patients. To evaluate if the same phenomenon occurs in our simulated networks we calculated the size of the largest connected component as a function of the graph density, with densities ranging from 0 to 100% (with 1% increment). We did it using the complete simulated set of 90 regions (same as used in Basset et al. (2012)) Remarkably, the same type of tendency was observed in simulated functional graphs (see Figure 71B left). Moreover, above 27% cost, all simulated graphs exhibited full connectedness, so at the costs used for graph theory (37-50%) all graphs are fully connected.

---

[1] See the *Methods* subsection *V.II.4 - Simulated BOLD signal and Functional Connectivity* for details.
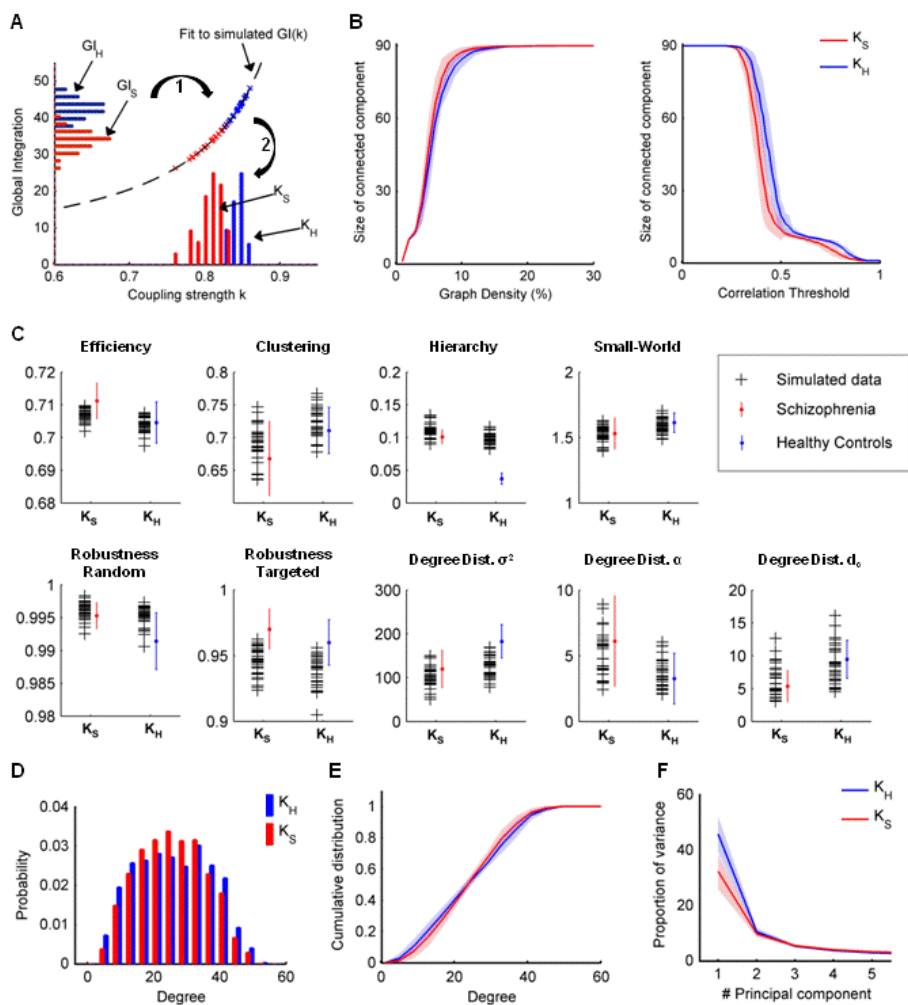
Figure 71 - Properties of simulated functional networks at the group level. (A) Definition of coupling values K_H and K_S representative of healthy controls and schizophrenia patients, based on the global integration values reported experimentally for the two groups, GI_H and GI_S. Using a fitting function, we searched which coupling values would give the same GI distributions, resulting in two distributions of couplings K_H (0.85±0.01STD) and K_S (0.81±0.02STD). **(B)** Fragmentation of simulated functional networks. Networks simulated with K_S were found to be more connected at lower densities when comparing equi-sparse graphs (left). However, comparing equi-threshold graphs, they fragmented at lower thresholds than networks obtained with K_H. **(C)** Graph theoretical metrics of simulated FC matrices (black +) together with experimental values in health (blue: mean±std) and schizophrenia (red mean±std) reported in Lynall at al. (2010). **(D-E)** Pooled degree probability density (D) and cumulative degree distribution (E) for the two populations obtained with K_H (blue) and K_S (red). **(F)** Percentage of variance accounted for by the first 10 principal components of the simulated BOLD signal.

In addition, we also estimated the sensitivity to fragmentation using equi-threshold graphs, where functional connections were considered as a link only when the correlation was above a certain threshold, ranging from 0 to 1 (0.01 increment) (see Figure 71B right). In this case, functional graphs from schizophrenia patients fragment at lower thresholds. This illustrates the fact that fragmentation, as well as other graph measures, depend largely on the thresholding technique. For the following analysis, we show the results using exactly the same thresholding method from Lynall and colleagues (2010) for a reliable comparison,

The graph metrics obtained for each population (K_H and K_S) are shown in Figure 71C (black +) in comparison with the equivalent experimental results (blue and red error bars). Notably, all the changes in the metrics followed the same tendency as reported experimentally. Namely, as can be observed in Figure 71C the functional graphs obtained at lower coupling (K_S) were more efficient, less clustered, more hierarchical, less small-world and more robust to both random and targeted attack than the functional graphs obtained with around 5% higher coupling (K_H). In addition, in the group with lower coupling the degree distributions had a smaller variance and fitted to gamma distributions with higher power exponent and smaller degree cut-off (Figure 71C-D). Functional graphs obtained at higher couplings, on the contrary, exhibit a degree distribution with a larger variance, which reflects in higher probability of both high and low degree nodes, as observed also by a less steep cumulative degree distribution (Figure 71E). Finally, the percentage of variance accounted for by the first PC was significantly reduced at lower couplings, as expected, but no significant difference was found in the remaining PCs (Figure 71F). Although most of the metrics were found to be in the same range as the ones reported experimentally (error bars in Figure 71C), some of the metrics, such as the robustness to targeted attack and the hierarchy in the healthy population, were consistently different from experiments.

These results show a tight relationship between the global integration of BOLD signals and graph theoretical properties of functional networks. Moreover, they corroborate our hypothesis that the functional network alterations observed in schizophrenia could result from a decrease in the coupling strength between cortical regions, which scales the global

integration of BOLD signals and consequently the properties of emergent functional networks. Please note that a homogeneous reduction in the coupling strength affects functional connectivity in a heterogeneous fashion. Again, we remind that this pathological disconnection could be originated either from disruption of axonal connectivity or by malfunction at the synaptic level, unifying current theories of schizophrenia.

V.IV - Discussion

In the present work, we used a modelling approach to investigate the role of structural connectivity in shaping functional networks as measured with fMRI during rest. Structural connectivity is ensured by brain mechanisms involved in long-range signal transmission in the brain, including axonal connectivity (dependent on the number, density and coherence of axon fibres) and synaptic mechanisms (e.g. neurotransmission and plasticity). As shown here, a disruption of these mechanisms, at either a global or a local level (such as occurring in certain brain pathologies), can have dramatic impacts on the resulting functional networks.

Large-scale neural models of brain dynamics are promising tools to explore the non-trivial relationship between anatomical and functional brain connectivity. In particular, these models allow investigating the role of different factors (here, the long-range excitation) in the BOLD signal dynamics, the resulting functional networks and their topological properties. Furthermore, investigating the impact of such factors in the AC-FC relationship helps understanding the mechanisms underlying healthy resting-state activity and its breakdown in disease. In general, our results show that resting-state functional networks depend largely on the structural coupling strength. The fact that these results are independent of the dynamics at the node level reinforces the role of the structural connectivity (which includes the global coupling) in shaping resting-state functional networks. Indeed, we expect that similar results could be reproduced with virtually any model of macroscopic brain dynamics with brain-inspired structural connectivity (as the ones described in section *I.III - Large-scale models of resting-state dynamics*). For that reason, the use of a simplified model of neural dynamics, with non-oscillatory behaviour at the node level,

is a good approach to solve analytically the effects of a structural disconnection on the network dynamics.

First, results obtained with both models show that stronger structural coupling (until a certain critical level) generates more globally correlated and globally integrated BOLD signals. In the Kuramoto model, this is due to increased synchronization across segregated regions, whereas in the non-oscillatory model this is due to the increased excitatory reverberation across the large-scale network, which increases the timescale and the relative variance of the slowest dynamical mode, in a faster way than for the other modes. Using a healthy anatomical connectome, we found an optimal structural coupling strength for which the simulated functional networks have graph-theoretical properties very similar to those of resting-state functional networks in healthy brains. Namely, simulated functional graphs exhibit small-world properties, characterized by high clustering and relatively high efficiency, low hierarchical organization, and a high probability of both high- and low-degree nodes, as indicated by the degree distribution parameters. Because of having more hub regions, the robustness to attacks is decreased. As the coupling is reduced, emergent functional graphs become successively more random and, in the case of an extreme disruption of the structural coupling (i.e. >50% of coupling decrease) the simulated functional networks share properties of random networks.

To study disconnection effects, we have first considered a uniform decrease in the structural connectivity strength. Nevertheless, pathological disconnections may happen only between specific brain regions and therefore affect distinct functional systems depending on the location of the disruption. To take into account the effects of local disconnections in our study, we have also considered pair-wise disconnections occurring in a random and non-uniform way (only with the non-oscillatory model though). As links are randomly removed from the anatomical connectome and the absolute coupling is kept constant, we find that the simulated functional networks reorganize in the same way as if the (relative) structural coupling was decreased. We provide a theoretical demonstration to explain why this is actually the case. For symmetric connectivity, we found that any type of disconnection, including the case where nodes are eliminated from the

network, would decrease the leading positive eigenvalue of the matrix. Therefore, the absolute coupling appears lower, generalizing our results for such type of connectivity. Moreover, we found that, when the AC is only partially pruned, it is possible to recover the graph properties of healthy functional networks by increasing the global coupling strength. Only when the underlying AC is further disconnected, then it is no more possible to obtain FC graph properties characteristic of humans, even at high coupling levels,

V.IV.1 - Disrupted functional networks in schizophrenia

In general, schizophrenia disease is thought to be linked to a pathological dysconnection, supported by mounting evidence of disrupted interregional functional interactions (detected with fMRI). However, the pathophysiological origin of this dysconnection remains under debate. Possible explanations rely mainly on the neural structures involved in signal transmission, i.e. axons and synapses. Importantly, in our model the coupling parameter, k, encompasses both mechanisms and therefore can be interpreted in the light of both theories of schizophrenia.

Results show that disrupted structural connectivity –or disconnection- occurring at either a global or a local level, is indeed a strong candidate to explain the alterations reported in functional brain networks of people with schizophrenia during rest. Actually, with a uniform decrease of only 5% in the coupling -or a removal of about the same proportion of existing links-, we found a very good quantitative agreement with the functional network reorganization observed in schizophrenia, characterized by a decrease in small-worldness and clustering and an increase in hierarchy, efficiency, robustness, degree homogeneity.

Knowing from existing experimental studies (Lynall et al., 2010, Bassett et al., 2012) that the BOLD signals from schizophrenia patients are significantly less globally integrated than the ones from healthy controls, we have defined a range of coupling values that originate, through the model, simulated BOLD signals with statistically similar values of global integration found in disease and healthy states. We found that less globally integrated simulated BOLD signals give rise to simulated functional networks with properties matching the ones characteristic of the schizophrenia disease.

Our results propose a general scenario for the schizophrenia disease, unifying structural (e.g. axonal and/or synaptic mechanisms), dynamical (e.g. BOLD signal integration) and functional connectivity studies (e.g. graph properties of functional networks) in schizophrenia.

V.IV.2 - Relationship between structural coupling strength and cognitive performance

The role of the topological organization of functional networks on the performance of cognitive integration has long been speculated (Sporns et al., 2004). For example, a small-world topology of functional networks is thought to support both modular and distributed processing dynamics (Sporns et al., 2002, Bassett and Bullmore, 2006), leading to optimal information processing in the brain. In addition, Lynall and colleagues (2010) found a strong link between a number of graph theoretical measures of functional networks and a verbal fluency score (indicative of cognitive performance).

Here we propose that the functional network (dis)organization leading to cognitive impairment can be directly linked to a disruption of the underlying structural connectivity (again axonal or synaptic). This hypothesis is corroborated by a number of studies that have reported a link between structural connectivity and behavioural/emotional symptoms in schizophrenia (Hoptman et al., 2004, Skelly et al., 2008, Stephan et al., 2009, Skudlarski et al., 2010). With the present model, we show the direct relationship between graph measures of functional networks (previously related to cognitive performance) and the underlying structural connectivity (linked as well to cognitive performance). These results reinforce the idea that a stronger structural coupling between cortical regions is necessary to obtain a better integration of BOLD signals and consequently, on optimal organization of functional networks, hypothetically leading to an increased cognitive performance. Note that a widespread decrease in the structural coupling between brain regions results in a heterogeneous decrease in interregional regional functional connectivity. Therefore, the relationship proposed herein between lower structural coupling and decreased cognitive performance should be seen as independent from functional connectivity strength. Indeed, the relationship between functional connectivity strength

and cognitive performance seems to be more complex. A recent study from Hawellek and colleagues (2011) has found that interregional functional connectivity within the default mode network increased (rather than decreased) with the decline of cognitive performance in multiple sclerosis. However since the global signal was regressed out in the pre-processing of BOLD signals -which complicates the interpretation of BOLD signal correlations (Murphy et al., 2009)-, it is premature to draw conclusions based on this result.

V.IV.3 - Relation to other modelling studies

Since the last few years, several large-scale models of the brain activity have studied how the resting FC could be derived from the AC and a local node neural mass model. Following several reduction lines, local node models have included a biophysical model (Honey et al., 2007, 2009; Alstott et al., 2009), the FitzHugh-Nagumo model (Ghosh et al., 2008), the Wilson-Cowan model (Deco et al., 2009) and the Kuramoto model (Cabral et al., 2011). Here, we have used the Kuramoto model and, in addition, we have used a model derived on the framework of the Fokker-Planck equation, which is able to describe the full network dynamics, taking into account the effect of noise. Under the hypothesis that the local dynamics is asynchronous and that deviations from this dynamical state are small, this simplified linear model provides a good description of the dynamics, with the advantage that the linearity of the model can be used for a theoretical understanding of the behaviour of the large-scale model and of the resulting FC. Such an understanding is much more involved in the other models, which are nonlinear. Moreover, the performance of this model in predicting empirical FC is very similar to the one of other models and there is still no clear demonstrated advantage to use a nonlinear local model to predict the resting FC.

Other modelling studies have studied the impact of lesions in functional connectivity during rest (Honey and Sporns, 2008, Alstott et al., 2009). Although lesions were simulated by removing nodes or cortical areas in the brain, it can be seen as a particular type of disconnection, where all links to a certain node (or area) are removed. One of the main findings was that FC alterations could be widespread even when the lesion is local. Moreover, FC

changes were found to be very dependent on the brain regions affected by the lesion (Alstott et al., 2009). Although a study of the spatial alterations in FC is beyond the scope of the present study, the present model sheds a new light on these results. In our model, the slowest modes are responsible for the low-frequency correlations, in particularly the slowest one. When we consider the case of a global disconnection, we do not change the connectivity matrix, and in that case, the smooth FC changes are mainly due to the change in relative variance of the first (slowest) mode, which reflects spatially in its spatial map. When we consider a local disconnection (or a lesion), the connectivity matrix changes and the spatial maps also change: therefore, FC changes non-locally, crucially and non-trivially depending on the lesion site, in the same way eigenvectors depend non-trivially on the underlying matrix.

V.IV.4 - Limitations and further studies

Although computational models serve to test existing theories and to make predictions, results must be interpreted in light of the model limitations.

First, we used averaged anatomical connectomes. Although averaging helps eliminating spurious connections detected by the tracking algorithm and therefore provide a robust and reliable version of the human connectome, the variability across subjects in those terms is neglected. In figure 4 we define variability across subjects by means of the structural coupling *k,* which is proposed to be one (but not the only) source of variability across subjects. Furthermore, the anatomical connectomes refer to healthy participants and disconnection effects were modelled by inducing uniform or heterogeneous alterations in the SC. We believe our model results would benefit if simulations were ran using anatomical connectomes from people with disconnection-related pathologies. Due to the increasing availability of anatomical connectomes in health and disease (e.g. from the Human Connectome Project www.humanconnectomeproject.org) such studies should be implemented in the future. In addition, the use of low-resolution parcellation templates (e.g. 66 and 90 regions) limits our model to reproduce only large-scale patterns of BOLD activity. Using connectomes with higher spatial resolution would allow a more comprehensive study regarding smaller substructures of the brain's network. Even so, in general

term, the characteristics of functional networks explored herein were found to vary with the structural coupling in a consistent way, with disregard to the parcellation schemes used (90 and 66 regions). Note that the graph measures reported by Lynall and colleagues (2010) and reproduced in this work can only be qualitatively compared because functional networks were derived in a similar way and the same thresholding technique was applied. For example, in a recent study from Yu et al. (2011) functional networks derived using independent component analysis exhibited higher (rather than lower) clustering coefficients and path lengths in schizophrenia. Therefore, we find it necessary to establish standardized methods for analyzing brain networks by means of graph theory, to allow a direct comparison of these measures across studies. In addition, it should be noted that the randomization effects observed not only in the model but also in experiments depend largely on the thresholding technique. In fact, to avoid comparing graphs with different densities, fixed cost values were established to build graphs, which forces then lower correlation thresholds and subsequently a decrease in correlation significance.

Using EEG signals, Rubinov and colleagues (2009) have reported an increase of FC in schizophrenia. However, since the present study was limited to the study of FC derived from BOLD signal correlations, the apparent contradiction with a BOLD FC decrease is hard to evaluate in the light of the current model.

Finally, it is important to have in mind that experimental results are also subject to methodological limitations due to limited sample sizes and artefacts introduced by the imaging techniques. For example, the mean FC strength reported in the experiments (Lynall et al., 2010) was consistently higher than in simulations. This correlation shift to higher positive values could be induced by some remaining global artefacts in the BOLD signal (like those due to heartbeat and respiration) since no pre-processing step was performed with the intention of eliminating them.

V – General discussion

'A fact is a simple statement that everyone believes.
It is innocent, unless found guilty.
A hypothesis is a novel suggestion that no one wants to believe.
It is guilty, until found effective.
Edward Teller

The focus of the work presented herein was to investigate if the complex spatiotemporal patterns observed in brain activity during rest could be explained by an underlying network dynamics. To this aim, we have used the Kuramoto model of coupled oscillators with brain-inspired connectivity and delays, and compared our results with fMRI and MEG data. Although this approach relies on arguable assumptions and implies a high degree of abstraction, the fact is that the dynamics emerging from this simple model could predict many features of resting-state activity. Here, we want to highlight the implications of using the Kuramoto model and discuss its value in comparison with other (more realistic) resting-state models. In addition, we comment on the dynamical regime that enabled the model to reproduce the experimental observations, and argue on the biological plausibility of such behaviour.

The Kuramoto model of coupled oscillators is one of the most abstract and fundamental models used to investigate phase interactions in oscillatory networks in nature (Pikovski et al., 2001, Strogatz, 2003). However, its application to model the interaction between brain areas requires the consideration that isolated brain areas behave intrinsically as oscillatory units. Theoretically, it has been shown that a large ensemble of densely coupled excitatory an inhibitory neurons can exhibit periodic synchronized firing leading to limit-cycle oscillations at different frequency bands (Brunel and Wang, 2003). Furthermore, electrophysiological recordings have revealed locally coherent oscillations in all cortical areas (Buzsaki and Draguhn, 2004). In this work, we assumed that uncoupled neural masses are in this dynamical regime during rest and display a natural frequency in the gamma-frequency range. The main reason for which we chose this dynamical regime -and subsequently to use the Kuramoto model- consists in

the fact that, in a previous resting-state model from our group, Deco et al. (2009) had found the spontaneous emergence of correlated slow (<0.1Hz) fluctuations when brain areas -modelled as Wilson-Cowan units- exhibited self-sustained oscillations in the gamma-frequency range[1]. On the other hand, other resting-state models have assumed different dynamical regimes at the node level (i.e. asynchronous fixed points or chaotic oscillations)[2] and obtained similar qualitative results (see Table 3). However, also these neural-mass models (and even the model of spiking neurons from Deco and Jirsa (2012)) are immense simplifications of the real mechanisms occurring in cortical areas. Actually, there is a never-ending degree of complexity in the brain as we reduce the level of abstraction (going even beyond layered cortical microcircuitry (Markram, 2006) or the specific position of ion-channels in the dendritic trees (Izhikevich and Edelman, 2008)). Generally, the desired degree of physiological detail in a network depends on the scientific questions posed. Here, we have been interested primarily in the macroscopic network dynamics of resting-state activity, and not in any molecular or pharmacological influences occurring at the neuron level. Neural-mass models such as the FizHugh-Nagumo or the Wilson-Cowan proved sufficient in a large number of modelling studies of this kind. However, they are generally implemented in simpler connectivity structures that allow pinpointing specific mechanisms underlying precise cognitive processes. When such neural-mass models are embedded in the space-time structure of the brain, a significant fit is obtained with resting-state fMRI recordings. However, the dynamics emerging from simulations is complex and the induction of the hidden mechanisms leading to correlated BOLD signal fluctuations is again an ill-posed problem (Ghosh et al., 2008). Therefore, we believe it is justified to introduce an even higher degree of abstraction to investigate these mechanisms. Using the Kuramoto model, the neural-mass dynamics is reduced to a single variable –the phase-. In this way, the exploration is restrained to the time-delayed phase interactions between connected cortical regions. The advantage of this reduction is that the dynamics of the Kuramoto model has been widely studied in the fields of physics and mathematics, and therefore the results can be interpreted in the light of the existing literature.

---

[1] See section *I.III.1.c - The Wilson-Cowan model.*
[2] See section *I.III - Large-scale models of resting-state dynamics.*

Table 3 - Comparison between models of BOLD resting-state activity.

	Node Model	Neural-mass in the network	Network Dynamics	Origin of BOLD fluctuations	BOLD correlations	Role of Delays	Role of Noise	Connectome
Honey et al. (2007,2009)	Conductance-based biophysical model	Chaotic activity	Chaotic activity with sporadic synchrony	Intermittent self-organizing patterns	Self-organizing patterns	No	No	Macaque 1 hemisphere
Ghosh et al. (2008)	FitzHugh-Nagumo Unit + noise	Stable asynchronous state with 10Hz oscillations	Network reverberation of oscillatory damped fluctuations	Slow modes for sufficient coupling	Slow modes dominate in variance	Yes	Yes	Macaque N=38
Deco et al. (2009)	Wilson-Cowan Unit + noise	Limit-cycle Oscillations (40Hz)	Slow fluctuations in synchrony degree	Slow fluctuations in the synchrony degree	Synchronization of structural modules	Yes	Yes	Macaque N=38
Deco and Jirsa (2012)	Network of spiking neurons + noise	Stable asynchronous state (no oscillations)	Noise induced wandering in the presence of ghost attractors	Noise excursions at the border of multistability	Ghost attractors	No	Yes	Human N=66
Cabral et al. (2011, 2012a)	Kuramoto Phase oscillator	Time-delayed oscillatory interactions	Intermittent modular synchronization	Slow fluctuations in the synchrony degree	Metastable Modular Synchronization	Yes	No	Human N=66 N=90
Cabral et al. (2012a)	Rate fluctuations + noise	Stable asynchronous state	Network reverberation of damped fluctuations	Slow modes for sufficient coupling	Slow modes dominate in variance	No	Yes	Human N=66

Most theoretical studies on the Kuramoto model have focused on studying and solving analytically the stability conditions of simple network structures. The extension of the Kuramoto model to heterogeneous time-delayed interactions with complex small-world connectivity like the brain has never been addressed theoretically. At the first sight, results from simulations in the metastability region seem chaotic. Yet, it was clearly in this parametric region that we obtained the best fit with both BOLD and MEG data. By comparing with theoretical predictions, we were able to make falsifiable predictions such as: Does the order parameter fluctuate in time? Are there groups of nodes synchronizing only transiently? Is there frequency suppression when synchrony occurs? Using this Popperian method, we explored exhaustively the chaotic-like dynamics emerging in the region of best agreement with brain data. Finally, we were able to extract a dynamical scenario that explains both BOLD and BLP fluctuations as a synchronization phenomenon. In this scenario, different subsets of connected regions have an intrinsic tendency to synchronize intermittently. Due to delays, these subsets of nodes are only able to synchronize at a reduced collective frequency. This collective frequency depends on 1) the mean delay between regions, 2) the number of regions engaged[1] and 3) the natural frequency of the oscillators (Niebur, 1991). While the cluster is synchronized, the power in this frequency is increased. However, if the coupling is sufficiently weak, this synchronized state is unstable and is naturally disrupted due to competitive mechanisms between nodes. When synchrony fades away, nodes disengage from the cluster ensemble and their power at the reduced frequency disappears. In this way, all nodes involved in the cluster dynamics will have correlated BLP when the carrier frequency coincides with the cluster frequency. Furthermore, these fluctuations can be tuned to the time scale of BOLD fluctuations by manipulating the global coupling strength between regions, which determines the duration (i.e. the dwell time) of metastable synchronized sates. Although this theoretical scenario explains how local gamma-band oscillators can give rise to correlated frequency specific band-limited power fluctuation, how far is this scenario plausible in the brain? Even if the reduction of cortical regions to phase-oscillators is an immense simplification of macroscopic brain dynamics, the Kuramoto model

---

[1] Note that the number of regions is multiplied by the mean delay, which is indicative of the size of the whole loop.

has proven to predict successfully to interaction of several oscillator systems in nature. One of the main limitations of the Kuramoto model is that it disregards amplitude interactions. In a recent study, Daffertshofer and van Wijk (2011) compared the phase synchronization patterns of interconnected Wilson-Cowan models vis-a-vis Kuramoto networks of phase oscillators finding that the functional connectivity of interconnected Wilson-Cowan models explicitly depends on the generating oscillators' amplitudes. In consequence, they conclude that a proper inference of structure from function requires more than a sole focus on phase synchronization. However, as we explain in the *Motivation*, the main goal of our work was to make a *falsifiable* prediction. In that direction, we have used identical oscillators with equal natural frequency and equal amplitude, focusing only on phase interactions. In no part of this work do we claim that the whole brain dynamics can be explained by the phase only (or by only one type of frequency generator). Instead, what we show is that the phase alone can already give rise to complicated phenomena, which can only be understood in these simplified conditions. From this point, increased realism can be added (such as a dispersion of frequencies at the node level or different amplitudes) and the results should be analyzed in the light of the results found herein. We expect that the inclusion of increased realism in the model will probably maintain some of the qualitative results presented in this thesis, but it will certainly make the underlying equations more complex and change their interpretation. Importantly, it would be necessary to verify if the phenomenon of metastable reduced collective frequencies is observed with reduced neural-mass models such as the FitzHugh-Nagumo or the Wilson-Cowan. In this way, we expect that our results will help understanding the complex dynamics emerging from (more realistic) neural-mass models.

In this model, we observe a key role of delays. On one side, they introduce a phase frustration that impedes the full synchronization of the network at low coupling. On the other, they play a role in determining the carrier frequency. Therefore, and although the power fluctuations are slow, this scenario defends an important role of delays in shaping resting-state dynamics on multiple time-scales.

Regarding the relationship between our results and BOLD signal fluctuations, a study by (Kilner et al., 2005) has compared hemodynamic changes with the spectral profile of ongoing EEG activity. Their analysis suggests that 'functional activation' -as indexed by increases in hemodynamic signals- is associated with a loss of power in lower EEG frequencies, relative to higher frequencies. In this heuristic, activation causes an acceleration of temporal dynamics (more spikes per second) leading to increased energy dissipation (and therefore an increase in local oxygen consumption). Importantly, our results can be interpreted in the light of this theoretical scenario since we have found a significant negative correlation between the slow fluctuations in the power at low and high frequencies. In other words, during metastable synchronized states, there is increased order in the system (as indicated by the order parameter) and the frequency is low. Based on the heuristic above, this could correspond to a state with less energy dissipation. When the cluster synchrony is disrupted, the power of individual units (at higher frequency) slightly increases (see Figure 55 on p.116). Since higher frequencies imply more spikes per second, the energy consumption would increase, leading to increased BOLD signal. This scenario goes in agreement with observations that BOLD signal correlates negatively with the expression of alpha and beta power and positively with the expression of higher frequencies (Scheeringa et al., 2011). Furthermore, it suggests that activation may correspond to an acceleration of dynamics, subserving more rapid computations. This sort of activation can manifest with no overall change in power but a change in the frequencies at which power is expressed (Kilner et al., 2005). In these terms, the signal is expressed through frequency modulation (FM) instead of amplitude modulation (AM) (see Figure 72 for an illustration).
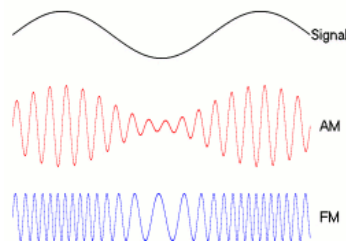
Figure 72 - A signal may be carried by an AM or FM wave (source: Wikipedia). The FM signal can be filtered into distinct carrier frequencies, giving rise to more than one signal.

In our model, if we consider the signal at all frequency bands (i.e. not frequency filtered), the amplitude (or total power) of the raw signal is constant since $sin(\theta) \in [-1\ 1]$. In that case, the network dynamics is expressed through FM (see Figure 73 left). Only when we filter the signal (and therefore eliminate the signal components in other frequencies) do we observe amplitude modulations (see Figure 73 middle and left).
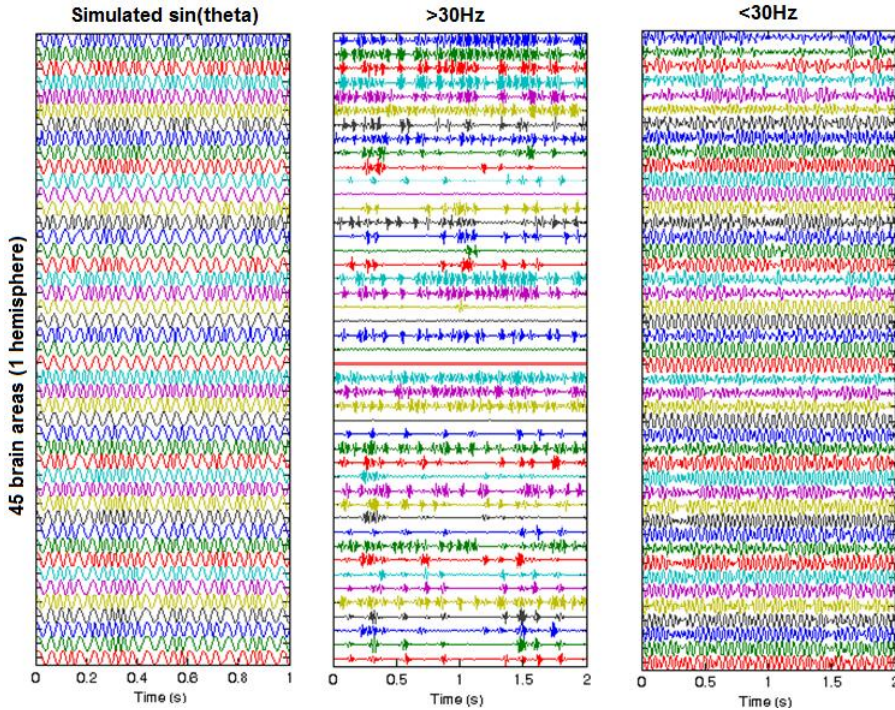
Figure 73 – Network dynamics expressed through FM or AM. (Left) Simulated $sin(\theta_n)$ for coupled cortical regions in the metastability region (AAL connectome, $\tau_m = 8$, $k = 3$, $\omega_n = 40Hz, \forall n$). (Middle) Simulated signal filtered above 30Hz. (Right) Simulated signal filtered below 30Hz. We observe that network interactions are expressed through FM in the raw signal, and expressed through AM when the signal is filtered in a frequency range.

Furthermore, since the total power is constant, if we separate the signal into two frequency bands (above and below a certain frequency threshold) we observe that the amplitude modulations are anti-correlated. However, since different frequencies can coexist in the system (due to different cluster frequencies) if we band-pass the signals into several frequency bands, we

can separate the network dynamics of different frequency specific sub-networks.

These results provide a theoretical scenario for the frequency interactions observed in brain activity. Again, we remind that this is only a very abstract case of N=90 identical gamma-band oscillators, without noise. However, we believe that the similarities with what is observed in the brain should not be disregarded. So far, apart from theoretical predictions of local pace-maker generators in the brain, no explicit fundamental mechanism has been suggested to explain the spontaneous emergence of these complex dynamics from the physical structure of the brain.

Finally, we found a crucial role for the coupling strength in shaping the network dynamics observed in brain activity during rest. On one side, the emergence of metastability in the system occurs for a specific range of couplings and delays. In addition, in agreement with the predictions from Niebur et al. (1991), the collective frequency of metastable synchronized clusters is found to be inversely correlated with the coupling (i.e., the higher the coupling, the lower the frequency). Furthermore, we have found that, as the coupling is decreased, the correlation of BOLD signals is decreased and the corresponding functional networks are less globally integrated, less clustered and less small-world. These results go in agreement with previous findings in patients with schizophrenia, a disease long time hypothesized to be a disconnection syndrome.

Taken overall, our results reinforce the importance of the structural connectivity (including coupling strength, wiring topology and delays), in the dynamics of resting-state activity. In addition, we show that a rich complex dynamics with multistability can emergence in the absence of noise and frequency dispersion. We believe that the results presented in this thesis should serve as the grounds for further investigations in both large-scale brain models and theoretical studies of the Kuramoto model.

VI – Conclusion

'Joy in looking and comprehending is nature's most beautiful gift.'
Albert Einstein

In this thesis, we have explored the complex dynamics emerging from Kuramoto oscillators with time delayed interactions when these are coupled with brain inspired connectivity and delays. The main purpose of this work was to investigate if the simple Kuramoto could provide insights about the network dynamics observed in brain activity during rest. We started by finding a good agreement with BOLD functional connectivity, in the same way as previously demonstrated with more realistic neural-mass models. In addition, due to the simple nature of the model, and based on previous theoretical literature on the Kuramoto model, we were capable of depicting the fundamental mechanisms at the genesis of correlated slow fluctuations. With the availability of resting-state MEG data, we further explored if the Kuramoto could explain the frequency specificity of band-limited power fluctuations observed at faster temporal scales. Notably, we have found that, in the same dynamical regime where BOLD patterns emerged (i.e. in the region of metastability) our results could explain MEG results with remarkable accuracy. Based on these results, we provide a new theoretical scenario to explain resting state activity at multiple temporal scales. A promising future endeavour would certainly be to extend the investigations to evoked neural activity.

To conclude, we expect that the theoretical/computational explanations and predictions of resting-state neuroimaging data that we have presented in this thesis complement and extend our current understanding of resting-state activity. Indeed, we believe that this study reflects the timely necessity to turn from the existing neural-mass models to more basic and phenomenological models in order to advance our understanding of the network dynamics underlying brain activity during rest.

165

A.I – List of regions in different brain parcellation schemes

Table 4 - Names and abbreviations of the brain regions considered in the human connectome from Hagmann et al. (2008) (in alphabetical order).

Abbreviation	Brain region
BSTS	Bank of the superior temporal sulcus
CAC	Caudal anterior cingulate cortex
CMF	Caudal middle frontal cortex
CUN	Cuneus
ENT	Entorhinal cortex
FP	Frontal pole
FUS	Fusiform gyrus
IP	Inferior parietal cortex
ISTC	Isthmus of the cingulate cortex
IT	Inferior temporal cortex
LING	Lingual gyrus
LOCC	Lateral occipital cortex
LOF	Lateral orbitofrontal cortex
MOF	Medial orbitofrontal cortex
MT	Middle temporal cortex
PARC	Paracentral lobule
PARH	Parahippocampal cortex
PC	Posterior cingulate cortex
PCAL	Pericalcarine cortex
PCUN	Precuneus
POPE	Pars opercularis
PORB	Pars orbitalis
PREC	Precentral gyrus
PSTC	Postcentral gyrus
PTRI	Pars triangularis
RAC	Rostral anterior cingulate cortex
RMF	Rostral middle frontal cortex
SF	Superior frontal cortex
SMAR	Supramarginal gyrus
SP	Superior parietal cortex
ST	Superior temporal cortex
TP	Temporal pole
TT	Transverse temporal cortex.

Table 5 - List of Brain regions considered in the human connectome according to the AAL parcellation. The regions discarded in the graph theoretical analysis in the same way as in Lynall et al. (2010) are indicated in bold.

Brain region	Left	Right
Precentral	**1**	**90**
Frontal Sup	2	89
Front Sup Orb	3	88
Front Mid	4	87
Front Mid Orb	5	86
Front Inf Ope	6	85
Front Inf Tri	7	84
Front Inf Orb	8	83
Rolandic Oper	9	82
Supp Motor Ar	10	81
Olfactory	**11**	**80**
Front Sup Med	12	79
Front Med Orb	13	78
Rectus	**14**	**77**
Insula	15	76
Cingulum Ant	16	75
Cingulum Mid	17	74
Cingulum Post	18	73
Hippocampus	19	72
ParaHippocamp	**20**	**71**
Amygdala	**21**	**70**
Calcarine	22	69
Cuneus	23	68
Lingual	24	67
Occipital Sup	25	66
Occipital Mid	26	65
Occipital Inf	27	64
Fusiform	**28**	**63**
Postcentral	29	62
Parietal Sup	30	61
Parietal Inf	31	60
SupraMarginal	32	59
Angular	33	58
Precuneus	34	57
Paracentr Lob	35	56
Caudate	36	55
Putamen	37	54
Pallidum	38	53
Thalamus	39	52
Heschl	40	51
Temporal Sup	41	50
Temporal Pole Sup	**42**	**49**
Temporal Mid	43	48
Tempral Pole Mid	**44**	**47**
Temporal Inf	**45**	**46**

A.II - MEG Data Collection and Analysis

This collection of data was performed by Prof. Morten Kringelbach, Morten Joensson and Hamid Mohseni at the CFIN/MindLab, Aarhus Univ., Aarhus, Denmark and the Department of Psychiatry, University of Oxford, United Kingdom.

The analysis was performed by Henry Luckhoo and Mark Woolrich at the Oxford Centre for Human Brain Activity, University of Oxford, United Kingdom.

Ten normal healthy participants underwent an eyes-closed resting state scan lasting five minutes. MEG data were gathered on an Elekta Neuromag (Elekta Neuromag Oy, Helsinki, Finland). Data were collected on 102 magnetometers and 102 pairs of orthogonal radial gradiometers at a sampling frequency of 1000Hz. Head localization was achieved using four head position indicator (HPI) coils which were periodically/continuously energised allowing the head to be localised within the scanner helmet. Each subject's head shape was recorded using a Pohemus Isotrack system. Structural MRIs were gathered on a [insert details for structurals].

Signal space separation (implemented using MaxFilter^{TM}) was applied to each data set to reduce any sources of interference from outside the scanner helmet. SSS projects the MEG data onto a basis set of spherical harmonics. Harmonics corresponding to sources originating from within the helmet are preserved whilst interfering sources from outside the helmet are rejected.

The MEG data was then epoched into 5s segments. Epochs with abnormally high variance, relative to all the epochs, were discarded. Channels which exhibit high variance relative to all the channels after removal of bad epochs were also discarded. The epoched MEG data was then concatenated into a resting state single trial.

Each dataset was co-registered to a standard (MNI) space by registering the subject's structural MRI to their head shape (as measured by the Polhemus Isotrack). A single homogenous shell forward model was then estimated using the subject's head shape. Both co-registration and estimation of the forward model were done using SPM8 (FIL, UCL).

The data were then band-pass filtered into 15 frequency bands (each 4Hz wide, between 0 and 60Hz). An LCMV beamformer(Van Veen et al., 1997, Robinson and Vrba, 1998) was used to reconstruct the activity at 90 locations defined by the AAL parcellation(Tzourio-Mazoyer et al., 2002). The beamformer is an adaptive spatial filter that uses the forward model to design a set of weights which reconstruct neural activity in a specific region whilst suppressing activity from all other locations. The source space data was constructed using only the planar gradiometers (done to avoid any issues with fusing multiple sensor type after SSS). The data covariance matrix, C, was regularised according to $C_{reg} = C + \mu I$ where μ equals 4 times the minimum eigenvalue of the unregularised data covariance matrix (Brookes et al., 2011b), C. Regularisation acts to spatially smooth the beamformed data and increase temporal signal to noise ratio.

The beamformer outputs 90 time series for each of the 15 frequency bands of interest. However, it has been shown that functional connectivity in MEG data is best measured by considering the oscillatory amplitude envelope of the time series at each location (Liu et al., 2010, Brookes et al., 2011a, Brookes et al., 2011b). This is found by estimating the absolute value of the analytic signal, computed via the Hilbert transform. The oscillatory amplitude envelope is equivalent to the instantaneous power of the signal. Resting state functional connectivity has been found to be linked to correlations in the low frequency power fluctuations in oscillatory power between regions (Mantini et al., 2007, Liu et al., 2010, Brookes et al., 2011a, Brookes et al., 2011b). Therefore, the oscillatory amplitude envelope is temporally down-sampled by dividing the envelope into equal windows of length 1 s and calculating the mean envelope value for each window; this effectively low-pass filters the envelope signal. For each frequency, the pair-wise correlation matrix was estimated, giving a total of 15 correlation matrices for each subject. The correlation matrices were averaged across the 10 subjects to give a single set of 15 correlation matrices.

A.III – DTI data collection and building of anatomical connectomes

This collection of data and analysis was performed by Prof. Morten Kringelbach at the Department of Psychiatry, University of Oxford, United Kingdom.

We extracted the structural brain networks using diffusion tensor imaging (DTI) from the brains of 21 healthy, normal participants (11 males and 10 females, age: 22 – 45 years) using a modified version of already published methods (Gong et al., 2009b). All scans were performed on the same Philips Achieva 1.5 Tesla Magnet. Diffusion MRI was acquired by using a single-shot echo planar imaging-based sequence with coverage of the whole brain; repetition time (TR), 9390 ms; echo time (TE), 65 ms. DTI images utilised 32 optimal nonlinear diffusion weighting directions (b = 1200 s/mm2) and 2 non-diffusion weighted volumes; reconstructed matrix=128x128x45; reconstructed voxel size 2.0mm x 2.0mm x 2.0mm. We also acquired T1-weighted structural images with a three-dimensional 'FLASH' sequence (TR=12 ms, TE=5.6 ms, flip angle=19˚, with elliptical sampling of k-space, giving a voxel size of 1x1x1mm in 5.05 minutes).

The extraction of weighted brain networks used a three steps process consisting of 1) brain parcellation, 2) interregional connectivity analysis and 3) extraction of weighted network. In the following we briefly outline the details involved in each step.

A.III.1 - Brain parcellation

We used the automated anatomical labeling (AAL) template to parcellate the entire brain into 90 cortical and subcortical regions (45 for each hemisphere), where each region represents a node of the brain network (Tzourio-Mazoyer et al., 2002). For each participant, we conducted the parcellation in the diffusion MRI native space.

We used the Flirt tool (FMRIB, Oxford) (Jenkinson et al., 2002) to linearly coregister the b0 image in diffusion MRI space to the T1-weighted structural image. The transformed T1-weighted image was then mapped to the T1 template of ICBM152 in MNI space (Collins et al., 1994). The resulting transformation was inversed and further applied to warp the AAL mask from

MNI space to the diffusion MRI native space, where interpolation using nearest-neighbour method ensured that the discrete labeling values were preserved.

A.III.2 - Analysis of interregional connectivity

We used the Fdt toolbox in FSL (www.fmrib.ox.ac.uk/fsl/, FMRIB, Oxford) to carry out the various stages of processing of the diffusion MRI. The initial preprocessing involved co-registering the diffusion-weighted images to a reference volume using an affine transformation for the correction of head motion as well as eddy current induced image distortion. Following this preprocessing, we estimated the local probability distribution of fibre direction at each voxel (Behrens et al., 2003). We then used the probtrackx algorithm allowing for automatic estimation of two fibre directions within each voxel, which can significantly improve the tracking sensitivity of non-dominant fiber populations in the human brain (Behrens et al., 2007).

We estimated the connectivity probability by applying probabilistic tractography using a sampling of 5000 streamline fibres per voxel. The connectivity probability from the seed voxel i to another voxel j was defined by the number of fibres passing through voxel j divided by the total number of fibres sampled from voxel i (Behrens et al., 2007). This was then extended from the voxel level to the level of each region, i.e. in a seed brain region consisting of n voxels, 5000*n fibres were sampled. The connectivity probability from the seed region to a given region is the number of fibres passing through a given region divided by 5000*n.

In our study, the seed regions selected for each of the parcellated brain region and the connectivity probability to each of the other 89 regions was calculated. It should be noted, however, that because of the dependence of tractography on the seeding location, the probability from i to j is not necessarily equivalent to that from j to i. However, these two probabilities are highly correlated across the brain for all subjects (the least Pearson $r =$ 0.70, $p < 10^{-50}$). We therefore defined the undirectional connectivity probability P_{ij} between region i and j by averaging these two probabilities. We implemented the calculation of regional connectivity probability using in-house Perl scripts.

A.III.3 - The weighted network

We constructed a weighted network/graph by defining a distance/weight associated with each edge. Similar to previous studies, we took the high connectivity probability between brain regions to be short distances in a graph. Specifically, we computed $W_{ij}=1-P_{ij}$ as the distance/weight between brain region i and j, as used in previous literature (Achard and Bullmore, 2007). It is important to note that the distance/weight here does not correspond to the physical length of the white matter pathway linking the brain regions, nor to the physical distance between brain regions in the real spatial space. For each subject, a 90x90 symmetric weighted cortical network/graph W was constructed, representing the anatomical organization of cerebral cortex.

A.IV - Demonstration that the leading (positive) eigenvalue of a symmetric connectivity matrix decreases with disconnection.

This demonstration was performed by Dr. Etienne Hugues, Center of Brain and Cognition, Universitat Pompeu Fabra, Barcelona, Spain.

Let's consider 2 any symmetric connectivity matrices: C and a disconnected version of it C'. For their coefficients, we have $C_{np} \geq C'_{np} \geq 0$. Their leading and positive eigenvalues are c_1 and c'_1, respectively. We want to prove that $c'_1 \leq c_1$.

From the Perron-Frobenius theorem, we know that c_1 and c'_1 are positive and the greatest eigenvalues in modulus for C and C', respectively. We also know that the respective first (right) eigenvectors V_1 and V'_1, when conveniently normalized (and with unit norm: $\|V_1\| = \|V'_1\| = 1$) have all their components positive: $V_{1p} \geq 0$ and $V'_{1p} \geq 0$.

Let's define a new matrix $\Delta = C - C'$. From the definition of C and C', this matrix has positive coefficients: $\Delta_{np} \geq 0$. The following identity

$$CV'_1 = C'V'_1 + \Delta V'_1$$

can be rewritten

$$CV'_1 = c'_1 V'_1 + W$$

where, from the positivity of the coefficients of Δ and of the components of V'_1, the vector W has also positive components. Taking the squared norm of this equality, we get

$$\|CV'_1\|^2 = c'^2_1 + 2c'_1 V'^T_1 W + \|W\|^2,$$

where the first term in the right hand side has been simplified because of the unit norm of V'_1. From the positivity of c'_1 and of the components of V'_1 and W, the second term is positive. The third one is also positive. Then, we have $\|CV'_1\| \geq c'_1 > 0$.

For a symmetric matrix, it is known that $\|CU\| \leq |c_1| . \|U\|$ for any vector U. In our case, and because of the unit norm of V'_1, this implies that

$\|CV'_1\| \le c_1$. Combining the two preceding inequalities, we finally get the result: $c'_1 \le c_1$.

A.IV.1 - Case of a lesion

In this case, some nodes could be eliminated from the network. Although link removal and node removal seem quite different manipulations of connectivity matrices, the last one can be seen as a particular case of the first. Indeed, from the model point of view, removing nodes is the same as considering the same initial nodes but cutting all the links between these nodes and the other ones (replacing the nodes' lines and columns by null values in the connectivity matrix), and just look at the network part made of the remaining nodes. In matrix terms, for a node ordering in which the L nodes of the lesion are placed at the end for simplicity, starting from the connectivity matrix C, the lesioned one C' writes (in block matrices)

$$C' = \begin{pmatrix} C^l & 0 \\ 0 & 0 \end{pmatrix},$$

where the second block matrix has L lines and columns. C' is a particular case of a disconnected matrix as defined above. Its eigenvalues are trivially the ones of C^l, plus L times the eigenvalue 0. Therefore, we have $c'_1 = c_1^l$ and, from the above result, $c_1^l \le c_1$, showing that, after lesion, the leading eigenvalue of the connectivity matrix entering the dynamical model (C^l) has decreased compared to the original one.

A.IV.2 - Consequences for the present model

In this study, to simulate the disconnection effects of a disease, we consider a fixed absolute coupling k_H/c_1, where these quantities refer to the healthy case. Therefore, for a disconnected matrix C^d, the equivalent coupling k^d we consider verifies $\frac{k_H}{c_1} = \frac{k^d}{c_1^d}$. Taking into account the previous results, we get $k^d = k_H \frac{c_1^d}{c_1} \le k_H$. In other words, this means that, in the model, disconnection is equivalent to a decrease in the coupling strength.

Bibliography

Acebron JA, Bonilla LL, Vicente CJP, Ritort F, Spigler R (2005) The Kuramoto model: A simple paradigm for synchronization phenomena. Rev Mod Phys 77:137-185.

Achard S, Bullmore E (2007) Efficiency and cost of economical brain functional networks. PLoS computational biology 3:e17.

Achard S, Salvador R, Whitcher B, Suckling J, Bullmore E (2006) A resilient, low-frequency, small-world human brain functional network with highly connected association cortical hubs. The Journal of neuroscience : the official journal of the Society for Neuroscience 26:63-72.

Aihara K (2008) Chaos in neurons. Scholarpedia 3(5):1786.

Aihara K, Takabe T, Toyoda M (1990) Chaotic Neural Networks. Phys Lett A 144:333-340.

Alstott J, Breakspear M, Hagmann P, Cammoun L, Sporns O (2009) Modeling the impact of lesions in the human brain. PLoS computational biology 5:e1000408.

Andrews-Hanna JR, Snyder AZ, Vincent JL, Lustig C, Head D, Raichle ME, Buckner RL (2007) Disruption of large-scale brain systems in advanced aging. Neuron 56:924-935.

Arenas A, Diaz-Guilera A, Perez-Vicente CJ (2006) Synchronization reveals topological scales in complex networks. Physical review letters 96.

Arieli A, Sterkin A, Grinvald A, Aertsen A (1996) Dynamics of ongoing activity: Explanation of the large variability in evoked cortical responses. Science 273:1868-1871.

Assisi CG, Jirsa VK, Kelso JAS (2005) Synchrony and clustering in heterogeneous networks with global coupling and parameter dispersion. Physical review letters 94.

Bacon F (2010) [Novum organum (1620)]. Vertex 21:465-469.

Bandettini PA, Jesmanowicz A, Wong EC, Hyde JS (1993) Processing strategies for time-course data sets in functional MRI of the human brain. Magnetic resonance in medicine : official journal of the Society of Magnetic Resonance in Medicine / Society of Magnetic Resonance in Medicine 30:161-173.

Barabasi AL, Albert R (1999) Emergence of scaling in random networks. Science 286:509-512.

Bartos M, Vida I, Jonas P (2007) Synaptic mechanisms of synchronized gamma oscillations in inhibitory interneuron networks. Nature reviews Neuroscience 8:45-56.

Basar-Eroglu C, Struber D, Schurmann M, Stadler M, Basar E (1996) Gamma-band responses in the brain: a short review of psychophysiological correlates and functional significance. International journal of psychophysiology : official journal of the International Organization of Psychophysiology 24:101-112.

Bassett DS, Brown JA, Deshpande V, Carlson JM, Grafton ST (2011) Conserved and variable architecture of human white matter connectivity. NeuroImage 54:1262-1279.

Bassett DS, Bullmore E (2006) Small-world brain networks. The Neuroscientist : a review journal bringing neurobiology, neurology and psychiatry 12:512-523.

Bassett DS, Bullmore E, Verchinski BA, Mattay VS, Weinberger DR, Meyer-Lindenberg A (2008) Hierarchical organization of human cortical networks in health and schizophrenia. The Journal of neuroscience : the official journal of the Society for Neuroscience 28:9239-9248.

Bassett DS, Bullmore ET (2009) Human brain networks in health and disease. Current opinion in neurology 22:340-347.

Bassett DS, Nelson BG, Mueller BA, Camchong J, Lim KO (2012) Altered resting state complexity in schizophrenia. NeuroImage 59:2196-2207.

Beckmann CF (2012) Modelling with independent components. NeuroImage.

Beckmann CF, DeLuca M, Devlin JT, Smith SM (2005) Investigations into resting-state connectivity using independent component analysis. Philosophical transactions of the Royal Society of London Series B, Biological sciences 360:1001-1013.

Behrens TE, Berg HJ, Jbabdi S, Rushworth MF, Woolrich MW (2007) Probabilistic diffusion tractography with multiple fibre orientations: What can we gain? NeuroImage 34:144-155.

Behrens TE, Woolrich MW, Jenkinson M, Johansen-Berg H, Nunes RG, Clare S, Matthews PM, Brady JM, Smith SM (2003) Characterization and propagation of uncertainty in diffusion-weighted MR imaging. Magnetic resonance in medicine : official journal of the Society of Magnetic Resonance in Medicine / Society of Magnetic Resonance in Medicine 50:1077-1088.

Berger HJ (1929) Über das Elektroenkephalogramm des Menschen. Archiv für Psychiatrie und Nervenkrankheiten 87:527-570.

Biswal B, Yetkin FZ, Haughton VM, Hyde JS (1995) Functional connectivity in the motor cortex of resting human brain using echo-planar MRI.

Magnetic resonance in medicine : official journal of the Society of Magnetic Resonance in Medicine / Society of Magnetic Resonance in Medicine 34:537-541.

Biswal BB, Mennes M, Zuo XN, Gohel S, Kelly C, Smith SM, Beckmann CF, Adelstein JS, Buckner RL, Colcombe S, Dogonowski AM, Ernst M, Fair D, Hampson M, Hoptman MJ, Hyde JS, Kiviniemi VJ, Kötter R, Li SJ, Lin CP, Lowe MJ, Mackay C, Madden DJ, Madsen KH, Margulies DS, Mayberg HS, McMahon K, Monk CS, Mostofsky SH, Nagel BJ, Pekar JJ, Peltier SJ, Petersen SE, Riedl V, Rombouts SA, Rypma B, Schlaggar BL, Schmidt S, Seidler RD, Siegle GJ, Sorg C, Teng GJ, Veijola J, Villringer A, Walter M, Wang L, Weng XC, Whitfield-Gabrieli S, Williamson P, Windischberger C, Zang YF, Zhang HY, Castellanos FX, Milham MP (2010) Toward discovery science of human brain function. Proceedings of the National Academy of Sciences of the United States of America 107:4734-4739.

Boccaletti S, Latora V, Moreno Y, Chavez M, Hwang D-U (2006) Complex networks: Structure and dynamics. Physics Reports 424:175-308.

Bonavita S, Gallo A, Sacco R, Corte MD, Bisecco A, Docimo R, Lavorgna L, Corbo D, Costanzo AD, Tortora F, Cirillo M, Esposito F, Tedeschi G (2011) Distributed changes in default-mode resting-state connectivity in multiple sclerosis. Multiple sclerosis 17:411-422.

Borgers C, Kopell N (2003) Synchronization in networks of excitatory and inhibitory neurons with sparse, random connectivity. Neural computation 15:509-538.

Braun U, Plichta MM, Esslinger C, Sauer C, Haddad L, Grimm O, Mier D, Mohnke S, Heinz A, Erk S, Walter H, Seiferth N, Kirsch P, Meyer-Lindenberg A (2012) Test-retest reliability of resting-state connectivity network characteristics using fMRI and graph theoretical measures. NeuroImage 59:1404-1412.

Breakspear M, Heitmann S, Daffertshofer A (2010) Generative models of cortical oscillations: neurobiological implications of the Kuramoto model. Frontiers in human neuroscience 4.

Breakspear M, Terry JR, Friston KJ (2003) Modulation of excitatory synaptic coupling facilitates synchronization and complex dynamics in a biophysical model of neuronal dynamics. Network 14:703-732.

Breakspear M, Williams LM, Stam CJ (2004) A novel method for the topographic analysis of neural activity reveals formation and dissolution of 'Dynamic Cell Assemblies'. Journal of computational neuroscience 16:49-68.

Bressler SL, Tognoli E (2006) Operational principles of neurocognitive networks. International journal of psychophysiology : official journal of the International Organization of Psychophysiology 60:139-148.

Brodmann K (1909) Vergleichende Lokalisationslehre der Grosshirnrinde. Leipzig : Johann Ambrosius Bart.

Brookes MJ, Hale JR, Zumer JM, Stevenson CM, Francis ST, Barnes GR, Owen JP, Morris PG, Nagarajan SS (2011a) Measuring functional connectivity using MEG: methodology and comparison with fcMRI. NeuroImage 56:1082-1104.

Brookes MJ, Woolrich M, Luckhoo H, Price D, Hale JR, Stephenson MC, Barnes GR, Smith SM, Morris PG (2011b) Investigating the electrophysiological basis of resting state networks using magnetoencephalography. Proceedings of the National Academy of Sciences of the United States of America 108:16783-16788.

Brunel N (2000) Dynamics of sparsely connected networks of excitatory and inhibitory spiking neurons. Journal of computational neuroscience 8:183-208.

Brunel N, Wang XJ (2001) Effects of neuromodulation in a cortical network model of object working memory dominated by recurrent inhibition. Journal of computational neuroscience 11:63-85.

Brunel N, Wang XJ (2003) What determines the frequency of fast network oscillations with irregular neural discharges? I. Synaptic dynamics and excitation-inhibition balance. Journal of neurophysiology 90:415-430.

Buckner RL, Andrews-Hanna JR, Schacter DL (2008) The brain's default network: anatomy, function, and relevance to disease. Annals of the New York Academy of Sciences 1124:1-38.

Buckner RL, Bandettini PA, O'Craven KM, Savoy RL, Petersen SE, Raichle ME, Rosen BR (1996) Detection of cortical activation during averaged single trials of a cognitive task using functional magnetic resonance imaging. Proceedings of the National Academy of Sciences of the United States of America 93:14878-14883.

Buckner RL, Snyder AZ, Sanders AL, Raichle ME, Morris JC (2000) Functional brain imaging of young, nondemented, and demented older adults. Journal of cognitive neuroscience 12 Suppl 2:24-34.

Bullmore E, Brammer M, Williams SC, Rabe-Hesketh S, Janot N, David A, Mellers J, Howard R, Sham P (1996) Statistical methods of estimation and inference for functional MR image analysis. Magnetic resonance in medicine : official journal of the Society of Magnetic Resonance in Medicine / Society of Magnetic Resonance in Medicine 35:261-277.

Bullmore E, Sporns O (2009) Complex brain networks: graph theoretical analysis of structural and functional systems. Nat Rev Neurosci 10:186-198.

Bullmore ET, Frangou S, Murray RM (1997) The dysplastic net hypothesis: an integration of developmental and dysconnectivity theories of schizophrenia. Schizophrenia research 28:143-156.

Buzsaki G, Draguhn A (2004) Neuronal oscillations in cortical networks. Science 304:1926-1929.

Cabral J, Hugues E, Kringelbach ML, Deco G (2012a) Modeling disconnection effects on resting-state functional connectivity. NeuroImage (In press).

Cabral J, Hugues E, Sporns O, Deco G (2011) Role of local network oscillations in resting-state functional connectivity. Neuroimage 57:130-139.

Cabral J, Kringelbach ML, Deco G (2012b) Functional graph alterations in schizophrenia: a result from a global anatomical decoupling? Pharmacopsychiatry In press.

Cammoun L, Gigandet X, Meskaldji D, Thiran JP, Sporns O, Do KQ, Maeder P, Meuli R, Hagmann P (2012) Mapping the human connectome at multiple scales with diffusion spectrum MRI. Journal of neuroscience methods 203:386-397.

Caton R (1875) Electrical Currents of the Brain. Chicago Journal of Nervous & Mental Disease 2:610.

Cohen D (1968) Magnetoencephalography - Evidence of Magnetic Fields Produced by Alpha-Rhythm Currents. Science 161:784-&.

Collins D, Neelin P, Peters T, Evans AC (1994) Automatic 3D intersubject registration of MR volumetric data in standardized Talairach space. Journal of computer assisted tomography 18:192-205.

Collins DL, Zijdenbos AP, Kollokian V, Sled JG, Kabani NJ, Holmes CJ, Evans AC (1998) Design and construction of a realistic digital brain phantom. IEEE transactions on medical imaging 17:463-468.

Cornew L, Roberts TP, Blaskey L, Edgar JC (2011) Resting-State Oscillatory Activity in Autism Spectrum Disorders. Journal of autism and developmental disorders.

Coyle JT, Tsai G, Goff D (2003) Converging evidence of NMDA receptor hypofunction in the pathophysiology of schizophrenia. Annals of the New York Academy of Sciences 1003:318-327.

Chen ZJ, He Y, Rosa-Neto P, Germann J, Evans AC (2008) Revealing modular architecture of human brain structural networks by using cortical thickness from MRI. Cerebral cortex 18:2374-2381.

Cherkassky VL, Kana RK, Keller TA, Just MA (2006) Functional connectivity in a baseline resting-state network in autism. Neuroreport 17:1687-1690.

Daffertshofer A, van Wijk BC (2011) On the Influence of Amplitude on the Connectivity between Phases. Frontiers in neuroinformatics 5:6.

Damoiseaux JS, Greicius MD (2009) Greater than the sum of its parts: a review of studies combining structural connectivity and resting-state functional connectivity. Brain structure & function 213:525-533.

Damoiseaux JS, Prater KE, Miller BL, Greicius MD (2012) Functional connectivity tracks clinical deterioration in Alzheimer's disease. Neurobiology of aging 33:828 e819-830.

Damoiseaux JS, Rombouts SA, Barkhof F, Scheltens P, Stam CJ, Smith SM, Beckmann CF (2006) Consistent resting-state networks across healthy subjects. Proceedings of the National Academy of Sciences of the United States of America 103:13848-13853.

Davis KL, Stewart DG, Friedman JI, Buchsbaum M, Harvey PD, Hof PR, Buxbaum J, Haroutunian V (2003) White matter changes in schizophrenia: evidence for myelin-related dysfunction. Archives of general psychiatry 60:443-456.

De Luca M, Beckmann CF, De Stefano N, Matthews PM, Smith SM (2006) fMRI resting state networks define distinct modes of long-distance interactions in the human brain. NeuroImage 29:1359-1367.

de Pasquale F, Della Penna S, Snyder AZ, Lewis C, Mantini D, Marzetti L, Belardinelli P, Ciancetta L, Pizzella V, Romani GL, Corbetta M (2010) Temporal dynamics of spontaneous MEG activity in brain networks. Proceedings of the National Academy of Sciences of the United States of America 107:6040-6045.

Deco G, Jirsa V, McIntosh AR, Sporns O, Kötter R (2009) Key role of coupling, delay, and noise in resting brain fluctuations. Proceedings of the National Academy of Sciences of the United States of America 106:10302-10307.

Deco G, Jirsa VK (2012) Ongoing cortical activity at rest: criticality, multistability, and ghost attractors. The Journal of neuroscience : the official journal of the Society for Neuroscience 32:3366-3375.

Deco G, Jirsa VK, McIntosh AR (2011) Emerging concepts for the dynamical organization of resting-state activity in the brain. Nature reviews Neuroscience 12:43-56.

Deco G, Jirsa VK, Robinson PA, Breakspear M, Friston K (2008) The dynamic brain: from spiking neurons to neural masses and cortical fields. PLoS computational biology 4:e1000092.

Desikan RS, Segonne F, Fischl B, Quinn BT, Dickerson BC, Blacker D, Buckner RL, Dale AM, Maguire RP, Hyman BT, Albert MS, Killiany RJ (2006) An automated labeling system for subdividing the human cerebral cortex on MRI scans into gyral based regions of interest. NeuroImage 31:968-980.

Earl MG, Strogatz SH (2003) Synchronization in oscillator networks with delayed coupling: a stability criterion. Physical review E, Statistical, nonlinear, and soft matter physics 67:036204.

Faivre A, Rico A, Zaaraoui W, Crespy L, Reuter F, Wybrecht D, Soulier E, Malikova I, Confort-Gouny S, Cozzone PJ, Pelletier J, Ranjeva JP, Audoin B (2012) Assessing brain connectivity at rest is clinically relevant in early multiple sclerosis. Multiple sclerosis.

Ferrarini L, Veer IM, Baerends E, van Tol MJ, Renken RJ, van der Wee NJ, Veltman DJ, Aleman A, Zitman FG, Penninx BW, van Buchem MA, Reiber JH, Rombouts SA, Milles J (2009) Hierarchical functional modularity in the resting-state human brain. Human brain mapping 30:2220-2231.

Fitzhugh R (1961) Impulses and Physiological States in Theoretical Models of Nerve Membrane. Biophysical journal 1:445-466.

Fornito A, Zalesky A, Bullmore ET (2010) Network scaling effects in graph analytic studies of human resting-state FMRI data. Frontiers in systems neuroscience 4:22.

Fox MD, Greicius M (2010) Clinical applications of resting state functional connectivity. Frontiers in systems neuroscience 4:19.

Fox MD, Raichle ME (2007) Spontaneous fluctuations in brain activity observed with functional magnetic resonance imaging. Nat Rev Neurosci 8:700-711.

Fox MD, Snyder AZ, Vincent JL, Corbetta M, Van Essen DC, Raichle ME (2005) The human brain is intrinsically organized into dynamic, anticorrelated functional networks. Proceedings of the National Academy of Sciences of the United States of America 102:9673-9678.

Freyer F, Roberts JA, Becker R, Robinson PA, Ritter P, Breakspear M (2011) Biophysical mechanisms of multistability in resting-state cortical rhythms. J Neurosci 31:6353-6361.

Fries P (2005) A mechanism for cognitive dynamics: neuronal communication through neuronal coherence. Trends in cognitive sciences 9:474-480.

Friston KJ (1996) Theoretical neurobiology and schizophrenia. British medical bulletin 52:644-655.

Friston KJ (1998) The disconnection hypothesis. Schizophr Res 30:115-125.

Friston KJ, Frith CD (1995) Schizophrenia: a disconnection syndrome? Clinical neuroscience 3:89-97.

Friston KJ, Frith CD, Frackowiak RS, Turner R (1995) Characterizing dynamic brain responses with fMRI: a multivariate approach. NeuroImage 2:166-172.

Friston KJ, Harrison L, Penny W (2003) Dynamic causal modelling. NeuroImage 19:1273-1302.

Friston KJ, Holmes AP, Worsley KJ, Poline JP, Frith CD, Frackowiak RSJ (1994) Statistical parametric maps in functional imaging: A general linear approach. Human brain mapping 2:189-210.

Friston KJ, Mechelli A, Turner R, Price CJ (2000) Nonlinear responses in fMRI: the Balloon model, Volterra kernels, and other hemodynamics. NeuroImage 12:466-477.

Gamez D (2012) From Baconian to Popperian Neuroscience. Neural systems & circuits 2:2.

Gardiner CW (2004) Handbook of Stochastic Methods for Physics, Chemistry and the Natural Sciences Springer-Verlag.

Ghosh A, Rho Y, McIntosh AR, Kötter R, Jirsa VK (2008) Noise during rest enables the exploration of the brain's dynamic repertoire. PLoS computational biology 4:e1000196.

Gong G, He Y, Concha L, Lebel C, Gross DW, Evans AC, Beaulieu C (2009a) Mapping anatomical connectivity patterns of human cerebral cortex using in vivo diffusion tensor imaging tractography. Cerebral cortex 19:524-536.

Gong G, Rosa-Neto P, Carbonell F, Chen ZJ, He Y, Evans AC (2009b) Age- and gender-related differences in the cortical anatomical network. The Journal of neuroscience : the official journal of the Society for Neuroscience 29:15684-15693.

Greicius M (2008) Resting-state functional connectivity in neuropsychiatric disorders. Current opinion in neurology 21:424-430.

Greicius MD, Flores BH, Menon V, Glover GH, Solvason HB, Kenna H, Reiss AL, Schatzberg AF (2007) Resting-state functional connectivity in major depression: abnormally increased contributions from subgenual cingulate cortex and thalamus. Biological psychiatry 62:429-437.

Greicius MD, Krasnow B, Reiss AL, Menon V (2003) Functional connectivity in the resting brain: a network analysis of the default mode hypothesis. Proceedings of the National Academy of Sciences of the United States of America 100:253-258.

Greicius MD, Srivastava G, Reiss AL, Menon V (2004) Default-mode network activity distinguishes Alzheimer's disease from healthy aging: evidence from functional MRI. Proceedings of the National Academy of Sciences of the United States of America 101:4637-4642.

Greicius MD, Supekar K, Menon V, Dougherty RF (2009) Resting-state functional connectivity reflects structural connectivity in the default mode network. Cerebral cortex 19:72-78.

Gusnard DA, Raichle ME, Raichle ME (2001) Searching for a baseline: functional imaging and the resting human brain. Nature reviews Neuroscience 2:685-694.

Hagmann P (2005) From diffusion MRI to brain connectomics. Ecole Polytechnique Fédérale de Lausanne (EPFL) PhD Thesis:127 p.

Hagmann P, Cammoun L, Gigandet X, Meuli R, Honey CJ, Wedeen VJ, Sporns O (2008) Mapping the structural core of human cerebral cortex. PLoS biology 6:e159.

Hagmann P, Kurant M, Gigandet X, Thiran P, Wedeen VJ, Meuli R, Thiran JP (2007) Mapping human whole-brain structural networks with diffusion MRI. PloS one 2:e597.

Hartman D, Hlinka J, Palus M, Mantini D, Corbetta M (2011) The role of nonlinearity in computing graph-theoretical properties of resting-state functional magnetic resonance imaging brain networks. Chaos 21:013119.

Hawellek DJ, Hipp JF, Lewis CM, Corbetta M, Engel AK (2011) Increased functional connectivity indicates the severity of cognitive impairment in multiple sclerosis. Proceedings of the National Academy of Sciences of the United States of America 108:19066-19071.

He BJ, Snyder AZ, Zempel JM, Smyth MD, Raichle ME (2008) Electrophysiological correlates of the brain's intrinsic large-scale functional architecture. Proceedings of the National Academy of Sciences of the United States of America 105:16039-16044.

He Y, Chen ZJ, Evans AC (2007) Small-world anatomical networks in the human brain revealed by cortical thickness from MRI. Cerebral cortex 17:2407-2419.

He Y, Evans A (2010) Graph theoretical modeling of brain connectivity. Current opinion in neurology 23:341-350.

Hipp JF, Hawellek DJ, Corbetta M, Siegel M, Engel AK (2012) Large-scale cortical correlation structure of spontaneous oscillatory activity. Nature neuroscience.

Hlinka J, Palus M, Vejmelka M, Mantini D, Corbetta M (2011) Functional connectivity in resting-state fMRI: is linear correlation sufficient? NeuroImage 54:2218-2225.

Honey CJ, Kötter R, Breakspear M, Sporns O (2007) Network structure of cerebral cortex shapes functional connectivity on multiple time scales. Proceedings of the National Academy of Sciences of the United States of America 104:10240-10245.

Honey CJ, Sporns O (2008) Dynamical consequences of lesions in cortical networks. Human brain mapping 29:802-809.

Honey CJ, Sporns O, Cammoun L, Gigandet X, Thiran JP, Meuli R, Hagmann P (2009) Predicting human resting-state functional connectivity from structural connectivity. Proceedings of the National Academy of Sciences of the United States of America 106:2035-2040.

Hoppensteadt FC, Izhikevich E (1997) Weakly Connected Neural Networks. New York, NY: Springer-Verlag.

Hoptman MJ, Ardekani BA, Butler PD, Nierenberg J, Javitt DC, Lim KO (2004) DTI and impulsivity in schizophrenia: a first voxelwise correlational analysis. Neuroreport 15:2467-2470.

Humphries MD, Gurney K (2008) Network 'small-world-ness': a quantitative method for determining canonical network equivalence. PloS one 3:e0002051.

Humphries MD, Gurney K, Prescott TJ (2006) The brainstem reticular formation is a small-world, not scale-free, network. Proceedings Biological sciences / The Royal Society 273:503-511.

Iturria-Medina Y, Canales-Rodriguez EJ, Melie-Garcia L, Valdes-Hernandez PA, Martinez-Montes E, Aleman-Gomez Y, Sanchez-Bornot JM (2007) Characterizing brain anatomical connections using diffusion weighted MRI and graph theory. NeuroImage 36:645-660.

Iturria-Medina Y, Sotero RC, Canales-Rodriguez EJ, Aleman-Gomez Y, Melie-Garcia L (2008) Studying the human brain anatomical network via diffusion-weighted MRI and Graph Theory. NeuroImage 40:1064-1076.

Izhikevich EM, Edelman GM (2008) Large-scale model of mammalian thalamocortical systems. Proceedings of the National Academy of Sciences of the United States of America 105:3593-3598.

Jenkinson M, Bannister P, Brady M, Smith S (2002) Improved optimization for the robust and accurate linear registration and motion correction of brain images. NeuroImage 17:825-841.

Jirsa VK (2004) Connectivity and dynamics of neural information processing. Neuroinformatics 2:183-204.

Jirsa VK (2009) Neural field dynamics with local and global connectivity and time delay. Philosophical transactions Series A, Mathematical, physical, and engineering sciences 367:1131-1143.

Jirsa VK, Ding M (2004) Will a large complex system with time delays be stable? Physical review letters 93:070602.

Jirsa VK, Kelso JA (2000) Spatiotemporal pattern formation in neural systems with heterogeneous connection topologies. Physical review E, Statistical physics, plasmas, fluids, and related interdisciplinary topics 62:8462-8465.

Jirsa VK, McIntosh AR (2007) Handbook of Brain Connectivity. Springer, Heidelberg, Germany pp 3-64.

Jirsa VK, Sporns O, Breakspear M, Deco G, McIntosh AR (2010) Towards the virtual brain: network modeling of the intact and the damaged brain. Archives italiennes de biologie 148:189-205.

Kelso JA (2012) Multistability and metastability: understanding dynamic coordination in the brain. Philosophical transactions of the Royal Society of London Series B, Biological sciences 367:906-918.

Kennedy DP, Redcay E, Courchesne E (2006) Failing to deactivate: resting functional abnormalities in autism. Proceedings of the National Academy of Sciences of the United States of America 103:8275-8280.

Kilner JM, Mattout J, Henson R, Friston KJ (2005) Hemodynamic correlates of EEG: a heuristic. NeuroImage 28:280-286.

Kim S, Park SH, Ryu CS (1997) Multistability in coupled oscillator systems with time delay. Physical review letters 79:2911-2914.

Knock SA, McIntosh AR, Sporns O, Kötter R, Hagmann P, Jirsa VK (2009) The effects of physiologically plausible connectivity structure on local and global dynamics in large scale brain models. Journal of neuroscience methods 183:86-94.

Koch MA, Norris DG, Hund-Georgiadis M (2002) An investigation of functional and anatomical connectivity using magnetic resonance imaging. NeuroImage 16:241-250.

Kötter R (2004) Online retrieval, processing, and visualization of primate connectivity data from the CoCoMac database. Neuroinformatics 2:127-144.

Kötter R, Wanke E (2005) Mapping brains without coordinates. Philosophical transactions of the Royal Society of London Series B, Biological sciences 360:751-766.

Kuramoto Y (1984) Chemical Oscillations,Waves, and Turbulence. Springer-Verlag, Berlin.

Lai MC, Lombardo MV, Chakrabarti B, Sadek SA, Pasco G, Wheelwright SJ, Bullmore ET, Baron-Cohen S, Consortium MA, Suckling J (2010) A shift to randomness of brain oscillations in people with autism. Biological psychiatry 68:1092-1099.

Larson-Prior LJ, Power JD, Vincent JL, Nolan TS, Coalson RS, Zempel J, Snyder AZ, Schlaggar BL, Raichle ME, Petersen SE (2011) Modulation of the brain's functional network architecture in the transition from wake to sleep. Progress in brain research 193:277-294.

Larter R, Speelman B, Worth RM (1999) A coupled ordinary differential equation lattice model for the simulation of epileptic seizures. Chaos 9:795-804.

Latora V, Marchiori M (2001) Efficient behavior of small-world networks. Physical review letters 87:198701.

Laufs H, Krakow K, Sterzer P, Eger E, Beyerle A, Salek-Haddadi A, Kleinschmidt A (2003) Electroencephalographic signatures of attentional and cognitive default modes in spontaneous brain activity fluctuations at rest. Proceedings of the National Academy of Sciences of the United States of America 100:11053-11058.

Lee WS, Ott E, Antonsen TM (2009) Large coupled oscillator systems with heterogeneous interaction delays. Physical review letters 103:044101.

Leicht EA, Newman ME (2008) Community structure in directed networks. Physical review letters 100:118703.

Leopold DA, Murayama Y, Logothetis NK (2003) Very slow activity fluctuations in monkey visual cortex: implications for functional brain imaging. Cerebral cortex 13:422-433.

Lerch JP, Worsley K, Shaw WP, Greenstein DK, Lenroot RK, Giedd J, Evans AC (2006) Mapping anatomical correlations across cerebral cortex (MACACC) using cortical thickness from MRI. NeuroImage 31:993-1003.

Liang M, Zhou Y, Jiang T, Liu Z, Tian L, Liu H, Hao Y (2006) Widespread functional disconnectivity in schizophrenia with resting-state functional magnetic resonance imaging. Neuroreport 17:209-213.

Lim KO, Hedehus M, Moseley M, de Crespigny A, Sullivan EV, Pfefferbaum A (1999) Compromised white matter tract integrity in schizophrenia inferred from diffusion tensor imaging. Archives of general psychiatry 56:367-374.

Liu HS, Stufflebeam SM, Sepulcre J, Hedden T, Buckner RL (2009) Evidence from intrinsic activity that asymmetry of the human brain is controlled by multiple factors. Proceedings of the National Academy of Sciences of the United States of America 106:20499-20503.

Liu Y, Liang M, Zhou Y, He Y, Hao Y, Song M, Yu C, Liu H, Liu Z, Jiang T (2008) Disrupted small-world networks in schizophrenia. Brain : a journal of neurology 131:945-961.

Liu Z, Fukunaga M, de Zwart JA, Duyn JH (2010) Large-scale spontaneous fluctuations and correlations in brain electrical activity observed with magnetoencephalography. NeuroImage 51:102-111.

Logothetis NK, Pauls J, Augath M, Trinath T, Oeltermann A (2001) Neurophysiological investigation of the basis of the fMRI signal. Nature 412:150-157.

Lu H, Zou Q, Gu H, Raichle ME, Stein EA, Yang Y (2012) Rat brains also have a default mode network. Proceedings of the National Academy of Sciences of the United States of America 109:3979-3984.

Lynall ME, Bassett DS, Kerwin R, McKenna PJ, Kitzbichler M, Muller U, Bullmore E (2010) Functional connectivity and brain networks in

schizophrenia. The Journal of neuroscience : the official journal of the Society for Neuroscience 30:9477-9487.

Mantini D, Perrucci MG, Del Gratta C, Romani GL, Corbetta M (2007) Electrophysiological signatures of resting state networks in the human brain. Proceedings of the National Academy of Sciences of the United States of America 104:13170-13175.

Markram H (2006) The blue brain project. Nature reviews Neuroscience 7:153-160.

Mattia M, Del Giudice P (2002) Population dynamics of interacting spiking neurons. Physical review E, Statistical, nonlinear, and soft matter physics 66:051917.

Mazoyer B, Zago L, Mellet E, Bricogne S, Etard O, Houde O, Crivello F, Joliot M, Petit L, Tzourio-Mazoyer N (2001) Cortical networks for working memory and executive functions sustain the conscious resting state in man. Brain research bulletin 54:287-298.

Meunier D, Achard S, Morcom A, Bullmore E (2009) Age-related changes in modular organization of human brain functional networks. NeuroImage 44:715-723.

Micheloyannis S, Vourkas M, Tsirka V, Karakonstantaki E, Kanatsouli K, Stam CJ (2009) The influence of ageing on complex brain networks: a graph theoretical analysis. Human brain mapping 30:200-208.

Miller KJ, Weaver KE, Ojemann JG (2009) Direct electrophysiological measurement of human default network areas. Proceedings of the National Academy of Sciences of the United States of America 106:12174-12177.

Mitelman SA, Newmark RE, Torosjan Y, Chu KW, Brickman AM, Haznedar MM, Hazlett EA, Tang CY, Shihabuddin L, Buchsbaum MS (2006) White matter fractional anisotropy and outcome in schizophrenia. Schizophrenia research 87:138-159.

Mobascher A, Warbrick T, Brinkmeyer J, Musso F, Stoecker T, Shah NJ, Vossel S, Winterer G (2011) Nicotine effects on attention in schizophrenia: a simultaneous EEG-fMRI study. Eur Neuropsychopharm 21:S515-S516.

Montbrio E, Pazo D, Schmidt J (2006) Time delay in the Kuramoto model with bimodal frequency distribution. Phys Rev E 74.

Morcom AM, Fletcher PC (2007) Does the brain have a baseline ? Why we should be resisting a rest. NeuroImage 37:1073-1082.

Morris C, Lecar H (1981) Voltage oscillations in the barnacle giant muscle fiber. Biophysical journal 35:193-213.

Murphy K, Birn RM, Handwerker DA, Jones TB, Bandettini PA (2009) The impact of global signal regression on resting state correlations: are anti-correlated networks introduced? NeuroImage 44:893-905.

Nagumo J, Arimoto S, Yoshizawa S (1962) An active pulse transmission line simulating nerve axon. Proc IRE 50:2061-2070.

Newman ME (2006) Modularity and community structure in networks. Proceedings of the National Academy of Sciences of the United States of America 103:8577-8582.

Niebur E, Schuster HG, Kammen DM (1991) Collective frequencies and metastability in networks of limit-cycle oscillators with time delay. Physical review letters 67:2753-2756.

Niedermeyer E, Lopes da Silva FH (1982) Electroencephalography, basic principles, clinical applications, and related fields. Urban & Schwarzenberg.

Nikouline VV, Linkenkaer-Hansen K, Huttunen J, Ilmoniemi RJ (2001) Interhemispheric phase synchrony and amplitude correlation of spontaneous beta oscillations in human subjects: a magnetoencephalographic study. Neuroreport 12:2487-2491.

Nir Y, Mukamel R, Dinstein I, Privman E, Harel M, Fisch L, Gelbard-Sagiv H, Kipervasser S, Andelman F, Neufeld MY, Kramer U, Arieli A, Fried I, Malach R (2008) Interhemispheric correlations of slow spontaneous neuronal fluctuations revealed in human sensory cortex. Nature neuroscience 11:1100-1108.

Ogawa S, Lee TM, Kay AR, Tank DW (1990) Brain magnetic resonance imaging with contrast dependent on blood oxygenation. Proceedings of the National Academy of Sciences of the United States of America 87:9868-9872.

Palva S, Palva JM (2012) Discovering oscillatory interaction networks with M/EEG: challenges and breakthroughs. Trends in cognitive sciences 16:219-230.

Penzias AA, Wilson RW (1965) A Measurement of Excess Antenna Temperature at 4080mc/S. Astrophys J 142:419-&.

Phelps ME, Hoffman EJ, Mullani NA, Ter-Pogossian MM (1975) Application of annihilation coincidence detection to transaxial reconstruction tomography. Journal of nuclear medicine : official publication, Society of Nuclear Medicine 16:210-224.

Pikovski A, Rosemblum M, Kurths J (2001) Synchronization, a Universal Concept in Nonlinear Sciences. Cambridge University Press, England.

Pikovsky A, Rosenblum M, Kurths J (2001) Synchronization: A Universal Concept in Nonlinear Sciences. Cambridge University Press.

Platen E (1999) An introduction to numerical methods for stochastic differential equations. Acta Numerica 197-246.

Popovych O, Tass P, Hauptmann C (2011) Desynchronization. Scholarpedia 6:1352.

Popovych OV, Maistrenko YL, Tass PA (2005) Phase chaos in coupled oscillators. Physical review E, Statistical, nonlinear, and soft matter physics 71:065201.

Popper K (1934) The Logic of Scientific Discovery (Logik der Forschung, English translation 1959).

Raichle ME (1985) Positron emission tomography. Progress in brain imaging. Nature 317:574-576.

Raichle ME, MacLeod AM, Snyder AZ, Powers WJ, Gusnard DA, Shulman GL (2001) A default mode of brain function. Proceedings of the National Academy of Sciences of the United States of America 98:676-682.

Ravasz E, Barabasi AL (2003) Hierarchical organization in complex networks. Physical review E, Statistical, nonlinear, and soft matter physics 67:026112.

Risken H (1989) The Fokker–Planck Equation: Methods of Solutions and Applications. Springer Series in Synergetics, Springer.

Robinson S, Vrba J (1998) Functional neuroimaging by synthetic aperture magnetometry. Recent Advances in Biomagnetism 302-305.

Rombouts SA, Barkhof F, Goekoop R, Stam CJ, Scheltens P (2005) Altered resting state networks in mild cognitive impairment and mild Alzheimer's disease: an fMRI study. Human brain mapping 26:231-239.

Rombouts SA, Damoiseaux JS, Goekoop R, Barkhof F, Scheltens P, Smith SM, Beckmann CF (2009) Model-free group analysis shows altered BOLD FMRI networks in dementia. Human brain mapping 30:256-266.

Rubinov M, Knock SA, Stam CJ, Micheloyannis S, Harris AW, Williams LM, Breakspear M (2009) Small-world properties of nonlinear brain activity in schizophrenia. Human brain mapping 30:403-416.

Rubinov M, Sporns O (2010) Complex network measures of brain connectivity: uses and interpretations. NeuroImage 52:1059-1069.

Salvador R, Suckling J, Coleman MR, Pickard JD, Menon D, Bullmore E (2005) Neurophysiological architecture of functional magnetic resonance images of human brain. Cerebral cortex 15:1332-1342.

Sanchez-Vives MV, McCormick DA (2000) Cellular and network mechanisms of rhythmic recurrent activity in neocortex. Nature neuroscience 3:1027-1034.

Sanz-Arigita EJ, Schoonheim MM, Damoiseaux JS, Rombouts SA, Maris E, Barkhof F, Scheltens P, Stam CJ (2010) Loss of 'small-world' networks in Alzheimer's disease: graph analysis of FMRI resting-state functional connectivity. PloS one 5:e13788.

Saxe R, Kanwisher N (2003) People thinking about thinking people - The role of the temporo-parietal junction in "theory of mind". NeuroImage 19:1835-1842.

Scheeringa R, Fries P, Petersson KM, Oostenveld R, Grothe I, Norris DG, Hagoort P, Bastiaansen MC (2011) Neuronal dynamics underlying high- and low-frequency EEG oscillations contribute independently to the human BOLD signal. Neuron 69:572-583.

Schoonheim MM, Geurts JJ, Landi D, Douw L, van der Meer ML, Vrenken H, Polman CH, Barkhof F, Stam CJ (2011) Functional connectivity changes in multiple sclerosis patients: A graph analytical study of MEG resting state data. Human brain mapping.

Shanahan M (2010) Metastable chimera states in community-structured oscillator networks. Chaos 20:013108.

Sheline YI, Barch DM, Price JL, Rundle MM, Vaishnavi SN, Snyder AZ, Mintun MA, Wang S, Coalson RS, Raichle ME (2009) The default mode network and self-referential processes in depression. Proceedings of the National Academy of Sciences of the United States of America 106:1942-1947.

Shmuel A, Leopold DA (2008) Neuronal correlates of spontaneous fluctuations in fMRI signals in monkey visual cortex: Implications for functional connectivity at rest. Human brain mapping 29:751-761.

Shulman GL, Fiez JA, Corbetta M, Buckner RL, Miezin FM, Raichle ME, Petersen SE (1997) Common blood flow changes across visual tasks .2. Decreases in cerebral cortex. Journal of cognitive neuroscience 9:648-663.

Skelly LR, Calhoun V, Meda SA, Kim J, Mathalon DH, Pearlson GD (2008) Diffusion tensor imaging in schizophrenia: relationship to symptoms. Schizophrenia research 98:157-162.

Skudlarski P, Jagannathan K, Anderson K, Stevens MC, Calhoun VD, Skudlarska BA, Pearlson G (2010) Brain connectivity is not only lower but different in schizophrenia: a combined anatomical and functional approach. Biological psychiatry 68:61-69.

Skudlarski P, Jagannathan K, Calhoun VD, Hampson M, Skudlarska BA, Pearlson G (2008) Measuring brain connectivity: diffusion tensor imaging validates resting state temporal correlations. NeuroImage 43:554-561.

Sporns O (2009) Connectome. Scholarpedia 5:5584.

Sporns O, Chialvo DR, Kaiser M, Hilgetag CC (2004) Organization, development and function of complex brain networks. Trends in cognitive sciences 8:418-425.

Sporns O, Honey CJ (2006) Small worlds inside big brains. Proceedings of the National Academy of Sciences of the United States of America 103:19219-19220.

Sporns O, Tononi G, Edelman GM (2000) Connectivity and complexity: the relationship between neuroanatomy and brain dynamics. Neural

networks : the official journal of the International Neural Network Society 13:909-922.

Sporns O, Tononi G, Edelman GM (2002) Theoretical neuroanatomy and the connectivity of the cerebral cortex. Behavioural brain research 135:69-74.

Sporns O, Tononi G, Kotter R (2005) The human connectome: A structural description of the human brain. PLoS computational biology 1:e42.

Sporns O, Zwi JD (2004) The small world of the cerebral cortex. Neuroinformatics 2:145-162.

Stam CJ, de Haan W, Daffertshofer A, Jones BF, Manshanden I, van Cappellen van Walsum AM, Montez T, Verbunt JP, de Munck JC, van Dijk BW, Berendse HW, Scheltens P (2009) Graph theoretical analysis of magnetoencephalographic functional connectivity in Alzheimer's disease. Brain : a journal of neurology 132:213-224.

Stephan KE, Baldeweg T, Friston KJ (2006) Synaptic plasticity and dysconnection in schizophrenia. Biological psychiatry 59:929-939.

Stephan KE, Friston KJ, Frith CD (2009) Dysconnection in schizophrenia: from abnormal synaptic plasticity to failures of self-monitoring. Schizophrenia bulletin 35:509-527.

Strogatz S (2003) Sync: The Emerging Science of Spontaneous

Order Hyperion, New York.

Strogatz SH (2001) Exploring complex networks. Nature 410:268-276.

Supekar K, Menon V, Rubin D, Musen M, Greicius MD (2008a) Network analysis of intrinsic functional brain connectivity in Alzheimer's disease. PLoS computational biology 4:e1000100.

Supekar K, Menon V, Rubin D, Musen M, Greicius MD (2008b) Network analysis of intrinsic functional brain connectivity in Alzheimer's disease. Plos Comput Biol 4:e1000100.

Ter-Pogossian MM, Phelps ME, Hoffman EJ, Mullani NA (1975) A positron-emission transaxial tomograph for nuclear imaging (PETT). Radiology 114:89-98.

Tononi G, Edelman GM, Sporns O (1998) Complexity and coherency: integrating information in the brain. Trends in cognitive sciences 2:474-484.

Tononi G, Sporns O, Edelman GM (1992) Reentry and the problem of integrating multiple cortical areas: simulation of dynamic integration in the visual system. Cerebral cortex 2:310-335.

Tononi G, Sporns O, Edelman GM (1994) A measure for brain complexity: relating functional segregation and integration in the nervous system. Proceedings of the National Academy of Sciences of the United States of America 91:5033-5037.

Tzourio-Mazoyer N, Landeau B, Papathanassiou D, Crivello F, Etard O, Delcroix N, Mazoyer B, Joliot M (2002) Automated anatomical labeling of activations in SPM using a macroscopic anatomical parcellation of the MNI MRI single-subject brain. NeuroImage 15:273-289.

Valencia M, Martinerie J, Dupont S, Chavez M (2008) Dynamic small-world behavior in functional brain networks unveiled by an event-related networks approach. Physical review E, Statistical, nonlinear, and soft matter physics 77:050905.

van den Heuvel MP, Hulshoff Pol HE (2010) Exploring the brain network: a review on resting-state fMRI functional connectivity. European neuropsychopharmacology : the journal of the European College of Neuropsychopharmacology 20:519-534.

van den Heuvel MP, Mandl RC, Kahn RS, Hulshoff Pol HE (2009) Functionally linked resting-state networks reflect the underlying structural connectivity architecture of the human brain. Human brain mapping 30:3127-3141.

van den Heuvel MP, Mandl RC, Stam CJ, Kahn RS, Hulshoff Pol HE (2010) Aberrant frontal and temporal complex network structure in schizophrenia: a graph theoretical analysis. The Journal of neuroscience : the official journal of the Society for Neuroscience 30:15915-15926.

van den Heuvel MP, Stam CJ, Boersma M, Hulshoff Pol HE (2008) Small-world and scale-free organization of voxel-based resting-state functional connectivity in the human brain. NeuroImage 43:528-539.

Van Veen BD, van Drongelen W, Yuchtman M, Suzuki A (1997) Localization of brain electrical activity via linearly constrained minimum variance spatial filtering. IEEE transactions on bio-medical engineering 44:867-880.

van Wijk BC, Stam CJ, Daffertshofer A (2010) Comparing brain networks of different size and connectivity density using graph theory. PloS one 5:e13701.

Veer IM, Beckmann CF, van Tol MJ, Ferrarini L, Milles J, Veltman DJ, Aleman A, van Buchem MA, van der Wee NJ, Rombouts SA (2010) Whole brain resting-state analysis reveals decreased functional connectivity in major depression. Frontiers in systems neuroscience 4.

Vincent JL, Patel GH, Fox MD, Snyder AZ, Baker JT, Van Essen DC, Zempel JM, Snyder LH, Corbetta M, Raichle ME (2007) Intrinsic functional architecture in the anaesthetized monkey brain. Nature 447:83-86.

Wagner AD, Shannon BJ, Kahn I, Buckner RL (2005) Parietal lobe contributions to episodic memory retrieval. Trends in cognitive sciences 9:445-453.

Wang J, Wang L, Zang Y, Yang H, Tang H, Gong Q, Chen Z, Zhu C, He Y (2009a) Parcellation-dependent small-world brain functional networks: a resting-state fMRI study. Human brain mapping 30:1511-1523.

Wang L, Zhu C, He Y, Zang Y, Cao Q, Zhang H, Zhong Q, Wang Y (2009b) Altered small-world brain functional networks in children with attention-deficit/hyperactivity disorder. Human brain mapping 30:638-649.

Watts DJ, Strogatz SH (1998) Collective dynamics of 'small-world' networks. Nature 393:440-442.

Wedeen VJ, Davis TL, Weisskoff RM, Toottell R, Rosen BR, Belliveau JW (1995) White matter connectivity explored by MRI. Proceedings of the First International Conference for Functional Mapping of the Human Brain, Paris P1.36.

Wedeen VJ, Hagmann P, Tseng WY, Reese TG, Weisskoff RM (2005) Mapping complex tissue architecture with diffusion spectrum magnetic resonance imaging. Magnetic resonance in medicine : official journal of the Society of Magnetic Resonance in Medicine / Society of Magnetic Resonance in Medicine 54:1377-1386.

Weng SJ, Wiggins JL, Peltier SJ, Carrasco M, Risi S, Lord C, Monk CS (2010) Alterations of resting state functional connectivity in the default network in adolescents with autism spectrum disorders. Brain research 1313:202-214.

Wernicke C (1906) Grundrisse der Psychiatrie. Leipzig, Germany. Thieme.

Wilson HR, Cowan JD (1972) Excitatory and inhibitory interactions in localised populations of model neurons. Biophysical journal 12.

Wilson HR, Cowan JD (1973) A mathematical theory of the functional dynamics of nervous tissue. Kybernetik 13:55-80.

Winterer G (2006) Cortical microcircuits in schizophrenia - The dopamine hypothesis revisited. Pharmacopsychiatry 39:S68-S71.

Winterer G (2010) Why do patients with schizophrenia smoke? Current opinion in psychiatry 23:112-119.

Winterer G, Weinberger DR (2004) Genes, dopamine and cortical signal-to-noise ratio in schizophrenia. Trends in neurosciences 27:683-690.

Womelsdorf T, Schoffelen JM, Oostenveld R, Singer W, Desimone R, Engel AK, Fries P (2007) Modulation of neuronal interactions through neuronal synchronization. Science 316:1609-1612.

Yeung MKS, Strogatz SH (1999) Time delay in the Kuramoto model of coupled oscillators. Physical review letters 82:648-651.

Yu Q, Sui J, Rachakonda S, He H, Gruner W, Pearlson G, Kiehl KA, Calhoun VD (2011) Altered topological properties of functional network connectivity in schizophrenia during resting state: a small-world brain network study. PloS one 6:e25423.

Zalesky A, Fornito A, Harding IH, Cocchi L, Yucel M, Pantelis C, Bullmore ET (2010) Whole-brain anatomical networks: does the choice of nodes matter? NeuroImage 50:970-983.

Zalesky A, Fornito A, Seal ML, Cocchi L, Westin CF, Bullmore ET, Egan GF, Pantelis C (2011) Disrupted axonal fiber connectivity in schizophrenia. Biological psychiatry 69:80-89.

Zanette DH (2000) Propagating structures in globally coupled systems with time delays. Phys Rev E 62:3167-3172.

Zhou J, Greicius MD, Gennatas ED, Growdon ME, Jang JY, Rabinovici GD, Kramer JH, Weiner M, Miller BL, Seeley WW (2010) Divergent network connectivity changes in behavioural variant frontotemporal dementia and Alzheimer's disease. Brain : a journal of neurology 133:1352-1367.

List of Abbreviations

AAL	Automated Anatomical Labelling
AC	Anatomical Connectivity
AD	Alzheimer's disease
AM	Amplitude Modulation
AMPA	α-amino-3-hydroxy-5-methyl-4-isoazoleproprionic acid
BLP	Band-Limited Power
BOLD	Blood-Oxygen-Level Dependent
cc	Correlation Coefficient
CoCoMac	Collation of Connectivity on the Macaque brain
DMN	Default-Mode Network
DSI	Diffusion Spectrum imaging
DTI	Diffusion Tensor Imaging
ECoG	Electrocorticography
EEG	Electroencephalography/Electroencephalogram
FC	Functional Connectivity
FM	Frequency Modulation
fMRI	Functional Magnetic Resonance Imaging
Hb	Haemoglobin
IC	Independent Component
ICA	Independent Component Analysis
LFP	Local-Field Potential
MEG	Magnetoencephalography/Magnetoencephalogram
MNI	Montreal Neurological Institute
MRI	Magnetic Resonance Imaging
NMDA	N-methyl-D-aspartate acid
PCA	Principal Component Analysis
PET	Positron Emission Tomography
PhD	Doctor of Philosophy
ROI	Regions of Interest
RSN	Resting State Network
SC	Structural Connectivity
SPM	Statistical Parametric Mapping
SQUID	Superconducting Quantum Interference Device
std	Standard Deviation
SW	Small-Worldness